Dissertation

submitted to the

Combined Faculty of Mathematics, Engineering and Natural Sciences

of Heidelberg University, Germany

for the degree of

Doctor of Natural Sciences

Put forward by

Titus Franz

born in: *Münster, Germany*

Oral examination: *November 10, 2022*

STUDIES OF OUT-OF-EQUILIBRIUM DYNAMICS OF DISORDERED HEISENBERG SPIN MODELS ON A RYDBERG QUANTUM SIMULATOR

How the emergence of localized clusters induces glassy dynamics and inhibits thermalization

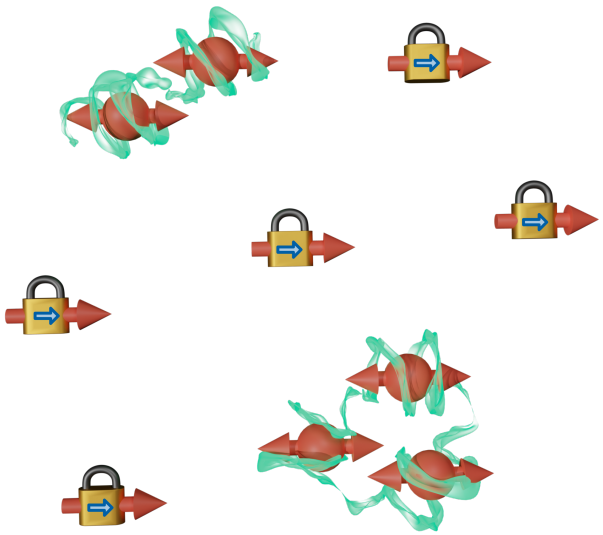

Referees: Prof. Dr. Matthias Weidemüller
Prof. Dr. Markus K. Oberthaler

ABSTRACT

In general, the dynamics of many-body quantum systems far-from-equilibrium is highly intricate, and it depends strongly on the initial conditions, the spatial geometry, and the type of the Hamiltonian. Nonetheless, at late times, almost all macroscopic systems will eventually lose memory of the initial state and thermalize. As a significant exception to this rule, strongly disordered systems can retain retrievable quantum correlations for long times, leading to a rich phenomenology ranging from anomalously slow relaxation to many-body localization (MBL).

This thesis studies the out-of-equilibrium dynamics of isolated, disordered quantum spin systems realized by a Rydberg quantum simulator where both the distribution of random coupling strengths and the type of the Hamiltonian can be tuned. In Part I, we observed sub-exponential, glassy dynamics well described by a stretched exponential law. This dynamics is independent of the type of Hamiltonian and the strength of disorder up to a critical value, showing a notion of universality in the relaxation dynamics of disordered systems far-from-equilibrium. A theoretical investigation revealed that the underlying nature leading to glassy dynamics is a scale-invariant distribution of interaction strengths. Part II reports on the discovery of the absence of thermalization in a quantum system out of thousands of spins. To achieve this, we developed a new protocol based on global magnetization measurements that can successfully distinguish thermalizing and non-thermalizing systems. Detailed exact numerical studies were able to confirm the breakdown of the Eigenstate Thermalization Hypothesis (ETH) for small strongly disordered systems of up to 16 spins. In addition, we have shown that pairs constitute effective integrals of motion providing thus an intuitive physical picture that also explains the universality of the relaxation dynamics. Both phenomena as described in Part I and II point toward the emergence of localization as the overarching principle governing out-of-equilibrium dynamics of disordered quantum spin systems.

ZUSAMMENFASSUNG

Im Allgemeinen ist die Dynamik von Nichtgleichgewichtszuständen von Quantenvielteilchensystemen hochgradig komplex und hängt stark von den Anfangsbedingungen, der räumlichen Geometrie und der Art des Hamiltonians ab. Trotzdem verlieren zu späten Zeiten fast alle makroskopischen Systeme die Information über ihren Anfangszustand und thermalisieren. Eine wichtige Ausnahme zu dieser Regel stellen stark ungeordnete Systeme dar, die rückgewinnbare Quantenkorrelationen für lange Zeiten beibehalten können, was zu vielseitigen Phänomenen führt, die von ungewöhnlich langsamer Relaxation bis zur Vielteilchenlokalisierung reichen.

Diese Arbeit studiert die Außergleichgewichtsdynamik von isolierten, ungeordneten Quantenspinsystemen, die in einem Rydbergquantensimulator realisiert werden, wobei sowohl die Verteilung der zufälligen Kopplungsstärken und die Art des Hamiltonians verändert werden können. In Teil I beobachten wir subexponentielle, gläserne Dynamik die durch eine gestreckte Exponentialfunktion beschrieben werden kann. Diese Dynamik ist unabhängig von der Art des Hamiltonians und bis zu einem kritischen Wert von der Unordnungsstärke, was von einer Form von Universalität der Relaxationsdynamik ungeordneter Außergleichgewichtssysteme zeugt. Eine theoretische Untersuchung ergab, dass gläserner Dynamik eine skaleninvariante Verteilung der Wechselwirkungsstärken zugrunde liegt. Teil II berichtet von der Entdeckung der Abwesenheit von Thermalisierung in Quantensystemen aus tausenden Spins. Um dies zu erreichen, wurde eine neues Protokoll entwickelt, welches auf globalen Magnetisierungsmessungen basiert, die erfolgreich zwischen thermalisierenden und nicht-thermalisierenden Systemen unterscheiden können. Detaillierte, exakte numerische Studien konnten den Zusammenbruch der Eigenzustandsthermalisierungshypothese für kleine, stark-ungeordnete Systeme aus bis zu 16 Spins bestätigen. Außerdem konnten wir zeigen, dass Paare effektive Integrale der Bewegung darstellen, wodurch ein intuitives physikalisches Bild bereitgestellt wird, welches auch die Universalität der Relaxationsdynamik erklärt. Beide Phänomene, die in Teil I and II beschrieben wurden, sprechen dafür, dass die Emergenz von Lokalisation das übergeordnete Prinzip darstellt, welches die Außergleichgewichtsdynamik von ungeordneten Quantenspinsystemen beherrscht.

PUBLICATIONS

This thesis is based on the following manuscripts and publications:

*These authors contributed equally to the work.

[1] Signoles*, A., **Franz*, T.**, Ferracini Alves, R., Gärttner, M., Whitlock, S., Zürn, G., and Weidemüller, M. **Jan. 2021**. "Glassy Dynamics in a Disordered Heisenberg Quantum Spin System." In: *Physical Review X* 11.1, p. 011011. ISSN: 2160-3308. DOI: 10.1103/PhysRevX.11.011011.

[2] Schultzen*, P., **Franz*, T.**, Geier, S., Salzinger, A., Tebben, A., Hainaut, C., Zürn, G., Weidemüller, M., and Gärttner, M. **Jan. 2022**. "Glassy Quantum Dynamics of Disordered Ising Spins." In: *Physical Review B* 105.2, p. L020201. DOI: 10.1103/PhysRevB.105.L020201.

[3] Schultzen*, P., **Franz*, T.**, Hainaut, C., Geier, S., Salzinger, A., Tebben, A., Zürn, G., Gärttner, M., and Weidemüller, M. **Mar. 2022**. "Semiclassical Simulations Predict Glassy Dynamics for Disordered Heisenberg Models." In: *Physical Review B* 105.10, p. L100201. DOI: 10.1103/PhysRevB.105.L100201.

[4] **Franz*, T.**, Geier*, S., Hainaut, C., Thaicharoen, N., Braemer, A., Gärttner, M., Zürn, G., and Weidemüller, M. **Sept. 2022**. "Observation of Universal Relaxation Dynamics in Disordered Quantum Spin Systems." In: DOI: 10.48550/ARXIV.2209.08080.

[5] **Franz, T.**, Geier, S., Hainaut, C., Signoles, A., Thaicharoen, N., Tebben, A., Salzinger, A., Braemer, A., Gärttner, M., Zürn, G., and Weidemüller, M. **July 2022**. "Absence of Thermalization in an Interacting System of Thousands of Quantum Spins." In: DOI: 10.48550/ARXIV.2207.14216.

[6] Braemer, A., **Franz, T.**, Weidemüller, M., and Gärttner, M. **July 2022**. "Pair Localization in Dipolar Systems with Tunable Positional Disorder." In: DOI: 10.48550/ARXIV.2207.14474.

The author furthermore contributed to the following manuscripts:

[7] Geier, S., Thaicharoen, N., Hainaut, C., **Franz, T.**, Salzinger, A., Tebben, A., Grimshandl, D., Zürn, G., and Weidemüller, M. **Nov. 2021**. "Floquet Hamiltonian Engineering of an Isolated Many-Body Spin System." In: *Science* 374.6571, pp. 1149–1152. ISSN: 0036-8075, 1095-9203. DOI: 10.1126/science.abd9547.

[8] Scholl, P., Williams, H. J., Bornet, G., Wallner, F., Barredo, D., Henriet, L., Signoles, A., Hainaut, C., **Franz, T.**, Geier, S., Tebben, A., Salzinger, A., Zürn, G., Lahaye, T., Weidemüller, M., and Browaeys, A. **Apr. 2022**. "Microwave Engineering of Programmable XXZ Hamiltonians in Arrays of Rydberg Atoms."

In: *PRX Quantum* 3.2, p. 020303. DOI: 10.1103/PRXQuantum.3.020303.

[9] Tebben, A., Hainaut, C., Salzinger, A., Geier, S., **Franz, T.**, Pohl, T., Gärttner, M., Zürn, G., and Weidemüller, M. **June 2021**. "Nonlinear Absorption in Interacting Rydberg Electromagnetically-Induced-Transparency Spectra on Two-Photon Resonance." In: *Physical Review A* 103.6, p. 063710. ISSN: 2469-9926, 2469-9934. DOI: 10.1103/PhysRevA.103.063710. arXiv: 2102.11654 [physics].

[10] Tebben, A., Hainaut, C., Salzinger, A., **Franz, T.**, Geier, S., Zürn, G., and Weidemüller, M. **Aug. 2021**. "A Stationary Rydberg Polariton." In: arXiv:2108.00657. DOI: 10.48550/arXiv.2108.00657. arXiv: 2108.00657 [quant-ph].

[11] Bharti, V., Sugawa, S., Mizoguchi, M., Kunimi, M., Zhang, Y., de Léséleuc, S., Tomita, T., **Franz, T.**, Weidemüller, M., and Ohmori, K. **Jan. 2022**. "Ultrafast Many-Body Dynamics in an Ultracold Rydberg-Excited Atomic Mott Insulator." In: DOI: 10.48550/arXiv.2201.09590.

[12] Salzinger, A., Geier, K., **Franz, T.**, Geier, S., Thaicharoen, N., Tebben, A., Hainaut, C., Ott, R., Gärttner, M., Hauke, P., Zürn, G., and Weidemüller, M. **Jan. 2022**. "Measuring the Fluctuation-Dissipation Relation of Single Driven Rydberg Qubits with Engineered Dephasing." In: *In preparation*.

[13] Ferreira-Cao, M., Gavryusev, V., **Franz, T.**, Alves, R. F., Signoles, A., Zürn, G., and Weidemüller, M. **Mar. 2020**. "Depletion Imaging of Rydberg Atoms in Cold Atomic Gases." In: *Journal of Physics B: Atomic, Molecular and Optical Physics* 53.8, p. 084004. ISSN: 0953-4075. DOI: 10.1088/1361-6455/ab7427.

CONTENTS

1 INTRODUCTION

On the question of which sentence contains the most information on physics captured by only a few words, Richard Feynman answers in his famous lecture series on physics with the atomistic worldview: "all things are made of atoms — little particles that move around in perpetual motion, attracting each other when they are a little distance apart, but repelling upon being squeezed into one another" [14]. According to Feynman, an enormous amount of information can be gained from this atomistic view of matter "if just a little imagination and thinking are applied". To give examples, Feynman explains based on the atomistic view how heat can be understood as the motion of molecules, how the phases of water are related to the arrangement of the atoms and he also describes how atomic processes or chemical reactions can be described based on microscopic models.

More generally speaking, Feynman addresses the idea to explain macroscopic phenomena by a microscopic description of matter. This approach is appealing since it promises to explain a plethora of phenomena like the expansion of a thermal gas [15] or phase transitions [16] from a simplistic model like a monoatomic ideal gas where the equations of motions of the elementary particles are typically well known and understood. But how could we possibly solve them for a macroscopic number of particles? A possible solution is provided by the *ergodic hypothesis* which was introduced by Boltzman in 1871 [17]. It states that the time a system spends in a certain region of phase space is proportional to the volume of the region. As a consequence, all interesting macroscopic properties like temperature or pressure of a system can be derived from a probability distribution of microstates, the statistical ensemble. Solving the exact time evolution of the many-body system is no longer required. Coming back to the sentence of Richard Feynman, we see that the ergodic hypothesis is a crucial assumption to simplify the microscopic description and to gain information from the atomistic view of matter.

In *classical* systems, the ergodic hypothesis is nowadays well understood as a consequence of non-linear equations of motion which lead to a chaotic time evolution. Due to chaos, the whole phase space is explored, and hence the system becomes ergodic. In contrast, the time-evolution of isolated *quantum* systems is determined by the Schroedinger equation which is linear, and hence not chaotic. In addition, for quantum systems, the concept of phase space is more complicated due to Heisenberg's uncertainty relation [18]. Therefore, no direct analog of chaos, ergodicity and thermalization exists for

quantum systems. Instead, we need to consider local subsystems which can build up entanglement with the rest of the quantum system. This allows to formulate the notion of ergodicity and thermalization for these local subsystems. In this thesis, we aim to benchmark the validity of these concepts by an experimental investigation of the far-from-equilibrium dynamics of disordered quantum spin systems.

The first objective of this thesis is to explore how a quantum system relaxes to equilibrium after a quench which prepares a system in a well-defined initial state far-from-equilibrium. Most classical systems will quickly become ergodic and reach thermal equilibrium after a quench. Let us consider for example two chambers, the left one is filled with a gas, and the right one contains a vacuum. After opening a door between the two chambers, the gas will uniformly fill both chambers, and the velocity of the particle will be perfectly characterized by the Maxwell distribution [19]. Especially, the system will have lost all memory of its initial state, whether at the beginning only the left or the right chamber was filled. However, some classical systems are not ergodic. Trivial examples are integrable systems like uncoupled harmonic oscillators. Beyond that, also in some complex many-body systems such as spin glasses, ergodicity can be broken because the dynamics are sufficiently slow such that the system remains out-of-equilibrium and does not explore the full phase space on experimentally relevant timescales [20, 21, 22]. In this thesis, we will explore whether disordered quantum systems can also break ergodicity in this sense and show anomalously slow relaxation dynamics after a quench. In addition, we will examine whether a notion of universal behavior exists that helps to understand these systems without the predictive power of ergodicity and thermal equilibrium.

Understanding the characteristics of the quantum system, once it is relaxed to a steady-state, is the second objective of this thesis. Especially, we aim to investigate whether this state is thermalized in the sense that the reduced density matrices of local subsystems are described by thermal ensembles [23]. The mechanism leading to quantum thermalization is the Eigenstate Thermalization Hypothesis (ETH) which states that almost all eigenstates of a generic, non-integrable many-body Hamiltonian are thermal in this sense [24, 25, 26]. Since, under very general conditions, quantum systems relax after a quench towards a steady-state compatible with the diagonal ensemble, i.e. the steady-state can be described as a mixture of eigenstates, the ETH ensures that the quantum system will eventually thermalize. Recently, many numerical studies [27, 28] and also some seminal experimental works [29, 30, 31] have shown that indeed most quantum systems thermalize and fulfill the ETH.

However, some notable exceptions exist where quantum systems do not thermalize according to ETH. Similar to classical systems, where integrability trivially leads to the breakdown of ergodicity, in-

tegrable quantum systems will never thermalize and be compatible with a microcanonical ensemble description because they feature an extensive number of conserved quantities [27]. A famous example for non-intuitive physics emerging in integrable systems is Anderson localization where strong disorder inhibits transport and local excitations remain localized even at infinite times [32].

If the integrability is broken by a small perturbation, the system is expected to exhibit prethermalization: After a quench, the system will relax first to a quasi-stationary, prethermal state being defined by the integrable part of the system's Hamiltonian before it possibly thermalizes on much longer time scales [33, 34, 35, 36, 23]. Strikingly, there have been indications that breaking the integrability of Anderson localizing systems by adding interactions leads to the phenomenon of many-body localization (MBL) where ETH is violated even at infinite times [37, 38]. These systems resemble integrable systems because strong disorder leads to the emergence of an extensive number of local integrals of motion (LIOMs) which are conserved quantities localized in finite regions of space [39, 40]. Therefore, similar to Anderson localization, transport is inhibited and the system never reaches thermal equilibrium. Many numerical studies of finite one-dimensional systems with disorder in external fields have shown the existence of MBL and investigated its characteristics like the properties of the eigenspectrum, the growth of entanglement, or the transition between a localized and a thermal regime as a function of disorder. However, the existence of an MBL phase in systems approaching thermodynamic limit has recently been questioned [41, 42, 43]. Especially, it remains an open question whether ETH can be violated in higher dimensional systems [41, 44, 45, 46, 42] and for off-diagonal disorder [47, 48, 49].

This difficulty to understand ETH and MBL is generic to many-body quantum systems and rooted in the so-called curse of dimensionality [50, 51]: Classical computers are not suited to brute-force solve high-dimensional problems, which is especially true for quantum systems where the dimension of the Hilbert space grows exponentially. This is problematic in peculiar for disordered quantum systems where finite-size effects strongly affect the study of quantum thermalization [28]. Therefore, in this thesis, we employ, in addition to exact diagonalization of small systems of up to 16 spins, also approximate methods like the semiclassical Discrete Truncated Wigner Approximation (DTWA) or Moving Average Cluster Expansion (MACE). For the integrable quantum Ising model, we derive an analytical solution for the dynamics, and we discuss physical intuition that can be gained from real-space renormalization group approaches [52, 53, 54, 55].

To overcome the limitations of small system sizes or approximate methods, quantum simulations can realize fully controlled model systems implemented by e.g. cold atomic gases [56, 57, 58, 59, 60, 61]. These experiments feature spatially resolved measurements which can

reveal the absence of transport and hence demonstrate the failure of thermalization [62, 63, 64, 65]. Moreover, recent works have achieved the direct detection of entanglement entropy as a microscopic probe of thermalization [29, 30, 31]. However, the scalability of these quantum simulations is limited due to the required full microscopic resolution.

In this thesis, complementary to the simulators with microscopic resolution, we implement systems with thousands of spins and use global observables to gain insight into the quantum systems of interest. We simulate the dynamics of a disordered quantum spin-1/2 system by exciting Rubidium-87 atoms to highly excited Rydberg states. The orbital radius of Rydberg atoms increases with the square of the principle quantum number n^2, therefore they possess enormous dipole moments [66]. This leads to strong dipolar or Van-der-Waals interactions between different Rydberg atoms [67]. These interaction strengths exceed the typical strength of external magnetic or electric noise, and also they are large compared to the spontaneous or blackbody decay rates of Rydberg atoms. This allows considering the Rydberg spin system as isolated during the dynamics. This property of Rydberg atoms is extremely important for this study to ensure that the relaxation dynamics are not induced due to coupling to a bath and that this bath does not thermalize the system.

In addition, the Rydberg platform is extremely versatile. For example, we can engineer different types of spin Hamiltonians depending on the choice of Rydberg states that constitute the spin-1/2 system [68, 69]. In addition, the Rydberg blockade effect imposes a minimal distance between the Rydberg spins [70, 71, 72] which allows tuning the strength of disorder in the system. A detailed explanation of how different spin Hamiltonians can be realized with Rydberg atoms, how microwave pulses allow the implementation of global spin rotations and how the magnetization can be measured via electric field ionization can be found in Chapter 2 of this thesis.

The thesis is organized as follows: First, we will give a short overview of how to use Rydberg atoms to explore many-body spin systems. This is followed by the two main parts of the thesis: Part I discusses universal slow relaxation dynamics in disordered quantum spin systems that is independent of the strength of disorder and the type of Hamiltonian. Part II reports on the absence of thermalization in systems consisting of thousands of spins, and it deduces an intuitive physical explanation of this phenomenon based on the localization of pairs. Each part features a detailed introduction to the main concepts, an outline of the research program and a conclusion of the main results. Finally, the last chapter presents an outlook on the next steps on the Heidelberg Rydberg quantum simulator platform which aim to explore the relation of isolated spin systems with random couplings to spin glasses and MBL through new experimental protocols and local measurements.

2 CONCEPTS: SPIN PHYSICS WITH RYDBERG ATOMS

Parts of this chapter are based on the publications Article [1] and [4], from which parts of the text have been taken verbatim.

This work studies the relaxation of isolated quantum spin systems. Part I focuses on the relaxation dynamics themselves, concluding that the interplay of disorder and unitary quantum dynamics leads to the build-up of entanglement within small clusters of spins leading to a unifying description of the resulting glassy dynamics via the stretched exponential law. Part II discusses whether the steady state is compatible with a thermal ensemble description leading to the discovery of the absence of thermalization in strongly disordered isolated quantum systems. Despite addressing a different phenomenology, the two parts share similar experimental challenges, and they benefit from the great versatility of the Rydberg quantum simulator platform to tune the type of interactions.

2.1 RYDBERG ATOMS AS A VERSATILE QUANTUM SIMULATOR PLATFORM

In this section, we first provide a comprehensive description of how to engineer a spin-1/2 Hamiltonian with different combinations of Rydberg states [74, 69]. Depending on the choice of the Rydberg states, this allows for tuning both the interaction range and also the type of interaction. In the second part of the section, we will discuss how the Rydberg blockade effect can be used to tune the strength of disorder in the spin system. This tuning of the disorder strength will allow us to investigate how disorder affects the unitary quantum dynamics of isolated quantum spin systems, and it will enable us to drastically

(a) Heidelberg Rydberg lab

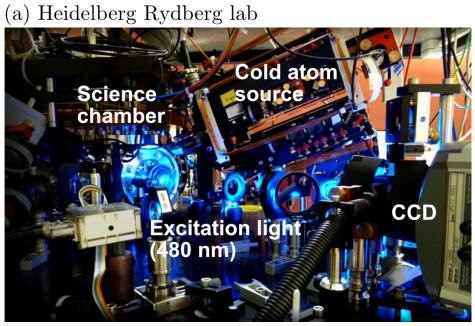

(b) Rydberg detector

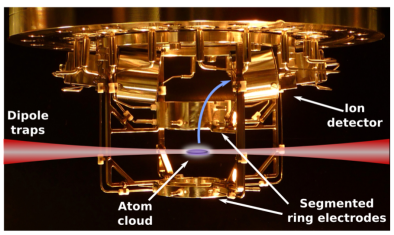

Figure 2.1: Fotograph of the Heidelberg Rydberg experiment (a) and the Rydberg detector (b). Adapted from [73].

modify the properties of the system from a thermalizing regime to a non-thermalizing regime.

2.1.1 *Realizing different Heisenberg XXZ-Hamiltonians with Rydberg atoms*

We consider a spin-1/2 system interacting with the following Heisenberg Hamiltonian ($\hbar = 1$)

$$\hat{H} = \sum_{i<j} \left(J_{ij}^{\perp}/2(\hat{s}_{+}^{i}\hat{s}_{-}^{j} + \hat{s}_{-}^{i}\hat{s}_{+}^{j}) + J_{ij}^{\parallel}\hat{s}_{z}^{i}\hat{s}_{z}^{j} \right). \tag{2.1}$$

Here, $\hat{s}_{+-}^{i} = \hat{s}_{x}^{i} \pm i\hat{s}_{y}^{i}$, where $\hat{s}_{\alpha}^{i}(\alpha \in x, y, z)$ are the spin-1/2 operator of spin i.

For general spin systems with global $U(1)$ symmetry, the coupling terms can be obtained by calculating the matrix elements of the interaction Hamiltonian. The Ising term

$$J_{ij}^{\parallel} = (E_{\uparrow_i\uparrow_j} + E_{\downarrow_i\downarrow_j}) - (E_{\downarrow_i\uparrow_j} + E_{\uparrow_i\downarrow_j}) \tag{2.2}$$

is defined as the energy difference between spins being aligned and being anti-aligned. Here, $E_{\alpha_i\beta_j} = \langle \alpha_i\beta_j|\hat{H}|\alpha_i\beta_j\rangle$ are the interaction energy of spin i and j with $\alpha, \beta \in [\uparrow, \downarrow]$. The exchange term is determined by

$$J_{ij}^{\perp} = \langle \downarrow_i\uparrow_j |\hat{H}| \uparrow_i\downarrow_j \rangle . \tag{2.3}$$

For a system consisting of states with opposite parity (see Figure 2.2 (b)), such as $|\downarrow\rangle = |nS\rangle$ and $|\uparrow\rangle = |nP\rangle$, where n is the principal quantum number, the dominant coupling is a direct dipolar interaction and can be described by the Hamiltonian

$$\hat{H}_{\mathrm{DDI}} = \frac{\hat{\mathbf{d}}_i \cdot \hat{\mathbf{d}}_j - 3\left(\hat{\mathbf{d}}_i \cdot \mathbf{e}_{r_{ij}}\right)\left(\hat{\mathbf{d}}_j \cdot \mathbf{e}_{r_{ij}}\right)}{r_{ij}^3}. \tag{2.4}$$

where $\hat{\mathbf{d}}_i$ is the dipole operator of atom i, $\mathbf{e}_{r_{ij}}$ is the unit vector connecting the two atoms and r_{ij} their distance. Mapped on the spin Hamiltonian of Eq. 2.1, the resulting interaction coefficient is $J_{ij}^{\perp} = \frac{C_3^{\perp}(1-3\cos^2\theta_{ij})}{r_{ij}^3}$ [75, 76]. Here, θ_{ij} is the angle between $\mathbf{e}_{r_{ij}}$ and the quantization axis and $C_3^{\perp}$ the coupling parameter. The Ising term $J_{ij}^{\parallel}$ is not present since interaction energy shifts $E_{\alpha_i\beta_j}$ are dipole forbidden. The strength of the dipolar interactions scales with the principle quantum number as n^4 [77], for example for a system of $61S$ and $61P$ states, the coupling constant is given by $C_3^{\perp}/2\pi = 3.14\,\mathrm{GHz}\,\mu\mathrm{m}^3$.

If the two states possess the same parity, such as the two atoms being in the same state nS, direct dipolar coupling is forbidden. Instead, the

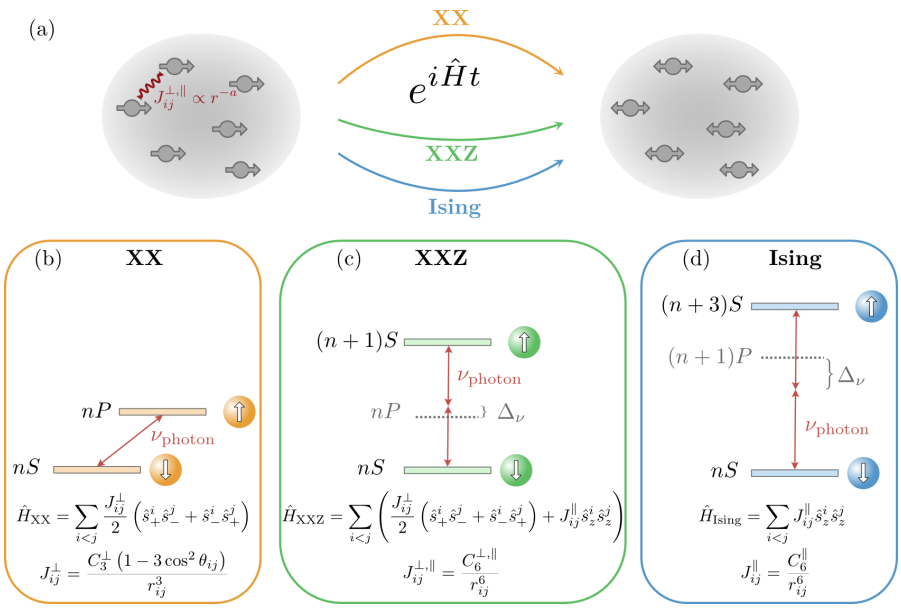

Figure 2.2: (a) Spins that are randomly distributed in space and interact via power-law interactions. The disorder can be decreased by the Rydberg blockade effect which imposes a minimal distance between the spins. The underlying Hamiltonian can be tuned by the choice of Rydberg states leading to Heisenberg XX (b), XXZ (c) or Ising (d) interactions. Adapted from Article [4].

interaction is a second-order process through a virtually excited pair state $|m\rangle$ and can be described by

$$\hat{H}_{vdW} = -\frac{1}{\hbar}\sum_m \frac{\hat{H}_{\mathrm{DDI}}\,|m\rangle\,\langle m|\,\hat{H}_{\mathrm{DDI}}}{\Delta_\nu}. \tag{2.5}$$

Here, the Foerster defect Δ_ν is the energy difference between the initial state and the virtually excited state $|m\rangle$. This Hamiltonian gives rise to power-law interactions $J_{ij} = C_6/r_{ij}^6$ that can be extremely large for Rydberg states as the interaction scales with n^{11}. Especially, this term is large if a pair state m with a small Foerster defect and a large dipolar coupling exists.

For example, an initial state $|\uparrow_i\uparrow_j\rangle = |nS, nS\rangle$ couples mainly to the pair state $|m\rangle = |(n-1)P, nP\rangle$. This gives rise to an energy offset $E_{\uparrow_i\uparrow_j}$ if two atoms are in the same Rydberg state. Many experiments exploit this effect by realizing a spin system where the ground state is coupled to a single Rydberg state, which can be mapped on an Ising model [78, 79, 80].

Similar interactions also exist for a spin system realized with two different Rydberg states $|\downarrow\rangle = |nS\rangle$ and $|\uparrow\rangle = |(n+1)S\rangle$ for all energy shifts in the Ising term (2.2). In addition, the Van-der-Waals Hamiltonian (2.5) can also induce the spin exchange term $J^\perp$ defined in (2.3) via the intermediate pair state $|m\rangle = |nP, nP\rangle$ (see Figure 2.2 (c)). In the case of $n = 61$, the Foerster defects of both the Ising and exchange

interactions are similar, therefore also the interactions are comparable resulting in $J^{\parallel}/J^{\perp} = 0.7$. Therefore, this spin system can be mapped onto an effective Heisenberg XXZ-Hamiltonian [1].

In order to realize an Ising Hamiltonian with two different Rydberg states, a state combination is needed where the exchange term (2.3) is small. This can be achieved by coupling $|\downarrow\rangle = |nS\rangle$ to $|\uparrow\rangle = |(n+3)S\rangle$. In this case, the largest contribution to the exchange term comes from $|m\rangle = |(n+1)P, (n+1)P\rangle$ where the Foerster defect is increased by an order of magnitude (see Figure 2.2 (d)) and also the matrix elements are small. For example, for $n = 61$, this spin system is characterized by a ratio of $J^{\parallel}/J^{\perp} = 400$, which is a good approximated to an Ising Hamiltonian ($J^{\perp} = 0$).

2.1.2 *Excitation of Rydberg spins*

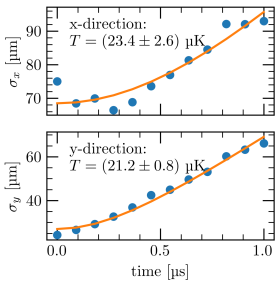

Figure 2.3: Time-of-flight measurement of the dipole trap to determine the temperature T. The orange line shows a fit of $\sqrt{w^2 + 2k_b T t^2/m_{Rb}}$ where w is the diameter of the dipole trap and m_{Rb} the mass of Rubidium.

To implement a Rydberg spin system in the experiment (see Figure 2.1 (a)), we prepare a gas of ^{87}Rb atoms in their electronic ground state $|g\rangle = |5S_{1/2}, F = 2, m_F = 2\rangle$ in an optical dipole trap at a temperature $T \sim 20\,\mu$K (see Figure 2.3). This temperature is low enough to freeze the motional degrees of freedom over the time scale of 10 µs of the experiment.

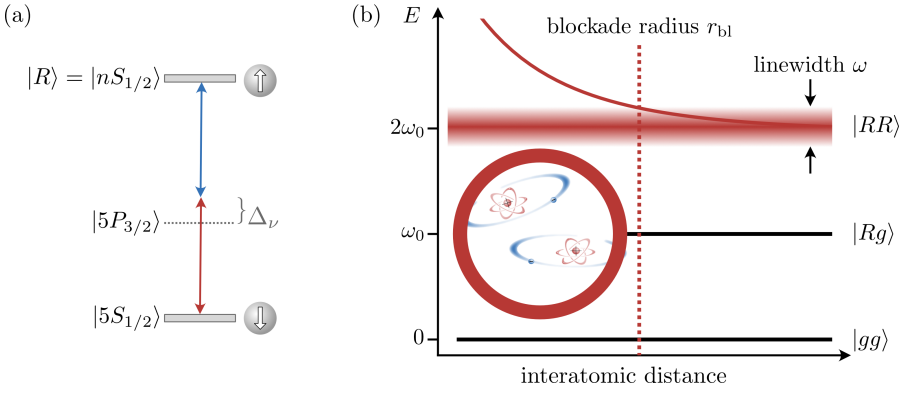

Figure 2.4: (a) Level scheme for the two-photon Rydberg excitation process. (b) Schematic of the Rydberg blockade effect.

A laser pulse of variable duration brings a controllable number of up to 4000 atoms to the $|\downarrow\rangle = |nS_{1/2}, m_j = +1/2\rangle$ Rydberg state where n is chosen typically between 48 and 61. For this we use a two-photon laser excitation at 780 nm and 480 nm, with a detuning $\Delta_\nu = 2\pi \times 100$ MHz from the intermediate state $|e\rangle = |5P_{3/2}, F = 3, m_F = 3\rangle$(see

Figure 2.4 (a)). During this process, the strong Van-der-Waals interactions $J(r) = C_6/r^6$ between atoms shift the atoms out of resonance if the interaction strength exceed the excitation bandwidth ω (see Figure 2.4 (b)). This prevents two atoms from being excited to Rydberg states if the distance is smaller than the blockade radius

$$r_{\mathrm{bl}} = \sqrt[6]{\frac{C_6}{\hbar\omega}}. \tag{2.6}$$

In the experiments presented in this thesis, the excitation bandwidth is typically Fourier limited by the duration of the excitation pulse. For example, the blockade effect induces a minimal distance of 5 µm for the Rydberg state $|48S\rangle$ for an excitation of 1 µs.

2.1.3 *Tuning the strength of disorder by the Rydberg blockade effect*

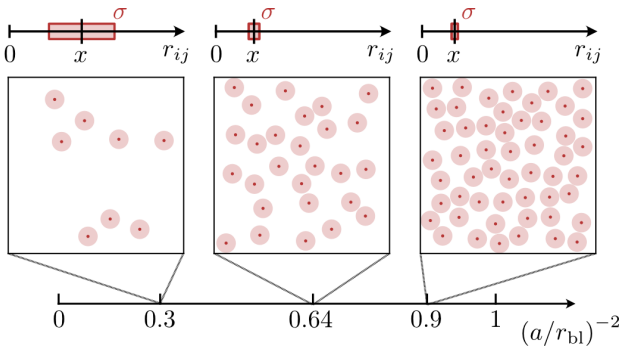

Figure 2.5: 2D illustration of how the Rydberg blockade affects the strength of disorder. At low density, the spins are randomly spaced and the standard deviation σ of the interparticle distances $\min_{i\neq j} r_{ij}$ is large (represented by the bar centered around the mean interparticle distance x). Increasing the density (left to right panel) decreases the strength of disorder characterized by the mean number of spins per blockade radius $(a_0/R_{\mathrm{bl}})^{-2}$. Adapted from Article [1].

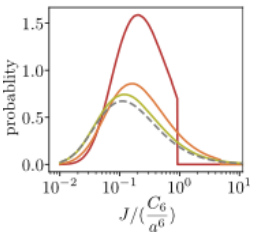

Figure 2.6: Probability distributions of nearest-neighbor interaction strengths for three different blockade radii (red line: large blockade radius, green line: small blockade radius). The dashed grey line shows the distribution of randomly placed spins. Adapted from Article [1].

The Rydberg blockade is an interesting many-body effect that is studied in many quantum simulation experiments which map the Rydberg excitation on an Ising spin system [78, 79, 80]. In this thesis, the excitation to the Rydberg state is only the preparation that determines the spatial Rydberg distribution, afterward, the excitation lasers are switched off, and the interaction with the ground states can be neglected.

At first glance, the Rydberg excitation influences mostly the density ρ. To the density, we can attribute a typical length scale of the system given by the typical interparticle distance which can be represented by the Wigner-Seitz radius $a = (4\pi\rho/3)^{-1/3}$. A high density or small interparticle distance would increase the typical interaction strength

leading to faster dynamics. However, this effect could be trivially compensated by rescaling time with interaction strength and it should not change the spin dynamics qualitatively. However, the Rydberg blockade effect introduces a second length scale which imposes a minimal interparticle distance or maximal interaction strength to the system. Therefore, rescaling time with density can not balance the effect of both length scales, a and r_{bl}, and the probability distribution functions of the nearest-neighbor interaction strengths differ qualitatively from each other (see Figure 2.6).

The ratio between blockade radius r_{bl} and Wigner-Seitz radius a can be seen as a way to control the degree of disorder (see Figure 2.5): For $a \gg r_{\mathrm{bl}}$ the blockade effect has little influence and the spins are randomly distributed, whereas the limit $a \approx r_{\mathrm{bl}}$ corresponds to a strongly ordered configuration. In between, the short distance cutoff imposed by the Rydberg blockade effect effectively reduces the strength of the disorder compared to fully uncorrelated random spin positions.

Another possibility to quantify disorder is to compare the blockade radius to $r_{\mathrm{max}} = 2[3\eta_{\mathrm{cp}}/(4\pi\rho)]^{1/3}$ which corresponds to the distance between the spins in a close-packed arrangement at same density ρ and packing fraction $\eta_{\mathrm{cp}} = \pi/\sqrt{18} \approx 0.74$. Here, $r_{\mathrm{bl}} = 0 r_{\mathrm{max}}$ corresponds to a fully disordered random system, and $r_{\mathrm{bl}} = r_{\mathrm{max}}$ describes the configuration of close-packing which can be found in a hexagonal close packing (hpc) or face-centred cubic (fcc) lattice without any disorder.

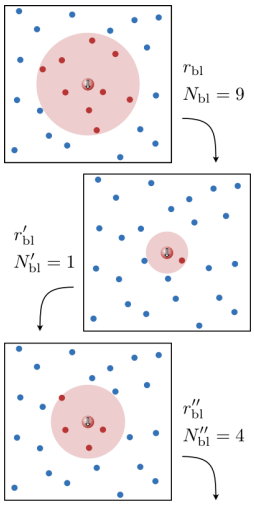

Figure 2.7: Self-consistent method to calculate the blockade radius. For a given blockade radius, the number of blockaded atoms N_{bl} is calculated which enhances the collective Rabi frequency by $\sqrt{N_{\mathrm{bl}}}$. The associated power broadening alters the blockade radius, again changing N_{bl}. This calculation is iterated until convergence. Adapted from [81].

2.1.4 *Imaging and simulation of the density distribution of Rydberg atoms*

To model the experimental 3D spin distribution, we employ a simplified description of the Rydberg excitation dynamics in a cloud of ground-state atoms [82, 83, 84, 81]. Although the experimental procedure creates a superposition of different configurations of atoms being excited to the Rydberg state, each configuration of this superposition can be regarded as an independent disorder realization. Indeed, the different configurations evolve independently from each other under the spin dynamics, and the final projective measurement randomly selects one of them. Thus, to create samples of such configurations of Rydberg excitations we iteratively select atoms randomly and excite them to the Rydberg state with a certain excitation probability which we set to zero if another atom within a distance of r_{bl} is already in the Rydberg state. The excitation probability includes a collective enhancement factor caused by the Rydberg blockade effect [71, 72, 85] (see Figure 2.7). We also take into account the spatial profile of the laser excitation, and the Gaussian density distribution of the ground-state atomic cloud. In our simulations, the peak two-photon Rabi frequency

was chosen such that the total number of excited atoms equals the one measured by field ionization.

2.2 COHERENT MANIPULATION OF RYDBERG SPINS

For both parts of this work, it is crucial that the experimental realization of the quantum system is well isolated from the environment such that the relaxation is not induced by decoherence caused by coupling to an external bath but by the build-up of entanglement generated by interactions within the quantum system. In addition, the experiments require a microwave setup that does not induce further decoherence effects and allows realizing pulse with arbitrary phases to enable pulse sequences like spin locking or a tomographic readout of the magnetization.

2.2.1 *Fast Rabi oscillations*

To accomplish $\pi/2$-pulses on time scales much faster than the typical interaction strength, it is decisive to realize fast and coherent Rabi oscillations. The Rabi oscillations are realized by coupling the Rydberg states using microwave radiation created by the Keysight M8195A arbitrary waveform generator (AWG). This features a resolution of 8 bit, a sample rate of 65 GSa/s and an analog bandwidth of 25 GHz which is sufficient to directly drive transition between $|nS_{1/2}\rangle$ and $|nP_{1/2}\rangle$ for a principal quantum number $n \geq 54$. Lower Rydberg states can be addressed by mixing the signal of the AWG with the Anritsu MG3697C signal generator that can output microwave frequencies up to 70 GHz. For some measurements as in Article [5], it is required to achieve high power for a fast $\pi/2$-pulse, followed by a spin-locking pulse at low fields. For these measurements, the increased sampling rate of 14 bit of the Keysight M8190A AWG (8 GSa/s sampling rate) is beneficial.

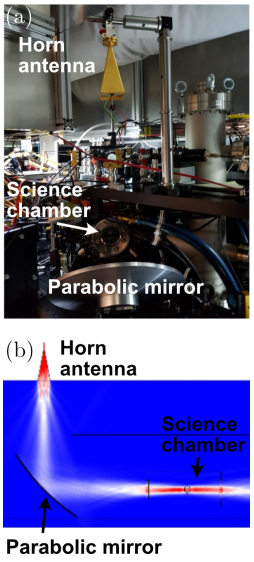

Figure 2.8: (a) Fotograph of the Rydberg microwave setup. (b) COMSOL® simulation of the microwave radiation. Adapted from [86].

To suppress the microwave coupling to unwanted transitions, we set up a microwave setup with a clean polarization [86]. For this purpose, we focus the microwave with a concave mirror into the science chamber and dump the outgoing radiation after the chamber in microwave absorbing foam. This avoids additional reflections from metallic surfaces with undefined polarization. As a result, the measured Rabi frequency for the transition $|48S_{1/2}, m_j = 1/2\rangle \leftrightarrow |48P_{3/2}, m_j = 1/2\rangle$ is approximately ten times larger compared to the unwanted transition $|48S_{1/2}, m_j = 1/2\rangle \leftrightarrow |48P_{3/2}, m_j = 3/2\rangle$. An additional benefit of this microwave setup is reduced shot-to-shot fluctuations and drifts of the microwave power which are typically caused by temporal varying reflections.

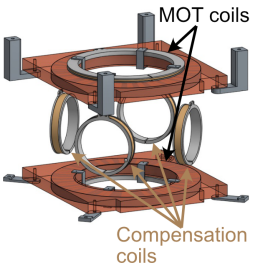

Figure 2.9: Setup of the magnetic fiel coils of the Rydberg experiment. Only the large MOT coils are water-cooled and do not overheat even at magnetic fields of up to 260 G.

With this microwave setup, and since Rydberg atoms possess large dipole moments, it would not be difficult to reach microwave radiation

with electric fields corresponding to Rabi frequencies of multiple GHz. However, to obtain a clean spin-1/2 system, special care needs to be taken that no additional Rydberg states are populated due to the microwave radiation. Therefore, we apply a strong magnetic field of up to 130 G which energetically splits the states with different magnetic quantum numbers. This large magnetic field is achieved by using the large and water-cooled MOT coils (see Figure 2.9) instead of the previously used compensation coils which would heat and break at the large currents required for these magnetic field strengths. To switch between the Antihelmholtz configuration required to realize the gradient field needed for the MOT and the Helmholtz configuration required for the constant magnetic field used during the Rydberg experiment, we invert the direction of the current in one of the MOT coils using an H-bridge.

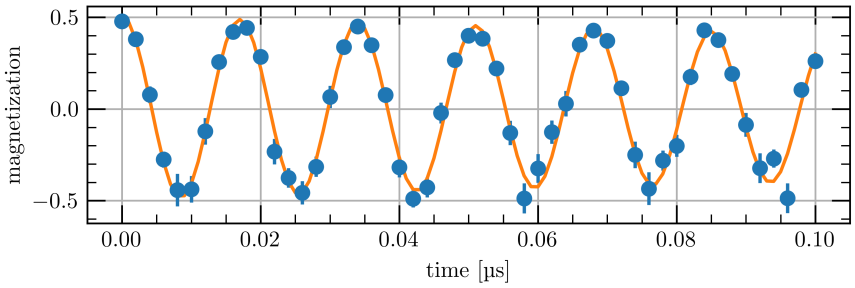

Figure 2.10: Rabi oscillations at 59 MHz between the Rydberg states $|48S\rangle$ and $|48P\rangle$. The orange line is a fit with a damped cosine oscillation.

Combining the large splitting of the magnetic Rydberg levels and the clean microwave setup, we achieve coherent Rabi oscillations of up to 60 MHz (see Figure 2.10). Additionally, we can generate an arbitrary microwave waveform. This was used to build pulse sequences for Floquet Hamiltonian engineering [87, 88] or to engineer dephasing which allows measuring the fluctuation-dissipation theorem [89]. In this thesis, the microwave is used to read out the magnetization in the xy-plane tomographically and to implement the spin-locking field (see Figure 2.11).

2.2.2 *Coherence times of the Rydberg spin system*

To achieve an isolated quantum spin system, we exploit the large dipole moment of Rydberg atoms leading to interaction strengths exceeding the typical decoherence effect like the Rydberg lifetime or fluctuations of the external fields. For example, exciting the Rydberg state $48S$ leads to a blockade radius of approximately $r_{\mathrm{bl}} \approx 5\,\mu\mathrm{m}$. For example, at this minimal distance, the dipolar interactions of the spin system $48S - 48P$ are $J^{\perp} = C_3/r_{\mathrm{bl}}^3 = 2\pi \times 9.2\,\mathrm{MHz}$ and the Van der

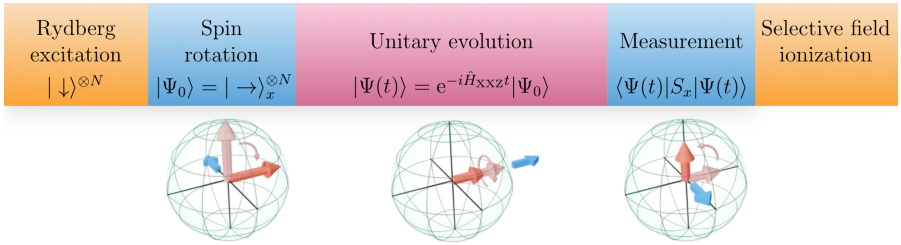

Figure 2.11: Experimental protocol for a Ramsey sequence. After Rydberg excitation of the $|\downarrow\rangle$ Rydberg state, a microwave $\pi/2$-pulse creates a superposition state. This state evolves unitarily either without a field applied (Ramsey sequence), or a microwave field 90° phase shifted with respect to the first $\pi/2$-pulse creates a spin locking field. Afterward, a second $\pi/2$-pulse with varying phases tomographically rotates the magnetization in the xy-plane to the z-direction. Finally, the z-magnetization is measured via state selective field ionization (see Section 2.3). Adapted from Article [1].

Waals interactions of $48S - 49S$ are $J_\perp = C_6/r_{\text{bl}}^6 = 2\pi \times 3.8\,\text{MHz}$. Consequently, the atoms undergo up to 100 interaction cycles within the typical experimental duration of 10 µs during which the spin system reaches the steady state. This time can still be considered short compared to the Rydberg spontaneous lifetime of 113 µs which determines the rate of Rydberg atoms decaying to the ground state. Since the interaction with the groundstate atoms can be neglected, this process does not directly reduce the coherence within the spin-1/2 manifold but effectively spins are removed from the system. Additionally, black body radiation from the 300 K hot vacuum chamber induces population transfer to energetically close Rydberg states at a rate of 9 kHz. This is the main source of decoherence and ultimately limits the coherence time of the Rydberg quantum simulator.

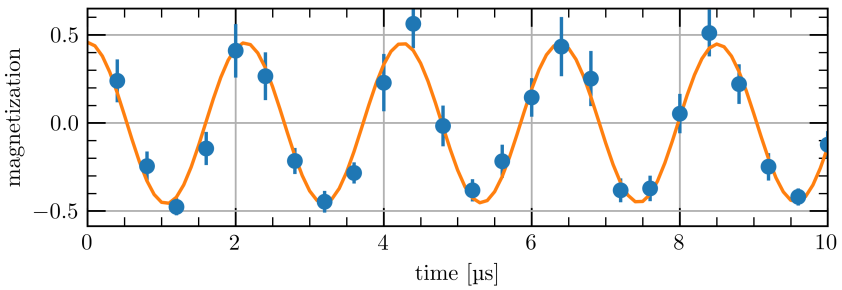

Figure 2.12: Ramsey oscillations at a detuning of 470 kHz between the Rydberg states $|48S\rangle$ and $|49S\rangle$. The orange line is a fit with a damped cosine oscillation. Adapted from Article [1].

To exclude other sources of decoherence like noise in magnetic or electric fields, we observe Ramsey oscillations at low densities where interactions are negligible (see Figure 2.12). These oscillations are perfectly coherent for experimental times of 10 µs. This measurement proves that decoherence effects on single atoms can be neglected. In addition, the Ramsey oscillations allow us to precisely determine the resonance frequency between the Rydberg states.

2.3 MEASUREMENT OF THE MAGNETIZATION BY FIELD IONIZATION

In the two previous sections, we have seen that Rydberg atoms feature strong and tunable interactions, long lifetimes, and they can be coherently controlled by fast microwave pulses. Here, we want to discuss how to detect Rydberg atoms and reconstruct the magnetization of the Rydberg spin system using field ionization. The magnetization

$$M_z = \frac{N_\uparrow - N_\downarrow}{2(N_\uparrow + N_\downarrow)} \tag{2.7}$$

of a Rydberg spin-1/2 system is defined as the difference of the populations $N_\updownarrow$ between the states $|\uparrow\rangle$ and $|\downarrow\rangle$. These can be measured individually by *selective field ionization* where the electric field is slowly ramped up such that the different states ionize at different times. Alternatively, one of the states can be *optically de-excited* and only the remaining atoms are ionized. This latter method requires a calibration measurement of the total atom number $N_{\text{tot}} = N_\uparrow + N_\downarrow$.

2.3.1 *Field Ionization of Alkali Rydberg atoms*

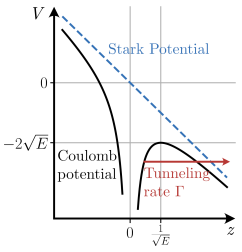

Figure 2.13: The Coulomb-Stark potential of a Rydberg atom in an electric field $\mathcal{E}$. The red arrow illustrates the tunneling process of the electron through the potential barrier.

The principle idea of Rydberg field ionization is to apply a strong electric field $\mathcal{E}$ in z-direction which imposes a potential gradient $\mathcal{E}z$ (blue dashed line in Figure 2.13). Combined with the Coulomb potential of the atomic core, the valence electron experience the potential

$$V_{\text{ionization}}(z) = -1/z + \mathcal{E}z \tag{2.8}$$

which is shown by the solid black line in Figure 2.13. This potential features a saddle point at $z = 1/\sqrt{\mathcal{E}}$ where the potential has a value of $V_{\text{b}} = -2\sqrt{\mathcal{E}}$. For the ionization process to occur classically, the energy of the Rydberg state needs to be above this potential barrier. This condition leads to the classical ionization threshold for a state with principle quantum number n (neglecting centrifugal potential and quantum defects) of

$$\mathcal{E}_{\text{classical}} = 1/16n^4. \tag{2.9}$$

In a quantum system, the electron can additionally tunnel through the barrier (indicated by the red arrow in Figure 2.13) at a rate Γ [90, 91, 92, 93].

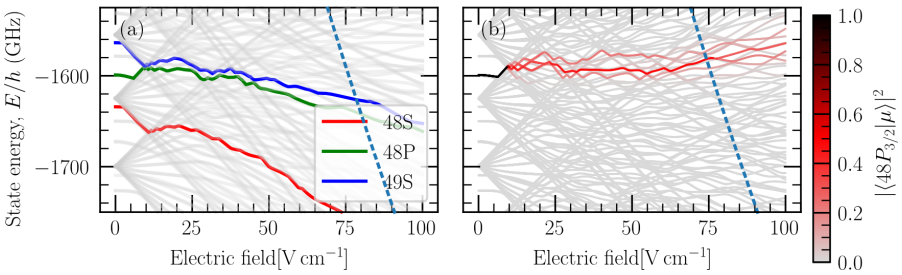

Figure 2.14: Stark map of the Rubidium atom. The grey lines show the energy of various Rydberg states. The dashed blue line represents the classical ionization threshold V_b. (a) The evolution of the states $48S$, $48P$ and $49S$ assuming adiabatic level crossings are highlighted in color. (b) The passage through the Stark map of the state $48P$ for a slow ramp of 60 µs. The Stark map was calculated using the ARC [94].

This simplified model of ionization ignores the Stark effect of the electric field which shifts the energy levels of the Rydberg atom and induces a multitude of avoided crossings (see Figure 2.14). Therefore, the time evolution of a Rydberg state through the Stark map strongly depends on how fast the electric field is increased leading to drastically different ionization fields depending on the field ramp. For example, Figure 2.14 (a) shows the time evolution of the Rydberg states $48S$ (red), $48P$ (green), and $49S$ (blue) assuming only adiabatic level crossings, i.e. an infinite slow ramp. For all these states, the Stark effect decreases the energy such that the states become more difficult to ionize compared to equation (2.9). Interestingly, the time evolutions of the states $48P$ and $49S$ meet at the first crossing of two different hydrogen manifolds, the so-called Inglis-Teller limit [95]. After this point, the passages through the Stark map are alike and the two different states ionize at similar field strengths. Therefore, it is possible to distinguish the spin systems $nS - nP$ or $nS - (n+1)S$ via field ionization, but not $nP - (n+1)S$.

For a more realistic ramp where the field is linearly increased within 10 µs from 0 to 100 V cm^{-1}, only the first avoided crossing is transitioned adiabatically. For larger fields, the system is partly adiabatic and diabatic leading to a spread of the population into different Rydberg states which ionize at slightly different times. For heavy atoms like Rubidium, this broadening is typically found to be on the order of 8% of the ionization field [96, 97], and can be even larger if the slew rate is too large and the avoided crossings at low electric fields below the Inglis-Teller limit are also partly diabatic [98].

2.3.2 *Experimental setup and peak detection*

To ionize the Rydberg atoms in the Heidelberg Rydberg experiment, we can apply voltages to segmented ring electrodes which creates a constant electric field at the positions of the atomic cloud (see Figure 2.1 (b)). The ions are then guided by two deflection electrodes towards a multichannel plate (MCP) ion detector (Hamamatsu F1551-21S) where the individual ions induce an electron avalanche which can be temporally resolved on an oscilloscope. The MCP allows for detecting a large number of ions before saturating because each channel of the MCP saturates independently. The detection efficiency of 40% is mostly determined by the open area ratio of the MCP.

An important experimental upgrade enabling selective field ionization was to build a high voltage amplifier that can generate field ramps at arbitrary slew rates and voltage thresholds [99]. Importantly, the electronic circuit needed to be designed such that the amplifier can also produce small offset fields with low noise which allows tuning the type of interactions of the spin system and does not induce further sources of decoherence for the spin experiments.

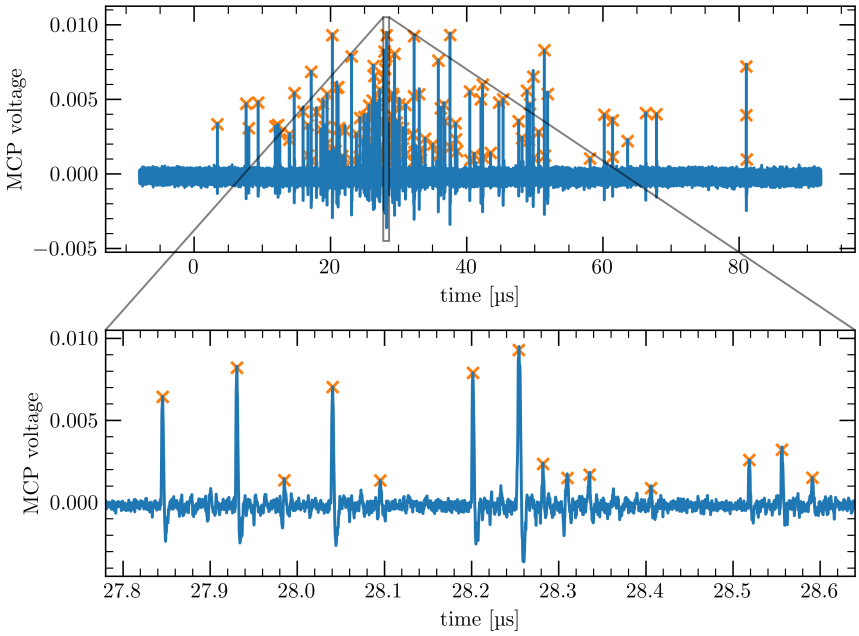

Figure 2.15: Typical voltage trace obtained from field ionization of the Rydberg state $|48P\rangle$. The electric field was ramped from 0 to 175 V cm^{-1} within 60 µs. The bottom plot shows a zoom of the signal into the highlighted region. The orange crosses highlight the peaks identified as ions by the peak-finding algorithm.

In experiments prior to the new high voltage amplifier, the electric field was switched on within a fraction of a microsecond. As a conse-

quence, the ions have also arrived bunched on the detector within less than a microsecond. Firstly, this resulted in overlapping peaks that could no longer be differentiated leading to an early saturation of the ion signal. Secondly, selective field ionization was impossible because the duration of switching on the electric field was small compared to the width of the arrival times of the peaks. The new amplifier has allowed realizing controlled field ramps where the electric field is increased within tens of microseconds from 0 to $175\,\mathrm{V\,cm^{-1}}$. For these slow ramp speeds, the ions arrive at the detector well separated in time within tens of microseconds (see Figure 2.15) which enables counting single peaks and has increased the saturation threshold of the detector.

2.3.3 *Magnetization reconstruction by state selective field ionization*

To reconstruct the magnetization via selective field ionization, we first take two calibration measurements to determine the typical distribution of arrival times of ion peaks for each Rydberg spin state.

The green histograms in Figure 2.16 show the density $\rho(t|M = +1/2)$ of ion peaks as a function of the arrival time t for the Rydberg state $|\uparrow\rangle = |48S\rangle$ for four different electric field ramps. Increasing the ramp time from 10 µs (top histogram) to 90 µs (bottom histogram) delays the average arrival time and increases the width of the distribution.

The Rydberg state $|48P\rangle$ has a larger energy level and are therefore expected to ionize slightly earlier compared to $|48S\rangle$. Indeed, the distribution $\rho(t|M = -1/2)$ of arrival times (orange histograms in Figure 2.16) is slightly shifted to earlier times compared to $|48S\rangle$. For the fast ramp of 10 µs (top histogram), this difference is only small and the two different distributions are barely distinguishable. For slower ramps of 30 µs to 60 µs, the relative distance between the maxima of the distributions is comparable to the widths of the distributions. In this regime, reconstructing the magnetization from the arrival times of the ions on the detector is possible. If the ramp is chosen to be too slow (90 µs ramp time), the relative distance between the peaks does not increase further, but the noise floor is substantially larger which effectively decreases the signal.

To infer the magnetization of a Rydberg system with unknown magnetization M, we can assume that the distribution $\rho(t|M)$ of arrival times of ions on the detector is a superposition of the distributions $\rho(t|M = \pm 1/2)$ where only a single state is populated:

$$\rho(t|M) = (\frac{1}{2} + M)\rho(t|M = +1/2) + (\frac{1}{2} - M)\rho(t|M = -1/2) \quad (2.10)$$

This function can be fitted to the measured distribution of arrival times, the best fit of M determines the most probable magnetization.

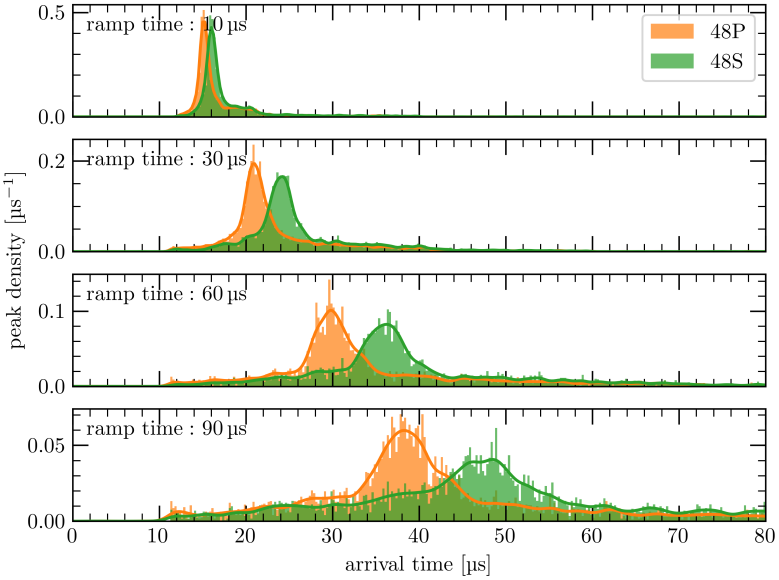

Figure 2.16: Histograms of the arrival times of the ion signals obtained by field ionization of the Rydberg states $|48S\rangle$ (green) and $|48P\rangle$ (orange) for linear electric field ramps from 0 to 175 V cm^{-1} within varying ramp times.

Alternatively, we can make use of Bayes theorem [100, 101] to calculate the posterior probability given the measured arrival times of ions

$$\rho(M|t) = \frac{\rho(t|M)\rho M}{\rho(t)} \tag{2.11}$$

where $\rho(M)$ is the prior and $\rho(t)$ the marginal probability. Without any assumptions on the measurement, the prior can be assumed to be uniform leading, in this case, the magnetization can be calculated from the maximum likelihood estimator. For multiple independent measured arrival times t_i, this can be calculated by minimizing

$$-\sum_i \log \rho(t_i|M) \; . \tag{2.12}$$

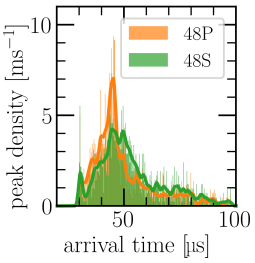

Figure 2.17: Field ionization of a Rydberg system at high density for a linear electric field ramp from 0 to 175 V cm^{-1} within 60 µs.

This method gives similar results for the magnetization compared to fitting the model function (2.10), but it can be generalized to arbitrary priors and this method is numerically more stable and faster.

Selective field ionization is a reliable method to calculate the magnetization at low Rydberg densities, and it can even be used to distinguish three different Rydberg states [89]. However, at high Rydberg densities, the distributions of arrival times broaden and distinguishing different Rydberg states becomes impossible (see Figure 2.17). At these high densities, the interactions between the spins become large

and the Stark map shown in Figure 2.14 is expected to be modified which could possibly change the ionization signal. Another possible explanation for this effect is that atoms which ionize early during the field ramp lead to avalanche ionization of nearby Rydberg atoms. This avalanche process might dominate at high Rydberg densities which explains the observed broadening and the indistinguishability of the Rydberg states.

2.3.4 *Magnetization reconstruction by optical de-excitation*

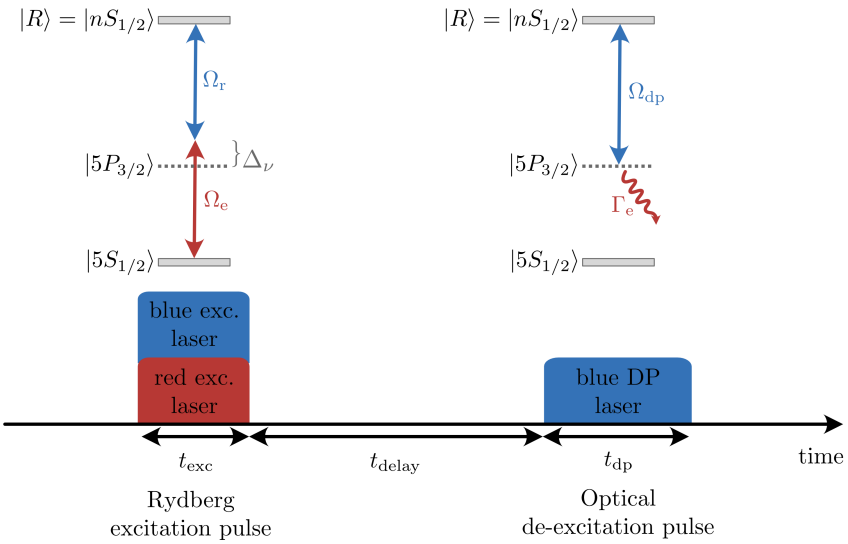

Figure 2.18: Scheme for the measurement of the magnetization via optical de-excitation. Initially, Rydberg atoms are excited by a resonant two-photon excitation pulse with red 780 nm and blue 480 nm light. The lasers are tuned such that the intermediate $|5P_{3/2}\rangle$ state is detuned by 98 MHz. After a delay time which can be used for Rydberg spin experiments, the Rydberg state $|R\rangle = |nS_{1/2}\rangle$ is optically deexcited by the blue laser being resonant to the intermediate $|5P_{3/2}\rangle$ state. The latter decays spontaneously at a rate of $\Gamma_e = 2\pi 6$ MHz. Adapted from [102]

An alternative measurement scheme to selective field ionization is the state selective optical de-excitation (see Figure 2.18). Here, the same blue 480 nm laser which is also used for exciting the Rydberg atoms, is tuned to be on resonance to the transition between the Rydberg state $|R\rangle = |nS_{1/2}\rangle$ and the state $|5P_{3/2}\rangle$. The latter decays spontaneously at rate of $\Gamma_e = 2\pi 6$ MHz. If the Rabi frequency Ω_{dp} of the blue laser is small compared to this rate, we expect an exponential relaxation of the Rydberg state at a rate determined by Ω_{dp}. After the de-excitation pulse, the remaining atoms can be ionized by field ionization.

To determine the efficiency of the de-excitation pulse, we have prepared Rydberg atoms in the state $|48S\rangle$, varied the duration t_{dp}

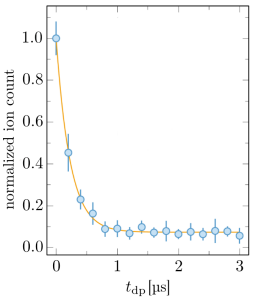

Figure 2.19: Normalized ion count measured after an optical de-excitation pulse of duration t_{dp}. An exponential fit is shown by the orange line. Adapted from [81].

of the de-excitation pulse, and measured the remaining number of Rydbergs by field ionization. The normalized ion count is shown in Figure 2.19. The experimental data can be well described by an exponential relaxation at a rate of 4.8 MHz.

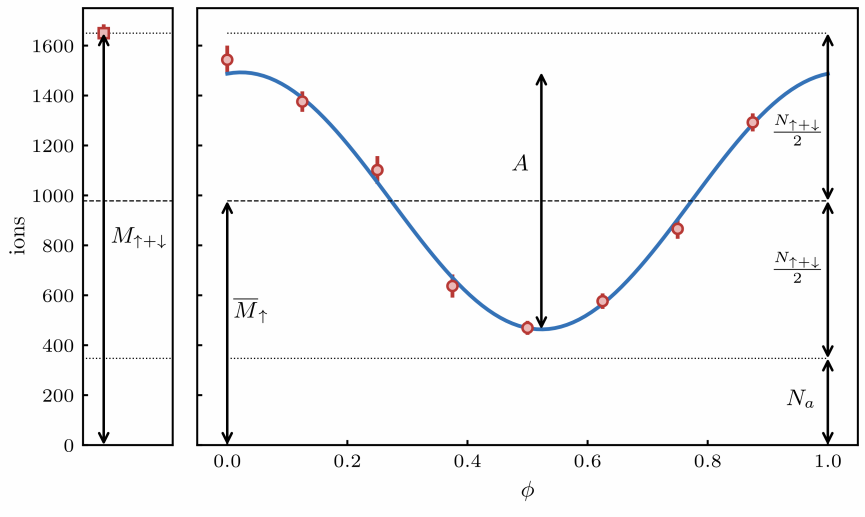

Figure 2.20: Reconstruction of the magnetization. Left panel: measurements of the total number of spins $M_{\uparrow+\downarrow}$. Right panel: measurement of the population in the $|\uparrow\rangle$ state $M_{\uparrow}(\phi)$ after a readout pulse of phase ϕ. Both are affected by the population in auxiliary states N_a. The measurement $M_{\uparrow}$ is fitted by a sinusoidal function (orange line), from which we extract the mean value $\overline{M}_{\uparrow}$. The amplitude A of the fit, normalized by the total number of spin $N_{\uparrow+\downarrow}$, indicates the magnetization in the xy plane. Adapted from Article [1].

With this method, the calculation of the magnetization is more complicated because adjacent Rydberg states might also be populated due to the finite black-body lifetime of the Rydberg states, the finite efficiency of the optical de-excitation, and a possible microwave transfer. This residual population leads to an offset in the measured ion signal, a number N_a of those atoms being energetically above the ionization threshold. In the following, we will describe how to calculate the magnetization from a tomographic readout of the magnetization (see Figure 2.20).

For the tomographic readout, the magnetization $\langle S\rangle_{\phi}$ is rotated by a $\pi/2$-pulse with phase ϕ to the z-direction. Now, the Rydberg state $|\downarrow\rangle$ is optically deexcited and the sum of N_a and the population $N_{\uparrow}(\phi)$ in the state $|\uparrow\rangle$ is ionized:

$$M_{\uparrow}(\phi) = N_{\uparrow}(\phi) + N_a \tag{2.13}$$

The measured quantity $M_{\uparrow}(\phi)$ is a sinusoidal function of ϕ, centered around its mean value

$$\overline{M}_{\uparrow} = \frac{N_{\downarrow+\uparrow}}{2} + N_a\,. \tag{2.14}$$

The amplitude A of the sinusoidal fit corresponds to the magnetization in the xy-plane but it needs to be normalized by the total number of spins $N_{\downarrow+\uparrow} = N_{\uparrow} + N_{\downarrow}$. The phase of the fit determines the direction of the spins in the xy-plane.

To determine the total number of spins, a second calibration measurement where no optical deexcitation is performed. This measurement of the total number of Rydberg atoms

$$M_{\downarrow+\uparrow} = N_{\downarrow+\uparrow} + N_a \,. \tag{2.15}$$

combined with (2.14), allows calculating the total number of spins.

Part I

GLASSY DYNAMICS

3

INTRODUCTION TO GLASSY DYNAMICS

This part of the thesis explores the relaxation dynamics of disordered quantum spin systems. The most famous type of relaxation is the exponential decay where a single relaxation timescale dominates the dynamics. An example of exponential relaxation is the conventional Debye relaxation where dipoles relax in an overdamped medium [103]. Similarly, in NMR systems both the spin-lattice (T_1 time) and spin-spin relaxation (T_2 time) follow a simple exponential law [104]. The typical origin of exponential relaxation is a decoherence mechanism that uniformly affects each particle of the system. A consequence of this decoherence is that these types of systems quickly reach thermal equilibrium, at a temperature determined by the bath.

However, relaxation is not always described by an exponential law. For example, in glassy systems, disorder and frustration can lead to an anomalously slow relaxation [105]. While these systems are generically expected to reach an ergodic thermal equilibrium state, this will happen only on timescales that typically exceed the experimental time window [20]. Therefore, on experimentally relevant timescales, glassy systems are non-ergodic [22]. The description of the slowly relaxing out-of-equilibrium state as a quasi-stationary state allows for building a common theoretical framework for glassy systems in analogy to thermal equilibrium including a generalized fluctuation-dissipation theorem and an effective temperature [106]. Most importantly, we can attribute to glassy systems the notion of a phase-transition [107]: At a certain, critical temperature, the response of spin glasses to external fields features a sharp cusp [108] and only below this temperature the spin-glass order parameter is finite. Close to this critical temperature, signatures of universality can be found [109, 110] which is typically known only from phase transitions in equilibrium physics [16, 111]. Therefore, despite being non-ergodic, spin glasses can be described by a common theoretical framework that explains the distinct features like glassy dynamics or the spin glass phase transitions based on a microscopic description [20].

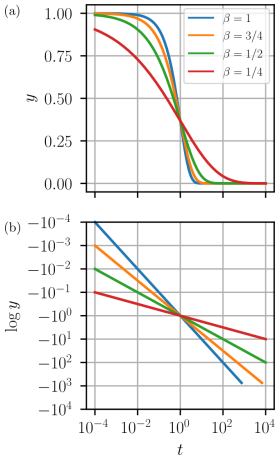

Figure 3.1: (a) Stretched exponential function (eq. (3.1)) plotted on a lin-log scale. (b) The stretched exponential becomes a linear function if the logarithm of the stretched exponential is plotted on a log-log scale.

The dynamics of glassy systems can generally be well described by the stretched exponential law [112]:

$$\exp^{-(t/\tau)^{\beta}} \tag{3.1}$$

which was introduced by Kohlrausch in 1854 [113] to describe the discharge of a Leyden jar, and is today known to fit relaxation of numerous classical systems [114]. The stretched exponential relaxation is characterized by a single number, the stretching exponent $\beta \in (0, 1)$,

which allows quantifying how much the dynamics deviate from an exponential decay thereby functioning as a proxy for glassy dynamics (see Figure 3.1). The limit $\beta = 1$ signifies a simple exponential relaxation, for small $\beta \ll 1$, the stretched exponential function can be expanded in β and is approximated by a logarithmic time dependence $\beta/e \log(t/\tau)$.

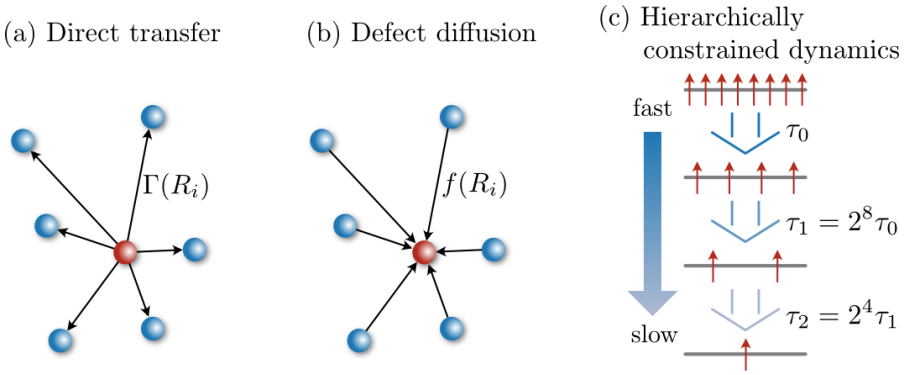

Figure 3.2: Illustration of the three classical mechanisms leading to stretched exponential relaxation. (a) In the direct transfer model, the central particle (red ball) relaxes by transferring energy to randomly distributed defects (blue balls) at a rate $\Gamma(R_i)$. (b) For the defect diffusion model, the central particle relaxes if it is reached by a defect that moves in a random walk toward the central particle. (c) The hierarchically constrained dynamics model considers a hierarchy of relaxation timescales from fast to slow. These timescales emerge because spins on a given level can only change if a cluster of spins on the previous level has acquired a specific spin configuration. Adapted from [115].

In a seminal paper from 1985, Klafter and Shlesinger classified various approaches to explain the stretched exponential relaxation based on microscopic models into three different mechanisms [115]: In the *Foerster-direct transfer mechanism*, a particle can relax by transferring energy to randomly distributed defects at a rate $\Gamma(R_i) \propto R_i^{-\alpha}$ that depends on the distance R_i between the particle and the defect i (see Figure 3.2 (a)). Averaging over the relaxations of all parallel relaxation channels, this model predicts a stretched exponential law with exponent $\beta = d/\alpha$ for a d-dimensional system. A similar idea of parallel relaxation channels is described by the *defect-diffusion model* where the particle decays if it is reached by randomly positioned defects that move in a random walk towards the particle (see Figure 3.2 (b)).

The third mechanism is the *hierarchically constrained dynamics model* and was originally by Palmer et al. [21]. It contrasts the first two mechanisms in the sense that the different relaxation channels do not exist in parallel but in series. The model considers spins on different levels n (see Figure 3.2 (c)). Spins on the first level ($n = 0$) can move on the fastest timescale τ_0. However, the spins on the next level ($n = 1$) are constrained by the spins on the first level and can only move if μ_0

spins on the first level have reached one out of the 2^{μ_0} configurations. On the next level, spins are again constrained by the level before, such that a hierarchy of relaxation time scales from initially fast to slow dynamics at late times exist. This third model was suggested to explain the stretched exponential relaxation of spin glasses, which was later confirmed by de Dominicis et al. who derived a hierarchically constrained dynamics model from the random free energy model of spin glasses [116].

Strikingly, Klafter and Shlesinger could demonstrate that, despite the different physical pictures, all these three mechanisms share a common mathematical framework that leads to stretched exponential relaxation: A scale invariant distribution of relaxation times.

The first part of this thesis discusses whether this notion of ergodicity breaking due to slow relaxation also exists in the quantum realm. Corresponding to glassy dynamics in classical systems, we find that disordered spin systems relax sub-exponentially, well-described by a stretched exponential law, remaining out-of-equilibrium for more than three orders of magnitude in time. Also, this glassiness can be attributed to the presence of strong disorder in the system and the existence of a scale-invariant distribution of time scales, the same underlying mathematical framework discussed by Klafter and Shlesinger in [115] to explain glassy dynamics in classical systems.

Moreover, we find that the glassy dynamics feature universal behavior when varying the type of Hamiltonian or the strength of disorder up to a critical value, hinting towards a unifying description of relaxation dynamics of disordered quantum spin systems. However, in contrast to classical spin glasses or other open quantum systems featuring slow dynamics [117, 118, 119], the disordered quantum system studied in this thesis is isolated. Therefore, the relaxation is not induced by coupling to an external bath. Also, the dynamics are not imposed by thermal fluctuations, which need to be small for a classical spin glass such that the system can remain in those metastable states, but instead, quantum fluctuations drive the system dynamics.

4

PUBLICATIONS

Part I of this thesis presents a collection of four studies that investigate the glassy relaxation dynamics of disordered quantum spin systems.

The first article *"Glassy Dynamics in a Disordered Heisenberg Quantum Spin System"* (Article [1]) reports on the discovery of slow relaxation dynamics in an isolated spin-1/2 system realized with Rydberg atoms. To initiate the dynamics, we create, by using a microwave $\pi/2$-pulse, a product state where each spin is in a superposition of the two Van-der-Waals interacting Rydberg states that constitute the spin-1/2 system. This initial state does not show any dynamics in a mean-field description such that all dynamics are caused by quantum fluctuations. Strikingly, we can fit the obtained dynamics of the global magnetization by a stretched exponential law $\exp^{-(t/\tau)^\beta}$ with a stretching exponent of $\beta = 0.32(2)$ which is similar to the exponents found in classical glassy systems, and notably far below the exponent of $\beta = 1$ signifying an exponential decay. This glassy dynamics was observed for different Rydberg densities, and the experimental data of the different relaxation curves collapse on a single curve after rescaling time with the typical interaction strength which depends on the coupling strength C_6 and the typical interparticle distance a_0. Since a different Rydberg density results in a different spatial disorder due to the Rydberg blockade effect, this scaling behavior signifies that the glassy dynamics is independent of microscopic details in the spatial distribution of the spins. To confirm this observation, we have simulated the relaxation dynamics using the semiclassical Discrete Truncated Wigner transformation (DTWA) [120] which shows good agreement with the experimental data. The DTWA simulations also allow probing of how the glassy dynamics depends on the disorder strength in a uniform density distribution. These simulations confirm that the stretching exponent is independent of disorder strength up to a critical value.

In this first article, the stretched exponential law was just used as a phenomenological fitting function. To establish the stretched exponential law from a microscopic model, the article *"Glassy Quantum Dynamics of Disordered Ising Spins"* (Article [2]) derives the stretched exponential law analytically from the exact Emch-Radin solution [121, 122] for an isolated system of Ising spins in the limit of strong disorder and infinite system size. The solution holds for an arbitrary dimension d and interaction range α and yields a stretching exponent of $\beta = d/\alpha$. Moreover, this ansatz extends the validity of the stretched exponential law to the relaxation dynamics of the average single spin purity which is described by the same stretching exponent, only the relaxation rate

is reduced. This signifies that the build-up of entanglement also shows glassy dynamics. Beyond the analytical derivation of the stretched exponential law in the limit of strong disorder, the exact Emch-Radin solution allows also to numerically solve the relaxation dynamics for large system sizes in a regime where a blockade radius decreases the disorder. These numerical simulations confirm that the stretching exponent is largely independent of the disorder strength up to a critical value. Finally, the derivation of the stretched exponential law from a microscopic model allows a better understanding of the underlying mechanism leading to glassy dynamics: A scale-invariant distribution of timescales leads to the emergence of the slow, subexponential relaxation dynamics. For classical systems, the timescales are due to coupling to a bath at different exponential relaxation rates, for the quantum Ising system, the timescales emerge from oscillation frequencies which are random due to the disorder in the interaction matrix.

In both discussed studies, it was found that the stretched exponential law describes the relaxation dynamics, either by experimental observation of the dynamics of a non-integrable Heisenberg XXZ model or by the analytical solution of the integrable Ising model. This raises the question of whether glassy dynamics exists independent of the type or symmetry of the spin Hamiltonian. The article *"Semiclassical Simulations predict Glassy Dynamics for Disordered Heisenberg Models"* (Article [3]) simulates with DTWA the relaxation dynamics of various Heisenberg XXZ and XYZ spin systems. These spin systems feature various symmetries, the isotropic XXX model is SU(2) symmetric, the XXZ model features a U(1) symmetry, and both of these symmetries are broken for a generic XYZ model. Moreover, these systems feature a variety of different many-body phases [123, 124, 125, 126, 127]. Since no analytical solution exists for these models and the exact diagonalization is feasible only for small system sizes due to the curse of dimensionality of quantum many-body systems, this study relies on the semiclassical DTWA solution which has proven to accurately simulate the experimental observation of Article [1]. Also, DTWA becomes exact for the dynamics of the magnetization of Ising spins oriented along the x-direction, such that this study using semiclassical approximations can be seen as a natural generalization of Article [2] which has derived the stretched exponential law analytically. To confirm that the observed dynamics is not a specificity of the semiclassical DTWA, we compare the predicted relaxation by employing the Moving Averaged Cluster Expansion (MACE) which computes the magnetization by exact diagonalization of local clusters of spins [128].

The previous study suggests that glassy dynamics is a generic feature of a general quantum spin system, but the study relies on numerical approximations like DTWA or MACE. To overcome this issue, we experimentally realize three different types of spin-1/2 Hamilto-

nians, the Ising, XX and XXZ Hamiltonian, by an appropriate choice of Rydberg levels. For each spin model, we implement a Ramsey sequence similar to Article [1] and present the observed dynamics in the article *"Observation of Universal Relaxation Dynamics in Disordered Quantum Spin Systems"* (Article [4]). By rescaling time with the typical interaction strength, we find that the relaxation dynamics of all three Hamiltonians collapse on a single curve which is in good agreement with the stretched exponential law. To explain this universal behavior, we introduce a simple model which only considers interactions between nearest neighbors. This model explains the independence of the dynamics on the type of Hamiltonian and reproduces qualitatively the obtained dynamics. Even better agreement can be obtained by MACE, signifying that small local clusters are sufficient to describe the quantum time evolution.

Glassy Dynamics in a Disordered Heisenberg Quantum Spin System

A. Signoles,[1,2,†] T. Franz,[1,†] R. Ferracini Alves,[1] M. Gärttner,[1,3] S. Whitlock,[1,4] G. Zürn,[1] and M. Weidemüller[1,5,*]

[1]*Physikalisches Institut, Universität Heidelberg, Im Neuenheimer Feld 226, 69120 Heidelberg, Germany*
[2]*Université Paris-Saclay, Institut d'Optique Graduate School, CNRS, Laboratoire Charles Fabry, 91127 Palaiseau, France*
[3]*Kirchhoff-Institut für Physik, Universität Heidelberg, Im Neuenheimer Feld 227, 69120 Heidelberg, Germany*
[4]*IPCMS (UMR 7504) and ISIS (UMR 7006), University of Strasbourg and CNRS, 67000 Strasbourg, France*
[5]*Hefei National Laboratory for Physical Sciences at the Microscale and Department of Modern Physics, and CAS Center for Excellence and Synergetic Innovation Center in Quantum Information and Quantum Physics, University of Science and Technology of China, Hefei, Anhui 230026, China*

(Received 21 January 2020; revised 28 July 2020; accepted 2 December 2020; published 19 January 2021)

Understanding the dynamics of strongly interacting disordered quantum systems is one of the most challenging problems in modern science, due to features such as the breakdown of thermalization and the emergence of glassy phases of matter. We report on the observation of anomalous relaxation dynamics in an isolated XXZ quantum spin system realized by an ultracold gas of atoms initially prepared in a superposition of two different Rydberg states. The total magnetization is found to exhibit subexponential relaxation analogous to classical glassy dynamics, but in the quantum case this relaxation originates from the buildup of nonclassical correlations. In both experiment and semiclassical simulations, we find the evolution toward a randomized state is independent of the strength of disorder up to a critical value. This hints toward a unifying description of relaxation dynamics in disordered isolated quantum systems, analogous to the generalization of statistical mechanics to out-of-equilibrium scenarios in classical spin glasses.

DOI: 10.1103/PhysRevX.11.011011

Subject Areas: Atomic and Molecular Physics, Quantum Information

I. INTRODUCTION

The far-from-equilibrium behavior of isolated quantum systems and in particular their relaxation toward equilibrium still evades a unifying description. It has been conjectured that these systems generically relax to a state of local thermal equilibrium according to the eigenstate thermalization hypothesis (ETH) [1]. However, the ETH does not explain how the equilibrium state will be reached, or even if it will be reached in experimentally accessible timescales. Particularly rich relaxation dynamics are found in disordered quantum systems, where the interplay between interactions and randomness can give rise to new and intrinsically nonequilibrium effects such as prethermalization [2–4], many-body localization [5–7], Floquet time crystals [8,9], and quantum scars [10,11].

In contrast, most natural systems (e.g., in condensed matter) are not fully isolated from their environment and hence always relax to thermal equilibrium imposed by the external bath [12]. But it is known that disorder and frustration effects can lead to a dramatic slowdown of thermalization, associated with the onset of glassy behavior [13]. A key signature of this behavior is that macroscopic observables relax in a characteristically nonexponential way, as encountered, for example, in doped semiconductors [14] and organic superconductors [15], quasicrystals [16], atoms in optical lattices [17], or diamond color centers [18,19]. This raises the question whether slow relaxation, which appears to be ubiquitous in open disordered systems, also emerges in isolated quantum systems.

A prototypical model for studying far-from-equilibrium quantum dynamics is the Heisenberg XXZ Hamiltonian for spin-1/2 particles. Compared to the Ising Hamiltonian, this class of spin systems has fewer conserved quantities and shows complex, chaotic far-from-equilibrium dynamics which are difficult to describe theoretically [20]. Here, we experimentally realize a disordered quantum

*Corresponding author.
weidemueller@uni-heidelberg.de
†These authors contributed equally to this work.

Heisenberg XXZ spin-1/2 model in an ultracold atomic gas by encoding the spin degree of freedom in two electronically excited (Rydberg) states of each atom. Spin-spin interactions arise naturally through the state-dependent dipolar interactions between Rydberg states, while disorder originates from the random positions of each atom in the gas which gives rise to distance-dependent couplings [21]. Using a strong microwave field pulse that couples the two Rydberg states, we initialize the spins in a far-from-equilibrium state and probe their time evolution, thus employing our system as a quantum simulator for unitary spin dynamics in a disordered system out of equilibrium [10,22–26].

In a large ensemble of Rydberg spins, we observe that the magnetization follows a subexponential dependence characterized by a stretching exponent that is independent of the strength of disorder up to a critical value. Our experiments and supporting numerical simulations suggest that such glassy dynamics, commonly known in disordered open systems, might also be a generic feature of isolated quantum spin systems, hinting toward a unifying effective theory description.

In Sec. II, we give a qualitative physical picture by solving the time-dependent Schrödinger equation for a few spins exactly. We then describe in Sec. III how to implement the Heisenberg XXZ spin model in a gas of ultracold atoms that are excited to Rydberg states. In Sec. IV, we experimentally characterize the relaxation dynamics, and we theoretically investigate the dependence on disorder strength and character in Sec. V. Finally, we discuss in Sec. VI our findings in comparison to other systems exhibiting glassy dynamics.

II. QUALITATIVE PICTURE OF THE QUANTUM DYNAMICS

We consider an ensemble of N spin-1/2 particles randomly positioned in space and all initialized in the $|{\rightarrow}\rangle_x^{\otimes N} = 1/\sqrt{2}(|{\uparrow}\rangle + |{\downarrow}\rangle)^{\otimes N}$ state, corresponding to an initial magnetization $\langle S_x^{(i)}\rangle = 1/2$. Here, $S_\alpha^{(i)}$ ($\alpha = \{x, y, z\}$) refers to the spin-1/2 operator of the ith spin. The experimental protocol is illustrated in Fig. 1(a). The unitary dynamical evolution of the system is governed by the Heisenberg XXZ Hamiltonian in the absence of magnetic fields (in units where $\hbar = 1$),

$$H_{\mathrm{XXZ}} = \frac{1}{2}\sum_{i,j} J_{ij}\left(S_x^{(i)}S_x^{(j)} + S_y^{(i)}S_y^{(j)} + \delta S_z^{(i)}S_z^{(j)}\right), \qquad (1)$$

where J_{ij} are the interaction couplings between the spins i and j and δ is the anisotropy parameter. To remain consistent with the experimental implementation (see Sec. III), we focus on an anisotropy parameter $\delta = -0.73$ and spin-spin interactions that decay as a power law $J_{ij} = C_6/r_{ij}^6$ with the interparticle distance r_{ij}.

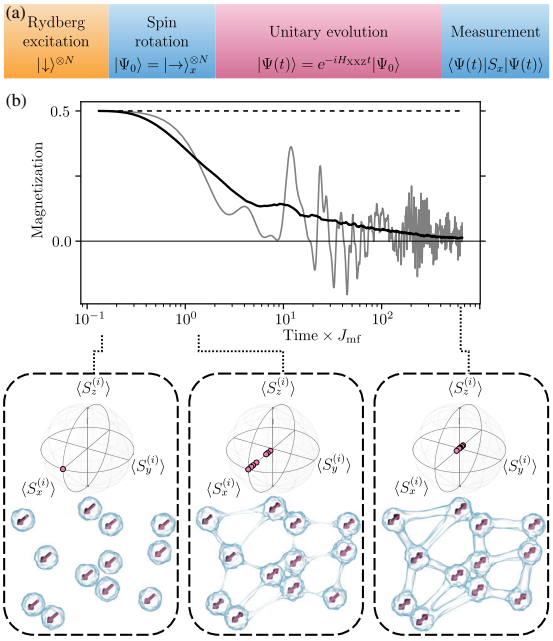

FIG. 1. Relaxation dynamics in a disordered quantum spin system. (a) Protocol for initialization and readout of the many-body spin system composed of Rydberg atoms. Spin states $|{\uparrow}\rangle$ and $|{\downarrow}\rangle$ correspond to two different Rydberg states. (b) Exact simulation of 12 spins interacting via a Heisenberg XXZ Hamiltonian. The plot shows the magnetization for a single realization (gray curve) and the disorder average over 1000 realizations (black curve) which relaxes as function of time given in units of the median of the mean-field interaction strengths J_{mf}. The dashed line indicates the mean-field prediction that does not relax. The microscopic expectation values of $\langle S_x^{(i)}\rangle$, $\langle S_y^{(i)}\rangle$, and $\langle S_z^{(i)}\rangle$ for each spin are plotted at three different time steps on the Bloch sphere. The reduction of the expectation values (magnetization) is a consequence of the spreading of entanglement (visualized by the blue bonds between spins).

To obtain a qualitative understanding of the quantum dynamics in this system, we perform a full quantum mechanical simulation on a small ensemble of $N = 12$ spins. In Fig. 1(b) we show the time evolution of the magnetization $\langle S_x\rangle_k = 1/N\sum_i\langle S_x^{(i)}\rangle_k$ for a single disorder realization k (gray curve). Because of the spatial disorder, spin-spin interactions give rise to complex many-body dynamics on strongly varying energy scales. This is in stark contrast to an effectively classical, mean-field prediction for this Hamiltonian [dashed line in Fig. 1(c)], which assumes each spin to evolve in the average field generated by all other spins, thus neglecting quantum correlations. The initial fully magnetized state is an eigenstate of the mean-field Hamiltonian which explains the total absence of relaxation.

Therefore, in the many-body case the loss of magnetization is not caused by classical dephasing, but by the buildup of entanglement between spins, witnessed by the

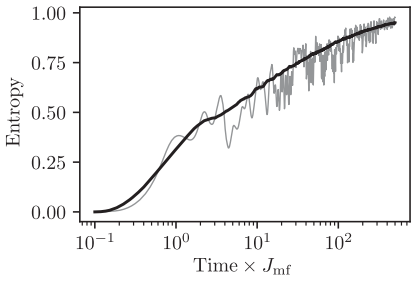

FIG. 2. Buildup of entanglement quantified by the time evolution of the second order Rényi entropy of the few-particle simulation from Fig. 1(b). The plot shows the ensemble averaged entropy for a single realization (gray curve) and the disorder average over 1000 realizations (black curve). Since the full system remains pure, the Rényi entropy is a measure of entanglement that increases on similar timescales to the maximal value of $\mathcal{S}_i^{(2)} = 1$ as the magnetization relaxes to zero.

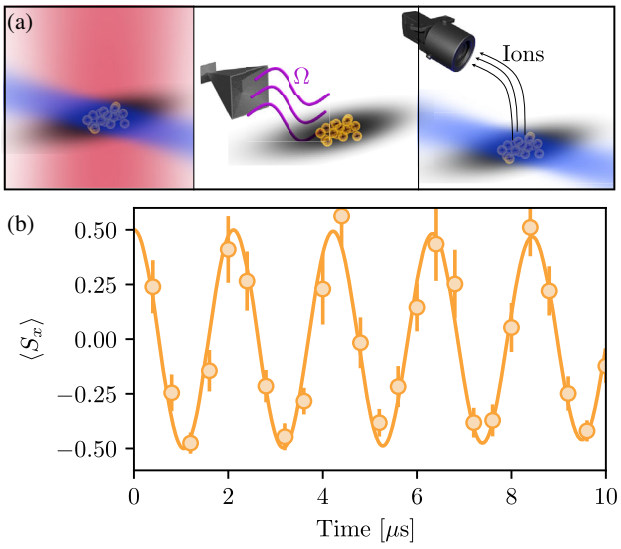

FIG. 3. Implementation of the XXZ spin-1/2 model in Rydberg gases. (a) Experimental procedure. Left: A laser pulse at 780 nm (red) and 480 nm (blue) excites a controlled fraction of the ^{87}Rb atoms to the $|\downarrow\rangle = |48S\rangle$ Rydberg state. Middle: A microwave field couples the $|\downarrow\rangle$ state to the $|\uparrow\rangle = |49S\rangle$ state to perform a Ramsey experiment. Right: A blue 480 nm laser depopulates the $|\downarrow\rangle$ Rydberg state, before the $|\uparrow\rangle$ state is ionized by an electric field. The ions are detected by a multichannel plate. (b) Ramsey fringes showing a high degree of phase coherence for a detuning of $\Delta/2\pi = 0.47$ MHz for a peak spin density of $\rho_S^0 = 6.0(15) \times 10^7$ cm^{-3}. The solid line shows discrete truncated Wigner approximation simulations for that density.

decrease of the local purity $\mathrm{Tr}(\rho_i^2)$ for each spin ρ_i being the single-spin reduced state $\rho_i = \mathrm{Tr}_{\neg i}\rho$. Since the dynamics are unitary and therefore the full system remains pure [$\mathrm{Tr}(\rho^2) = 1$], we can quantify entanglement by the second order Rényi entropy,

$$\mathcal{S}_i^{(2)} = -\log_2[\mathrm{Tr}(\rho_i^2)], \tag{2}$$

which increases to $\mathcal{S}_i^{(2)} = 1$ on a similar timescale as the relaxation of the magnetization (see Fig. 2). After ensemble and disorder averaging, the magnetization approaches a fully randomized state with $\langle S_{x,y,z}\rangle = 0$ [see black curve in Fig. 1(b)], consistent with the ETH prediction. However, this relaxation occurs very slowly compared to the timescales associated with spin-spin interactions.

III. REALIZING A HEISENBERG XXZ SPIN SYSTEM WITH RYDBERG ATOMS

From a few-body perspective, one may wonder whether glassy dynamics can actually be observed in fully isolated quantum many-body systems and to what extent it shares common features with classical spin glasses. We address this question experimentally using a gas of ultracold rubidium atoms prepared in a superposition of two different Rydberg states. For well chosen pairs of states, the electric dipole-dipole coupling leads to the XXZ model [27,28]. Here we use the two low angular momentum states $|\downarrow\rangle = |48s\rangle$ and $|\uparrow\rangle = |49s\rangle$ to realize the Hamiltonian (1), with $C_6/2\pi = 59$ GHz μm^6 characterizing the strength of the power law interactions (for the derivation of the Hamiltonian, see the Appendix A).

The experimental procedure [Fig. 3(a)] starts with a gas of ^{87}Rb atoms prepared in their electronic ground state $|g\rangle = |5S_{1/2}, F = 2, m_F = 2\rangle$ in an optical dipole trap and with a temperature $\mathrm{T} \sim 50$ μK, low enough to freeze the motional degrees of freedom over the timescale of the experiment. A laser pulse of variable duration brings a controllable number of atoms $N \leq 1200$ to the $|\downarrow\rangle = |48S_{1/2}, m_j = +1/2\rangle$ Rydberg state. For this we use a two-photon laser excitation at 780 and 480 nm, with a detuning $-2\pi \times 100$ MHz from the intermediate state $|e\rangle = |5P_{3/2}, F = 3, m_F = 3\rangle$ and an effective Rabi frequency of $2\pi \times 150$ kHz. To individually address two specific Rydberg states, including Zeeman substructure, we continuously apply a magnetic field of 6 G. To characterize the resulting three-dimensional Gaussian Rydberg density distribution, we perform depletion imaging, where the Rydberg density is deduced by absorption imaging of the ground-state atoms before and after the Rydberg excitation laser pulse [29].

A two-photon microwave field is then used to couple the $|\downarrow\rangle$ state to the $|\uparrow\rangle = |49S_{1/2}, m_j = +1/2\rangle$ Rydberg state. The single-photon frequency $\nu = 35.2$ GHz is detuned from the intermediate state $|48P_{3/2}\rangle$ by 170 MHz, far enough to guarantee that the population in this state due to off-resonant coupling is smaller than 2%. The atoms can therefore be considered as two-level systems described by a pseudospin degree of freedom. In this description the

microwave field acts as an external field described by the Hamiltonian

$$H_{\mathrm{ext}} = \sum_i \left(\Omega \sin\phi S_x^{(i)} - \Omega \cos\phi S_y^{(i)} + \Delta S_z^{(i)} \right), \quad (3)$$

with Ω the Rabi frequency, Δ the two-photon detuning, and ϕ the phase of the field. The Rabi frequency is calibrated from the period of Rabi oscillations between the two spin states.

To perform the Ramsey sequence shown in Fig. 1(a), a resonant microwave $\pi/2$ pulse at an effective Rabi frequency $\Omega/2\pi = 3.00(1)$ MHz rotates all spins to the fully magnetized state $|{\rightarrow}\rangle_x^{\otimes N}$ with all spins pointing along the x direction on the Bloch sphere. Uncertainties in the duration and amplitude of the pulses as well as interaction effects lead to imperfect initial spin state preparation. Based on simulations, we estimate the fidelity to be higher than 96%.

After a free-evolution time t in the absence of the microwave field ($\Omega = 0$), a second microwave $\pi/2$ pulse with adjustable phase ϕ is applied to rotate the equatorial magnetization components,

$$\langle S_\phi \rangle = \cos\phi \langle S_x \rangle + \sin\phi \langle S_y \rangle, \quad (4)$$

to the detection basis $\{|{\downarrow}\rangle, |{\uparrow}\rangle\}$. In this way we effectively read out the $\langle S_x \rangle$ and $\langle S_y \rangle$ magnetizations from population measurements of the Rydberg states using electric field ionization (see Appendix B).

To ensure unitary Hamiltonian dynamics, we restrict the experimental timescales to a maximum of 10 μs, which is short compared to the spontaneous decay time and redistribution by black-body radiation (113 and 121 μs, respectively, for the chosen Rydberg states [30]). To verify that the single-spin phase coherence is preserved during experimental time, we perform a Ramsey measurement with finite detuning Δ at low spin densities where interactions can be neglected [31,32]. The full contrast oscillation shows that the single-spin phase coherence is preserved over the duration of the experiment, as shown in Fig. 3(b).

IV. EXPERIMENTAL OBSERVATION OF RELAXATION DYNAMICS

A. Glassy dynamics

We now study the relaxation dynamics due to spin-spin interactions for increasing spin densities. Figure 4 shows the experimentally observed relaxation of the magnetization using tomographic spin-resolved readout of $\langle S_x \rangle$ and $\langle S_y \rangle$. Starting from the almost fully magnetized state $\langle S_x \rangle = 1/2, \langle S_y \rangle \approx 0$, we observe that the magnetization decays toward the unmagnetized state $\langle S_x \rangle = 0, \langle S_y \rangle = 0$ within ~ 10 μs. This is much shorter than the single-spin phase coherence time measured in Fig. 3 but still slower than the characteristic timescale of interactions,

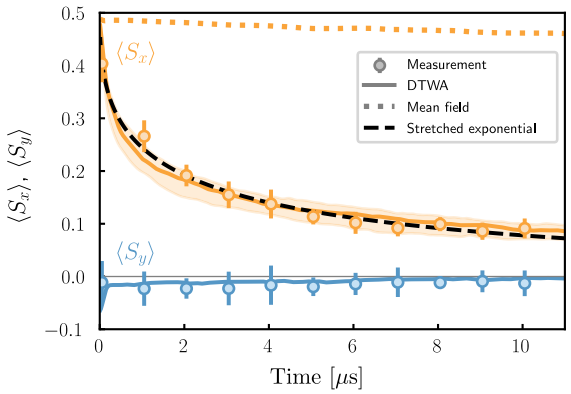

FIG. 4. Many-body relaxation dynamics of a Heisenberg XXZ Rydberg spin system. The dots show the temporal evolution of the two magnetization components $\langle S_x \rangle$ and $\langle S_y \rangle$ from a tomographic spin readout. Error bars are determined from 120 realizations of the experiment at a peak spin density of $\rho_S^0 = 1.2(3) \times 10^9$ cm^{-3}. The observed dynamics are clearly inconsistent with the mean-field prediction including imperfect initial state preparation (dotted line). The solid lines are DTWA predictions without free parameters. The shaded area indicates the systematic uncertainty of the measured density. The dashed line depicts a fit of the data with a stretched exponential function yielding a stretching exponent of $\beta = 0.32(2)$.

$[C_6/(2\pi)/a_0^6]^{-1} = 0.7(3)$ μs. Here, $a_0 = (4\pi\rho_S^0/3)^{-1/3}$ represents the mean interparticle distance. It is defined as the Wigner-Seitz radius of the Gaussian spin density distribution [33], whose peak density ρ_S^0 is given by the initial peak density of spin-down Rydberg atoms.

The time evolution seen in the experiment is qualitatively similar to the dynamics obtained by exact diagonalisation in Fig. 1(b). Even when accounting for imperfect preparation of the initial state $\langle S_x \rangle \lesssim 1/2$ the mean-field prediction shows essentially no relaxation on the experimentally relevant timescales (see dotted line in Fig. 4 and Appendix C). The qualitative failure of the mean-field description is different from our earlier observation [21] of a density-dependent dephasing of $\langle S_z \rangle$. In this previous work, mean field also predicted a damping of Rabi oscillations, yet failing to provide a quantitatively consistent description of the dynamics. Here, the absence of dynamics at the mean-field level implies that the relaxation seen in the experiment is closely related to buildup of entanglement also apparent in the exact diagonalization calculations.

We find that the relaxation is well described by a stretched exponential, in apparent similarity with glassy dynamics in classical disordered media [18,34–36]:

$$\langle S_x(t) \rangle = \frac{1}{2} \exp[-(\gamma_J t)^\beta], \quad (5)$$

where β is the stretching exponent and γ_J defines an effective relaxation rate. The exponent β characterizes

the deviation from a simple exponential ($\beta = 1$) toward a purely logarithmic decay ($\beta \to 0$) [see Appendix D]. The experimental data are well described by this phenomenological function (dashed line in Fig. 4) yielding an exponent $\beta = 0.32(2)$. This value clearly rules out a pure exponential decay, i.e., $\beta = 1$, that could be expected on the basis of single-particle dephasing.

B. Insensitivity to microscopic details

To further investigate how slow relaxation and the characteristic exponent depend on microscopic details, we control the degree of spatial disorder by taking advantage of the Rydberg blockade effect in the state preparation stage [37–39]. During laser excitation the strong van der Waals interactions between Rydberg states prevent two spins from being prepared at distances smaller than the Rydberg blockade radius R_{bl}. The degree of disorder is thus controlled by the ratio between blockade radius R_{bl} and Wigner-Seitz radius a_0 [Fig. 5(a)].

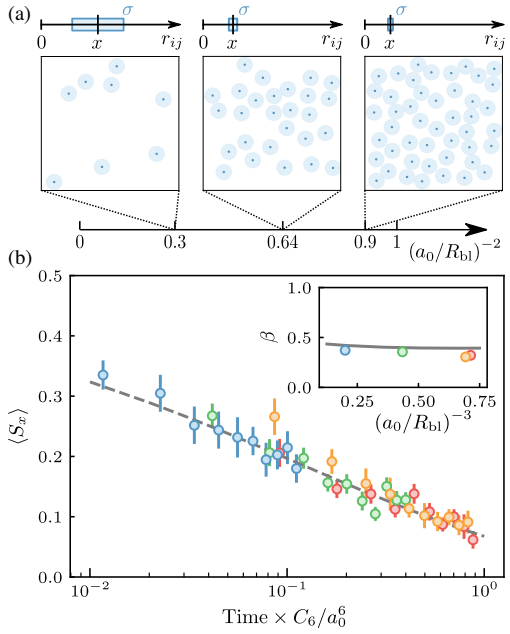

FIG. 5. Rescaled magnetization dynamics for different densities and disorder strengths. (a) 2D representation of a spin system with different densities and thus strengths of disorder, characterized by the mean number of spins per blockade radius $(a_0/R_{\mathrm{bl}})^{-2}$. The bar denotes the mean x and standard deviation σ of the interparticle distances $\min_{i\neq j} r_{ij}$. (b) Data points represent measurements of the averaged magnetization $\langle S_x \rangle$ for spin densities $\rho_S^0 = 0.43(11) \times 10^9$ cm^{-3} (blue), $0.8(2) \times 10^9$ cm^{-3} (green), $1.2(3) \times 10^9$ cm^{-3} (orange and red, corresponding to two different datasets). By rescaling time with the effective interaction strength C_6/a_0^6, the data collapse on a single curve described by a stretched exponential function with stretching exponent $\beta = 0.32(2)$ (dashed line). The inset shows β as a function of the corresponding ratio $(a_0/R_{\mathrm{bl}})^{-3}$ for the experimental data and DTWA calculations (solid gray line).

For $a_0 \gg R_{\mathrm{bl}}$, the blockade effect has little influence and the spins are randomly distributed, whereas the limit $a_0 \approx R_{\mathrm{bl}}$ corresponds to a strongly ordered configuration. In between, the short distance cutoff imposed by the Rydberg blockade effect effectively reduces the strength of the disorder compared to fully uncorrelated random spin positions.

In the experiment we can tune the disorder strength by changing the peak spin density ρ_S^0 and thus the mean number of spins per blockade sphere $(a_0/R_{\mathrm{bl}})^{-3}$ from 0.20(5) to 0.7(2) [two-dimensional representations of corresponding distributions are depicted in Fig. 5(a)]. Remarkably, we find the stretching exponent β to be almost constant over this range [inset in Fig. 5(b)]. Furthermore, after rescaling the time axis by the characteristic energy scale C_6/a_0^6, the time-dependent data collapse onto a single line [Fig. 5(b)]. From this we conclude that the dynamics is insensitive to the disorder strength which is modified by the blockade effect. These experimental observations are indicative of a universal behavior in the sense that the dynamics does not depend on the microscopic details of the system. This unexpected feature will be explored further in numerical simulations.

Because of the large number of spins in the experiment, an exact computer simulation of the unitary dynamics under the Hamiltonian Eq. (1) is not possible. Instead, quantum effects can be partially taken into account by applying the semiclassical discrete truncated Wigner approximation (DTWA; see Appendix C) [40,41] which has recently been shown to describe the dynamics of Rydberg interacting spin systems very well [21]. To model the present experiments, all physical parameters entering the simulation are determined through independent measurements, such as the spatial density distribution, total number of spins, and the microwave coupling strength Ω used in the preparation and readout stages. The initial spin distribution is generated from a random excitation model of the Rydberg atoms, including a cutoff distance to account for the blockade effect. This classical sampling of the spatial spin distribution is justified on the basis that neither the microwave pulses nor the Rydberg-Rydberg interactions couple different terms of the collectively excited many-body state, each of which satisfy the blockade constraint (see Appendix E). The numerical simulations describe the glassy dynamics and the insensitivity with respect to changes of the distribution function of the interaction strength very well [solid line in Fig. 4 and in the inset of Fig. 5(b)], further confirming the validity of the DTWA approximation for treating the dynamics of disordered quantum systems.

V. NUMERICAL STUDY OF THE ROLE OF DISORDER STRENGTH

Theoretical modeling using the DTWA allows to further test the role of disorder for the glassy dynamics, while

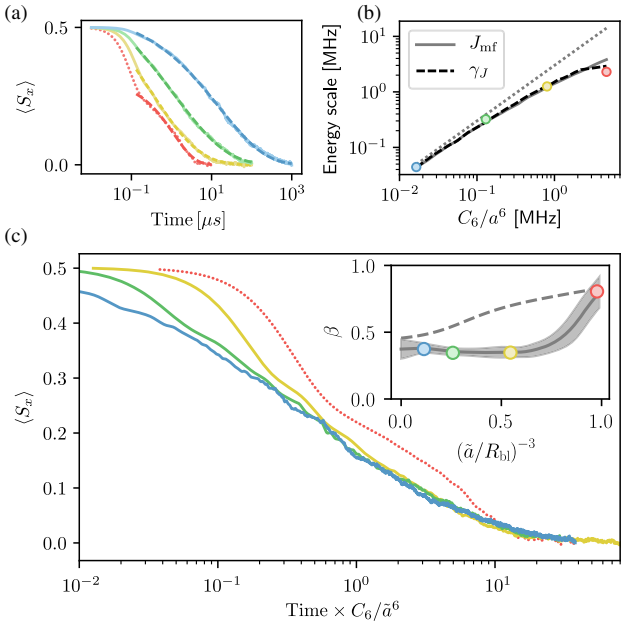

FIG. 6. Numerical simulation of the dynamics for a uniform density distribution using the DTWA. (a) The simulated dynamics before rescaling. After the quadratic onset, the magnetization decay is fitted well by the stretched exponential function (dashed lines). (b) The fitted decay rate γ_J (dashed black line) agrees well with the median of the mean-field interaction strengths J_{mf} (solid gray line), which is the typical energy scale of the system. In the weakly interacting limit, J_{mf} scales linearly with C_6/a^6 (dotted gray line). The colored dots denote the decay rate derived from the four simulations depicted in (a). (c) For small ($\rho_S = 1.25 \times 10^8 \mathrm{cm}^{-3}$, blue line and blue dot in the inset) and intermediate densities ($\rho_S = 3.51 \times 10^8 \mathrm{cm}^{-3}$, green line and green dot in inset and $\rho_S = 8.73 \times 10^8 \mathrm{cm}^{-3}$, yellow line and yellow dot in the inset), the numerical data collapses on one curve after rescaling time with $C_6/\tilde{a}^6$, where $\tilde{a}$ plays the role of an effective distance that takes into account the roles of disorder and power law interactions. For densities as large as $\rho_S = 2.11 \times 10^9\ \mathrm{cm}^{-3}$ (dotted red line and red dot in the inset), the spatial order introduced by the blockade is so large that the dynamics does not follow the universal behavior observed for smaller densities. Inset: disorder averaged stretching exponent β (solid line) as a function of the order in the system expressed by $(\tilde{a}/R_{\mathrm{bl}})^{-3}$. Below a critical value of $(\tilde{a}/R_{\mathrm{bl}})^{-3} \lesssim 0.7$ the exponent becomes constant. The shaded area indicates statistical uncertainty. The dots denote the exponent β resulting from the single disorder realizations of (a). The dashed line is obtained from the fluctuator model [see Eq. (6) in Sec. VI].

excluding possible effects of the inhomogeneous spin density resulting from the optical trap. The simulated spin dynamics for a uniform density distribution ρ_S are shown by the solid lines in Fig. 6(a). For early times where $t \leq 2\pi R_{\mathrm{bl}}^6/C_6$, the leading order quadratic Hamiltonian evolution is clearly visible. For times beyond the perturbative short-time regime, the relaxation is well described by a stretched exponential [dashed lines in Fig. 6(a); see Appendix D], proving that the glassy dynamics is an intrinsic many-body effect and not a result of the density inhomogeneities.

Figure 6(b) shows the fitted relaxation rate γ_J of the four simulations from Fig. 6(a) (colored dots, the disorder average is shown as a dashed black line). This rate does not scale with C_6/a^6 [$a = (4\pi\rho_S/3)^{-1/3}$ (dotted line)] but with the median of the mean-field interaction strengths J_{mf} (solid line), which plays the role of the characteristic energy scale in the system (see Appendix E). This scale $J_{\mathrm{mf}} = C_6/\tilde{a}^6$ defines an effective Wigner-Seitz radius $\tilde{a}$, that coincides with the usual Wigner-Seitz radius a for small spin densities but deviates at larger densities when spatial correlations induced by the Rydberg blockade effect become important. Rescaling the time with $C_6/\tilde{a}^6$, the simulated data from Fig. 6(a) collapse on a single stretched exponential curve [see Fig. 6(c)], similarly to the experimental observations in Fig. 5(b).

This insensitivity to changes in the cutoff energy induced by the blockade effect substantiates the nature of the universal relaxation dynamics. This is further confirmed by the fitted stretching exponent β shown in the inset of Fig. 6(c) obtained after disorder averaging [the solid line depicts the mean, the gray shaded area shows the standard deviation, the colored dots the single disorder realizations from Fig. 6(a)]. We find β to be approximately constant for large disorder strengths where spatial correlations are weak [i.e., $(\tilde{a}/R_{\mathrm{bl}})^{-3} \lesssim 0.7$], with a value of 0.36, close to the experimental value of $\beta = 0.32(2)$. In fact, the range of densities in the inhomogeneous experimental distribution falls well into the regime of a constant stretching exponent [see inset in Fig. 5(b)].

The simulations allow us to access even higher densities than those accessible in the experiment, corresponding to more correlated spatial configurations of the atoms. For $(\tilde{a}/R_{\mathrm{bl}})^{-3} = 1$, the DTWA simulations show significantly different dynamics [dotted line in Fig. 6(a)] that translates into a stretching exponent β that becomes sensitive to the strength of the disorder above a certain threshold [see inset in Fig. 6(c)].

To understand the behavior of β when changing the disorder, we analyze the influence of the blockade effect on the distribution of coupling strengths. Figure 7 shows for four different densities the distribution function of nearest-neighbor interaction strength rescaled by C_6/a^6. At low densities, where we observe a disorder-independent stretching exponent, the rescaled distributions do not fully coincide due to the blockade effect, but their shape remains qualitatively the same. Their functional form is mostly modified at large interaction strengths which influences only the short-time dynamics. At large density, however, the distribution is strongly altered by the high-energy cutoff which renders the distribution much more peaked.

It is thus tempting to conjecture that the insensitivity of the dynamics below a certain disorder strength is related to negligible changes in the distribution of

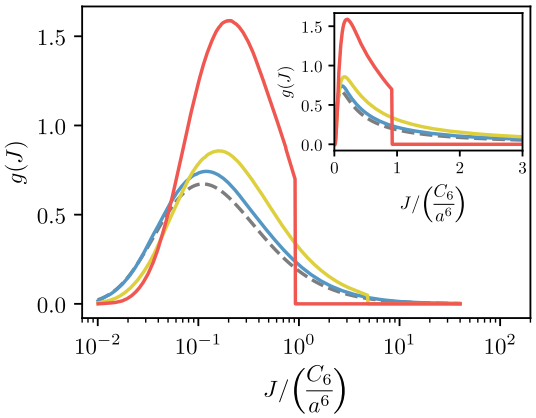

FIG. 7. Normalized probability distribution of nearest-neighbor interactions $g(J)$ for the densities given in Fig. 6 (blue line, $\rho_S = 1.25 \times 10^8$ cm^{-3}; yellow line, $\rho_S = 8.73 \times 10^8$ cm^{-3}; red line, $\rho_S = 2.11 \times 10^9$ cm^{-3}). The dashed line depicts a distribution corresponding to randomly placed spins. The blockade effect induces correlations in the system and hence the probability distribution at high densities becomes more peaked. This results in a decreased disorder compared to the completely random case. The inset shows the same data with linear axis to illustrate the narrowing of the distribution functions.

interaction strength. Nonetheless, the changes at low density are significant enough to predict a nonconstant β when applying a simple model such as the fluctuator model discussed in the next section, ruling out such a simple interpretation based on energy rescaling.

VI. COMPARISON TO OTHER SYSTEMS EXHIBITING GLASSY DYNAMICS

It is instructive to compare our findings to other systems exhibiting glassy dynamics. In *isolated* quantum systems, glassy dynamics has been observed for the Ising model which is exactly solvable by the Emch-Radin ansatz [36,42,43]. In this analytical solution the averaging over oscillatory terms results in a stretching exponent of $\beta = 1/2$ for disordered spin systems which was also confirmed experimentally [44,45]. Such a treatment is not possible for an arbitrary Heisenberg XXZ Hamiltonian since the Emch-Radin ansatz is based on the commutativity between the terms in the Hamiltonian, which is only given for the Ising model. Since the additional exchange interactions of the Heisenberg XXZ model make the system inaccessible to analytical treatment, quantum simulations are essential to investigate the problem for a large number of spins [20]. In this respect, our observation of slow dynamics in a Heisenberg XXZ model in 3D with long-range interactions reveals that glassy dynamics is not an extraordinary property of the special case of Ising systems, but a more generic feature applicable to isolated disordered spin systems. In our quantum simulation experiment, we observed a value of $\beta = 0.32(2)$, significantly lower than $1/2$.

A more general approach to explaining glassy dynamics can be deduced from *open* disordered systems where subexponential relaxation is a ubiquitous phenomenon [34]. Here, the incoherent averaging over a distribution of decay rates leads to the stretched exponential. The origin giving rise to a specific distribution depends on the exact physical system or model.

A commonly used model that predicts glassy dynamics is the fluctuator model, where each spin is embedded in a local bath that determines its decay rate. For example, this model has been applied to NV centers where spins couple to randomly distributed fluctuators [8,18,19]. A similar approach is taken for dissipative many-body localized systems where random decay rates originate from the disordered potential at each lattice site [17,46]. For our system, we apply the fluctuator model assuming that the relaxation of each spin can be effectively described by an incoherent coupling to its environment, which is determined by the local rate γ_i sampled from the probability distribution of nearest-neighbor interactions from Fig. 7 (qualitatively the same results are obtained for sampling the decay rates from the distribution of mean-field interaction strengths):

$$\langle S_x^{(i)}(t)\rangle = \frac{1}{2}\exp\left[-\gamma_i t\right]. \tag{6}$$

This model predicts a stretched exponential relaxation as observed in the experiment. However, we find two discrepancies. First, the model predicts stretching exponents of $\beta > 1/2$ inconsistent with our previous finding of β being smaller than $1/2$. Second, the fluctuator model predicts a stretching exponent varying as a function of disorder strength, as shown by the dashed line in the inset of Fig. 6(c). Hence this model is sensitive to the change in the distribution functions of the interaction strength introduced by the cutoff, as depicted in Fig. 7, already in the regime of large disorder. Therefore, the fluctuator model does not capture the collapse of dynamics onto a single curve after rescaling.

The most prominent example of open systems exhibiting slow dynamics is spin glasses where, at low temperatures, the relaxation of the macroscopic magnetization is described by a temperature-dependent stretching exponent [13,47]. Similar to the fluctuator model, this can be explained by incoherent averaging over random relaxation times. However, these times do not result from a local environment of each spin, but from a random distribution of free energies [48]. In this approach, concepts from equilibrium statistical mechanics like thermodynamic potentials are applied to describe the long-time evolution of the system. Although our system does not exhibit sign-changing interactions [49] or contain geometric frustration [50] characteristic for spin glasses, the observation of stretched exponential decay indicates that at long times a similar quasiequilibrium approach might be applicable.

This conjecture is supported by the fact that our system is expected to thermalize in the sense of the ETH, but approaches this limit only at exponentially long times in analogy to classical spin glasses.

VII. CONCLUSION

In this work we implemented the XXZ Hamiltonian in 3D using a frozen gas of Rydberg atoms. We studied the out-of-equilibrium dynamics of this model starting from an almost zero entropy initial state, which lacks a thorough theoretical understanding and is hard to simulate by classical means. We observed glassy dynamics in close analogy to the subexponential relaxation known from open disordered systems described by a stretched exponential function. While the latter is driven by thermal fluctuations, the dynamics of the disordered isolated quantum system is governed by quantum fluctuations and spreading of entanglement going beyond mean-field approximations. The observation that the dynamics of the magnetization is well described by semiclassical truncated Wigner simulations suggests that quantum interference effects become less important as the system approaches its equilibrium state. This is in line with previous findings that the long-time dynamics of generic thermalizing quantum many-body systems simplifies also in the sense that states can be represented efficiently due to limited entanglement [51].

In the experiment, disorder is changed by exploiting the Rydberg blockade, which shifts the upper cutoff scale in the distribution of interaction strengths. Remarkably, the stretching exponent β takes on a constant value above a certain disorder strength, as confirmed by both experiment and semiclassical simulations. The long-time evolution is therefore insensitive to the microscopic details of the system parameters on high-energy scales. We interpret the independence of the dynamics to changes in the distribution function of interaction strengths as universal behavior. This and the validity of a semiclassical description as a strong hint that the dynamics of many-body quantum systems might be amenable to a simplified description of the late-time dynamics in terms of effective low-energy degrees of freedom. Concretely, this could be approached within the framework of the strong disorder renormalization group, iteratively integrating out the highest energy degrees of freedom resulting from most strongly interacting spins or clusters of spins [52]. Furthermore, spin glasses in the aging regime have been found to show certain quasithermal properties. For example, a fluctuation dissipation theorem has been found to hold [53] and the spin-glass transition shows similarities to a thermal phase transition [54]. Thus, the similarities to dynamics in open glassy systems observed in this work are encouraging to extend such an effective thermal-like description to *quantum* glassy dynamics.

ACKNOWLEDGMENTS

We thank J. Berges, A. Piñiero Orioli, M. Rigol, and J. Schachenmayer for fruitful discussions. This work is part of and supported by the DFG Collaborative Research Centre "SFB 1225 (ISOQUANT)," the DFG Priority Program "GiRyd 1929," the European Union H2020 projects FET Proactive project RySQ (Grant No. 640378) and FET flagship project PASQuanS (Grant No. 817482), and the Heidelberg Center for Quantum Dynamics. S. W. acknowledges support by "Investissements d'Avenir" program through the Excellence Initiative of the University of Strasbourg (IdEx). T. F. acknowledges funding by a graduate scholarship of the Heidelberg University (LGFG) and R. F. A. from the Brazilian fund Ciência sem Fronteiras. This work is supported by Deutsche Forschungsgesellschaft (DFG, German Research Foundation) under Germany's Excellence Strategy EXC2181/1-390900948 (the Heidelberg STRUCTURES Excellence Cluster).

APPENDIX A: CALCULATION OF RYDBERG INTERACTIONS AND SPIN MODEL

In order to describe the interaction between two Rydberg excitations, the Hamiltonian is expanded in multipoles. This is well justified, as the minimal distance between the Rydberg atoms that is determined by the blockade radius R_{bl} is much larger than the LeRoy radius R_{LR} that describes the typical spread of the electron wave function. The leading order term of this expansion is the dipole-dipole interaction Hamiltonian,

$$\hat{H}_{\mathrm{DDI}} = \frac{\hat{\boldsymbol{d}}_i \cdot \hat{\boldsymbol{d}}_j - 3(\hat{\boldsymbol{d}}_i \cdot \mathbf{e}_r)(\hat{\boldsymbol{d}}_j \cdot \mathbf{e}_r)}{R^3}, \tag{A1}$$

that couples Rydberg atoms with different angular moment quantum number l. For dipolar forbidden transitions, the second order term in perturbation theory needs to be calculated giving rise to the van der Waals Hamiltonian,

$$H_{\mathrm{vdW}} = -\frac{1}{\hbar}\sum_m \frac{H_{\mathrm{DDI}}|m\rangle\langle m|H_{\mathrm{DDI}}}{\Delta_F}\delta(\omega_{fm} + \omega_{mi}), \tag{A2}$$

where the Foerster defect $\Delta_F = E_m - E_i$ is the energy difference between the intermediate and initial state, and $\delta(\omega)$ the Dirac function. Aiming for a simpler notation, the two different Rydberg states can be identified as spin states $|\uparrow\rangle$ and $|\downarrow\rangle$. In the pair state basis $(|\uparrow\uparrow\rangle, |\uparrow\downarrow\rangle, |\downarrow\uparrow\rangle, |\downarrow\downarrow\rangle)$, the total Hamiltonian describing the interaction between two atoms i and j can be written in matrix form as

$$\hat{H}_{i,j}^{\mathrm{tot}} = \begin{pmatrix} E_{\uparrow\uparrow} & 0 & 0 & 0 \\ 0 & E_{\downarrow\uparrow} & \frac{J_{\mathrm{ex}}}{2} & 0 \\ 0 & \frac{J_{\mathrm{ex}}}{2} & E_{\downarrow\uparrow} & 0 \\ 0 & 0 & 0 & E_{\downarrow\downarrow} \end{pmatrix}, \tag{A3}$$

with the matrix elements $E_{\uparrow\uparrow} = \langle\uparrow\uparrow|H_{\mathrm{vdW}}|\uparrow\uparrow\rangle$, $E_{\downarrow\uparrow} = \langle\downarrow\uparrow|H_{\mathrm{vdW}}|\downarrow\uparrow\rangle$, $E_{\downarrow\downarrow} = \langle\downarrow\downarrow|H_{\mathrm{vdW}}|\downarrow\downarrow\rangle$, and $J_{\mathrm{ex}} = \langle\uparrow\downarrow|H_{\mathrm{vdW}}|\downarrow\uparrow\rangle$. This Hamiltonian can be identified as the Heisenberg XXZ Hamiltonian,

$$H_{\mathrm{XXZ}} = \frac{1}{2}\sum_{i,j} J_{ij}\left(S_x^{(i)}S_x^{(j)} + S_y^{(i)}S_y^{(j)} + \delta S_z^{(i)}S_z^{(j)}\right) + \sum_i \Delta_{\mathrm{vdW}} S_z^{(i)},$$

where $J_{ij} = 2J_{\mathrm{ex}}$, $\delta = (E_{\downarrow\downarrow} + E_{\uparrow\uparrow} - 2E_{\downarrow\uparrow})/J_{ij}$, and $\Delta_{\mathrm{vdW}} = (E_{\downarrow\downarrow} - E_{\uparrow\uparrow})/2$. The additional single-spin detuning Δ_{vdW} is an order of magnitude smaller than the interaction strength J_{ij} and thus negligible.

The matrix elements $E_{\uparrow\uparrow}$, $E_{\downarrow\uparrow}$, $E_{\downarrow\downarrow}$, and J_{ex} were calculated using the PYTHON module ARC [30]. For the Rydberg states $|48S_{1/2}, +\frac{1}{2}\rangle$ and $|49S_{1/2}, +\frac{1}{2}\rangle$ this yields the interaction strength $J_{ij} = C_6/r_{ij}$ with $C_6/(2\pi) = 59\ \mathrm{GHz}\,\mu\mathrm{m}^6$ and $\delta = -0.73$.

APPENDIX B: DETERMINATION OF THE MAGNETIZATION

The magnetization is extracted from population measurements of the Rydberg states after the readout pulse. To vary the phase ϕ of this pulse rapidly enough in order to explore the short-time dynamics, the microwave field is generating using frequency up-conversion with a radio-frequency field of frequency 400 MHz, offering time resolution of 10 ns. The populations of the Rydberg states are then extracted using electric field ionization [55]. At the end of the sequence, a strong electric field of $100\ \mathrm{V\,cm^{-1}}$ is switched on and the resulting ions are guided toward a multichannel plate detector. To calibrate the detection efficiency, we combine ionization measurements and depletion imaging [29]. We deduce a detection efficiency $\eta = 0.173 \pm 0.043$ from four different calibration curves.

At time t we access the magnetization $\langle S_\phi\rangle$ by counting after the readout pulse both the population of the $|\uparrow\rangle$ state $N_\uparrow(\phi)$ and the total spin number $N_{\downarrow+\uparrow}$, according to

$$\langle S_\phi\rangle = \frac{N_\uparrow(\phi) - N_\downarrow(\phi)}{2N_{\uparrow+\downarrow}} = \frac{N_\uparrow(\phi)}{N_{\uparrow+\downarrow}} - \frac{1}{2}. \tag{B1}$$

Since the ionization is not state selective, $N_\uparrow(\phi)$ is inferred by counting the spin number after depopulating the $|\downarrow\rangle$ state. It is performed by optically coupling the $|\downarrow\rangle$ state to the short-lived intermediate state $|e\rangle$ during 1.5 μs.

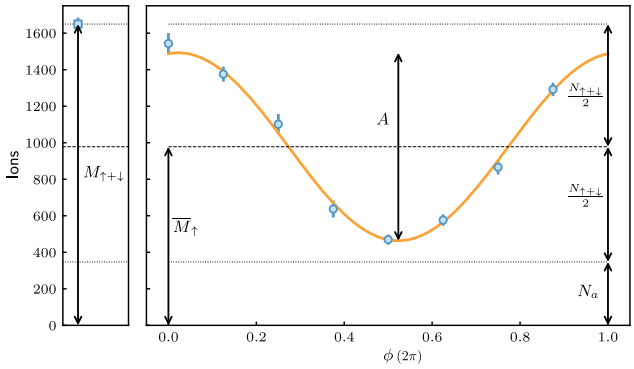

FIG. 8. Reconstruction of the magnetization. Left: measurements of the total number of spins $M_{\uparrow+\downarrow}$. Right: measurement of the population in the $|\uparrow\rangle$ state $M_\uparrow(\phi)$ after a readout pulse of phase ϕ. Both are affected by the population in auxiliary states N_a. The measurement $M_\uparrow$ is fitted by a sinusoidal function (orange line), from which we extract the mean value $\bar{M}_\uparrow$. The amplitude A of the fit, normalized by the total number of spin $N_{\uparrow+\downarrow}$, indicates the magnetization in the xy plane.

Because of the finite lifetime of the spin states and microwave transfer, auxiliary Rydberg states might also be populated. This residual population leads to an offset in the measured ion signal, a number N_a of those atoms being energetically above the ionization threshold (see Fig. 8). As a consequence, what we measure instead of $N_\uparrow(\phi)$ and $N_{\downarrow+\uparrow}$ are two quantities $M_\uparrow(\phi)$ and $M_{\downarrow+\uparrow}$ given by

$$M_\uparrow(\phi) = N_\uparrow(\phi) + N_a, \tag{B2}$$

$$M_{\downarrow+\uparrow} = N_{\downarrow+\uparrow} + N_a. \tag{B3}$$

The measured quantity $M_\uparrow$ is a sinusoidal function of ϕ, centered around its mean value:

$$\bar{M}_\uparrow = \frac{N_{\downarrow+\uparrow}}{2} + N_a. \tag{B4}$$

We determine from a sinusoidal fit the values $M_\uparrow(\phi)$ and $\bar{M}_\uparrow$ and thus compute the magnetization $\langle S_\phi\rangle$ using Eqs. (B1)–(B4). The amplitude A of the sinusoidal fit, normalized by $N_{\uparrow+\downarrow}$, corresponds to the magnetization in the xy plane. Following this procedure, we deduce that the number of atoms in the auxiliary states N_a increases linearly in time with a rate of 7 kHz, consistent with the blackbody decay of the spin states toward Rydberg states above the ionization threshold.

APPENDIX C: THEORETICAL MODELS

To compare the experiment to the mean-field prediction, we solve the classical equations of motion that are obtained from the classical Hamiltonian function [41],

$$H_C = \frac{1}{2}\sum_{i,j} J_{ij}\left(s_x^{(i)}s_x^{(j)} + s_y^{(i)}s_y^{(j)} + \delta s_z^{(i)}s_z^{(j)}\right), \quad \text{(C1)}$$

via Hamilton's equation

$$\dot{s}_x^{(j)} = \{s_x^{(j)}, H_C\}. \quad \text{(C2)}$$

Here, $s^{(i)} = (s_x^{(i)}, s_y^{(i)}, s_z^{(i)})$ are classical spins and $\{\cdots\}$ denotes the Poisson bracket. The system of ordinary differential equations is solved by Tsitouras's 5/4 Runge-Kutta method [56] using the JULIA differential equations package [57]. For a perfect initial state where all spins are aligned in the x direction, mean-field theory does not predict any dynamics. However, the interactions present during the first $\pi/2$ pulse of the Ramsey protocol induce small fluctuations in the initial state. We take these imperfections into account by including the preparation and readout pulses in the simulations, which leads to the dynamics shown by the dotted line in Fig. 4. For the relevant timescale of the experiment, these dynamics are negligible.

For the considered dynamics, the initial state is an eigenstate of the mean-field Hamiltonian. The relaxation is thus triggered by the initial quantum fluctuations, meaning that mean-field approaches fail in this case. Instead, we use a discrete truncated Wigner approximation (DTWA), which still performs classical evolution of the spins following Eq. (C2) but includes the initial quantum fluctuations into statistical ensembles of the initial state by sampling Monte Carlo trajectories on discrete phase space [40,41]. For the simulations in this paper, we sample over 100 initial conditions, which is sufficient for the magnetization to be converged. Simulating far-from-equilibrium dynamics of disordered spin systems has been successfully applied to spin systems in recent work [21]. Imperfections of the preparation and readout are taken into account by simulating the whole Ramsey sequence including those two microwave pulses. We also compared DTWA with an approximate quantum mechanical model, the so-called moving average cluster expansion (MACE) [58], which qualitatively gives similar results (see Fig. 9).

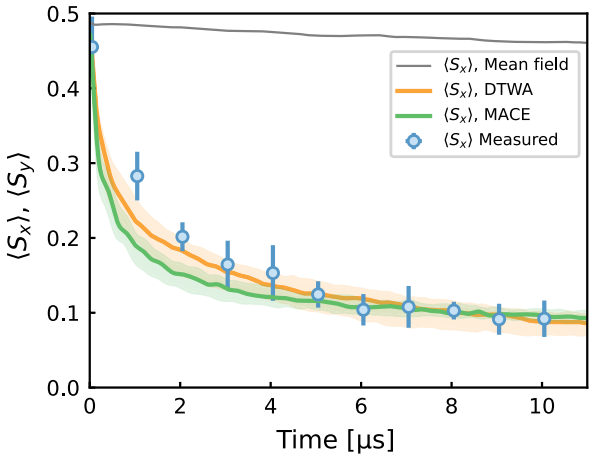

FIG. 9. Comparison between DTWA and MACE. Both moving average cluster expansion (MACE) and DTWA perform well to describe the experimental data at late times. At intermediate times (between 1 and 3 μs), MACE predicts faster depolarization dynamics.

APPENDIX D: QUANTIFICATION OF SLOW DYNAMICS BY A STRETCHED EXPONENTIAL

A phenomenological approach to describe slow dynamics in disordered systems is a fit of the magnetization with a stretched exponential,

$$\langle S_x\rangle(t) = \frac{1}{2}\exp[-(\gamma_J t)^\beta], \quad \text{(D1)}$$

with relaxation rate γ_J and stretching exponent β. This was already proposed by Kohlrausch in 1847 [59]; a review on the stretching exponent in numerical simulations and in experimental data of various materials can be found in Ref. [34].

For $\beta = 1$, the stretched exponential describes an exponential decay. In the limit $\beta \to 0$, the stretched exponential approaches the logarithmic decay which can be seen by performing a Taylor expansion at small β:

$$\exp[-(t/\tau)^\beta] = \frac{1}{e} - \frac{\beta\log(\frac{t}{\tau})}{e} + \mathcal{O}(\beta^3). \quad \text{(D2)}$$

So, the stretching exponent β quantifies how slow a system relaxes: A small value signifies that the dynamics are close to logarithmic and slow; a large value indicates fast dynamics.

The magnetization at early times can be calculated by the Baker-Campbell-Haussdorff formula:

$$\begin{aligned}\langle S_x(t)\rangle &= \langle e^{iHt}S_x e^{-iHt}\rangle \\ &= \langle S_x\rangle + it\langle[H,S_x]\rangle - t^2/2\langle[H,[H,S_x]]\rangle + \cdots.\end{aligned} \quad \text{(D3)}$$

Since the initial state $|\rightarrow\rangle_x^{\otimes N}$ is an eigenstate of S_x, the expectation value of the commutator $[H, S_x]$ vanishes for this state and we expect the initial dynamics to be quadratic in time. However, this does not hold for the stretched exponential function that is a power law with exponent β for short times $t \ll (1/\gamma_J)$:

$$\langle S_x\rangle(t) = 1/2[1 - \beta(\gamma_J t)^\beta]. \quad \text{(D4)}$$

Therefore, we exclude the very early dynamics from the fit where $t < 1/J_{\max}$ (see Fig. 6).

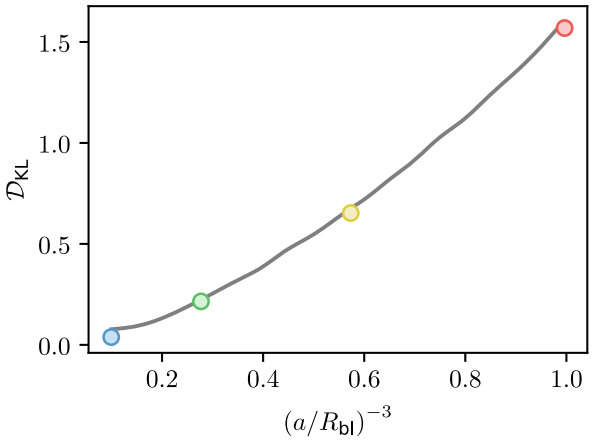

FIG. 10. Scaling of the disorder strength as a function of density. The Kullback-Leibler divergence $\mathcal{D}_{\mathrm{KL}}$ increases monotonically with $(a/R_{\mathrm{bl}})^{-3}$. This quantifies the additional correlations induced by the Rydberg blockade effect. The dots indicate the Kullback-Leibler divergence corresponding to the specific simulations presented in Fig. 6.

APPENDIX E: SPATIAL SPIN DISTRIBUTION AND DISORDER STRENGTH

To model the experimental 3D spin distribution, we employ a simplified description of the Rydberg excitation dynamics in a cloud of ground-state atoms. Although the experimental procedure creates a superposition of different configurations of atoms being excited to the Rydberg state, each configuration of this superposition can be regarded as an independent disorder realization. Indeed, the different configurations evolve independently from each other under the spin dynamics, and the final projective measurement randomly selects one of them (see Appendix B). Thus, to create samples of such configurations of Rydberg excitations we iteratively select atoms randomly and excite them to the Rydberg state with a certain excitation probability which we set to zero if another atom within a distance of R_{bl} is already in the Rydberg state. The excitation probability includes a collective enhancement factor caused by the Rydberg blockade effect [60,61]. We also take into account the profile of the laser excitation, characterized by a Gaussian distribution of the two-photon Rabi frequency with measured radius $\sigma = 70.6(3)$ μm ($e^{-1/2}$), and the Gaussian density distribution of the ground-state atomic cloud [measured radii at $e^{-1/2}$: $\sigma_x = 203(3)$ μm, $\sigma_y = \sigma_z = 35(1)$ μm]. In our simulations, the peak two-photon Rabi frequency was chosen such that the total number of excited atoms equals the one measured by field ionization.

For simulations of a homogeneous system, the spins are randomly distributed in a uniform box taking into account a blockade radius of 5 μm until the desired density ρ_S is reached. In the limit of no blockade effect, the nearest-neighbor distribution for a given Wigner-Seitz radius $a = (4\pi\rho/3)^{-1/3}$ would be given by [33]

$$h(r) = \frac{3}{a}(r/a)^2 \exp[-(r/a)^3], \tag{E1}$$

yielding the distribution of coupling strengths $h(J) = h(r)(\partial r/\partial J)$. Instead, the blockade effect modifies the nearest-neighbor distribution, resulting in a different coupling distribution $g(J)$ [see Fig. 7(a)]. We quantify the disorder strength of the spin system with the Kullback-Leibler divergence [62],

$$\mathcal{D}_{\mathrm{KL}}(g\|h) = \int g(J)\log\left(\frac{g(J)}{h(J)}\right)dJ, \tag{E2}$$

i.e., the amount of information that is gained by updating from the distribution $h(J)$. Indeed, the Kulback-Leibler divergence increases almost linearly with density (see Fig. 10). This confirms that $(a/R_{\mathrm{bl}})^{-3}$ is a relevant scale to describe the disorder strength.

When investigating the universal character of the spin dynamics for a homogeneous system, we have concluded that the typical energy scale should be determined by the median of the mean-field energy $J_{\mathrm{mf}} = \mathrm{median}(C_6/\tilde{r}_i^6)$, with $\tilde{r}_i^{-6} = \sum_j r_{ij}^{-6}$ (see Fig. 6). The effective distance $\tilde{a}$, defined by $J_{\mathrm{mf}} = C_6/\tilde{a}^6$, thus corresponds to the median of the non-Gaussian distribution $\{\tilde{r}_i\}$.

APPENDIX F: SUMMARY OF PARAMETERS

Table I summarizes the parameters of the individual measurements shown in Figs. 2 and 3 of the main text.

TABLE I. Experimental parameters. t_{exc} denotes the time of laser excitation from the ground to the Rydberg state. ρ_{gs}^0 denotes the measured ground-state density. ρ_S^0 the derived peak spin density, N_S the derived number of total spins. R_{bl} is the blockade radius derived from the excitation time and laser coupling strength. a denotes the Wigner-Seitz radius, C_6/a^6 the van der Waals coefficient, and β is the exponent of the stretching exponential derived from a fit to the relaxation curves.

Figure	t_{exc} (μs)	ρ_{gs}^0 10^{11} (cm^{-3})	ρ_S^0 10^9 (cm^{-3})	$N_S \times 1000$	R_{bl} (μm)	a (μm)	$(a/R_{\mathrm{bl}})^{-3}$	$C_6/(2\pi)/a^6$ (MHz)	β
2, 3	1.0	1.79(9)	1.2(3)	1.2(3)	5.21	5.8(5)	0.7(2)	1.5(8)	0.32(2)
3	0.6	1.69(12)	0.43(11)	0.4(1)	4.81	8.2(7)	0.20(5)	0.195(97)	0.37(2)
3	0.8	1.73(9)	0.8(2)	0.8(2)	5.03	6.6(6)	0.43(11)	0.7(3)	0.36(4)
3	1.0	1.64(15)	1.2(3)	1.1(3)	5.21	5.9(5)	0.7(2)	1.4(7)	0.305(14)

[1] M. Rigol, V. Dunjko, and M. Olshanii, *Thermalization and Its Mechanism for Generic Isolated Quantum Systems*, Nature (London) **452**, 854 (2008).

[2] M. Prüfer, P. Kunkel, H. Strobel, S. Lannig, D. Linnemann, C. M. Schmied, J. Berges, T. Gasenzer, and M. K. Oberthaler, *Observation of Universal Dynamics in a Spinor Bose Gas Far from Equilibrium*, Nature (London) **563**, 217 (2018).

[3] C. Eigen, J. A. Glidden, R. Lopes, E. A. Cornell, R. P. Smith, and Z. Hadzibabic, *Universal Prethermal Dynamics of Bose Gases Quenched to Unitarity*, Nature (London) **563**, 221 (2018).

[4] S. Erne, R. Bücker, T. Gasenzer, J. Berges, and J. Schmiedmayer, *Universal Dynamics in an Isolated One-Dimensional Bose Gas far from Equilibrium*, Nature (London) **563**, 225 (2018).

[5] N. Y. Yao, C. R. Laumann, S. Gopalakrishnan, M. Knap, M. Müller, E. A. Demler, and M. D. Lukin, *Many-Body Localization in Dipolar Systems*, Phys. Rev. Lett. **113**, 243002 (2014).

[6] J. Smith, A. Lee, P. Richerme, B. Neyenhuis, P. W. Hess, P. Hauke, M. Heyl, D. A. Huse, and C. Monroe, *Many-Body Localization in a Quantum Simulator with Programmable Random Disorder*, Nat. Phys. **12**, 907 (2016).

[7] J. Y. Choi, S. Hild, J. Zeiher, P. Schauß, A. Rubio-Abadal, T. Yefsah, V. Khemani, D. A. Huse, I. Bloch, and C. Gross, *Exploring the Many-Body Localization Transition in Two Dimensions*, Science **352**, 1547 (2016).

[8] S. Choi, J. Choi, R. Landig, G. Kucsko, H. Zhou, J. Isoya, F. Jelezko, S. Onoda, H. Sumiya, V. Khemani, C. von Keyserlingk, N. Y. Yao, E. Demler, and M. D. Lukin, *Observation of Discrete Time-Crystalline Order in a Disordered Dipolar Many-Body System*, Nature (London) **543**, 221 (2017).

[9] J. Zhang, P. W. Hess, A. Kyprianidis, P. Becker, A. Lee, J. Smith, G. Pagano, I.-D. Potirniche, A. C. Potter, A. Vishwanath, N. Y. Yao, and C. Monroe, *Observation of a Discrete Time Crystal*, Nature (London) **543**, 217 (2017).

[10] H. Bernien, S. Schwartz, A. Keesling, H. Levine, A. Omran, H. Pichler, S. Choi, A. S. Zibrov, M. Endres, M. Greiner, V. Vuletic, and M. D. Lukin, *Probing Many-Body Dynamics on a 51-Atom Quantum Simulator*, Nature (London) **551**, 579 (2017).

[11] C. J. Turner, A. A. Michailidis, D. A. Abanin, M. Serbyn, and Z. Papić, *Weak Ergodicity Breaking from Quantum Many-Body Scars*, Nat. Phys. **14**, 745 (2018).

[12] S. A. Parameswaran, A. C. Potter, and R. Vasseur, *Eigenstate Phase Transitions and the Emergence of Universal Dynamics in Highly Excited States*, Ann. Phys. (Berlin) **529**, 1600302 (2017).

[13] K. Binder and A. P. Young, *Spin Glasses: Experimental Facts, Theoretical Concepts, and Open Questions*, Rev. Mod. Phys. **58**, 801 (1986).

[14] E. Ladizinsky *et al.*, *Phase Transitions in a Programmable Quantum Spin Glass Simulator*, Science **361**, 162 (2018).

[15] J. Gezo, T. K. Lui, B. Wolin, C. P. Slichter, R. Giannetta, and J. A. Schlueter, *Stretched Exponential Spin Relaxation in Organic Superconductors*, Phys. Rev. B **88**, 140504(R) (2013).

[16] M. Dzugutov and J. C. Phillips, *Structural Relaxation in an Equilibrium Quasicrystal*, J. Non-Cryst. Solids **192–193**, 397 (1995).

[17] H. P. Lüschen, P. Bordia, S. S. Hodgman, M. Schreiber, S. Sarkar, A. J. Daley, M. H. Fischer, E. Altman, I. Bloch, and U. Schneider, *Signatures of Many-Body Localization in a Controlled Open Quantum System*, Phys. Rev. X **7**, 011034 (2017).

[18] J. Choi, S. Choi, G. Kucsko, P. C. Maurer, B. J. Shields, H. Sumiya, S. Onoda, J. Isoya, E. Demler, F. Jelezko, N. Y. Yao, and M. D. Lukin, *Depolarization Dynamics in a Strongly Interacting Solid-State Spin Ensemble*, Phys. Rev. Lett. **118**, 093601 (2017).

[19] G. Kucsko, S. Choi, J. Choi, P. C. Maurer, H. Zhou, R. Landig, H. Sumiya, S. Onoda, J. Isoya, F. Jelezko, E. Demler, N. Y. Yao, and M. D. Lukin, *Critical Thermalization of a Disordered Dipolar Spin System in Diamond*, Phys. Rev. Lett. **121**, 023601 (2018).

[20] K. R. A. Hazzard, S. R. Manmana, M. Foss-Feig, and A. M. Rey, *Far-from-Equilibrium Quantum Magnetism with Ultracold Polar Molecules*, Phys. Rev. Lett. **110**, 075301 (2013).

[21] A. P. Orioli, A. Signoles, H. Wildhagen, G. Günter, J. Berges, S. Whitlock, and M. Weidemüller, *Relaxation of an Isolated Dipolar-Interacting Rydberg Quantum Spin System*, Phys. Rev. Lett. **120**, 063601 (2018).

[22] J. Simon, W. S. Bakr, R. Ma, M. E. Tai, P. M. Preiss, and M. Greiner, *Quantum Simulation of Antiferromagnetic Spin Chains in an Optical Lattice*, Nature (London) **472**, 307 (2011).

[23] D. S. Jin, K. R. A. Hazzard, S. A. Moses, B. Gadway, B. Yan, J. P. Covey, A. M. Rey, and J. Ye, *Observation of Dipolar Spin-Exchange Interactions with Lattice-Confined Polar Molecules*, Nature (London) **501**, 521 (2013).

[24] H. Labuhn, D. Barredo, S. Ravets, S. De Léséleuc, T. Macrì, T. Lahaye, and A. Browaeys, *Tunable Two-Dimensional Arrays of Single Rydberg Atoms for Realizing Quantum Ising Models*, Nature (London) **534**, 667 (2016).

[25] S. Lepoutre, J. Schachenmayer, L. Gabardos, B. Zhu, B. Naylor, E. Maréchal, O. Gorceix, A. M. Rey, L. Vernac, and B. Laburthe-Tolra, *Out-of-Equilibrium Quantum Magnetism and Thermalization in a Spin-3 Many-Body Dipolar Lattice System*, Nat. Commun. **10**, 1714 (2019).

[26] A. Patscheider, B. Zhu, L. Chomaz, D. Petter, S. Baier, A.-M. Rey, F. Ferlaino, and M. J. Mark, *Controlling Dipolar Exchange Interactions in a Dense Three-Dimensional Array of Large-Spin Fermions*, Phys. Rev. Research **2**, 023050 (2020).

[27] S. Whitlock, A. W. Glaetzle, and P. Hannaford, *Simulating Quantum Spin Models Using Rydberg-Excited Atomic Ensembles in Magnetic Microtrap Arrays*, J. Phys. B **50**, 074001 (2017).

[28] T. L. Nguyen, J. M. Raimond, C. Sayrin, R. Cortiñas, T. Cantat-Moltrecht, F. Assemat, I. Dotsenko, S. Gleyzes, S. Haroche, G. Roux, T. Jolicoeur, and M. Brune, *Towards Quantum Simulation with Circular Rydberg Atoms*, Phys. Rev. X **8**, 011032 (2018).

[29] M. Ferreira-Cao, V. Gavryusev, T. Franz, R. F. Alves, A. Signoles, G. Zürn, and M. Weidemüller, *Depletion Imaging*

of Rydberg Atoms in Cold Atomic Gases, J. Phys. B **53**, 084004 (2020).

[30] N. Šibalić, J. D. Pritchard, C. S. Adams, and K. J. Weatherill, *ARC: An Open-Source Library for Calculating Properties of Alkali Rydberg Atoms*, Comput. Phys. Commun. **220**, 319 (2017).

[31] J. D. Carter and J. D. D. Martin, *Coherent Manipulation of Cold Rydberg Atoms near the Surface of an Atom Chip*, Phys. Rev. A **88**, 043429 (2013).

[32] C. Hermann-Avigliano, R. C. Teixeira, T. L. Nguyen, T. Cantat-Moltrecht, G. Nogues, I. Dotsenko, S. Gleyzes, J. M. Raimond, S. Haroche, and M. Brune, *Long Coherence Times for Rydberg Qubits on a Superconducting Atom Chip*, Phys. Rev. A **90**, 040502(R) (2014).

[33] P. Hertz, *Über den Gegenseitigen Durchschnittlichen Abstand von Punkten, die mit Bekannter Mittlerer Dichte im Raume Angeordnet Sind*, Math. Ann. **67**, 387 (1909).

[34] J. C. Phillips, *Stretched Exponential Relaxation in Molecular and Electronic Glasses*, Rep. Prog. Phys. **59**, 1133 (1996).

[35] M. H. Fischer, M. Maksymenko, and E. Altman, *Dynamics of a Many-Body-Localized System Coupled to a Bath*, Phys. Rev. Lett. **116**, 160401 (2016).

[36] R. Mukherjee, T. C. Killian, and K. R. A. Hazzard, *Accessing Rydberg-Dressed Interactions Using Many-Body Ramsey Dynamics*, Phys. Rev. A **94**, 053422 (2016).

[37] P. Schauß, M. Cheneau, M. Endres, T. Fukuhara, S. Hild, A. Omran, T. Pohl, C. Gross, S. Kuhr, and I. Bloch, *Observation of Mesoscopic Crystalline Structures in a Two-Dimensional Rydberg Gas*, Nature (London) **491**, 87 (2012).

[38] S. Bettelli, D. Maxwell, T. Fernholz, C. S. Adams, I. Lesanovsky, and C. Ates, *Exciton Dynamics in Emergent Rydberg Lattices*, Phys. Rev. A **88**, 043436 (2013).

[39] A. Urvoy, F. Ripka, I. Lesanovsky, D. Booth, J. P. Shaffer, T. Pfau, and R. Löw, *Strongly Correlated Growth of Rydberg Aggregates in a Vapor Cell*, Phys. Rev. Lett. **114**, 203002 (2015).

[40] A. Polkovnikov, *Phase Space Representation of Quantum Dynamics*, Ann. Phys. (Amsterdam) **325**, 1790 (2010).

[41] J. Schachenmayer, A. Pikovski, and A. M. Rey, *Many-Body Quantum Spin Dynamics with Monte Carlo Trajectories on a Discrete Phase Space*, Phys. Rev. X **5**, 011022 (2015).

[42] G. G. Emch, *Non-Markovian Model for the Approach to Equilibrium*, J. Math. Phys. (N.Y.) **7**, 1198 (1966).

[43] C. Radin, *Approach to Equilibrium in a Simple Model*, J. Math. Phys. (N.Y.) **11**, 2945 (1970).

[44] N. Takei, C. Sommer, C. Genes, G. Pupillo, H. Goto, K. Koyasu, H. Chiba, M. Weidemüller, and K. Ohmori, *Direct Observation of Ultrafast Many-Body Electron Dynamics in an Ultracold Rydberg Gas*, Nat. Commun. **7**, 13449 (2016).

[45] C. Sommer, G. Pupillo, N. Takei, S. Takeda, A. Tanaka, K. Ohmori, and C. Genes, *Time-Domain Ramsey Interferometry with Interacting Rydberg Atoms*, Phys. Rev. A **94**, 053607 (2016).

[46] B. Everest, I. Lesanovsky, J. P. Garrahan, and E. Levi, *Role of Interactions in a Dissipative Many-Body Localized System*, Phys. Rev. B **95**, 024310 (2017).

[47] J.-P. Bouchaud, L. F. Cugliandolo, J. Kurchan, and M. Mezard, *Out of Equilibrium Dynamics in Spin-Glasses and Other Glassy Systems*, in *Spin Glasses and Random Fields*, edited by A. P. Young (World Scientific, Singapore, 1997), p. 161.

[48] C. De Dominicis, H. Orland, and F. Lainée, *Stretched Exponential Relaxation in Systems with Random Free Energies*, J. Phys. (Paris), Lett. **46**, 463 (1985).

[49] A. P. Young and H. Rieger, *Numerical Study of the Random Transverse-Field Ising Spin Chain*, Phys. Rev. B **53**, 8486 (1996).

[50] Y. Crespo, A. Andreanov, and N. Seriani, *Competing Antiferromagnetic and Spin-Glass Phases in a Hollandite Structure*, Phys. Rev. B **88**, 014202 (2013).

[51] E. Leviatan, F. Pollmann, J. H. Bardarson, D. A. Huse, and E. Altman, *Quantum Thermalization Dynamics with Matrix-Product States*, arXiv:1702.08894.

[52] F. Iglói and C. Monthus, *Strong Disorder RG Approach—A Short Review of Recent Developments*, Eur. Phys. J. B **91**, 290 (2018).

[53] D. Hérisson and M. Ocio, *Fluctuation-Dissipation Ratio of a Spin Glass in the Aging Regime*, Phys. Rev. Lett. **88**, 257202 (2002).

[54] P. W. Anderson, *Spin Glass II: Is There a Phase Transition?*, Phys. Today, **41**, No. 3, 9 (1988).

[55] S. A. Edelstein and T. F. Gallagher, in *Advances in Atomic and Molecular Physics*, Cambridge Monographs on Atomic, Molecular and Chemical Physics, Vol. 14 (Cambridge University Press, Cambridge, England, 1979), pp. 365–392.

[56] C. Tsitouras, *Runge–Kutta Pairs of Order 5(4) Satisfying Only the First Column Simplifying Assumption*, Comput. Math. Appl. **62**, 770 (2011).

[57] C. Rackauckas and Q. Nie, *DifferentialEquations.jl—A Performant and Feature-Rich Ecosystem for Solving Differential Equations in Julia*, J. Open Res. Software **5**, 15 (2017).

[58] K. R. A. Hazzard, B. Gadway, M. Foss-Feig, B. Yan, S. A. Moses, J. P. Covey, N. Y. Yao, M. D. Lukin, J. Ye, D. S. Jin, and A. M. Rey, *Many-Body Dynamics of Dipolar Molecules in an Optical Lattice*, Phys. Rev. Lett. **113**, 195302 (2014).

[59] R. Kohlrausch, *Theorie des Elektrischen Rückstandes in der Leidener Flasche*, Ann. Phys. (Berlin) **167**, 56 (1854).

[60] H. Weimer, R. Löw, T. Pfau, and H. P. Büchler, *Quantum Critical Behavior in Strongly Interacting Rydberg Gases*, Phys. Rev. Lett. **101**, 250601 (2008).

[61] M. Gärttner, K. P. Heeg, T. Gasenzer, and J. Evers, *Finite-Size Effects in Strongly Interacting Rydberg Gases*, Phys. Rev. A **86**, 033422 (2012).

[62] S. Kullback and R. A. Leibler, *On Information and Sufficiency*, Ann. Math. Stat. **22**, 79 (1951).

Letter

Glassy quantum dynamics of disordered Ising spins

P. Schultzen,[1,*] T. Franz,[1,*] S. Geier,[1] A. Salzinger,[1] A. Tebben,[1] C. Hainaut,[1] G. Zürn,[1] M. Weidemüller,[1] and M. Gärttner[1,2,3,†]

[1]*Physikalisches Institut, Universität Heidelberg, Im Neuenheimer Feld 226, 69120 Heidelberg, Germany*
[2]*Kirchhoff-Institut für Physik, Universität Heidelberg, Im Neuenheimer Feld 227, 69120 Heidelberg, Germany*
[3]*Institut für Theoretische Physik, Ruprecht-Karls-Universität Heidelberg, Philosophenweg 16, 69120 Heidelberg, Germany*

(Received 1 April 2021; accepted 20 December 2021; published 19 January 2022; corrected 27 January 2022)

We study the out-of-equilibrium dynamics of the quantum Ising model with power-law interactions and positional disorder. For arbitrary dimension d and interaction range $\alpha \geqslant d$ we analytically find a stretched-exponential decay of the global magnetization and ensemble-averaged single-spin purity with a stretch power $\beta = d/\alpha$ in the thermodynamic limit. Numerically, we confirm that glassy behavior persists for finite system sizes and sufficiently strong disorder. We identify dephasing between disordered coherent pairs as the main mechanism leading to a relaxation of global magnetization, whereas genuine many-body interactions lead to a loss of single-spin purity which signifies the buildup of entanglement. The emergence of glassy dynamics in the quantum Ising model extends prior findings in classical and open quantum systems, where the stretched-exponential law is explained by a scale-invariant distribution of timescales, to both integrable and nonintegrable quantum systems.

DOI: 10.1103/PhysRevB.105.L020201

Statistical mechanics provides a well-established framework for describing the macroscopic properties of matter in thermal equilibrium. In contrast, no general theoretical framework exists for describing dynamics out of equilibrium. Of particular interest are extremely slow relaxation processes observed in disordered materials such as spin glasses [1,2]. Phenomenologically, relaxation in these systems can be described by a stretched-exponential law $\exp[-(\gamma\tau)^{\beta}]$ with decay rate γ and stretch power β [3]. Despite the widespread success of this heuristic description, a derivation of the stretched-exponential law starting from first principles in a microscopic model has been achieved for few systems only, in particular amorphous solids [2] and spin glasses [2,4]. By generalizing three prototypical models, Klafter and Shlesinger conjectured that a scale-invariant distribution of relaxation times is the unifying basis of stretched-exponential relaxation phenomena [5].

Recently, glassy dynamics has been found to emerge also in disordered quantum systems. Subexponential relaxation dynamics was observed in experiments with nitrogen-vacancy centers in diamond [6–8] and in many-body localized systems under the influence of dissipation [9]. These studies involve *open* quantum systems where dissipation arising from coupling to an external bath explains the slow relaxation. In the generic fluctuator model [6], each particle is coupled to a local bath resulting in an average over different decay rates and thus a stretched-exponential decay law. Recently, glassy relaxation was also found in a *closed* quantum system governed by purely unitary dynamics [10]. In the absence of dissipation, the question arises whether and how glassy dynamics in isolated quantum systems is related to the degree of disorder and to the buildup of entanglement.

Understanding the dynamics of strongly interacting disordered quantum many-body systems is notoriously difficult due to the lack of applicable theoretical approaches. The absence of a small parameter in the model impedes the use of perturbative methods, and the exponential complexity of quantum many-body problems generally limits numerical simulations to very small system sizes. A paradigmatic exception is the quantum Ising model, where analytical solutions are available even for the disordered case [11,12]. This model is diagonal in a product-state basis but, if prepared initially in a superposition of different eigenstates, features intrinsically quantum properties, namely dephasing between its eigenstate components leading to relaxation and the buildup of entanglement. Previous studies addressed the buildup of correlations [13], decoherence [14], the effect of long-range interactions [15–17], and the decay of the Ramsey contrast [18,19].

Here, we introduce a generalized approach to obtain stretched-exponential relaxation of the transversal magnetization and purity in the quantum Ising model extending earlier studies of special cases [15,19]. Analytical results are provided for arbitrary dimensionality and power-law interactions, applicable to multiple experimental settings, e.g., in NMR [20], quantum information [21,22], trapped ions [23], and Rydberg atoms [10,24]. The analytic solution for the magnetization and purity of the microscopic model allows one to differentiate dephasing between disordered coherent pairs from genuine many-body effects. Furthermore, finding glassy dynamics in the quantum Ising model with a scale-invariant distribution of interactions constitutes a generalization of the Klafter-Shlesinger conjecture [5] to the quantum realm.

*These authors contributed equally to this work.
†Corresponding author: marting@kip.uni-heidelberg.de

We consider N spin-1/2 particles, whose dynamics are governed by the Ising model ($\hbar = 1$)

$$\mathcal{H}_{\text{Ising}} = \sum_{i<k} J_{ik} \hat{\sigma}_z^i \otimes \hat{\sigma}_z^k, \tag{1}$$

where $\hat{\sigma}_\alpha^{i,k}$ ($\alpha = \{x, y, z\}$) are the Pauli operators acting on spin i and k and J_{ik} describes the interaction between them. We consider isotropic power-law interactions $J_{ik} = C_\alpha/|\mathbf{r}_i - \mathbf{r}_k|^\alpha$ with particle positions $\mathbf{r}_i$, realized by a variety of quantum simulation platforms, such as polar molecules ($\alpha = 3$) [25,26], Rydberg atoms ($\alpha = 3, 6$) [10,27–29], or trapped ions ($0 \leqslant \alpha < 3$) [23,30] (see Ref. [13] for a more complete list). For the initial state $|\psi_0\rangle = |{\rightarrow}\rangle^{\otimes N}$, we are interested in the relaxation of the ensemble-averaged transversal magnetization $\overline{\langle \hat{s}_x \rangle} = N^{-1} \sum_i \langle \hat{\sigma}_x^i \rangle/2$, where the overline denotes the ensemble average and $\langle \cdots \rangle$ the quantum mechanical expectation value. Here, $|{\rightarrow}\rangle$ is the $\hat{\sigma}_x$ eigenstate with $\hat{\sigma}_x |{\rightarrow}\rangle = |{\rightarrow}\rangle$.

The dynamics of Ising spins initialized in $|\psi_0\rangle$ was described analytically by Emch [11] and Radin [12] as

$$\overline{\langle \hat{s}_x(\tau) \rangle} = \frac{1}{2} \sum_i \frac{1}{N} \langle \hat{\sigma}_x^i(\tau) \rangle = \frac{1}{2} \sum_i \frac{1}{N} \prod_{k \neq i}^{N} \cos(2 J_{ik} \tau), \tag{2}$$

which shows that the ensemble average is determined by products of oscillations with frequencies given by the couplings J_{ik} between a given spin i and its neighbors k. From the Emch-Radin solutions also follows $\langle \hat{\sigma}_y^i \rangle = \langle \hat{\sigma}_z^i \rangle = 0$ such that the analytical expression $\langle \hat{\sigma}_x^i(\tau) \rangle = \prod_{k \neq i}^{N} \cos(2 J_{ik} \tau)$ already fully determines the one-particle reduced density matrix $\rho^i = [\mathbb{1} + \langle \hat{\sigma}_x^i \rangle \hat{\sigma}_x^i]/2$ of spin i. Thus, the single-particle purity is

$$\text{tr}[(\rho^i)^2] = \tfrac{1}{2} \left[1 + \langle \hat{\sigma}_x^i(\tau) \rangle^2 \right]. \tag{3}$$

Similar to the magnetization, we define the ensemble-averaged single-particle purity as $\overline{\text{tr}(\rho^2)} = \frac{1}{2}[1 + \overline{\langle \hat{\sigma}_x(\tau) \rangle^2}]$, where

$$\overline{\langle \hat{\sigma}_x(\tau) \rangle^2} = \sum_i \frac{1}{N} \langle \hat{\sigma}_x^i(\tau) \rangle^2 = \sum_i \frac{1}{N} \prod_{k \neq i}^{N} \cos^2(2 J_{ik} \tau). \tag{4}$$

The purity of a subsystem (here, a single spin) of a closed quantum system $1/2 \leqslant \text{tr}[(\rho^i)^2] \leqslant 1$ quantifies the entanglement between the subsystem and its complement, and determines the second-order Rényi entropy $S_2 = -\log\{\text{tr}[(\rho^i)^2]\}$. For our initial product state $S_2 = 0$, as the single-particle reduced state ρ^i is pure, and the subsystem entropy takes its maximal value $S_2 = \log(2)$ in the late-time limit.

The Emch-Radin solutions hold for arbitrary choices of the couplings J_{ik}. Here, we consider disorder in the couplings due to random spin positions drawn from a uniform distribution within a d-dimensional sphere and power-law interaction with exponent $\alpha \geqslant d$. To illustrate the characteristic dynamics emerging in this situation we show the relaxation of the transversal magnetization in Fig. 1(a) for a van der Waals interaction ($\alpha = 6$) in $d = 3$ dimensions. Time is scaled by the median nearest-neighbor (NN) interaction strength J_{NN} [10]. The random positions lead to a strongly disordered J_{ik} distribution which causes oscillations on a broad range of different timescales. Curves showing fast oscillations correspond to spins interacting strongly with their nearest neighbors. Due to disorder, these oscillations between coherent pairs lose their phase correlations. Consequently, the ensemble-averaged magnetization (red dashed line) shows smooth subexponential decay closely following the analytical solution in the thermodynamic limit $N \to \infty$ (black curve) derived below, which is a stretched-exponential function.

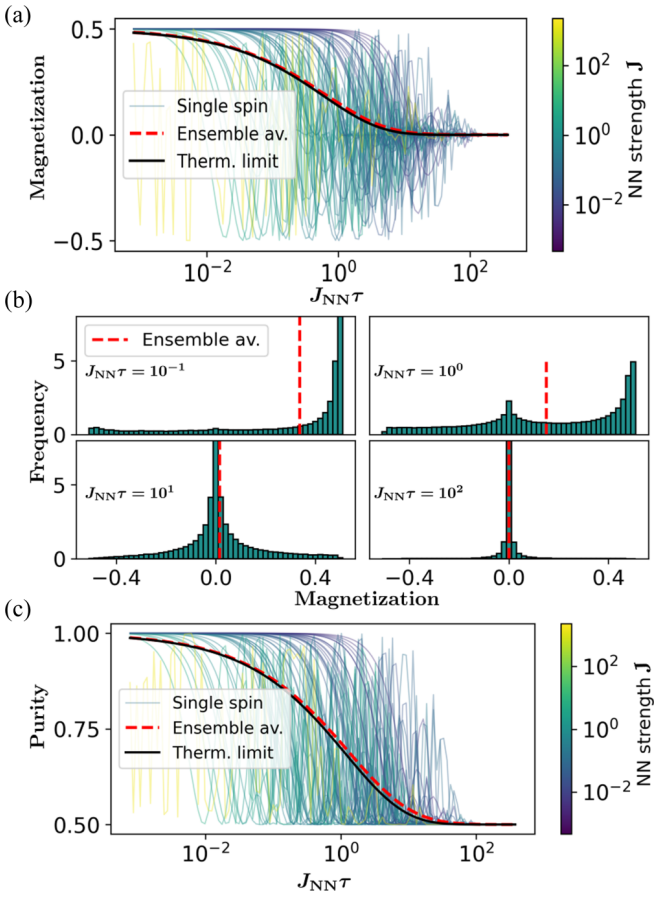

FIG. 1. (a) Magnetization decay for a uniform random spin distribution in $d = 3$ with $\alpha = 6$ for 1300 spins. The single-spin magnetizations $\langle \hat{s}_x^i(\tau) \rangle$ for 50 different spins are shown, featuring the oscillatory behavior predicted by Eq. (2). The line color encodes the nearest-neighbor (NN) interaction strength and is thus a measure for the onset and fastest frequency of each oscillation. Its median J_{NN} is furthermore used as the unit for the relaxation time. Additionally, the ensemble-averaged decay is plotted (red dashed line), showing monotonous subexponential relaxation, which is well captured by a stretched-exponential function predicted analytically in the large N limit (black line). Remaining deviations from the analytical solution can be attributed to the finite system size used for the simulation. (b) Histograms showing the frequency of occurrence of single-spin magnetization values at different times. The fluctuations relax on a slower timescale than the mean value, which is directly connected to the decay of the purity. (c) Single-spin purities and ensemble average, analogous to (a).

Figure 1(b) shows the frequency of occurrence of single-spin magnetizations at fixed evolution times, showing a bimodal distribution at intermediate times. For $J_{\text{NN}}\tau = 10$, the ensemble-averaged value nearly reached its equilibrium, while still showing large fluctuations around the mean value. These fluctuations are directly connected to the purity [cf.

Eq. (4)] showing already that the decay of magnetization and purity happen on different timescales. In this particular case, the timescales differ by a factor of 2, where in general this factor depends on α/d and can become large as discussed below. Figure 1(c) shows the ensemble-averaged purity along with the purity of individual spins. Similar to Fig. 1(a), the purity of individual spins shows oscillations. Following the same argument that explains the full relaxation of magnetization, the dephasing of these oscillations would result in an average purity of 0.75. Instead, the ensemble-averaged purity relaxes to its minimum value of 0.5, which accounts for an irreversible buildup of entanglement with the whole ensemble. We again find a smooth stretched-exponential curve in the ensemble average.

To derive an analytical expression for Eq. (2) in the limit of $N \to \infty$, the ensemble average can be replaced by an average over all possible configurations of placing the surrounding spins of a reference spin [18,19] thus leading to a scale-invariant distribution of interaction strengths. Without loss of generality, we fix the position of the reference spin at $\mathbf{r}_1 = \mathbf{0}$ and choose a finite spherical integration volume V in which N' atoms are placed. We will later take the limit $N' \to \infty$ keeping the density $n = N'/V$ constant. Therefore, Eq. (2) transforms into the integral form

$$\overline{\langle \hat{s}_x(\tau)\rangle} = \frac{1}{2}\int_V d\mathbf{r}_2 \cdots d\mathbf{r}_{N'} P(\mathbf{r}_2 \cdots \mathbf{r}_{N'}) \prod_{k=2}^{N'} \cos(2J_{1k}\tau). \quad (5)$$

The spin positions are chosen independently following a homogeneous distribution over the volume V, i.e., $P(\mathbf{r}_2 \cdots \mathbf{r}_{N'}) = \prod_k p(\mathbf{r}_k)$ with $p(\mathbf{r}_k) = 1/V$. Thus, the integral in Eq. (5) factorizes into a product of identical integrals

$$\overline{\langle \hat{s}_x(\tau)\rangle} = \frac{1}{2}\left[\frac{1}{V}\int_V d\mathbf{r} \cos(2J_{\mathbf{r}}\tau)\right]^{N'-1}, \quad (6)$$

where $J_{\mathbf{r}} = C_\alpha/|\mathbf{r}|^\alpha$.

We now introduce a lower distance cutoff r_b on the integration volume [31]. Note that imposing an exclusion distance r_b between any pair of atoms violates the assumption of independent atom positions and scale-invariant distributions of interactions. For our analytical calculations this inconsistency is irrelevant as we will send r_b to zero eventually. We show below that our results also describe the dynamics well for a finite exclusion radius as long as r_b is much smaller than the average nearest-neighbor distance in the ensemble.

Defining r_0 as the radius of the spherical integration volume V and carrying out the angular part of the integration we obtain

$$\overline{\langle \hat{s}_x(\tau)\rangle} = \frac{1}{2}\left[\frac{d}{r_0^d - r_b^d}\int_{r_b}^{r_0} dr\, r^{d-1} \cos\left(2\frac{C_\alpha}{r^\alpha}\tau\right)\right]^{N'-1}. \quad (7)$$

We now evaluate this expression in the limits $r_b \to 0$ and $r_0, N' \to \infty$ for arbitrary d and $\alpha \geqslant d$, thus generalizing previous results. The scale invariance of the system now becomes obvious as Eq. (7) is invariant under a rescaling of space ($r \to \lambda r$) and time ($\tau \to \lambda^\alpha \tau$). The main result of our derivation

$$\overline{\langle \hat{s}_x(\tau)\rangle} = \frac{1}{2}\exp\left[-\kappa_{d,\alpha}\Gamma\left(\frac{\alpha-d}{\alpha}\right)\sin\left(\pi\frac{\alpha-d}{2\alpha}\right)\tau^{d/\alpha}\right] \quad (8)$$

is a stretched exponential $\overline{\langle \hat{s}_x(\tau)\rangle} = \exp[-(\gamma_m\tau)^{\beta_m}]/2$ with decay rate $\gamma_m = [\kappa_{d,\alpha}\Gamma(\frac{\alpha-d}{\alpha})\sin(\pi\frac{\alpha-d}{2\alpha})]^{\alpha/d}$ and stretch power $\beta_m = \frac{d}{\alpha}$ [for details, see Supplemental Material (SM) [32] containing Ref. [33]]. Here, the index m stands for magnetization and we have introduced $\kappa_{d,\alpha} = \pi^{d/2}n(2C_\alpha)^{d/\alpha}/\Gamma(d/2+1)$. Since $\beta_m \leqslant 1$ our result shows that the characteristic subexponential relaxation typically observed in glassy systems appears in the out-of-equilibrium unitary dynamics under the Ising Hamiltonian. In the case $\alpha = d$ Eq. (8) simplifies to a pure exponential decay $\overline{\langle \hat{s}_x(\tau)\rangle}_{\alpha=d} = \exp(-\pi\kappa_{d,\alpha}\tau/2)/2$ where we used that $\lim_{\alpha-d\to 0}[\Gamma(\frac{\alpha-d}{\alpha})\sin(\pi\frac{\alpha-d}{2\alpha})] = \pi/2$. Note, that the derivation of a stretched exponential remains valid even for a broad class of anisotropic interactions, whose anisotropy yields a change only in the rate γ, whereas β remains unchanged (see SM [32]).

Remarkably, the stretch power $\beta = d/\alpha$ is the same as for the *Förster direct-transfer model* with parallel channels discussed by Klafter and Shlesinger [5]. This classical model features the same spatial distribution and power-law interaction but relies on exponential relaxation, instead of coherently interacting spins showing microscopic oscillatory behavior.

Beyond classical models, genuine quantum effects occur in the quantum Ising model. Therefore, we focus on the ensemble-averaged purity which describes the buildup of entanglement [cf. Eq. (4)]. As for the magnetization, one can convert the ensemble average of the term $\overline{\langle \hat{\sigma}_x(\tau)\rangle^2}$ into an integral over atom positions in the asymptotic large N limit, resulting in

$$\begin{aligned}\overline{\langle \hat{\sigma}_x(\tau)\rangle^2} &= \left[\frac{d}{r_0^d - r_b^d}\int_{r_b}^{r_0} dr\, r^{d-1}\cos^2\left(2\frac{C_\alpha}{r^\alpha}\tau\right)\right]^{N'-1} \\ &= \left[\frac{1}{2} + \frac{d}{r_0^d - r_b^d}\int_{r_b}^{r_0} dr\frac{r^{d-1}}{2}\cos\left(4\frac{C_\alpha}{r^\alpha}\tau\right)\right]^{N'-1},\end{aligned} \quad (9)$$

where the identity $\cos^2(x) = 1/2 + \cos(2x)/2$ is used. The integral now has the same shape as the one for the magnetization (7) with a global prefactor of $1/2$ and twice the frequency $C_\alpha \to 2C_\alpha$. We can thus use the same approach to obtain

$$\overline{\mathrm{tr}(\rho^2)} = \tfrac{1}{2}\{1 + \exp[-(\gamma_p\tau)^{\beta_p}]\} \quad (10)$$

for the relaxation of the ensemble-averaged single-particle purity with $\gamma_p = 2^{1-\alpha/d}\gamma_m$ and $\beta_p = \beta_m = d/\alpha$. This formalism can be extended to all higher moments $\overline{\langle \hat{\sigma}_x(\tau)\rangle^j}$ with $j \in \mathbb{N}$ shown in SM [32]. Note that the decay rate of the purity is generally smaller than that of the magnetization by a factor $\gamma_p/\gamma_m = 2^{1-\alpha/d} \leqslant 1$. The slower decay of purity is visible in the fluctuations of the single-spin magnetizations [cf. Fig. 1(b)] that are still present when the mean magnetization has already decayed. This separation of timescales gets large in the case of $\alpha \gg d$.

We numerically investigate whether glassy dynamics persist for systems with finite exclusion radius r_b and finite system size N. We evaluate Eqs. (2) and (4) for $d = 1, 2, 3$, $\alpha = d, \ldots, 10$, and random atom positions. We average the results over N_s random realizations to decrease statistical fluctuations from random sampling and fit the averaged relaxation curves with a general stretched-exponential function described by $f(\tau) = A \exp[-(\gamma\tau)^\beta]$ and we compare the resulting β to the analytical solution d/α derived previously of the thermodynamic limit.

The exclusion radius r_b is incorporated in the process of generating random position samples by rejecting atoms that are closer than r_b to one of their neighbors. This process is equivalent to the random sequential absorption (RSA) model of randomly placing nonoverlapping spheres [34,35]. The packing density can be quantified by the ratio $x = N r_b^d / r_0^d$, where a small value of x corresponds to strong disorder, i.e., uncorrelated atom positions, while large x implies more densely packed and thus more regularly spaced, less disordered spins. We note that in experiments with Rydberg atoms x is tunable over a wide range [10].

The dependence of β on x is shown in Fig. 2(a) for both magnetization and purity in the case of a van der Waals interaction $\alpha = 6$ and $d = 3$ for a system size of $N = 100$ and $N_s = 200$ samples. In the sufficiently disordered regime ($x \lesssim 0.01$) β reaches a constant value (dashed lines), which shows that the description by glassy dynamics obtained in the limit $r_b \to 0$ are robust with respect to finite exclusion radius. In this regime the blockade radius is sufficiently small, such that the system can be considered as effectively scale invariant. Similar results are obtained in all studied cases of dimension and interaction range.

Next we study the effect of finite N in the strongly disordered regime ($x \ll 1$). Figure 2(b) shows the deviation of the fitted β from the analytical result d/α as a function of N. Analogous plots for $\alpha = 6$ in $d = 1$ and $d = 2$ dimensions are shown in the SM [32]. We observe an algebraic decrease of the error for both magnetization and purity. A power-law fit $\propto N^{-p}$ shows good agreement. The point at $N = 1300$ corresponds to the data shown in Figs. 1(a) and 1(c), where the comparison to the analytical solution matches nearly perfectly.

We systematically extract the exponent p describing the scaling of the error with N for various d and α (see SM [32] for the choice of parameters N and N_s). The range of particle numbers is chosen such that the deviation from the analytical solution does not fall below $\sim$1%. This value corresponds to the size of statistical fluctuations due to finite disorder averaging giving a lower bound on the observable deviation. In particular the 1D case converges already for small N, therefore we need to increase the samples N_s to reduce statistical fluctuations. The results, shown in Fig. 2(c), indicate that the finite-size scaling behavior is independent of α, but convergence is slower for increasing d. In all cases, an algebraic convergence to the analytical result is obtained, showing the robustness of our analytical results with respect to finite-size effects.

Our analytical and numerical studies show that the far-from-equilibrium dynamics of the quantum Ising model exhibits glassy behavior. In addition to the global magnetization, we investigated the single-spin purity, which quantifies

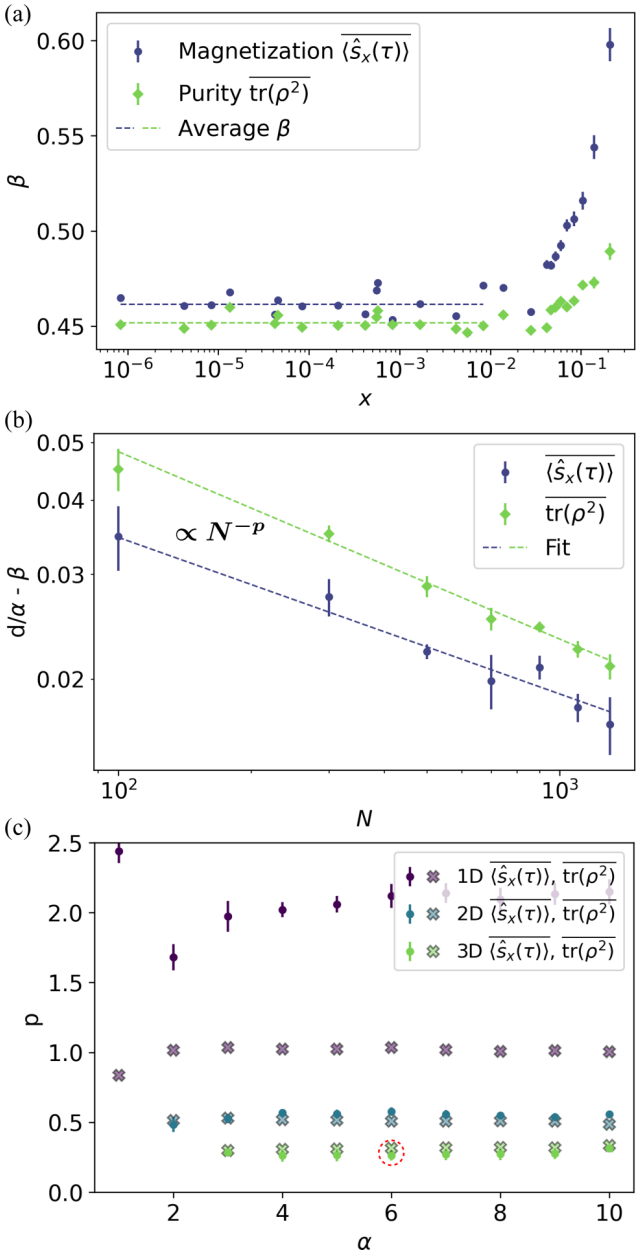

FIG. 2. (a) Fit parameter β as a function of the disorder parameter $x = N r_b^d / r_0^d$ for the magnetization (blue dots) and purity (green dots) for $N = 100$ and $N_s = 200$ for the case of $\alpha = 6$ in $d = 3$. At strong disorder ($x \lesssim 0.01$) β becomes independent of x. Dashed lines show the averages within this regime. Error bars describe the parameter uncertainty of β obtained from the fit. (b) Deviation of the fitted β from the analytical solution $d/\alpha = 0.5$ as a function of N. We average β over five different blockade radii within the strongly disordered regime. The error bars correspond to the standard error of the mean of the latter, which is the dominant uncertainty [cf. (a)]. Dashed lines are power-law fits. (c) Fitted power-law exponent p for all simulated cases $d = 1, 2, 3$ and $\alpha = d, \ldots, 10$. The red circle highlights the points corresponding to the data shown in (b). See Supplemental Material for the choice of parameters N and N_s.

entanglement between local spins and their environment. Especially for a short interaction range $\alpha \gg d$, the timescales between magnetization and purity differ largely. This discrepancy is due to differences in the involved relaxation

mechanisms. For qualitatively explaining the decay of the global magnetization it is sufficient to consider the interaction of spins with their nearest neighbors. Due to disorder, these coherent pair dynamics oscillate at different frequencies resulting in dephasing and hence a loss of global magnetization. In contrast, the full relaxation of single-spin purity is a genuine many-body effect, which is eventually due to the irreversible dephasing between many-body eigenstates.

Similar to known classical models showing glassy dynamics, the quantum Ising model features a scale-invariant distribution of timescales. Therefore, our findings extend the conclusion of Ref. [5], that scale invariance is sufficient to explain the emergence of a stretched-exponential law, to the quantum realm. This argument is not limited to observables such as the magnetization with a classical analog, but also applies to the single spin purity, a genuine quantum property, which shows the same stretched-exponential relaxation. An interesting direction for future research is the investigation of the dynamics of entanglement entropy beyond single-spin subsystems. This includes entanglement scaling with subsystem size [36,37] in view of constraints on the spreading of correlations [38–41].

In conclusion, stretched-exponential relaxation is found in classical models as well as in open quantum systems and, as we have shown, also in the quantum Ising model prototypical for isolated integrable quantum systems. Despite the vastly different underlying physics, all of these systems feature scale-invariant distributions of timescales. Thus, the analytical results presented here are in line with the conclusion of Ref. [5], extending the sufficiency of scale invariance for the emergence of glassy dynamics to quantum systems. Based on recent numerical investigations of a more general family of Heisenberg Hamiltonians, where glassy dynamics is observed for almost any anisotropy parameter [42], as well as experimental findings [10], we expect the conjecture to hold even for nonintegrable quantum systems if scale invariance is given.

We thank Adrian Braemer and Peter Kaposvari for helpful discussions. This work is supported by the Deutsche Forschungsgemeinschaft (DFG, German Research Foundation) under Germany's Excellence Strategy EXC2181/1-390900948 (the Heidelberg STRUCTURES Excellence Cluster), within the Collaborative Research Center SFB1225 (ISOQUANT) and the DFG Priority Program 1929 "GiRyd" (DFG WE2661/12-1). We acknowledge support by the European Commission FET flagship project PASQuanS (Grant No. 817482) and by the Heidelberg Center for Quantum Dynamics. C.H. acknowledges funding from the Alexander von Humboldt foundation and T.F. from a graduate scholarship of the Heidelberg University (LGFG).

[1] K. Binder and A. P. Young, Rev. Mod. Phys. **58**, 801 (1986).
[2] J. C. Phillips, Rep. Prog. Phys. **59**, 1133 (1996).
[3] R. Kohlrausch, Ann. Phys. **167**, 56 (1854).
[4] C. De Dominicis, H. Orland, F. Lainée, and H. Orland, J. Phys. Lett. **46**, 463 (1985).
[5] J. Klafter and M. F. Shlesinger, Proc. Natl. Acad. Sci. USA **83**, 848 (1986).
[6] J. Choi, S. Choi, G. Kucsko, P. C. Maurer, B. J. Shields, H. Sumiya, S. Onoda, J. Isoya, E. Demler, F. Jelezko, N. Y. Yao, and M. D. Lukin, Phys. Rev. Lett. **118**, 093601 (2017).
[7] G. Kucsko, S. Choi, J. Choi, P. C. Maurer, H. Zhou, R. Landig, H. Sumiya, S. Onoda, J. Isoya, F. Jelezko, E. Demler, N. Y. Yao, and M. D. Lukin, Phys. Rev. Lett. **121**, 023601 (2018).
[8] E. J. Davis, B. Ye, F. Machado, S. A. Meynell, T. Mittiga, W. Schenken, M. Joos, B. Kobrin, Y. Lyu, D. Bluvstein, S. Choi, C. Zu, A. C. B. Jayich, and N. Y. Yao, arXiv:2103.12742.
[9] B. Everest, I. Lesanovsky, J. P. Garrahan, and E. Levi, Phys. Rev. B **95**, 024310 (2017).
[10] A. Signoles, T. Franz, R. Ferracini Alves, M. Gärttner, S. Whitlock, G. Zürn, and M. Weidemüller, Phys. Rev. X **11**, 011011 (2021).
[11] G. G. Emch, J. Math. Phys. **7**, 1198 (1966).
[12] C. Radin, J. Math. Phys. **11**, 2945 (1970).
[13] K. R. A. Hazzard, M. van den Worm, M. Foss-Feig, S. R. Manmana, E. G. Dalla Torre, T. Pfau, M. Kastner, and A. M. Rey, Phys. Rev. A **90**, 063622 (2014).
[14] M. Foss-Feig, K. R. A. Hazzard, J. J. Bollinger, and A. M. Rey, Phys. Rev. A **87**, 042101 (2013).
[15] E. B. Fel'dman and S. Lacelle, J. Chem. Phys. **104**, 2000 (1996).
[16] M. Kastner, Phys. Rev. Lett. **106**, 130601 (2011).
[17] M. van den Worm, B. C. Sawyer, J. J. Bollinger, and M. Kastner, New J. Phys. **15**, 083007 (2013).
[18] R. Mukherjee, T. C. Killian, and K. R. A. Hazzard, Phys. Rev. A **94**, 053422 (2016).
[19] C. Sommer, G. Pupillo, N. Takei, S. Takeda, A. Tanaka, K. Ohmori, and C. Genes, Phys. Rev. A **94**, 053607 (2016).
[20] W. Wu, B. Ellman, T. F. Rosenbaum, G. Aeppli, and D. H. Reich, Phys. Rev. Lett. **67**, 2076 (1991).
[21] R. Harris, Y. Sato, A. J. Berkley, M. Reis, F. Altomare, M. H. Amin, K. Boothby, P. Bunyk, C. Deng, C. Enderud, S. Huang, E. Hoskinson, M. W. Johnson, E. Ladizinsky, N. Ladizinsky, T. Lanting, R. Li, T. Medina, R. Molavi, R. Neufeld *et al.*, Science **361**, 162 (2018).
[22] R. Raussendorf and H. J. Briegel, Phys. Rev. Lett. **86**, 5188 (2001).
[23] J. W. Britton, B. C. Sawyer, A. C. Keith, C. C. Wang, J. K. Freericks, H. Uys, M. J. Biercuk, and J. J. Bollinger, Nature (London) **484**, 489 (2012).
[24] H. Labuhn, D. Barredo, S. Ravets, S. D. Léséleuc, T. Macrì, T. Lahaye, and A. Browaeys, Nature (London) **534**, 667 (2016).
[25] B. Yan, S. A. Moses, B. Gadway, J. P. Covey, K. R. A. Hazzard, A. M. Rey, D. S. Jin, and J. Ye, Nature (London) **501**, 521 (2013).
[26] K. R. Hazzard, B. Gadway, M. Foss-Feig, B. Yan, S. A. Moses, J. P. Covey, N. Y. Yao, M. D. Lukin, J. Ye, D. S. Jin, and A. M. Rey, Phys. Rev. Lett. **113**, 195302 (2014).
[27] A. P. Orioli, A. Signoles, H. Wildhagen, G. Günter, J. Berges, S. Whitlock, and M. Weidemüller, Phys. Rev. Lett. **120**, 063601 (2018).
[28] P. Scholl, M. Schuler, H. J. Williams, A. A. Eberharter, D. Barredo, K.-N. Schymik, V. Lienhard, L.-P. Henry, T. C. Lang,

T. Lahaye, A. M. Läuchli, and A. Browaeys, Nature (London) **595**, 233 (2021).
[29] S. Ebadi, T. T. Wang, H. Levine, A. Keesling, G. Semeghini, A. Omran, D. Bluvstein, R. Samajdar, H. Pichler, W. W. Ho, S. Choi, S. Sachdev, M. Greiner, V. Vuletic, and M. D. Lukin, Nature (London) **595**, 227 (2021).
[30] C. Monroe, W. C. Campbell, L. M. Duan, Z. X. Gong, A. V. Gorshkov, P. Hess, R. Islam, K. Kim, N. Linke, G. Pagano, P. Richerme, C. Senko, and N. Y. Yao, Rev. Mod. Phys. **93**, 025001 (2021).
[31] This is motivated physically: Arbitrarily closely spaced spins would have an arbitrarily large interaction strength requiring a high-energy cutoff. Also, in experimental realizations with Rydberg atoms, a natural lower distance cutoff is given by the dipole blockade radius [43].
[32] See Supplemental Material at http://link.aps.org/supplemental/10.1103/PhysRevB.105.L020201 for details on analytical calculations, numerical parameters, and further plots.
[33] R. J. Mathar, arXiv:1211.3963.
[34] Z. Adamczyk and P. Weroński, J. Chem. Phys. **105**, 5562 (1996).
[35] E. L. Hinrichsen, J. Feder, and T. Jøssang, Phys. Rev. A **41**, 4199 (1990).
[36] D. A. Abanin, E. Altman, I. Bloch, and M. Serbyn, Rev. Mod. Phys. **91**, 021001 (2019).
[37] M. P. Hertzberg and F. Wilczek, Phys. Rev. Lett. **106**, 050404 (2011).
[38] E. H. Lieb and D. W. Robinson, Commun. Math. Phys. **28**, 251 (1972).
[39] Z.-X. Gong, M. Foss-Feig, S. Michalakis, and A. V. Gorshkov, Phys. Rev. Lett. **113**, 030602 (2014).
[40] M. Foss-Feig, Z.-X. Gong, C. W. Clark, and A. V. Gorshkov, Phys. Rev. Lett. **114**, 157201 (2015).
[41] M. B. Hastings and T. Koma, Commun. Math. Phys. **265**, 781 (2006).
[42] P. Schultzen, T. Franz, C. Hainaut, S. Geier, A. Salzinger, A. Tebben, G. Zürn, M. Gärttner, and M. Weidemüller, arXiv:2107.13314.
[43] D. Comparat and P. Pillet, J. Opt. Soc. Am. B **27**, A208 (2010).

Correction: The surname of the eighth author appeared incorrectly due to a conversion error and has been fixed.

Letter

Semiclassical simulations predict glassy dynamics for disordered Heisenberg models

P. Schultzen,[1,*] T. Franz,[1,*] C. Hainaut,[1,*] S. Geier,[1] A. Salzinger,[1] A. Tebben,[1] G. Zürn,[1] M. Gärttner,[1,2,3] and M. Weidemüller[1,†]

[1]*Physikalisches Institut, Universität Heidelberg, Im Neuenheimer Feld 226, 69120 Heidelberg, Germany*
[2]*Kirchhoff-Institut für Physik, Universität Heidelberg, Im Neuenheimer Feld 227, 69120 Heidelberg, Germany*
[3]*Institut für Theoretische Physik, Ruprecht-Karls-Universität Heidelberg, Philosophenweg 16, 69120 Heidelberg, Germany*

(Received 30 July 2021; revised 13 December 2021; accepted 14 February 2022; published 23 March 2022)

We numerically study out-of-equilibrium dynamics in a family of Heisenberg models with $1/r^6$ power-law interactions and positional disorder. Using the semiclassical discrete truncated Wigner approximation (dTWA) method, we investigate the time evolution of the magnetization and ensemble-averaged single-spin purity for a strongly disordered system after initializing the system in an out-of-equilibrium state. We find that both quantities display robust glassy behavior for almost any value of the anisotropy parameter of the Heisenberg Hamiltonian. Furthermore, a systematic analysis allows us to quantitatively show that, for all the scenarios considered, the stretch power lies close to the one analytically obtained in the Ising limit. This indicates that glassy relaxation behavior occurs widely in disordered quantum spin systems, independent of the particular symmetries and integrability of the Hamiltonian.

DOI: 10.1103/PhysRevB.105.L100201

I. INTRODUCTION

Recent experimental progress and the development of more advanced numerical tools allow the exploration of far-from-equilibrium physics of many-body systems, e.g., transport [1,2], localization [3,4], and dynamical phase transitions [5]. In disordered quantum systems, peculiarly rich relaxation dynamics has been found where the interplay of interactions and randomness results in new and intrinsically nonequilibrium effects such as prethermalization [6,7], quantum scars [8], and aging [9].

Strikingly, a large variety of disordered materials [10–13] feature slow subexponential relaxation behaviors. Phenomenologically, these can be described by a stretched exponential law $\exp[-(t/\tau)^\beta]$ with relaxation time τ and stretch power β [14]. Despite the huge success of this law in capturing the relaxation dynamics of disordered systems, derivations of this function from microscopic models are rare [11]. By exploring relaxation behaviors of three different classical disordered models, Klafter and Shlesinger [15] concluded that the scale-invariant property of the relaxation timescales is the underlying feature resulting in the appearance of stretched exponential law. Similarly, this behavior has also been observed in a disordered open quantum system where the decay rates, coupling the system to an environment, display scale invariance [16,17].

In contrast to dissipative systems, closed quantum systems are subjected to unitary dynamics where relaxation can solely be explained by interactions. In recent work, we have analytically derived the occurrence of stretched exponential law for the disordered quantum Ising model in the thermodynamic limit, where the interactions between different spins feature a scale-invariant distribution [18]. Intuitively, spins that interact strongly with their surrounding spins relax faster compared to spins that are spatially more isolated. This leads to a hierarchy of scales resulting in a subexponential relaxation. These observations indicate also in disordered *quantum* systems that scale invariance implies glassy dynamics. Scrutinizing this hypothesis requires studying more general classes of disordered quantum spin systems. A suitable candidate for this is the XXZ Heisenberg model for which we recently observed glassy dynamics in an experiment with Rydberg atoms [19]. Nevertheless, in contrast to the integrable quantum Ising model the XXZ Heisenberg model is in general nonintegrable, which prevents direct analytical derivations beyond the disorder-free one-dimensional case [20]. Furthermore, due to the exponentially increasing size of the Hilbert space, exact numerical studies are limited to small system sizes. Among different approximate numerical methods, the semiclassical method of the discrete truncated Wigner approximation (dTWA) [21] already succeeded in capturing the glassy behavior observed in a Rydberg spin experiment [19]. In addition, this method becomes exact for describing the evolution of the magnetization in the Ising limit [21]. These arguments imply that this method is a natural candidate to address the glassy dynamics of disordered systems composed of a large number of particles.

Within this work, we use the dTWA method (see Appendix A for details on the numerical method and benchmark calculations) to investigate the occurrence of glassy dynamics for the relaxation of magnetization and ensemble-averaged single-spin purity in the general XYZ Heisenberg model. This Letter is organized as follows: In Sec. II we introduce the system and the relevant observable, and in Sec. III we

*These authors contributed equally to this work.
†Corresponding author: weidemueller@uni-heidelberg.de

focus on the dynamics of the particular scenario of the XXZ Heisenberg model. In Sec. IV this investigation is extended to the XYZ Hamiltonian.

II. XYZ HEISENBERG MODEL

We investigate the dynamics of N spin-1/2 particles described by the general XYZ Hamiltonian

$$H = \frac{1}{2}\sum_{i,j}\frac{J_{ij}}{|J|}\left(J_x\hat{\sigma}_x^i\hat{\sigma}_x^j + J_y\hat{\sigma}_y^i\hat{\sigma}_y^j + \Delta\hat{\sigma}_z^i\hat{\sigma}_z^j\right), \tag{1}$$

where for each spin i the Pauli matrices $\hat{\sigma}_\alpha^i$ with $\alpha \in \{x, y, z\}$ are introduced. The spins interact via van der Waals interactions $J_{ij} = 1/r_{ij}^6$ with r_{ij} being the distance between spins i and j. The prefactors J_x, J_y, and Δ describe the contributions of the different interaction terms and are normalized by $|J| = (J_x^2 + J_y^2 + \Delta^2)^{1/2}$. In the case of $J_x = J_y = \Delta = 1$, the system is SU(2) symmetric which implies a conservation of all the three components of the transverse magnetization, $\overline{\langle\hat{\sigma}_x\rangle}$, $\overline{\langle\hat{\sigma}_y\rangle}$, and $\overline{\langle\hat{\sigma}_z\rangle}$, where $\overline{\langle\hat{\sigma}_\alpha\rangle}$ are defined as

$$\overline{\langle\hat{\sigma}_\alpha\rangle} = \frac{1}{N}\sum_{i=1}^{N}\langle\hat{\sigma}_\alpha^i\rangle. \tag{2}$$

As this peculiar isotropic case displays no relaxation dynamics, we will exclude it from numerical investigations in the following. In the case of $J_x = J_y = 1$ the model of Eq. (1) reduces to the anisotropic XXZ Heisenberg model featuring U(1) symmetry. Finally, we note that in the limits $\Delta \to \pm\infty$ the (anti)ferromagnetic quantum Ising model is recovered.

In this Letter, we numerically study the dynamics of an ensemble of spins homogeneously distributed in three dimensions. We focus on the dynamics of the transverse magnetization $\overline{\langle\hat{\sigma}_x\rangle}$ and the ensemble-averaged single-spin purity

$$\overline{\mathrm{tr}(\rho)^2} = \tfrac{1}{2}(1 + \overline{\langle\hat{\sigma}_x\rangle}^2 + \overline{\langle\hat{\sigma}_y\rangle}^2 + \overline{\langle\hat{\sigma}_z\rangle}^2) \tag{3}$$

after having initialized the system in the state $|\Psi_0\rangle = |{\rightarrow}\rangle^N$, where $|{\rightarrow}\rangle$ is the $\hat{\sigma}_x$ eigenstate with a positive eigenvalue. The purity quantifies the entanglement between each single spin and its environment. The purity of a single spin can take values of $1/2 \leqslant \overline{\mathrm{tr}(\rho)^2} \leqslant 1$ and is directly connected to the second-order Rényi entropy $S_2 = -\log(\mathrm{tr}[\rho^2])$.

III. STRETCHED EXPONENTIAL RELAXATION IN THE HEISENBERG XXZ MODEL

Considering the particular case of the XXZ Hamiltonian we perform numerical simulations using the dTWA method to obtain the dynamics of the transverse magnetization. Exemplarily, the observed decay of the magnetization for $\Delta = -0.7$ is shown in Fig. 1(a) (blue curve). Additionally, a stretched exponential law was fitted yielding nearly perfect agreement (red dashed line). Note that we have rescaled time with the fitted decay time τ. Figure 1(b) shows the residual of the applied fit to the data which lies in the percentage regime. We explore different regimes of anisotropy in Fig. 1(c) showing the dynamical behavior of $\log\overline{\langle\hat{\sigma}_x\rangle}$ for $\Delta = \{-2.0, -0.7, 0.0, 0.7, 2.0\}$ [for relaxation dynamics including the fit similar to Fig. 1(a), see Appendix C]. In this double

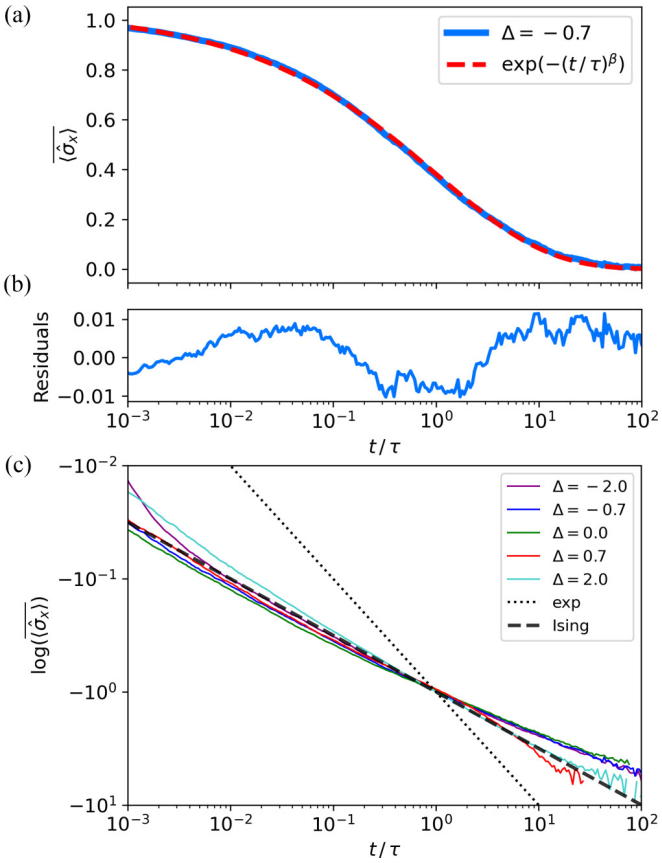

FIG. 1. (a) Relaxation dynamics of the transverse magnetization $\overline{\langle\hat{\sigma}_x\rangle}$ for an XXZ Heisenberg model with $\Delta = -0.7$ as a function of rescaled time t/τ. The dashed (red) curve shows a fit by a stretched exponential function. (b) Residuals of the stretched exponential fit applied to the relaxation dynamics shown in (a). (c) The logarithm of the transverse magnetization $\log\overline{\langle\hat{\sigma}_x\rangle}$ as a function of rescaled time t/τ for different Δ. Note that both axes are in logarithmic scale. A pure exponential decay and the limit of the Ising model are added as the dotted and dashed curve, respectively.

logarithmic plot a stretched exponential law corresponds to a line with slope $-\beta$. The comparison to an exponential decay ($\beta = 1$, black dotted line) shows that the decay is clearly subexponential in all cases. The linear behavior over five decades indicates the suitability of a stretched exponential law to describe the relaxation dynamics. Strikingly, all five observed cases agree well with each other, resulting in similar slopes. These slopes are consistent with the exact solution of the Ising limit $|\Delta| \to \infty$ (black dashed line) which yields analytically a stretched exponential with $\beta = 0.5$ in the thermodynamic limit [18].

Next, we investigate the stretched exponential relaxation of the system systematically over a broad range of values of the anisotropy parameter Δ. For this we extract the two characteristic parameters β and τ from the fit to the relaxation dynamics of magnetization and purity for each value of the anisotropy parameter. The stretch power is largely independent of disorder strength in the regime of strong disorder and convergence with respect to system size is investigated as we show in detail in Appendix B.

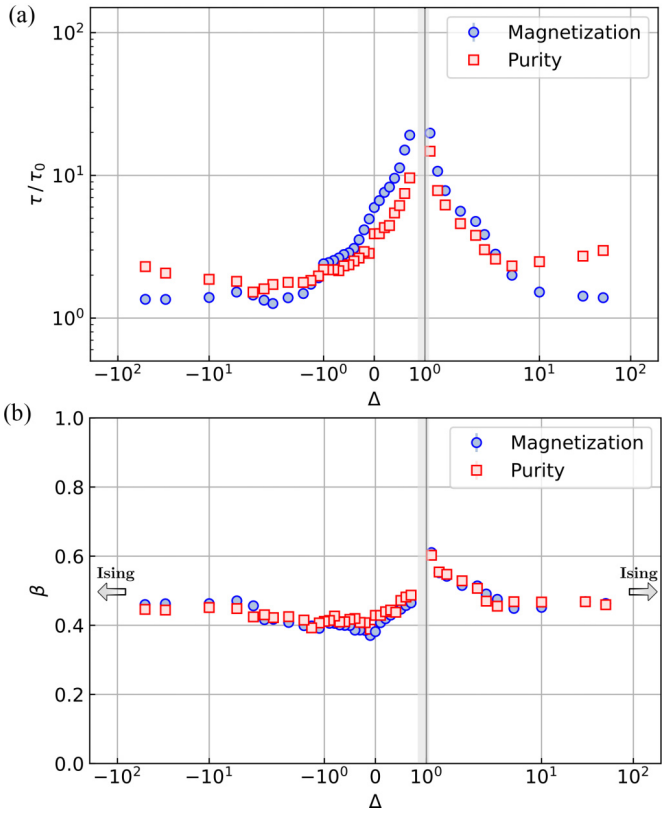

FIG. 2. Fit parameters (a) τ/τ_0 and (b) β for magnetization (circles) and ensemble-averaged single-spin purity (squares) as a function of anisotropy Δ for an XXZ Hamiltonian. Within the gray shaded area, the relaxation dynamics is not properly described by stretched exponential law.

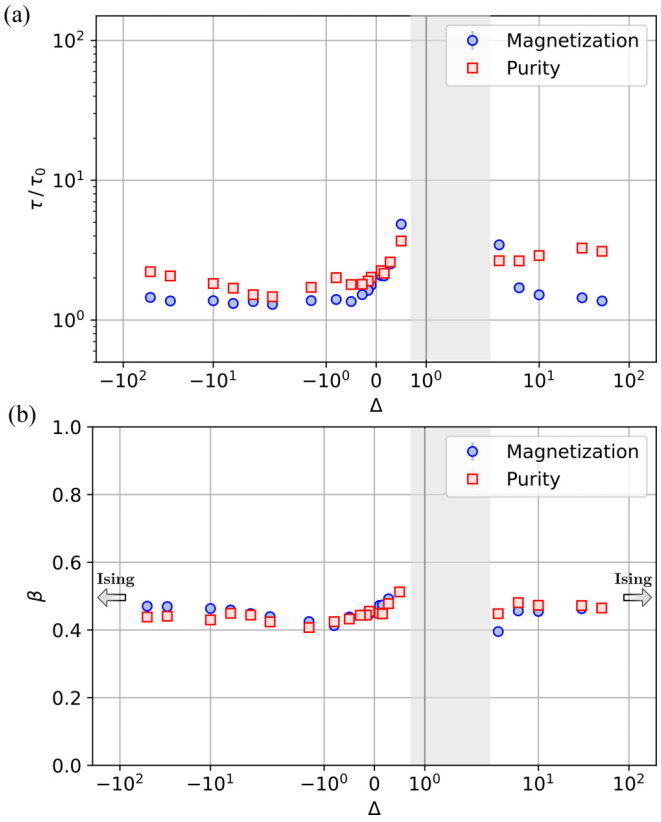

FIG. 3. Fit parameters (a) τ/τ_0 and (b) β for magnetization (circles) and ensemble-averaged single-spin purity (squares) as a function of Δ for a general XYZ Hamiltonian with $J_x = 0.5$, $J_y = 1$. Within the gray shaded area, the relaxation dynamics is not properly described by stretched exponential law.

The relaxation time τ of the magnetization (blue dots) and purity (red dots) is shown in Fig. 2(a) as a function of Δ. The y axis is rescaled by the timescale τ_0 corresponding to the magnetization's decay in the thermodynamic limit of the Ising model [18] which is obtained for $|\Delta| \to \infty$ in Eq. (1). For this model, it can be shown analytically that dTWA gives the exact solution [21].

The figure shows that this limit is well recovered for $|\Delta| \gg 1$ as the extracted τ lies close to τ_0. Similar behavior is observed for the purity, where the value of $2\tau_0$ is expected in the Ising limit. Remaining discrepancies are attributed to the finite system size. By approaching $\Delta = 1$, the observed dynamics for both quantities is remarkably slowed down compared to the Ising case. This behavior is expected since no dynamics occur in the fully isotropic Heisenberg model. We point out the fact that within the region closer to $\Delta = 1$, represented by the gray shaded area, relaxation dynamics become prohibitively slow. As a result, magnetization and purity have not fully relaxed at numerically accessible times t, and the dynamics is not captured well by stretched exponential law. This region is therefore excluded from further discussion.

In Fig. 2(b) the corresponding stretch powers for both purity and magnetization are shown. Remarkably, although timescales vary strongly as a function of Δ, the resulting stretch powers are within a narrow range (from $\beta = 0.4$ to $\beta = 0.6$) around the Ising value of $\beta = 0.5$. This indicates that the glassy property of the relaxation, characterized by the stretch power β, is not strongly dependent on the underlying anisotropy and is similar for systems possessing different conservation laws.

IV. GENERALIZATION TO XYZ HEISENBERG MODELS

We further explore the generality of the stretched exponential law by investigating a more general class of spin models, where the U(1) symmetry corresponding to conservation of the z magnetization is broken. Specifically, we relax the constraint of $J_x = J_y$, thus realizing an XYZ model. As a particular example, we set $J_x = 0.5$ and $J_y = 1$ and vary Δ. Another example, realizing a YZ Heisenberg model, where $J_x = 0$, is presented in Appendix D.

The characteristic parameters of the fit are displayed in Fig. 3 in analogy to Fig. 2. The resulting behaviors of β and τ are similar to the results of Fig. 2. One main difference is that the region around $\Delta = 1$ where the relaxation time becomes long and we cannot extract reliable quantities is broader than in the XXZ case. Exemplarily, we provide the relaxation dynamics in this specific region in Appendix C. Nevertheless, the obtained stretch powers are still close to $\beta = 0.5$, confirming that breaking the symmetry does not alter drastically the glassy relaxation behavior of the system.

V. CONCLUSIONS

Motivated by the experimental findings of glassy dynamics in the XXZ Heisenberg model for $\Delta \approx -0.7$ and the analytical observation of stretched exponential law in the quantum Ising model, we have systematically investigated in this Letter the magnetization and ensemble-averaged purity dynamics of XYZ Heisenberg models. In all investigated cases, glassy dynamics characterized by stretched exponential relaxation are observed. We found that independent of the symmetries and Hamiltonian parameters, the stretch power lies close to the one analytically predicted for the Ising limit ($\beta = 0.5$).

The numerical investigations in this Letter have been carried out using the semiclassical dTWA method, allowing us to simulate hundreds of particles in the strong disorder regime. Hereby dTWA takes primordial quantum fluctuations into account, that are required to trigger relaxation dynamics [22]. The application of dTWA is justified, since it is expected to successfully approximate the dynamics of one-point correlations [21]. Furthermore, we cross validated the method with a moving average cluster expansion (MACE), which takes into account the full quantum dynamics but may suffer from finite size artifacts (see Appendix A). In addition, dTWA succeeded in the past to reproduce experimentally observed relaxation dynamics in disordered Heisenberg models [19,22]. The obtained results on disordered XYZ models can be experimentally tested, as recently the Floquet engineering of Rydberg spins has enabled the possibility to experimentally implement Heisenberg Hamiltonians with tunable interaction coefficients [23]. In the future we aim to use this experimental platform to extend the investigation of glassy dynamics to two-time quantities such as the susceptibility and we expect phenomena such as aging or the reminiscence of possible phase transitions to emerge.

Our observations of a stretched exponential law in both XXZ and XYZ Heisenberg systems possessing a scale-invariant distribution of interaction strengths extend the connection between scale invariance and glassy dynamics beyond open systems and the quantum Ising model. This highlights that glassy dynamics is neither a speciality of open systems nor of the quantum Ising model, but it appears naturally in a wide variety of XYZ Hamiltonians with different symmetries that feature scale invariance. Furthermore, the presented work shows that this connection also constitutes a reality for nonintegrable quantum spin systems.

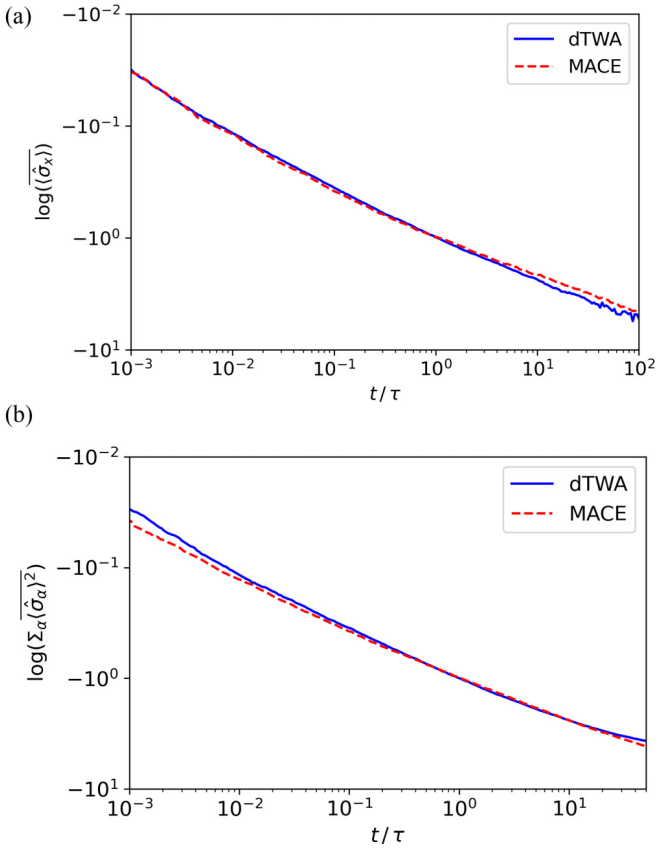

FIG. 4. Logarithm of (a) the transverse magnetization $\log \overline{\langle\hat{\sigma}_x\rangle}$ and (b) $\log(\sum_\alpha \overline{\langle\hat{\sigma}_\alpha\rangle^2})$ used for the purity [Eq. (3)] as a function of rescaled time t/τ for the dTWA (solid line) and MACE (dashed line) for a XXZ Heisenberg model with anisotropy $\Delta = -0.7$. For the MACE simulation, clusters of 12 surrounding spins are chosen and the same spin positions were used. For these numerical simulations, we chose $N = 100$ and $x = 8 \times 10^{-3}$.

ACKNOWLEDGMENTS

This work is supported by the Deutsche Forschungsgemeinschaft (DFG, German Research Foundation) under Germany's Excellence Strategy EXC2181/1-390900948 (the Heidelberg STRUCTURES Excellence Cluster), within the Collaborative Research Center SFB1225 (ISOQUANT) and the DFG Priority Program 1929 "GiRyd" (DFG WE2661/12-1). We acknowledge support by the European Commission FET flagship project PASQuanS (Grant No. 817482) and by the Heidelberg Center for Quantum Dynamics. C.H. acknowledges funding from the Alexander von Humboldt foundation and T.F. from a graduate scholarship of the Heidelberg University (LGFG). The authors acknowledge support by the state of Baden-Württemberg through bwHPC and the German Research Foundation (DFG) through Grant No. INST 40/575-1 FUGG (JUSTUS 2 cluster).

APPENDIX A: DISCRETE TRUNCATED WIGNER APPROXIMATION

dTWA can be understood as a Monte Carlo average over trajectories sampled from the Wigner distribution of the system's initial state and evolved according to the mean-field equations of motions, thus accounting for quantum fluctuations [21]. dTWA has been used successfully to model the dynamics of one- and two-point correlations for the Ising model and the XY Heisenberg model [21] and with experimental observations of the decay of transverse magnetization in Heisenberg models [19,22]. In addition, it has been shown that dTWA is capable of describing genuine quantum features such as entanglement [24] and correctly reproduces the diffusive long time dynamics of generic nonintegrable quantum systems [25]. While these arguments support the applicability of dTWA in the system under study, we compare in the following the resulting dynamics to another numerical method based on exact diagonalization. The moving average cluster

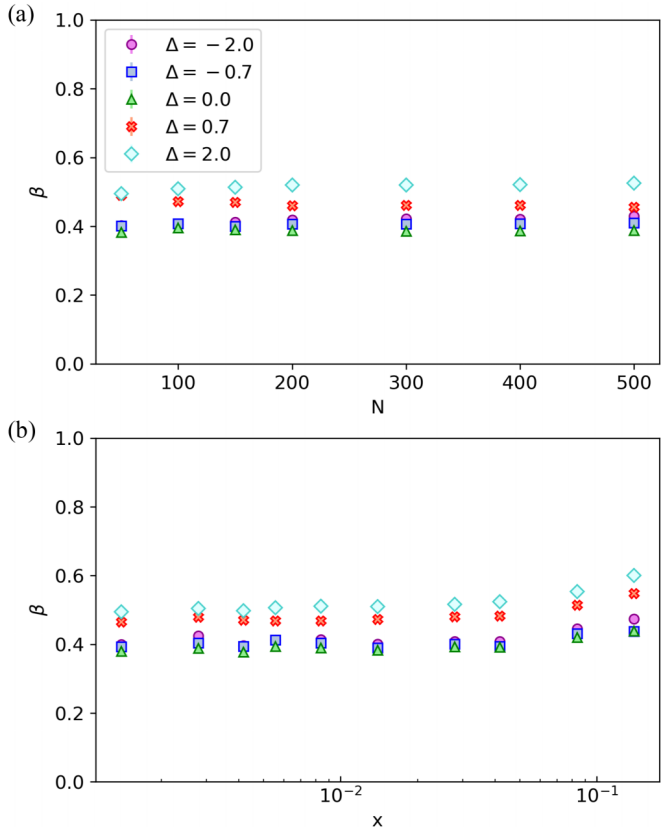

FIG. 5. Stretch power β obtained from a stretched exponential fit to the numerically simulated transverse magnetization dynamics for different anisotropies Δ as a function of (a) particle number N and (b) disorder strength x.

expansion (MACE) [26] solves clusters of spins exactly. This method takes the full quantum dynamics into account, as long as the correlation length is smaller than the cluster size. We present in Fig. 4 the relaxation dynamics of the transverse magnetization $\overline{\langle\hat{\sigma}_x\rangle}$ for both methods over five decades for an XXZ Heisenberg model with $\Delta = -0.7$. Remarkably good agreement is found, thus cross validating both methods. In the work of this Letter, we decided to use dTWA as it requires less computational resources, which allows us to explore a broader parameter space. In addition to the averaging performed via the Monte Carlo trajectories, we perform disorder averages over different spin configurations drawn from the same uniform distribution. We point out that the dynamics of the magnetization are converged for 20 trajectories and 200 disorder averages, whereas for the purity it requires 200 trajectories and 40 disorder averages.

APPENDIX B: DEPENDENCE ON SYSTEM SIZE AND DISORDER STRENGTH

In this Letter we consider a system of N spins drawn from a homogeneous spatial distribution in three dimensions characterized by the density n. Motivated by the realization of spin systems with Rydberg atoms where the blockade effect imposes a minimal distance between Rydberg spins, we consider a minimal distance r_b between different spins. Disorder is coming from the random spin positions resulting in a broad

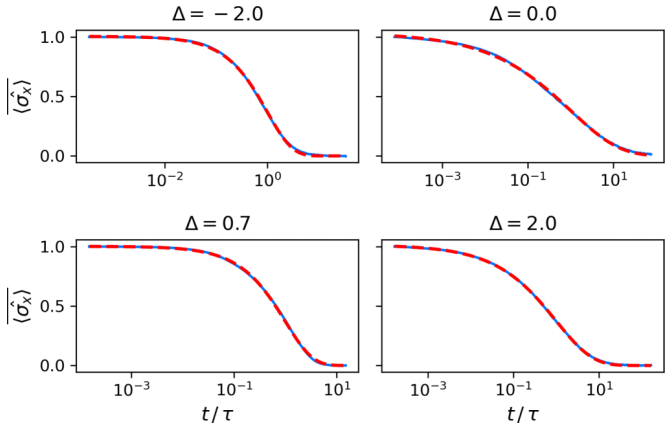

FIG. 6. Transverse magnetization as a function of rescaled time t/τ for different anisotropies. Numerical data (solid blue line) are obtained for $N = 100$ and $x = 8 \times 10^{-3}$. The dashed red line shows the fitted stretched exponential law.

distribution of interaction strengths. As a disorder quantifier we define $x = nV_b$, where V_b is the spherical volume with radius r_b [18]. For large x, the induced correlations of r_b play a significant role, and a more regular structure is obtained due to only slightly varying distances between the spins. For sufficiently small x, the induced correlations can be neglected and uncorrelated spin positions are reobtained, which justifies the choice of x as the disorder parameter.

Additionally, we perform a systematic investigation of the scaling of the numerical results with particle number N in order to assure that the remaining finite size effects are negligible in comparison to the structure obtained in Fig. 2(b). In the following we focus on the glassy dynamics of the transverse magnetization. In Fig. 5(a), we see that the stretched power β, for a given Δ, is only slightly dependent on the particle number between 50 and 500. No global trends are visible and the remaining fluctuations resulting from finite size effects are varying from 0.01 ($\Delta = 0.0$) to 0.03 ($\Delta = 0.7$). Note that for the Ising limit, the resulting stretch power for $N = 100$ particles varies by 0.03 from the analytical result of the thermodynamic limit [18], which can also be seen in the large $|\Delta|$ limit of Figs. 2(b) and 3(b). Nevertheless, the remaining finite size artifacts are negligible in comparison to the obtained values and structure obtained from these figures. Therefore, we fix $N = 100$ for all simulations shown.

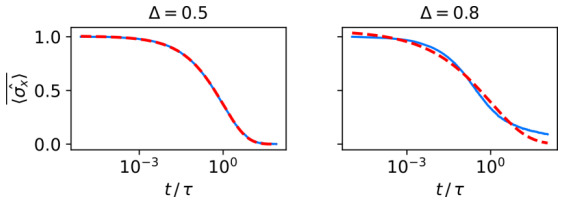

FIG. 7. Transverse magnetization as a function of rescaled time t/τ for the XYZ Heisenberg Hamiltonian with $J_x = 0.5$ and $J_y = 1$ with $\Delta = 0.5$ and $\Delta = 0.8$ (gray-shaded region in Fig. 3). Numerical data (solid blue line) are obtained for $N = 100$ and $x = 8 \times 10^{-3}$. The dashed red line shows the stretched exponential fit.

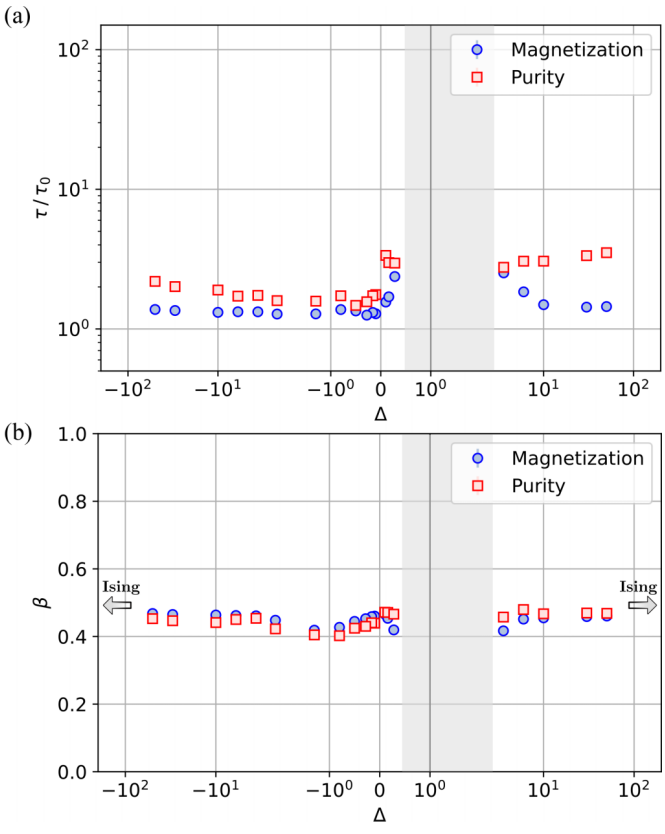

FIG. 8. Fit parameters (a) τ/τ_0 and (b) β for magnetization (circles) and ensemble-averaged single-spin purity (squares) as a function of Δ for an XYZ Hamiltonian with $J_x = 0$ and $J_y = 1$. Within the gray shaded area, the relaxation dynamics is not properly described by stretched exponential law.

Glassy relaxation has been found to be a robust feature for disorder strengths above a certain threshold [19]. To ensure that the chosen disorder parameter x is within this universal strong disorder regime we investigate how the stretch power β changes when we actively modify the disorder strength by varying x. In Fig. 5(b), we show the resulting stretch powers for different Δ values in the case of an XXZ Hamiltonian. We see that if x lies below a value of 0.05, the β exponent obtain from the fit to the dynamics gets disorder independent. Within this Letter, we have chosen to work in this limit by choosing $x = 8 \times 10^{-3}$.

APPENDIX C: ADDITIONAL AGREEMENT OF STRETCHED EXPONENTIAL LAW

Complementary to the data presented in Fig. 1(a) we provide the relaxation dynamics of the transverse magnetization with a linear y scale for the remaining anisotropies of Fig. 1(c), $\Delta = \{-2.0, 0.0, 0.7, 2.0\}$, in Fig. 6. We highlight the remarkable agreement between numerical data and the stretched exponential law.

Similar good agreement can be found for the relaxation dynamics of the general XYZ Heisenberg Hamiltonian provided in Fig. 3 ($J_x = 0.5$, $J_y = 1$). Exemplarily, the left panel of Fig. 7 shows the decay of the transverse magnetization for $\Delta = 0.5$. In contrast, the right panel shows the case of $\delta = 0.8$ close to 1, which lies in the gray-shaded region featuring prohibitively large timescales τ. The stretched exponential fit (dashed red line) can no longer capture the full dynamics. Especially at long times, the magnetization stalls at a finite value.

APPENDIX D: INVESTIGATION ON A YZ HEISENBERG HAMILTONIAN

We present in Fig. 8 a complementary plot to the one presented in Fig. 3 where this time $J_x = 0$ and $J_y = 1$. The resulting fit parameters are similar to the ones presented in Fig. 3.

[1] P. N. Jepsen, J. Amato-Grill, I. Dimitrova, W. W. Ho, E. Demler, and W. Ketterle, Nature (London) **588**, 403 (2020).
[2] K. X. Wei, C. Ramanathan, and P. Cappellaro, Phys. Rev. Lett. **120**, 070501 (2018).
[3] R. Nandkishore and D. A. Huse, Annu. Rev. Condens. Matter Phys. **6**, 15 (2015).
[4] D. A. Abanin and Z. Papić, Ann. Phys. **529**, 1700169 (2017).
[5] P. Jurcevic, H. Shen, P. Hauke, C. Maier, T. Brydges, C. Hempel, B. P. Lanyon, M. Heyl, R. Blatt, and C. F. Roos, Phys. Rev. Lett. **119**, 080501 (2017).
[6] C. Eigen, J. A. P. Glidden, R. Lopes, E. A. Cornell, R. P. Smith, and Z. Hadzibabic, Nature (London) **563**, 221 (2018).
[7] M. Gring, M. Kuhnert, T. Langen, T. Kitagawa, B. Rauer, M. Schreitl, I. Mazets, D. A. Smith, E. Demler, and J. Schmiedmayer, Science **337**, 1318 (2012).
[8] C. J. Turner, A. A. Michailidis, D. A. Abanin, M. Serbyn, and Z. Papić, Nat. Phys. **14**, 745 (2018).
[9] D. Hérisson and M. Ocio, Phys. Rev. Lett. **88**, 257202 (2002).
[10] K. Binder and A. P. Young, Rev. Mod. Phys. **58**, 801 (1986).
[11] J. C. Phillips, Rep. Prog. Phys. **59**, 1133 (1996).
[12] W. Gotze and L. Sjogren, Rep. Prog. Phys. **55**, 241 (1992).
[13] R. Böhmer, K. L. Ngai, C. A. Angell, and D. J. Plazek, J. Chem. Phys. **99**, 4201 (1993).
[14] R. Kohlrausch, Ann. Phys. Chem. **167**, 56 (1854).
[15] J. Klafter and M. F. Shlesinger, Proc. Natl. Acad. Sci. USA **83**, 848 (1986).
[16] J. Choi, S. Choi, G. Kucsko, P. C. Maurer, B. J. Shields, H. Sumiya, S. Onoda, J. Isoya, E. Demler, F. Jelezko, N. Y. Yao, and M. D. Lukin, Phys. Rev. Lett. **118**, 093601 (2017).
[17] G. Kucsko, S. Choi, J. Choi, P. C. Maurer, H. Zhou, R. Landig, H. Sumiya, S. Onoda, J. Isoya, F. Jelezko, E. Demler, N. Y. Yao, and M. D. Lukin, Phys. Rev. Lett. **121**, 023601 (2018).
[18] P. Schultzen, T. Franz, S. Geier, A. Salzinger, A. Tebben, C. Hainaut, G. Zürn, M. Weidemüller, and M. Gärttner, Phys. Rev. B **105**, L020201 (2022).

[19] A. Signoles, T. Franz, R. Ferracini Alves, M. Gärttner, S. Whitlock, G. Zürn, and M. Weidemüller, Phys. Rev. X **11**, 011011 (2021).

[20] F. Franchini, *An Introduction to Integrable Techniques for One-Dimensional Quantum Systems*, Lecture Notes in Physics (Springer, Cham, 2017), Vol. 940, pp. 71–92.

[21] J. Schachenmayer, A. Pikovski, and A. M. Rey, Phys. Rev. X **5**, 011022 (2015).

[22] A. P. n. Orioli, A. Signoles, H. Wildhagen, G. Günter, J. Berges, S. Whitlock, and M. Weidemüller, Phys. Rev. Lett. **120**, 063601 (2018).

[23] S. Geier, N. Thaicharoen, C. Hainaut, T. Franz, A. Salzinger, A. Tebben, D. Grimshandl, G. Zürn, and M. Weidemüller, Science **374**, 1149 (2021).

[24] S. Lepoutre, J. Schachenmayer, L. Gabardos, B. Zhu, B. Naylor, E. Maréchal, O. Gorceix, A. M. Rey, L. Vernac, and B. Laburthe-Tolra, Nat. Commun. **10**, 1714 (2019).

[25] A. Schuckert, I. Lovas, and M. Knap, Phys. Rev. B **101**, 020416(R) (2020).

[26] K. R. A. Hazzard, B. Gadway, M. Foss-Feig, B. Yan, S. A. Moses, J. P. Covey, N. Y. Yao, M. D. Lukin, J. Ye, D. S. Jin, and A. M. Rey, Phys. Rev. Lett. **113**, 195302 (2014).

Observation of universal relaxation dynamics in disordered quantum spin systems

T. Franz,[1,*] S. Geier,[1,*] C. Hainaut,[1] N. Thaicharoen,[1,2]
A. Braemer,[1,3] M. Gärttner,[1,3,4] G. Zürn,[1] and M. Weidemüller[1,†]

[1] *Physikalisches Institut, Universität Heidelberg, Im Neuenheimer Feld 226, 69120 Heidelberg, Germany*
[2] *Research Center for Quantum Technology, Faculty of Science, Chiang Mai University 239 Huay Kaew Road, Muang, Chiang Mai, 50200, Thailand*
[3] *Kirchhoff-Institut für Physik, Universität Heidelberg, Im Neuenheimer Feld 227, 69120 Heidelberg, Germany*
[4] *Institut für Theoretische Physik, Ruprecht-Karls-Universität Heidelberg, Philosophenweg 16, 69120 Heidelberg, Germany*

(Dated: September 19, 2022)

A major goal toward understanding far-from-equilibrium dynamics of quantum many-body systems consists in finding indications of universality in the sense that the dynamics no longer depends on microscopic details of the system. We realize a large range of many-body spin systems on a Rydberg atom quantum simulator by choosing appropriate Rydberg state combinations. We use this platform to compare the magnetization relaxation dynamics of disordered Heisenberg XX-, XXZ- and Ising Hamiltonians in a scalable fashion. After appropriate rescaling of evolution time, the dynamics collapse onto a single curve. We find that the observed universal behavior is captured by theoretical models that only consider local pairs of spins. Associated to each pair is a local quasi-conserved quantity, allowing us to describe the early time dynamics of the system in terms of an integrable model similar to systems featuring prethermalization. Since the dynamics of pairs are independent of the type of Hamiltonian up to a scaling factor, this integrable model explains the observed universal relaxation dynamics of disordered Heisenberg quantum spin systems.

I. INTRODUCTION

Far-from equilibrium dynamics of isolated quantum systems displays a wide range of emergent phenomena, such as dynamical phase transitions [1, 2], quantum many-body scars [3–5] and many-body localization (MBL) [6–10]. The time evolution of these systems after a quench generally depends strongly on the type of interactions and the distribution of interaction strengths between the particles [11]. A notable exception are systems showing (metastable) prethermal phases, where relaxation dynamics can show universal behavior, i.e. the dynamics become independent of details of the microscopic model [12–16].

When considering the role of disorder for the dynamics of quantum many-body systems, a striking characteristic of the dynamics is that they can be non-ergodic [17], which is found for example in spin glasses [18] and MBL [19]. Associated with non-ergodicity is often an anomalously slow relaxation, which was observed in disordered quantum spin systems that feature sub-exponential dynamics [20–24]. Remarkably, a unified description of the sub-exponential dynamics, the stretched exponential law, emerges as long as the degree of disorder is sufficiently strong [20]. This raises the question of whether this apparently robust phenomenon also persists for spin Hamiltonians possessing different symmetry properties and how we can explain its appearance in various systems.

In classical systems, such universality is known and can be understood. In a seminal work, by comparing three different physical mechanisms, Klafter and Shlesinger have found that a scale-invariant distribution of timescales is the underlying mathematical structure that induces stretched-exponential relaxation [25]. In order to get an intuitive understanding of the underlying physics, we consider an ensemble of initially fully polarized spins. All the spins are coupled to an external bath at a different strength sampled from a scale-invariant distribution (denoted as "many parallel channels model" in [25]). Due to the coupling to the bath, each spin decays exponentially on a different timescale. Thus, the global polarization of the system yields a stretched exponential form resulting from the averaging over all the spins.

For isolated quantum systems, where the dynamics are unitary, there is no notion of decay to a bath. However, in a disordered system where the spins are randomly positioned in space, the interaction strengths between the spins can be distributed scale-invariantly. For example, it was shown analytically for the dynamics of the quantum Ising model that this distribution of coupling strengths induces a stretched exponential law [26]. This analytic solution is only possible because the Ising model features an extensive number of conserved quantities, i.e. it is integrable. Thus, for non-integrable models, no analytic solution exists, and it remains an open question in which manner the system relaxes after a quantum quench. Semi-classical simulations suggest that non-integrable Heisenberg XYZ Hamiltonians present out-of-equilibrium dynamics that follow a stretched exponential law like the Ising model independent of their symmetry [27]. However, these semiclassical approximations neglect quantum effects beyond initial quantum fluctua-

* These authors contributed equally to this work.
† weidemueller@uni-heidelberg.de

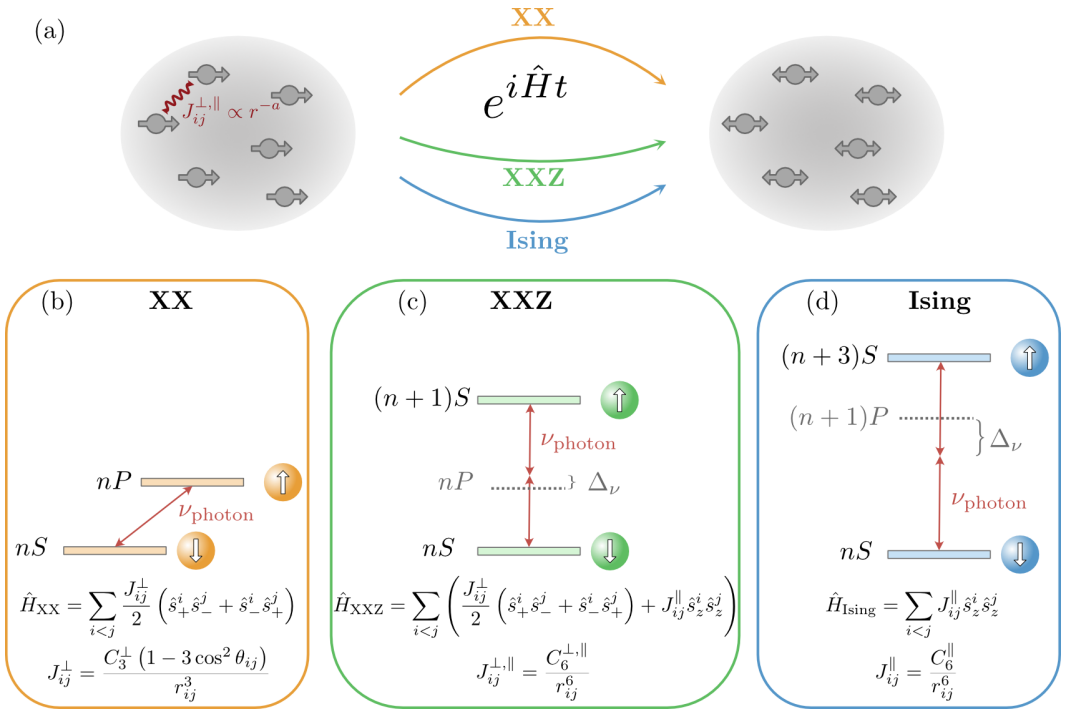

FIG. 1. Rydberg quantum simulator platform. (a) Illustration of out-of-equilibirum disordered spin systems relaxing with respect to different Hamiltonians (b) Illustration of the experimental realization of a Heisenberg XX Hamiltonian by coupling a Rydberg $|nS\rangle$ state to a $|nP\rangle$ state, possessing opposite parity. The interaction is dipolar and falls of as r_{ij}^3. Coupling two Rydberg states with the same parity results in Heisenberg XXZ Hamiltonian (b) for state combinations $|nS\rangle$ and $|(n+1)S\rangle$, while state combinations $|nS\rangle$ and $|(n+3)S\rangle$ results in a Ising Hamiltonian (c). In the two latter cases, the interactions is of van der Waals nature with a r_{ij}^6 dependence.

tions and may miss relaxation behaviors owing to large scale correlation propagation associated to build up of entanglement. Investigating the exact time evolution numerically is challenging due to the exponential growth of the Hilbert space with system size in quantum many-body systems.

This challenge can be addressed by studying the time evolution for given Hamiltonians with highly tunable quantum simulators on elaborated experimental apparatus [28–31]. In this work, we use different combinations of states of highly excited Rydberg atoms to realize different types of spin Hamiltonians thus making use of the full versatility of this platform [9, 20, 32–36]. Rydberg atoms are ideally suited to study unitary quantum dynamics because the time scales of the interacting dynamics vastly exceed those of the typical decoherence mechanisms. We observe the relaxation dynamics of three different Heisenberg Hamiltonians: the integrable Ising model and the non-integrable XX and XXZ models with power-law interactions and positional disorder (see Fig. 1 (a)). For all models we observe the same characteristic decay of magnetization, well-described by a stretched exponential function, which causes the data to collapse onto a single universal curve after appropriate rescaling of time. This behavior can be qualitatively explained by an integrable model which neglects all interactions beyond nearest-neighbor pairs. This implies that his relaxation is not a consequence of spreading of correlations beyond the nearest neighbor and thus the observed universality is associated to the integrable property of the disordered quantum spin systems [6, 37]

II. HEISENBERG SPIN SYSTEMS ON A RYDBERG-ATOM QUANTUM SIMULATOR

We consider a spin-1/2 system interacting with the following Heisenberg Hamiltonian ($\hbar = 1$)

$$\hat{H} = \sum_{i<j} \left(J_{ij}^{\perp}/2(\hat{s}_+^i \hat{s}_-^j + \hat{s}_-^i \hat{s}_+^j) + J_{ij}^{\parallel} \hat{s}_z^i \hat{s}_z^j \right). \quad (1)$$

Here, $\hat{s}_{\pm}^i = \hat{s}_x^i \pm i\hat{s}_y^i$, where $\hat{s}_\alpha^i (\alpha \in x, y, z)$ are the spin-1/2 operator of spin i and $J_{ij}^{\perp,\parallel} = C_a^{\perp,\parallel}/r^a$. These types of Heisenberg XXZ Hamiltonians with disordered couplings feature a rich phenomenology of different phases and relaxation behaviors. For example, increasing the ratio $J_{ij}^{\parallel}/J_{ij}^{\perp}$ leads to a crossover from a many-body localized to a spin glass phase [38]. The Ising case where $J_{ij}^{\perp} = 0$ features additional symmetries under local spin rotations $\hat{s}_z^i$ that commute with the Hamiltonian. Therefore, $\langle \hat{s}_z^i \rangle$ constitute an extensive number of conserved

quantities which make this Hamiltonian integrable. For $J_{ij}^{\perp} \neq 0$, $\hat{s}_z^i$ are no longer conserved and the Hamiltonian is non-integrable.

In the following, we provide a comprehensive description of how to engineer this Hamiltonian with different combinations of Rydberg states [39, 40]. Especially, this gives us the opportunity to explain how to engineer an Ising Hamiltonian in a spin system realized by two different Rydberg states.

For general spin systems with global $U(1)$ symmetry, the coupling terms can be obtained by calculating the matrix elements of the interaction Hamiltonian. The Ising term

$$J_{ij}^{\parallel} = (E_{\uparrow_i\uparrow_j} + E_{\downarrow_i\downarrow_j}) - (E_{\downarrow_i\uparrow_j} + E_{\uparrow_i\downarrow_j}) \tag{2}$$

is defined as the energy difference between spins being aligned and being anti-aligned. Here, $E_{\alpha_i\beta_j} = \langle\alpha_i\beta_j|\hat{H}|\alpha_i\beta_j\rangle$ are the interaction energy of spin i and j with $\alpha, \beta \in [\uparrow, \downarrow]$. The exchange term is determined by

$$J_{ij}^{\perp} = \langle\downarrow_i\uparrow_j |\hat{H}| \uparrow_i\downarrow_j\rangle . \tag{3}$$

For a system consisting of states with opposite parity, such as $|\downarrow\rangle = |nS\rangle$ and $|\uparrow\rangle = |nP\rangle$ (see Fig. 1 (b)), where n is the principal quantum number, the dominant coupling is a direct dipolar interaction and can be described by the Hamiltonian

$$\hat{H}_{\mathrm{DDI}} = \frac{\hat{\mathbf{d}}_i \cdot \hat{\mathbf{d}}_j - 3\left(\hat{\mathbf{d}}_i \cdot \mathbf{e}_{r_{ij}}\right)\left(\hat{\mathbf{d}}_j \cdot \mathbf{e}_{r_{ij}}\right)}{r_{ij}^3}. \tag{4}$$

where $\hat{\mathbf{d}}_i$ is the dipole operator of atom i, $\mathbf{e}_{r_{ij}}$ is the unit vector connecting the two atoms and r_{ij} their distance. Mapped on the spin Hamiltonian of Eq. 1, the resulting interaction coefficient is

$$J_{ij}^{\perp} = \frac{C_3^{\perp}(1 - 3\cos^2\theta_{\mathrm{ij}})}{r_{ij}^3}. \tag{5}$$

. Here, θ_{ij} is the angle between $\mathbf{e}_{r_{ij}}$ and the quantization axis and $C_3^{\perp}$ the coupling parameter [35, 36]. The Ising term $J_{ij}^{\parallel}$ is not present since interaction energy shifts $E_{\alpha_i\beta_j}$ are dipole forbidden. Therefore this is a way to realize an XX model as depectied in figure 1b). In this work, we have chosen $61S$ and $61P$ leading to $C_3^{\perp}/2\pi$= 3.14 GHz µm^3.

If the two states possess the same parity, such as the two atoms being in the same state nS, direct dipolar coupling is forbidden. Instead, the interaction is a second-order process through a virtually excited pair state $|m\rangle$ and can be described by

$$\hat{H}_{vdW} = -\frac{1}{\hbar}\sum_m \frac{\hat{H}_{\mathrm{DDI}}\,|m\rangle\,\langle m|\,\hat{H}_{\mathrm{DDI}}}{\Delta_\nu}. \tag{6}$$

Here, Foerster defect Δ_ν is the energy difference between the initial state and the virtually excited state $|m\rangle$. This Hamiltonian gives rise to power-law interactions $J_{ij} = C_6/r_{ij}^6$ that scales with n^{11}. Especially, this term is large if a pair state m with a small Foerster defect and a large dipolar coupling exists. Many experiments exploit these interactions by realizing a spin system where the ground state is coupled to a single Rydberg state. These systems feature the Rydberg blockade effect and can be mapped on an Ising model [3, 33, 34].

Similar interactions also exist for a spin system realized with two different Rydberg states $|\downarrow\rangle = |nS\rangle$ and $|\uparrow\rangle = |(n+1)S\rangle$ for all energy shifts in the Ising term (2). In this case, the Van-der-Waals Hamiltonian (6) also induce a spin exchange term because the two Rydberg states are coupled via the intermediate pair state $|m\rangle = |nP, nP\rangle$ (see Fig. 1 (c)). In the case of $n = 61$, the Foerster defects of both the Ising and exchange interactions are similar, therefore also the interactions are comparable resulting in $J^{\parallel}/J^{\perp} = -0.7$. Therefore, this spin system can be mapped onto an effective Heisenberg XXZ-Hamiltonian [20].

In order to realize an Ising Hamiltonian with two different Rydberg states, a state combination is needed where the exchange term (3) is small because the Foerster defect is large. This can be achieved by coupling $|\downarrow\rangle = |nS\rangle$ to $|\uparrow\rangle = |(n+3)S\rangle$. In this case, the largest contribution to the exchange term comes from $|m\rangle = |(n+1)P, (n+1)P\rangle$ where the Foerster defect is increased by an order of magnitude (see Fig. 1 (d)) and also the matrix elements are small. For example, for $n = 61$, this spin system is characterized by a ratio of $J^{\parallel}/J^{\perp} = 400$, which is a good approximation to an Ising Hamiltonian ($J^{\perp} = 0$).

III. EXPERIMENTAL OBSERVATION OF SCALING BEHAVIOR AND GLASSY DYNAMICS

In order to observe the relaxation dynamics of the three different spin models, we implement a Ramsey protocol in our Rydberg experiment. The experiment starts with trapping Rubidium-87 atoms loaded in a crossed dipole trap of size 65 µm × 45 µm × 45 µm at a temperature of 20 µK. The atoms are excited from the ground $|g\rangle = |5S_{1/2}, F = 2, m_F = 2\rangle$ to the Rydberg state $|61S_{1/2}, m_j = 0.5\rangle$ by a two-photon transition with red (780 nm) and blue (480 nm) lasers that are detuned by $2\pi \cdot 98$ MHz from the intermediate state $|e\rangle = |5P_{3/2}, F = 3, m_F = 3\rangle$. For this state, the Rydberg lifetime of 100 µs exceeds the duration of the spin experiment of 30 µs. The excitation process leads to a three-dimensional cloud of N≈ 80 − 250 Rydberg atoms that are distributed randomly. The Van-der-Waals interaction during the excitation process imposes a minimal distance of $r_{\mathrm{bl}} \approx 10$ µm between the spins (Rydberg blockade effect). The state $|61S_{1/2}, m_j = 0.5\rangle$ is the $|\downarrow\rangle$ state of all three different spin systems, the main difference is the second Rydberg states that is addressed

by choosing proper microwave coupling using an AWG setup.

To realize the Heisenberg-XX model, a single-photon microwave transition at $2\pi \cdot 16\,\mathrm{GHz}$ with a Rabi frequency of $\Omega = 2\pi \cdot 18\,\mathrm{MHz}$ couples this state to $|\uparrow\rangle = |61P_{3/2}, m_j = 1/2\rangle$. In the case of XXZ interactions, two microwave photons at $2\pi \cdot 16\,\mathrm{GHz}$ couple to $|\uparrow\rangle = |62S_{1/2}, m_j = 1/2\rangle$. Here, a single photon Rabi frequency of $\Omega = 2\pi \cdot 48\,\mathrm{MHz}$ with a detuning $\Delta_\nu = 2\pi \cdot 170\,\mathrm{MHz}$ leads to a two photon Rabi frequency of $\Omega_{2\gamma} = 2\pi \cdot 6.8\,\mathrm{MHz}$. For Ising interactions, where the state $|61S\rangle$ is coupled to $|64S\rangle$, the detuning of $\Delta_\nu = 2\pi \cdot 1.426\,\mathrm{GHz}$ is too large to efficiently couple the states with two microwave photons of the same frequency $2\pi \cdot 47\,\mathrm{GHz}$. Therefore, we combine two frequencies differing by $2\pi \cdot 1.563\,\mathrm{GHz}$ such that the effective detuning to the intermediate state $|62P\rangle$ is $2\pi \cdot 136\,\mathrm{MHz}$. For a single photon Rabi frequency of $\Omega = 2\pi \cdot 30\,\mathrm{MHz}$ this results in an effective two-photon Rabi frequency of $\Omega_{2\gamma} = 2\pi \cdot 3.3\,\mathrm{MHz}$ (see Figure 1 (b-d) for the microwave photonic transitions).

After having excited the ground states atoms to the down spin state, we initialize the dynamics be performing a first $\pi/2$-pulse microwave pulse which set the whole system is the state $|{\rightarrow}\rangle^{\otimes \mathrm{N}} = 1/\sqrt{2}(|\uparrow\rangle + |\downarrow\rangle)^{\otimes \mathrm{N}}$ and let the system evolve under the natural Hamiltonian over 4 orders of magnitude in time up to $30\,\mu\mathrm{s}$. A second $\pi/2$-pulse at a different readout phase followed by optical de-excitation and field ionization allows a tomographic measurement of the x magnetization $\langle \hat{S}_x^i \rangle = \sum_i \langle \hat{s}_x \rangle$ [20].

The resulting relaxation dynamics of the Ising, Heisenberg XX, and XXZ models are shown in Fig. 2 (a-c). At early times, the magnetization seems to be almost perfectly conserved at $\langle \hat{S}_x \rangle = 0.5$ before the relaxation begins. This effect is attributed to the Rydberg blockade that induces a maximal interaction strength that determines the system's fastest time scale. For each model, the system relaxes to zero magnetization within less than $10\,\mu\mathrm{s}$. which is understood in disordered system by considering symmetry arguments: Indeed, the magnetization can be rewritten using the commutator relation for Pauli matrices $\langle \hat{S}_x \rangle = -i\langle [\hat{S}_y, \hat{S}_z] \rangle$. The latter term vanishes for each eigenstate $|\phi\rangle$ of the XXZ Hamiltonian because each eigenstate is also an eigenstate of $\hat{S}_z |\phi\rangle = \sum_i \hat{s}_z^{(i)} |\phi\rangle = S_z |\phi\rangle$ due to the global U(1) symmetry leading to $\langle [\hat{S}_y, \hat{S}_z] \rangle = S_z \langle [\hat{S}_y, 1] \rangle = 0$.

To compare the relaxation curves to numerical predictions, the positions of the Rydberg spins are needed. We use a hard-sphere model where each Rydberg excitation is described by a superatom [41] with a given blockade radius and effective Rabi frequency [20]. Without free parameters, only taking into account the geometry of the ground state atomic could, the size and linewidth of the excitation laser beams, and the measured number of Rydberg atoms, that are evaluated through additional measurements, we can use this model to predict a distribution of atoms thus having full access to the distribution of distance-dependent interaction strengths.

We simulate the exact time-evolution of the Ising model $\langle \hat{S}_x \rangle (t) = 1/(2N) \sum_i \prod_{j \neq i} \cos(2J_{ij}^{\parallel} t)$ derived by Emch [42] and Radin [43] (solid line in Fig. 2 (a)). This prediction agrees within the error bars with the measured dynamics providing a benchmark whether the experimental data can be reproduced assuming unitary dynamics and a given distribution of Rydberg spins. In the case of XX and XXZ Hamiltonians, no analytical solution is known. However, the Discrete Truncated Wigner Approximation (DTWA) naturally generalizes the Emch-Radin solution as in the limiting case of only Ising interaction DTWA predicts the magnetization exactly [44]. Compared to the experimental data in Fig. 2 (b) and (c), DTWA also shows good agreement within the experimental uncertainties. The small deviation between simulations and experiments can be mostly attributed to an inaccuracy of the atom distribution obtained from the simplified excitation model (see appendix).

Despite stemming from three different spin systems, the dynamics in Fig. 2 (a-c) look strikingly similar in a log-linear plot. Indeed, by rescaling time with the typical timescale of each system given by $|J^{\perp}_{\mathrm{median}} - J^{\parallel}_{\mathrm{median}}|$, all relaxation curves coincide within the experimental errors. Here, $J^{\perp,\parallel}_{\mathrm{median}}$ is the median of the average absolute interaction strengths $1/N \sum_j |J_{ij}^{\perp,\parallel}|$. This choice of typical interaction time scale is motivated by the oscillation frequency of a single pair of interacting spins governed by (1), which will be further discussed in the following section. This scaling behavior shows universal relaxation dynamics which is independent of the type of Hamiltonian. The striking collapse allows us to infer the functional form of the relaxation dynamics of the non-integrable models: For the Ising model, it is known that the relaxation follows exactly the stretched exponential law $e^{-(t/\tau)^\beta}$ [26] with stretching exponent β and timescale τ. The logarithm of the stretched exponential law is a power-law. Plotted on a double logarithmic scale, this power-law becomes a linear function (dashed line in the inset of Fig. 2 (d)). In this representation, the rescaled experimental data also show a linear behavior over two decades. This confirms the hypothesis that the stretched exponential law is the unifying description of the relaxation for the integrable quantum Ising model and also for the non-integrable XX and XXZ Hamiltonians.

IV. EFFECTIVE INTEGRABILITY BY LOCALIZED ENSEMBLES

In order to explain the emergence of the scaling behavior, we aim for a simplified model which captures the relevant time scales of the system.

In order to explain the emergence of the scaling behavior, we aim for a description of relaxation dynamics that exploits the possibility of separating the time-scales in the system. This is possible in disordered samples

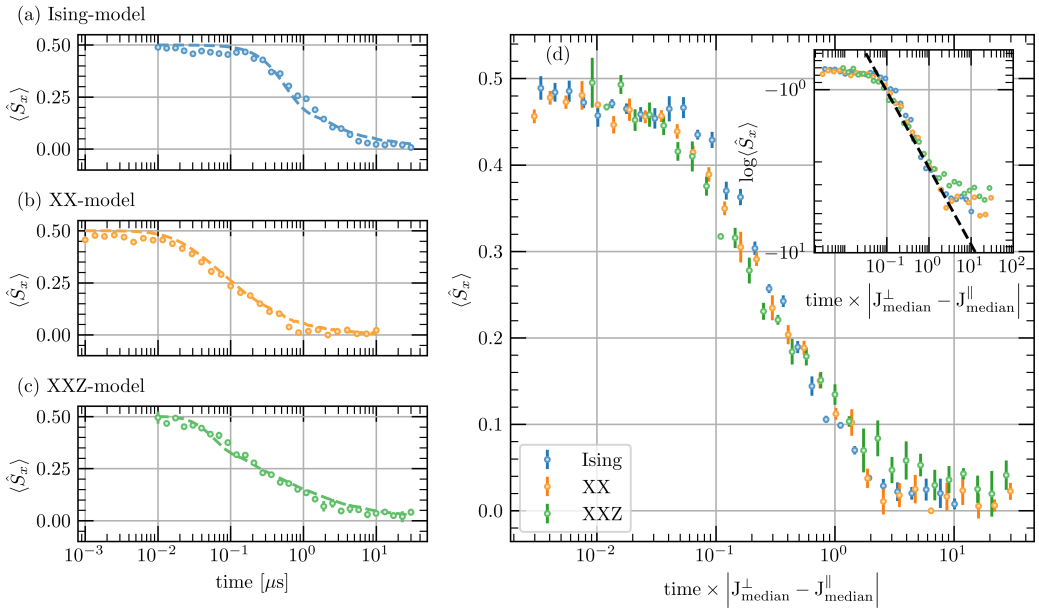

FIG. 2. Relaxation dynamics of disordered quantum spin systems. Magnetization dynamics as a function of time for the Ising-model (a), the XX-model (b), and the XXZ-model (c). The solid line shows the exact solution for the Ising-model and dahed lines are DTWA simulations for the XX- and XXZ-model. Error bars are the statistical errors resulting from the repetition of the experiment. (d) Magnetization dynamics of the three models as a function of the time rescaled by the typical interaction strength $2\pi|J^{\perp}_{\text{median}} - J^{\parallel}_{\text{median}}| = 2.1\,\text{MHz}$ (Ising-model), 19 MHz (XX-model), 3.5 MHz (XXZ-model). Inset: Data points of (c) plotted on as loglog vs log. Dashed line is a guide to the eye indicating a stretched exponential relaxation.

where the closest pairs interact on the fastest time-scales. A similar approach is used in disorder renormalization group theories where the fastest time scales are integrated first followed by renormalization steps [45–48]. Here, we do not aim to proceed further in this renormalization scheme, but instead, we use the basis of eigenstates of strongly interacting pairs to derive an intuitive understanding of the physics within mean-field theory. Following this idea, we introduce a model where each spin only interacts with its nearest neighbor. Since interactions between different pairs are neglected, we can solve the time-evolution of each pair individually which results in an integrable model. In the following, we show that this crude approximation indeed qualitatively explains the data. Each pair oscillates between the fully polarized states $|{\rightarrow}{\rightarrow}\rangle$ and $|{\leftarrow}{\leftarrow}\rangle$ via the maximally entangled Bell states $1/\sqrt{2}\,(|{\rightarrow}{\rightarrow}\rangle \pm |{\leftarrow}{\leftarrow}\rangle)$ (see Fig. 3 (a)) [49]. The resulting oscillation of the magnetization (shown in Fig. 3 (b)) is independent of the specific XXZ Hamiltonian, only the frequency $J^{\perp}_{ij} - J^{\parallel}_{ij}$ differs depending on the Ising and exchange interaction strengths. This indepence explains the observed universality of relaxation dynamics.

To compare the pair approximation to the experimental setting, we calculate the magnetization of each spin assuming it interacts only with its nearest neighbor. The global magnetization is the moving average over all of these pairs:

$$\langle \hat{S}_x^{\text{pair}} \rangle (t) = \frac{1}{2N} \sum_i \cos(2 \max_j (J^{\perp}_{ij} - J^{\parallel}_{ij}) t). \qquad (7)$$

The resulting relaxation is shown by the solid black line in Fig. 3 (c-e). Qualitatively, it shows a similar behavior compared to DTWA or the experimental data despite all long-range interactions and correlations beyond isolated pairs being completely neglected. In the case of Ising interactions, the magnetization simulated with the pair model dips at 1 µs slightly below the experimental data. This is a reminiscence of the blockade effect which leads to some pairs separated by the blockade radius that oscillate at the same frequency. In the case of dipolar interactions (XX model), which are long-range with interaction exponent $a = 3$, the pair model overestimates the magnetization slightly at early times as all interactions beyond the nearest neighbor are neglected. For the XXZ model, where the blockade radius is small (see appendix) and the Van-der-Waals interactions are short range with $a = 6$, the pair model shows the best agreement and coincides with the DTWA simulation.

To investigate the effects of higher order correlations on the dynamics, we explore clusters of spins using Moving Average Cluster Expansion (MACE) [50]. Here, the expectation value of every single spin is calculated by exact diagonalization of the cluster of surrounding spins. For a cluster size of 10 spins, the resulting dynamics are shown

as a dashed grey line in Fig. 3 (c-d). MACE predicts nearly the same relaxation behavior as DTWA (dotted grey line in Fig. 3 (c-d)) including the overestimation of the magnetization at late time compared to the experimental data. Therefore, we conclude that it is possible to capture the complete quantum dynamics of the magnetization by simulating only small clusters of spins.

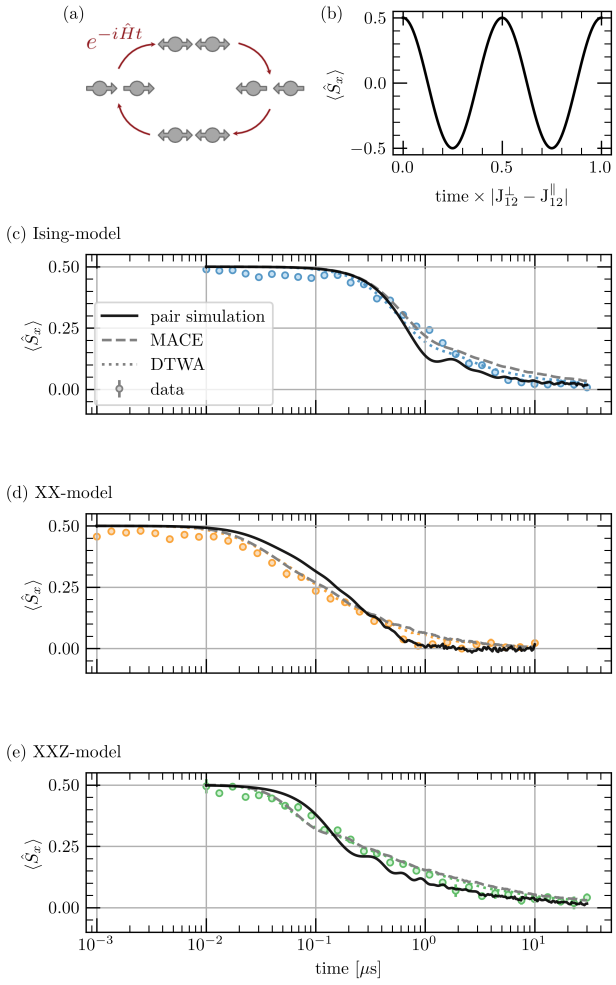

FIG. 3. Effective description by localized pairs. (a) Illustration of the oscillation of a single pair under an arbitrary Heisenberg XXZ Hamiltonian. A fully polarized state $|{\rightarrow}{\rightarrow}\rangle$ (left) evolves via the the maximally entangled Bell state $1/\sqrt{2}\,(|{\rightarrow}{\rightarrow}\rangle + |{\leftarrow}{\leftarrow}\rangle)$ (top) to the state $|{\leftarrow}{\leftarrow}\rangle$ (right). Then, it returns to the origin via the other Bell state $1/\sqrt{2}\,(|{\rightarrow}{\rightarrow}\rangle - |{\leftarrow}{\leftarrow}\rangle)$ (bottom). (b) Oscillation of the magnetization for a single pair initialized in $|{\rightarrow}{\rightarrow}\rangle$. (c-e) Comparison of the pair approximation (solid black line) and MACE (dashed grey line) with DTWA (dotted lines) and the experimental data of Fig. 2 (error bars) for Ising (c), XX (d) and XXZ model (e).

V. RELATION TO PRETHERMALIZATION

The observed magnetization relaxation dynamics for the different models show a universal behavior in the sense that the essential features of a large class of disordered quantum systems are independent of the microscopic details of the system. Such universal behavior is famously known from equilibrium physics where different materials share the same scaling functions and critical exponents near phase transitions, which is why these materials can be attributed to universality classes [51–53]. Recently, the concept of universality and scaling behavior has also been introduced to relaxation dynamics in the context of prethermalization [12, 14, 16, 54]. In systems showing prethermalization, the Hamiltonian of a near-integrable system can be divided in an integrable part and a small perturbation that breaks integrability. The integrable part has an extensive number of conserved quantities, therefore it will always keep memory of the initial state which is a signature of non-thermalization. On the other hand, a non-integrable system is expected to thermalize according to Eigenstate Thermalization Hypothesis [12, 55–59]. Thus, a near-integrable system first relaxes to a quasi steady-state, the non-thermal fixed point, which is universally described by the General Gibbs ensemble of the integrable part. At much later times, the integrability-breaking perturbation leads to thermalization in a non-universal fashion.

Is the universal relaxation observed in this work related to prethermalization? At first glance, a general Heisenberg XXZ Hamiltonian seems to be not divisible in a non-integrable part and a small perturbation. However, as we have revealed in the previous section, relaxation dynamics is well captured by a non-interacting ensemble of pairs for sufficiently disordered spin systems. In the framework of prethermalization, the description in terms of pairs would then provide the integrable part of the Hamiltonian, the interaction between pairs would be the integrability-breaking perturbations. Strikingly, the description of the dynamics in terms of pairs is not only valid at early times, but it agrees well with the data for the whole relaxation of the magnetization, which lasts for over three decades in time. This coincides with the main consequence of prethermalization that the system stays at the non-thermal fixed point defined by the integrable part of the Hamiltonian for long times before reaching thermal equilibrium. Indeed, recent studies have found signatures for localization and the absence of thermalization even at times much larger than the relaxation times of the magnetization [60, 61].

VI. CONCLUSION

Our work demonstrates the ability of Rydberg atom quantum simulators to synthesize a variety of many-body Hamiltonians on a single experimental platform. By choosing the appropriate state combination, we real-

ized XX-, XXZ-, and for the first time, a quantum Ising model within the Rydberg manifold. This versatility of the platform has enabled us to directly study and compare the relaxation dynamics of three different quantum spin systems far-from-equilibrium.

We have observed universal relaxation dynamics, i.e. dynamics independent of the microscopic details of the system after appropriate rescaling, in strongly disordered Heisenberg quantum spin systems which can be explained by an effective description of the system in terms of small localized clusters. This explanation of universality due to an emergent integrability appears to be consistent with the concept of prethermalization. To confirm this interpretation of the dynamics, a strong-disorder renormalization group treatment might directly reveal possible universality classes. We are currently pursuing first attempts into this direction. Experimentally, further investigations could reveal whether the relaxation of disordered quantum spin systems is also universal with respect to different initial states, or whether the energy density of the initial state affects the dynamics, indicative of a possible phase transition [62]. In addition, the measurement of higher-order correlation functions will shed further light on the dynamics and might reveal whether localized pairs remain stable or delocalize at late times.

ACKNOWLEDGMENTS

We thank Andre Salzinger and Annika Tebben for important contributions to maintaining the experimental apparatus, and Eduard Braun for helpful support at a late stage of the experiment. Furthermore, we thank Hengyun Zhou, Nathan Leitao, and Leigh Martin for helpfull discussions. This work is part of and supported by the Deutsche Forschungsgemeinschaft (DFG, German Research Foundation) under Germany's Excellence Strategy EXC2181/1-390900948 (the Heidelberg STRUCTURES Excellence Cluster), within the Collaborative Research Centre "SFB 1225 (ISOQUANT)," the DFG Priority Program "GiRyd 1929," the European Union H2020 projects FET Proactive project RySQ (Grant No. 640378), and FET flagship project PASQuanS (Grant No. 817482), and the Heidelberg Center for Quantum Dynamics. T. F. acknowledges funding by a graduate scholarship of the Heidelberg University (LGFG).

Appendix A: Details on experiment

In the main text, we have highlighted that the typical timescale of the relaxation is given by the pair oscillation frequency $|J_{\parallel} - J_{\perp}|$. For the Heisenberg XXZ Hamiltonian, both exchange and Ising interactions exist. Therefore, another possibility of rescaling would only involve $J_{\perp}$ which would disregard the anisotropy $\delta = J_{\parallel}/J\perp$. In Figure 4, we have compared both possibilities of rescaling time. The rescaling by the oscillation frequency shows a more precise collapse of the experimental data. This demonstrates that this frequency indeed determines the relevant timescale of the system. In addition, this indicates that the Rydberg interactions can be mapped onto the Heisenberg XXZ Hamiltonian with $\delta = -0.7$.

In Fig. 5, we show the sensitivity of the DTWA simulations to different densities and blockade radii. For most simulations, these parameters have only a small, quantitative effect on the simulated dynamics. A notable exception is the Ising system. Here, the Rydberg cloud is largely saturated and the blockade radius is the relevant length scale of the system. Therefore, a variation of the blockade radius changes drastically the early time dynamics. In contrast, the density of the sample featuring XX-interaction is low, therefore the blockade effect can be neglected. For the Heisenberg XXZ Hamiltonian, the simulations show that the blockade radius of 8.3 µm fits the observed dynamics slightly better than the value of 10 µm expected from the simplified excitation model assuming no phase noise of the laser.

[1] M. Heyl, A. Polkovnikov, and S. Kehrein, Physical Review Letters **110**, 135704 (2013).
[2] J. Zhang, G. Pagano, P. W. Hess, A. Kyprianidis, P. Becker, H. Kaplan, A. V. Gorshkov, Z.-X. Gong, and C. Monroe, Nature **551**, 601 (2017).
[3] H. Bernien, S. Schwartz, A. Keesling, H. Levine, A. Omran, H. Pichler, S. Choi, A. S. Zibrov, M. Endres, M. Greiner, V. Vuletić, and M. D. Lukin, Nature **551**, 579 (2017).
[4] M. Serbyn, D. A. Abanin, and Z. Papić, Nature Physics **17**, 675 (2021).
[5] D. Bluvstein, H. Levine, G. Semeghini, T. T. Wang, S. Ebadi, M. Kalinowski, A. Keesling, N. Maskara, H. Pichler, M. Greiner, V. Vuletić, and M. D. Lukin, Nature **604**, 451 (2022).
[6] D. A. Abanin, E. Altman, I. Bloch, and M. Serbyn, Reviews of Modern Physics **91**, 021001 (2019).
[7] J. Smith, A. Lee, P. Richerme, B. Neyenhuis, P. W. Hess, P. Hauke, M. Heyl, D. A. Huse, and C. Monroe, Nature Physics **12**, 907 (2016).
[8] M. Schreiber, S. S. Hodgman, P. Bordia, H. P. Lüschen, M. H. Fischer, R. Vosk, E. Altman, U. Schneider, and I. Bloch, Science **349**, 842 (2015).
[9] A. Lukin, M. Rispoli, R. Schittko, M. E. Tai, A. M. Kaufman, S. Choi, V. Khemani, J. Léonard, and M. Greiner, Science **364**, 256 (2019).
[10] J.-y. Choi, S. Hild, J. Zeiher, P. Schauß, A. Rubio-Abadal, T. Yefsah, V. Khemani, D. A. Huse, I. Bloch, and C. Gross, Science **352**, 1547 (2016).
[11] A. Polkovnikov, K. Sengupta, A. Silva, and M. Vengalattore, Reviews of Modern Physics **83**, 863 (2011).
[12] M. Ueda, Nature Reviews Physics **2**, 669 (2020).
[13] P. Peng, C. Yin, X. Huang, C. Ramanathan, and P. Cappellaro, Nature Physics **17**, 444 (2021).

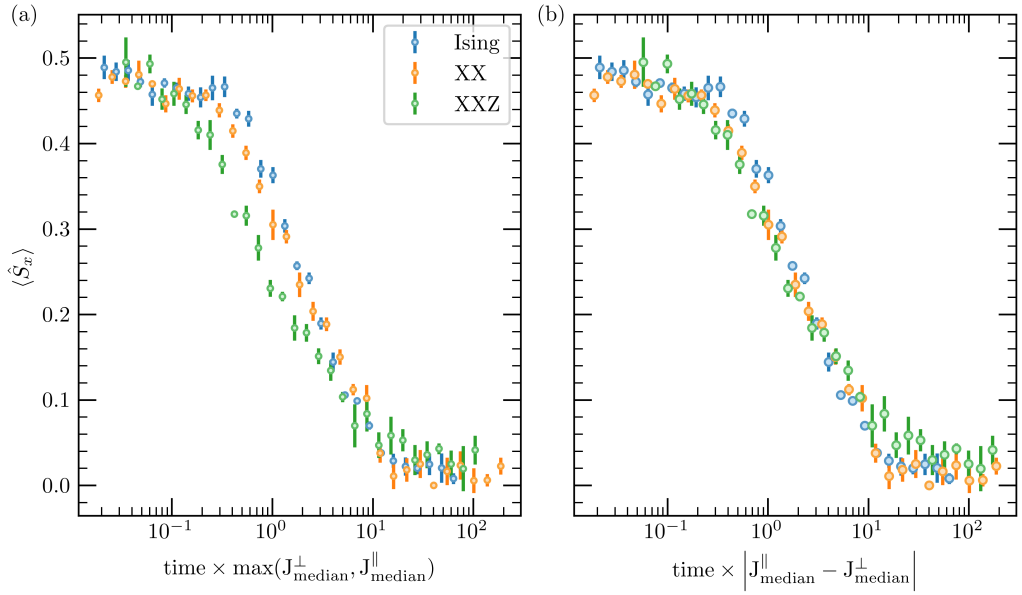

FIG. 4. Comparison of the scaling behavior for rescaling time either by the median interaction matrix (a) or by the median of the pair oscillation frequency (b). $\max(J^{\perp}_{\text{median}}, J^{\parallel}_{\text{median}})$ is defined as $J^{\perp}_{\text{median}}$ for the Heisenberg XX and XXZ model, and as $J^{\perp}_{\text{median}}$ for the Ising model.

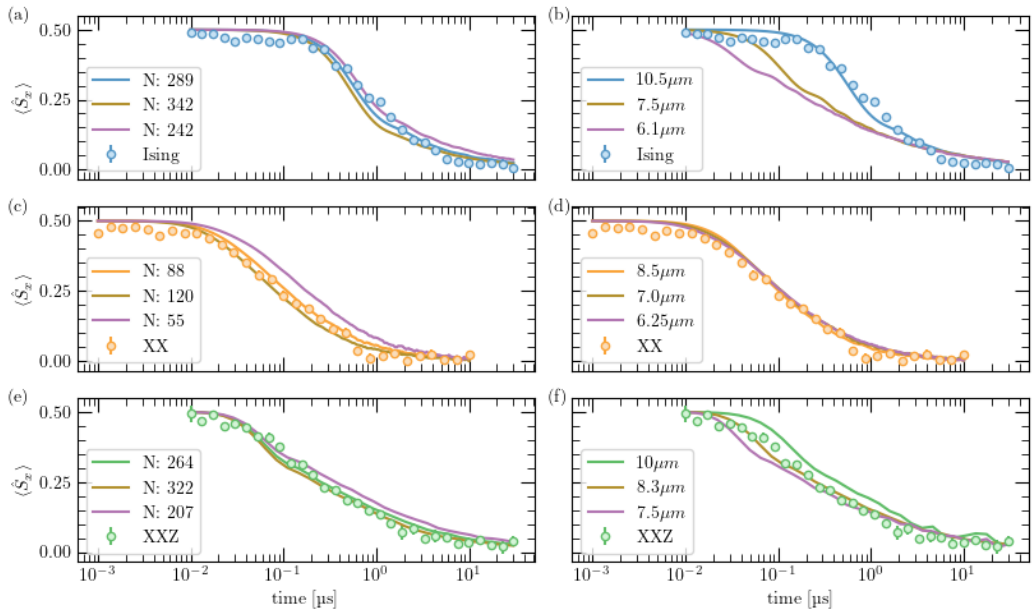

FIG. 5. Influence of the density and the blockade radius on the DTWA simulations.

[14] M. Prüfer, P. Kunkel, H. Strobel, S. Lannig, D. Linnemann, C.-M. Schmied, J. Berges, T. Gasenzer, and M. K. Oberthaler, Nature **563**, 217 (2018).

[15] A. Rubio-Abadal, M. Ippoliti, S. Hollerith, D. Wei, J. Rui, S. Sondhi, V. Khemani, C. Gross, and I. Bloch, Physical Review X **10**, 021044 (2020).

[16] C. Eigen, J. A. P. Glidden, R. Lopes, E. A. Cornell, R. P. Smith, and Z. Hadzibabic, Nature **563**, 221 (2018).

[17] G. Benettin, R. Livi, and G. Parisi, Large Deviations in Physics , 29 (2014).

[18] M. Bernaschi, A. Billoire, A. Maiorano, G. Parisi, and F. Ricci-Tersenghi, Proceedings of the National Academy of Sciences **117**, 17522 (2020).

[19] S. A. Parameswaran, A. C. Potter, and R. Vasseur, An-

nalen der Physik **529**, 1600302 (2017).
[20] A. Signoles, T. Franz, R. Ferracini Alves, M. Gärttner, S. Whitlock, G. Zürn, and M. Weidemüller, Physical Review X **11**, 011011 (2021).
[21] J. Choi, S. Choi, G. Kucsko, P. C. Maurer, B. J. Shields, H. Sumiya, S. Onoda, J. Isoya, E. Demler, F. Jelezko, N. Y. Yao, and M. D. Lukin, Physical Review Letters **118**, 093601 (2017).
[22] G. Kucsko, S. Choi, J. Choi, P. Maurer, H. Zhou, R. Landig, H. Sumiya, S. Onoda, J. Isoya, F. Jelezko, E. Demler, N. Yao, and M. Lukin, Physical Review Letters **121**, 023601 (2018).
[23] C. Sommer, G. Pupillo, N. Takei, S. Takeda, A. Tanaka, K. Ohmori, and C. Genes, Physical Review A **94**, 053607 (2016).
[24] N. Takei, C. Sommer, C. Genes, G. Pupillo, H. Goto, K. Koyasu, H. Chiba, M. Weidemüller, and K. Ohmori, Nature Communications **7**, 13449 (2016).
[25] J. Klafter and M. F. Shlesinger, Proceedings of the National Academy of Sciences **83**, 848 (1986).
[26] P. Schultzen, T. Franz, S. Geier, A. Salzinger, A. Tebben, C. Hainaut, G. Zürn, M. Weidemüller, and M. Gärttner, Physical Review B **105**, L020201 (2022).
[27] P. Schultzen, T. Franz, C. Hainaut, S. Geier, A. Salzinger, A. Tebben, G. Zürn, M. Gärttner, and M. Weidemüller, Physical Review B **105**, L100201 (2022).
[28] I. Bloch, J. Dalibard, and W. Zwerger, Reviews of Modern Physics **80**, 885 (2008).
[29] R. Blatt and C. F. Roos, Nature Physics **8**, 277 (2012).
[30] I. M. Georgescu, S. Ashhab, and F. Nori, Reviews of Modern Physics **86**, 153 (2014).
[31] C. Gross and I. Bloch, Science **357**, 995 (2017).
[32] A. Browaeys and T. Lahaye, Nature Physics **16**, 132 (2020).
[33] D. Jaksch, J. I. Cirac, P. Zoller, S. L. Rolston, R. Côté, and M. D. Lukin, Physical Review Letters **85**, 2208 (2000).
[34] H. Weimer, M. Müller, I. Lesanovsky, P. Zoller, and H. P. Büchler, Nature Physics **6**, 382 (2010).
[35] D. Barredo, H. Labuhn, S. Ravets, T. Lahaye, A. Browaeys, and C. S. Adams, Physical Review Letters **114**, 113002 (2015).
[36] A. P. Orioli, A. Signoles, H. Wildhagen, G. Günter, J. Berges, S. Whitlock, and M. Weidemüller, Physical Review Letters **120**, 063601 (2018).
[37] R. Nandkishore and D. A. Huse, Annual Review of Condensed Matter Physics **6**, 15 (2015).
[38] K. Slagle, Y. Z. You, and C. Xu, Physical Review B **94**, 014205 (2016).
[39] v. Bijnen, R.M.W., *Quantum Engineering with Ultracold Atoms*, Phd Thesis 1 (Research TU/e / Graduation TU/e), Technische Universiteit Eindhoven, Eindhoven (2013).
[40] S. Whitlock, A. W. Glaetzle, and P. Hannaford, Journal of Physics B: Atomic, Molecular and Optical Physics **50**, 074001 (2017).
[41] M. D. Lukin, M. Fleischhauer, R. Cote, L. M. Duan, D. Jaksch, J. I. Cirac, and P. Zoller, Physical Review Letters **87**, 037901 (2001).
[42] G. G. Emch, Journal of Mathematical Physics **7**, 1198 (1966).
[43] C. Radin, Journal of Mathematical Physics **11**, 2945 (1970).
[44] J. Schachenmayer, A. Pikovski, and A. M. Rey, Physical Review X **5**, 011022 (2015).
[45] R. Vosk and E. Altman, Physical Review Letters **110**, 067204 (2013).
[46] D. Pekker, G. Refael, E. Altman, E. Demler, and V. Oganesyan, Physical Review X **4**, 011052 (2014).
[47] R. Vasseur, A. C. Potter, and S. A. Parameswaran, Physical Review Letters **114**, 217201 (2015).
[48] R. Vasseur, A. J. Friedman, S. A. Parameswaran, and A. C. Potter, Physical Review B **93**, 134207 (2016).
[49] P. Scholl, H. J. Williams, G. Bornet, F. Wallner, D. Barredo, L. Henriet, A. Signoles, C. Hainaut, T. Franz, S. Geier, A. Tebben, A. Salzinger, G. Zürn, T. Lahaye, M. Weidemüller, and A. Browaeys, PRX Quantum **3**, 020303 (2022).
[50] K. R. A. Hazzard, B. Gadway, M. Foss-Feig, B. Yan, S. A. Moses, J. P. Covey, N. Y. Yao, M. D. Lukin, J. Ye, D. S. Jin, and A. M. Rey, Physical Review Letters **113**, 195302 (2014).
[51] L. P. Kadanoff, W. Götze, D. Hamblen, R. Hecht, E. A. S. Lewis, V. V. Palciauskas, M. Rayl, J. Swift, D. Aspnes, and J. Kane, Reviews of Modern Physics **39**, 395 (1967).
[52] H. E. Stanley, Rev. Mod. Phys. **71**, 9 (1999).
[53] S. Sachdev, *Quantum Phase Transitions*, 2nd ed. (Cambridge University Press, 2011).
[54] T. Langen, T. Gasenzer, and J. Schmiedmayer, Journal of Statistical Mechanics: Theory and Experiment **2016**, 064009 (2016).
[55] J. M. Deutsch, Physical Review A **43**, 2046 (1991).
[56] M. Srednicki, Physical Review E **50**, 888 (1994).
[57] M. Srednicki, Journal of Physics A: Mathematical and General **32**, 1163 (1999).
[58] M. Rigol, V. Dunjko, and M. Olshanii, Nature **452**, 854 (2008).
[59] L. D'Alessio, Y. Kafri, A. Polkovnikov, and M. Rigol, Advances in Physics **65**, 239 (2016), arXiv:1509.06411.
[60] T. Franz, S. Geier, C. Hainaut, A. Signoles, N. Thaicharoen, A. Tebben, A. Salzinger, A. Braemer, M. Gärttner, G. Zürn, and M. Weidemüller, (2022), 10.48550/ARXIV.2207.14216.
[61] A. Braemer, T. Franz, M. Weidemüller, and M. Gärttner, "Pair localization in dipolar systems with tunable positional disorder," (2022), arXiv:2207.14474 [cond-mat, physics:quant-ph].
[62] L. Rademaker and D. A. Abanin, Physical Review Letters **125**, 260405 (2020).

5 CONCLUSION

PATH TO EQUILIBRIUM OF DISORDERED QUANTUM SPIN SYSTEMS

Part I of this thesis has investigated how isolated quantum spin systems relax towards equilibrium, where we have discovered that disorder induces slow, glassy dynamics, which is largely independent of microscopical details like the type of Hamiltonian or the strength of disorder up to a critical value.

In the following, we aim to map a general path towards equilibrium for disordered quantum spin systems. We will argue that a simplified model which only considers pairs of spins is sufficient to explain the main features of the relaxation, especially the observed universality. Finally, we will discuss the relation of the here studied disordered quantum spin system to spin glasses.

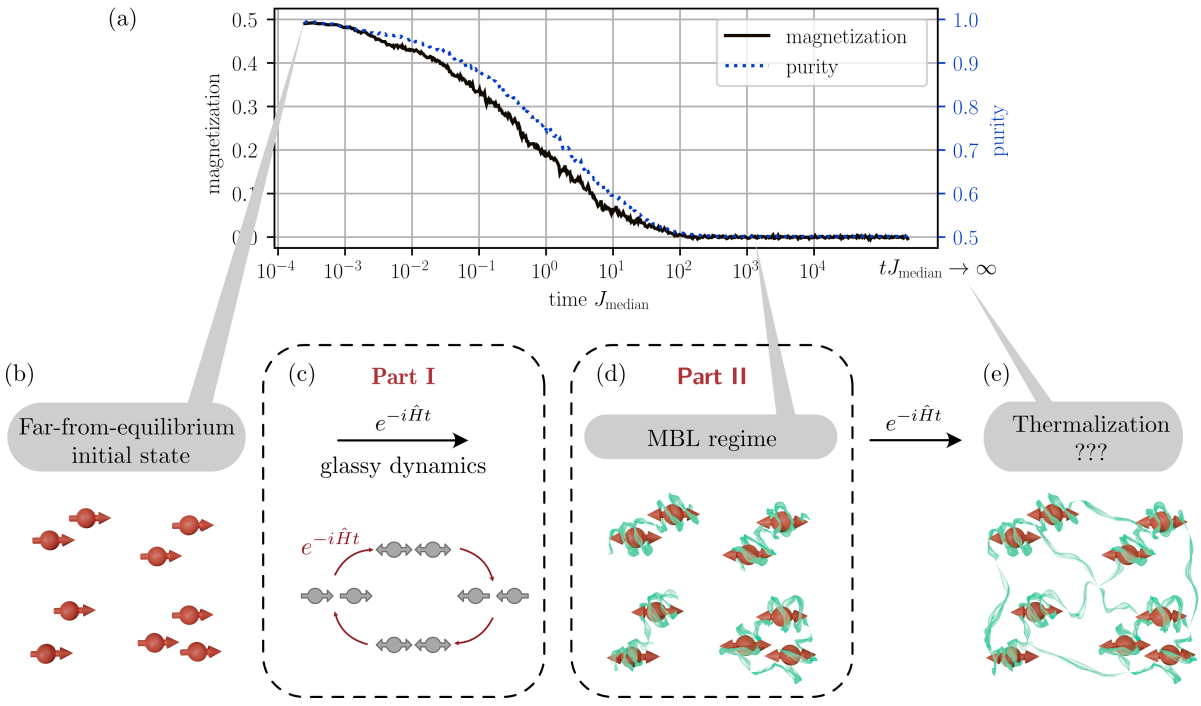

Figure 5.1: Relaxation dynamics of a disordered quantum spin system. (a) Simulation of the relaxation of the magnetization (solid black line) and the ensemble-averaged single-spin purity (dotted blue line) of 14 spins in the limit of strong disorder ($r_{\text{bl}} = 0.1 r_{\text{max}}$ following the notation from Article [4]). (b) The far-from-equilibrium initial state is a disordered sample of spins aligned in x-direction. (c) The time evolution features slow, glassy dynamics which can be qualitatively captured by an ensemble of pairs of spins, each oscillating at a specific frequency. (d) At late times, the magnetization and single-spin purity has relaxed to zero. However, this state is not compatible with a thermal ensemble description and is therefore labeled as an MBL regime. (e) It is still an open question whether the system might reach thermal equilibrium in the thermodynamic limit at infinite late times and infinite system size.

Figure 5.1 (a) shows the numerically calculated time evolution of a disordered system (similar to Figure 1 in Article [1]), and the sketches in Figure 5.1 (b) to (e) outline the path a disordered quantum system takes on its way toward a steady state. Initially (Figure 5.1 (b)), the system is prepared in the fully polarized state (magnetization $\langle \hat{S} \rangle_x = 0.5$), where all spins are aligned in the x-direction. Because this is a product state, this state has zero entropy or, equivalently, the purity of each subsystem is maximal. The fully polarized initial state is a steady state within mean-field prediction: In this approximation, the spins generate a mean-field that is aligned in the direction of the spins, which locks the spins instead of inducing spin rotations. Therefore, a mean-field or equivalently classical approximation predicts no dynamics of the magnetization for this initial state. Any dephasing mechanism where spins are rotated in individual directions that occur, for example, in NMR systems [129] or NV centers [117] due to inhomogeneities in the external field, is absent. Therefore, any dynamics observed for the fully polarized initial state can be attributed to the build-up of entanglement.

In this thesis, we could qualitatively explain the time evolution of the disordered quantum system by a collection of pairs of spins (see Article [4]). These oscillate collectively between product states, where both spins are aligned, and maximally entanglement Bell states (Figure 5.1 (c)). Due to disorder, the timescales of these oscillations follow a scale-invariant distribution which leads to a subexponential, glassy relaxation that lasts multiple orders of magnitude in time (solid black line in Figure 5.1 (a)). This subexponential relaxation can be described as a stretched exponential decay with stretching exponent $\beta < 1$. At later times, different pairs of spins additionally start to interact with each other. As a result, the pair oscillations lose coherence, and the single-spin purity relaxes to its minimal value of $\langle S_x^2 \rangle = 1/2$ for each spin (dashed blue line in Figure 5.1 (a)). The ensemble-averaged single-spin purity also follows a stretched exponential relaxation with the same stretching exponent as the magnetization, which can also be attributed to a scale-invariant distribution of timescales. The anomalously slow relaxation of the magnetization represents one possibility of how ergodicity can be broken in isolated quantum systems. Since ergodicity is only meaningfully defined for a steady state, the system remains non-ergodic during the relaxation, which continues for multiple decades.

In Part II of this thesis, we will explore whether the system becomes ergodic at late times when both magnetization and single-spin purity have relaxed to zero (Figure 5.1 (d-e)).

UNIVERSAL RELAXATION DYNAMICS IN THE VIEW OF PRETHERMALIZATION AND RENORMALIZATION GROUP THEORY

The main discovery of this part of the thesis is the insensitivity of this relaxation with respect to disorder (Article [1] and [2]) and the type and symmetry of the Hamiltonian (Article [3] and [4]). These findings are also independent of the type of simulations, we could show qualitatively similar relaxation dynamics in semiclassical DTWA simulations, in cluster expansion methods like MACE, in the analytical Emch-Radin solution of the quantum Ising model, and also in the quantum simulation of the Rydberg experiment. In the following, we discuss how this universality can be explained by the existence of localized clusters which leads to an emergent integrability of the system.

As a first signature of universality, we have found that the stretching exponent is independent of the strength of disorder up to a critical value. In this regime of disorder, the blockade radius affects only the strongest interacting pairs of atoms. These will depolarize on the fastest timescale and can be integrated out at late times. For the remaining pairs, the blockade effect can be neglected such that they constitute a system that is effectively more disordered. This explains why the late time dynamics agrees with the completely disordered limit.

The second signature of universality is the insensitivity with respect to the type of the Heisenberg XYZ Hamiltonian. This can also be explained by pairs of spins that remain localized throughout the entire duration of the relaxation dynamics. The magnetization of isolated pairs oscillates coherently independent of the type of the Heisenberg XXZ Hamiltonian, only the oscillation frequency differs. Therefore, after rescaling time with this oscillation frequency which is specific to each Hamiltonian, the relaxation dynamics of different types of Hamiltonians collapse onto a single curve.

In addition to explaining the qualitative features of the system like the universal relaxation dynamics, the description in terms of localized pairs also features a good quantitative approximation to the observed dynamics. This approximation can be further improved by MACE simulations that consider slightly larger clusters of spins.

Importantly, this model of the system as an ensemble of isolated clusters is an effectively integrable description of the many-body system. Only at late times, the effective integrability might be broken by higher-order terms, which cause entanglement to grow between different clusters of spins, potentially leading to thermalization at infinite late times (see Part II of this thesis for a more detailed discussion of quantum thermalization). In this view, the description in terms of isolated clusters corresponds to a prethermal, intermediate state. Associated with prethermalization is a notion of universality of the re-

laxation of the intermediate, prethermal state towards asymptotically long times. This relaxation should depend only on few parameters, whereas microscopic details like the blockade radius do not influence the dynamics.

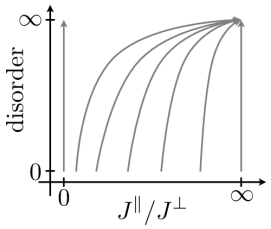

Figure 5.2: Illustration of a possible renormalizaton group flow towards infinite disorder and Ising interactions ($J^{\parallel}/J^{\perp} \to \infty$).

A more general understanding of the universality observed in this thesis could become possible via a disorder real-space renormalization group approach (RSRG) [55, 130, 54, 131, 127]. The description of the many-body system as a non-interacting collection of pairs can be seen as the first step of this method, higher orders would additionally consider the interactions between the pairs. In this approach, the blockaded atoms are integrated out in each step leading to an effective increase of disorder (see Figure 5.2). Additionally, the leading term of the effective Hamiltonian obtained after each RG step would be the Ising interaction [53] such that we can expect a renormalization group flow towards the Ising limit. For future studies, it would be exciting to investigate a minimal disorder strength required for applicability of the disorder RSRG approach and to quantitatively study the RG flow and its implications on the relaxation dynamics.

RELATION TO SPIN GLASSES

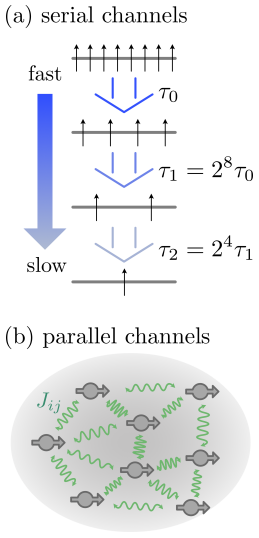

Figure 5.3: Mechanisms leading to glassy dynamics. (a) In case of serial channels, the decay rate is time dependent and becomes slower in time. Adapted from [115]. (b) For parallel channels, different spins relax due to different coupling to their neighbors.

In this part, we have observed a breakdown of ergodicity in disordered quantum spin systems in the sense that the system remains out-of-equilibrium for extensively long times. A similar breakdown of ergodicity can be observed in classical spin glasses, which are also disordered spin systems that relax so slowly that they typically do not reach thermal equilibrium on experimentally accessible timescales [20]. In spin glasses, the interplay of disorder and frustration leads to a rugged free energy landscape with many quasi-degenerate valleys [132, 133]. Spin relaxation can be described within this model as a hierarchical process where the system relaxes from one local minimum to the next, with each step featuring a slower relaxation time [21, 116]. This results in a scale-invariant distribution of relaxation times, that also yields glassy dynamics well described by a stretched exponential law [115]. This mathematical framework of a scale-invariant distribution of timescales is the same in spin glasses and the disordered quantum system discussed in this thesis, but the microscopic origin differs significantly: In spin glasses, the distribution emerges from different timescales occurring sequentially one after another, whereas in this thesis the timescales exist in parallel and can be directly related to the disordered distribution of interaction strengths (see Figure 5.3). In Chapter 9, we will discuss how to prepare initial states at low energy density on the Heidelberg Rydberg experiment, which will pave the way towards further studying the relation to spin glasses by measurements of the response to an external field.

Part II

ABSENCE OF THERMALIZATION

6

INTRODUCTION TO QUANTUM THERMALIZATION AND LOCALIZATION

This part of the thesis explores whether quantum spin systems generically thermalize, or whether strong disorder can lead to localization and the absence of thermalization. In the following, we aim to give a short introduction to classical thermalization, and we will discuss how the Eigenstate Thermalization Hypothesis (ETH) explains quantum thermalization (a more detailed and mathematically rigorous review of thermalization can be found in [134]). Finally, we will derive how the assumptions of ETH are broken in many-body localized (MBL) systems.

Classical thermalization

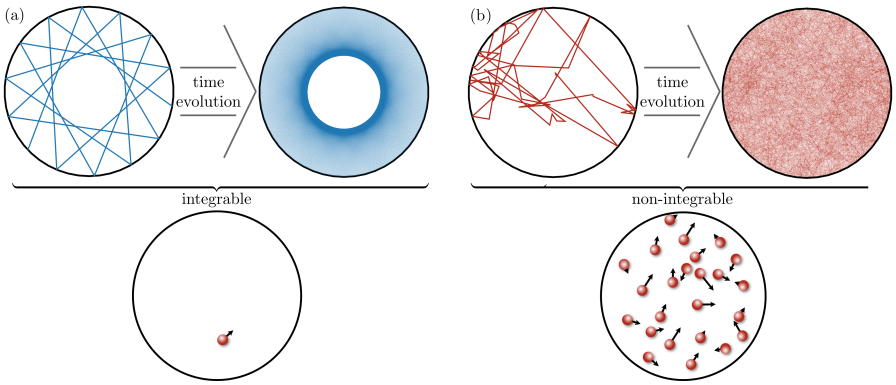

Figure 6.1: Time evolution of a billiard ball that bounces at the boundary of a sphere. (a) A single billiard ball follows regular, non-chaotic dynamics. (b) In a system of 300 balls that collide with each other, the dynamics of the billiard ball becomes chaotic.

In classical systems, two conditions need to be fulfilled such that a system thermalizes. Firstly, the system needs to be *ergodic*, i.e. the system explores all parts of the phase space uniformly. In Figure 6.1, we exemplarily show how a non-linear equation leads to chaotic dynamics which ensures ergodicity: If a system is integrable, like a billiard ball that scatters off the boundary of a perfect circle, the dynamics is non-chaotic (Figure 6.1 (a)). Even at late times, parts of phase space are never reached by the ball. In Figure 6.1 (b), we simulate 300 billiard balls that collide with each other, the red line shows the trajectory of one out of the 300 balls. This trajectory is clearly chaotic, and indeed at late times, the ball has uniformly explored the whole circle.

The second necessary condition for classical thermalization is *typicality*, meaning that the vast majority of microstates share the same macroscopic quantities. For example, most configurations of billiard balls equally occupy the left and the right half circles.

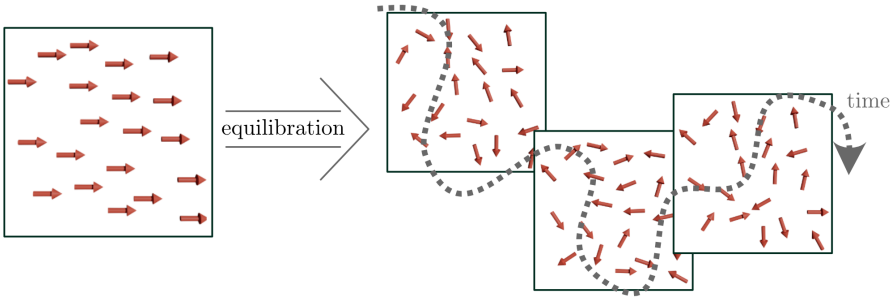

Figure 6.2: Illustration of thermalization of a disordered system of classical spins. Initialized in a polarized state, the spins start to rotate due to spin-spin interactions such that they dephase. In thermal equilibrium, the spins continue to rotate, but the total magnetization remains zero.

If these two conditions of ergodicity and typicality are fulfilled, any classical system will reach thermal equilibrium in the sense that the microscopic degrees of freedom still evolve in time, but all macroscopic quantities are well described by the ensemble average. This thermal equilibrium state is illustrated in Figure 6.2 using the example of classical spins: Starting from a fully polarized state where all spins are aligned in x-direction, the spins are rotated by spin-spin interactions such that the system quickly dephases. In thermal equilibrium, each spin continues to rotate, only the temporal average over the rotation agrees with the thermal expectation of zero magnetization.

Quantum thermalization

In contrast, the dynamics of a quantum systems with Hamiltonian $\hat{H}$ is determined by Schroedinger equation $i\hbar\partial_t |\psi(t)\rangle = \hat{H} |\psi(t)\rangle$. This is a linear equation, thus no notion of chaos in the classical sense can exist. Instead, quantum chaotic systems are defined as systems where the classical analog is chaotic, and they are characterized by a Wigner-Dyson distribution of spacings between eigenenergies [135] or an exponential growth of out-of-time-ordered correlators [136]. This difference between classical and quantum chaos shows that quantum thermalization is inherently different from its classical analog.

The time evolution of a state $|\psi(t)\rangle$ and an operator $\hat{A}$ can be expressed in terms of eigenstates $|\alpha\rangle$ and eigenvalues E_α of $\hat{H}$ as

$$\langle\psi(t)|\hat{A}|\psi(t)\rangle = \sum_{\alpha,\beta} c_\alpha^* c_\beta e^{i(E_\alpha - E_\beta)t} A_{\alpha\beta} \tag{6.1}$$

with $c_\alpha = \langle\psi(t=0)|\alpha\rangle$ and $A_{\alpha\beta} = \langle\alpha|\hat{A}|\beta\rangle$. Under extremely general assumptions, we can assume that the coherences $e^{i(E_\alpha - E_\beta)t}$ in Equation 6.1 dephase such that the system reaches a steady-state given by the *diagonal ensemble* [137]:

$$\langle\hat{A}\rangle_{\text{diagonal}} = \sum_\alpha |c_{\alpha\alpha}|^2 A_{\alpha\alpha} \tag{6.2}$$

where the expectation value is determined by the average over all eigenstate expectation values (EEV) $A_{\alpha\alpha}$ weighted by the eigenstate occupation numbers (EON) $|c_{\alpha\alpha}|^2$. This relaxation to the diagonal ensemble expectation value, the equilibration of the quantum system, is the first necessary condition (condition (1)) for quantum thermalization.

The diagonal ensemble still involves the EONs which contain a lot of information about the initial state. To understand how a quantum system can effectively lose this information and thermalize, we divide the system into a small subsystem s and a large bath $B = \neg s$ (see Figure 6.3). Due to interactions, these two subsystems will become entangled, such that the reduced density matrix ρ^s_ψ is a mixed state. A state is *typical* if the reduced density matrix is almost the same as the density matrix of the microcanonical ensemble

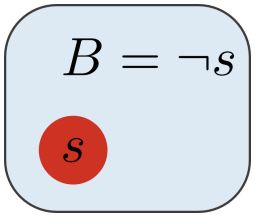

Figure 6.3: Illustration of a system acting as its own bath for the subsystem s. Adapted from [37].

$$\rho^s_\psi \approx \rho^s_{\text{mc}}. \tag{6.3}$$

Canonical typicality requires that almost all states ψ within a given energy shell are typical [138].

Figure 6.4 illustrates how this concept of typicality in quantum systems drastically changes the notion of thermalization compared to the classical systems: Starting from an atypical state which is fully polarized, each spin in a quantum system is expected to build up entanglement with the remaining system. Therefore, it will reach a typical state where the reduced density matrix of each individual spin is a mixed state with zero magnetization expectation value (illustrated by the two-sided arrows). In this sense, the vanishing polarization of a spin in thermal equilibrium is caused by quantum instead of temporal fluctuations.

In order to give a criterion of whether a system thermalizes or not, we need to specify exactly which states are typical. This criterion is the Eigenstate Thermalization Hypothesis (ETH) which asserts that *all* eigenstates are typical [24, 25, 26]. This second condition (condition (2)) necessary for thermalization assures that the eigenstate expectation values of any local operator $A_{\alpha\alpha}$ are a smooth function of energy, i.e. the variance of the EEV is small within a small energy window (see red line in Figure 6.5 (a)). If the initial state is also localized in energy (condition (3)) (see blue line in Figure 6.5 (a)), then the diagonal

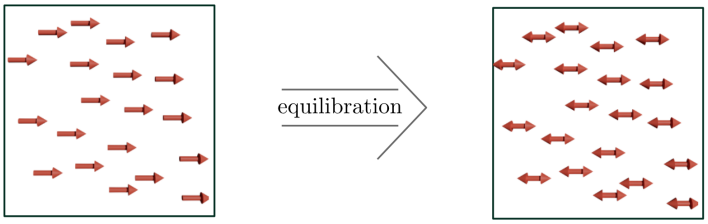

Figure 6.4: Illustration of quantum thermalization. Quantum thermalization can be understood as the time evolution from an atypical state (for example a fully polarized state, left panel), to a typical state (each spin has zero magnetization expectation value, right panel).

ensemble expectation value is equal to the microcanonical ensemble expectation value

$$\langle \hat{A} \rangle_{\text{diagonal}} \stackrel{!}{=} \langle \hat{A} \rangle_{\text{microcanonical}} := \frac{1}{\mathcal{N}_{E_0,\Delta E}} \sum_{\substack{\alpha \\ |E_0 - E_\alpha| < \Delta E}} A_{\alpha\alpha} \tag{6.4}$$

which averages over all eigenstate expectation values within the energy window ΔE centered around E_0 (see green line in Figure 6.5 (b)). The normalization $\mathcal{N}_{E_0,\Delta E}$ counts the number of eigenstates in the energy window. Equation 6.4 explains why expectation values of vastly different initial states with similar energy E_0 relax to the same thermal equilibrium value $\langle \hat{A} \rangle_{\text{mc}}$.

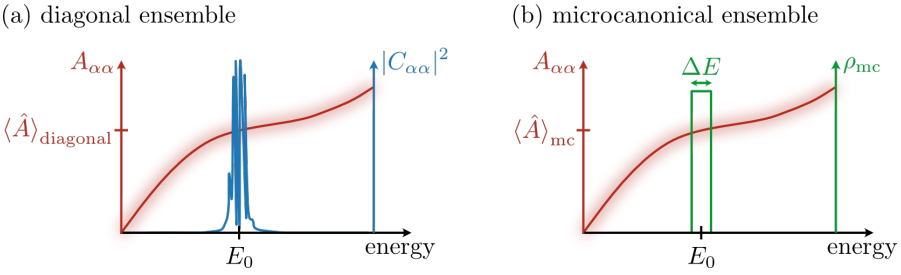

Figure 6.5: Illustration of the calculation of the diagonal (a) and microcanonical (b) ensemble in a system fulfilling ETH. According to ETH, the eigenstate expectation values $A_{\alpha\alpha}$ (red line in (a) and (b)) are a smooth function of energy. In this case, the average of $A_{\alpha\alpha}$ weighted by the eigenstate occupation numbers $|C_{\alpha\alpha}|^2$ (blue line in (a) is the same as the average over all eigenstates within an energy window ΔE centered at E_0(green line in (b)).

ETH is generically expected to hold in non-integrable systems and is supported by various numerical studies of cold atom and spin systems [27, 28]. Even some experimental evidence for ETH exists, where the entanglement was observed to grow as expected from quantum thermalization [29, 139].

If the system features additional conserved quantities beyond the energy like the number of particles, these need to be taken into account

by computing the thermal ensemble expectation values with respect to a grand canonical ensemble. This approach can be even extended to integrable systems possessing an extensive number of conserved quantities. [27, 140]. In this case, ETH is still expected to hold when the microcanonical ensemble is computed only for eigenstates with the same expectation values of the conserved quantities [141].

Many-body localization

A notable exception to ETH is the phenomenon of localization. Already in 1958, P. W. Anderson recognized that, in non-interacting systems, strong disorder can lead to interference effects that suppress diffusion and localize wavepackets at their origin [32] (for a review of Anderson localization, see for example [142]). Strikingly, localization can also occur in interacting systems if the disorder is sufficiently strong [37, 38]. This phenomenon is known as many-body localization (MBL).

To understand how ETH is broken, we investigate transport in a chain of spins initialized in the Néel state $|\psi_{\text{Néel}}\rangle = |\uparrow\downarrow\uparrow\downarrow\ldots\rangle$. To probe whether the system delocalizes, we compute the imbalance $\hat{\mathcal{I}} = \frac{1}{N}\sum_{i=0}^{N-1}(-1)^i \hat{s}_z^{(i)}$ (here, $\hat{s}_z = \hat{\sigma}_z/2$ are spin operators) which is $\langle\hat{\mathcal{I}}\rangle_{\text{Néel}} = 0.5$ for the initial state and zero for a delocalized system. If the system thermalizes according to ETH, we expect that the expectation values $\langle\hat{\mathcal{I}}\rangle_\alpha$ are a smooth function of the eigenenergy for eigenstates α (condition (2)) and that only eigenstates with zero imbalance are occupied (typicality).

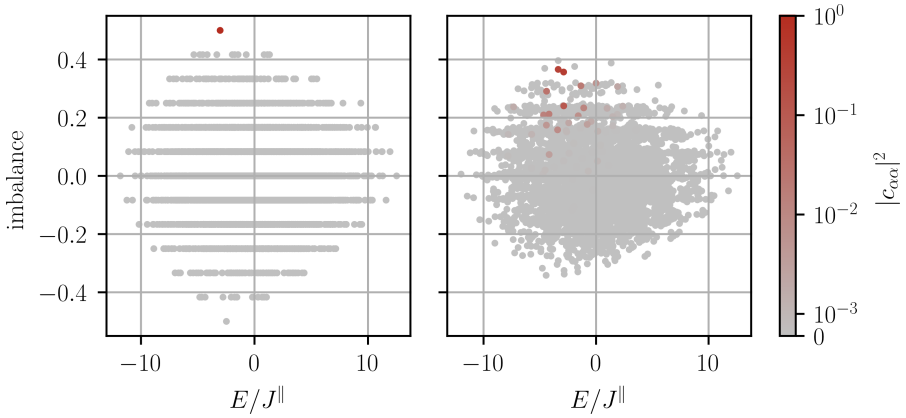

Figure 6.6: Imbalance expectation value of the eigenstates for (a) the integrable Ising model and (b) the non-integrable Heisenberg XXZ model. The color encodes the EON $|c_{\alpha\alpha}|^2$.

We consider the prototypical MBL system, the Heisenberg XXZ model with nearest-neighbor interactions and random longitudinal field $h_i \in [-\Delta, \Delta]$ with $\Delta = 4$

$$\hat{H}_{\text{Ising}} = \sum_{i=0}^{N-1}\left(\frac{J^\perp}{2}\left(\hat{s}_+^{(i)}\hat{s}_-^{(i+1)} + \hat{s}_-^{(i)}\hat{s}_+^{(i+1)}\right) + J^{\parallel}\hat{s}_z^{(i)}\hat{s}_z^{(i+1)} + h_i\hat{s}_z^{(i)}\right). \quad (6.5)$$

In the case of Ising interactions ($J^{\perp} = 0$ and $J^{\parallel} = 1$), this model is symmetric under rotations $\hat{s}_z^{(i)}$, which yields an extensive set of conserved quantities and hence the Ising model is integrable. Therefore, the eigenstates are product states $|\prod_{i=0}^{N-1} \updownarrow^{(i)}\rangle$ ($\updownarrow^{(i)}{=}\uparrow$ if $s_z^{(i)} = 1/2$, else $\updownarrow^{(i)}{=}\downarrow$) are the eigenstates of the conserved quantities $\hat{s}_z^{(i)}$. Figure 6.6 (a) shows both the imbalance and the EON $|c_{\alpha\alpha}|^2$ of each eigenstate. The imbalance $1/N \sum_{i=0}^{N-1} (-1)^i s_z^{(i)}$ of each eigenstate is a multiple of $1/(2N)$, whereas its energy is mostly determined by the strong disordered field term and hence random. Therefore, condition (2) is not fulfilled. Also, the initial state is already an eigenstate with an imbalance of 0.5, hence the state is atypical.

Since the Ising model is integrable, the failure of ETH is expected. To break the integrability, we increase the exchange interaction to $J^{\perp} = 0.5$ in Figure 6.6 (b). Strikingly, the properties of the eigenstate expectation values are only slightly perturbed and condition (2) is still broken. In addition, only a few eigenstates with large imbalances are occupied, so typicality is also not fulfilled for the non-integrable Heisenberg XXZ Hamiltonian. Since only eigenstates with large imbalance are occupied, we can also conclude that the system will remain in a state with a large imbalance, hence the initial state stays localized.

The example of the integrable system has shown us that local conserved quantities are the reason for the absence of thermalization. The MBL system can be seen as a perturbation of the integrable system in the sense that quasilocal integrals of motion (LIOMs) exist [39, 40]. For the prototypical MBL model discussed above, these are given by $\hat{\tau}_z^{(i)} = \hat{U} \hat{s}_z^{(i)} \hat{U}$ where $\hat{U}$ is a quasilocal unitary transformation. If these LIOMs are known, they reveal an effective integrable description of the non-integrable Hamiltonian. This allows us to solve the dynamics of the system and calculate the properties of the eigenspectrum.

In this part of the thesis, we investigate whether ETH holds for Heisenberg XXZ Hamiltonians where the disorder is due to random couplings or whether thermalization can be absent similar to the MBL system discussed above. We also argue that in case of strong disorder in the couplings, the LIOMs are given by the projectors onto localized pairs.

7

PUBLICATIONS

The article *"Absence of Thermalization in an Interacting System of Thousands of Quantum Spins"* (Article [5]) reports on the observation of the absence of thermalization in an isolated system of thousands of quantum spins in a three-dimensional geometry. In contrast to the standard scenario of many-body localization, where disorder is created exclusively by a spatially fluctuating external field [143, 124], in our system disorder emerges intrinsically from the spatial distribution of the quantum spins. This disorder can be tuned by exploiting the Rydberg blockade effect which induces strong spatial correlations in a dense sample allowing to probe both a thermalizing and a localized regime. This observation was possible through the development of a measurement protocol that only relies on the measurement of the dependence of the global magnetization on the strength of an applied spin locking field [144]. The magnetization shows a smooths dependence of the transverse field if the system thermalizes, but it features a sharp cusp, a point of non-analytic behavior, in the absence of thermalization. The benefit of this method is that no spatial resolution is required which was the case in previous experiments probing MBL. The simplicity of this measurement scheme allows to scale the size of the quantum system and enables to study thermalization in three-dimensional systems. Importantly, this approach is readily extendable to other quantum simulator platforms including nuclear spins [145], color centers in diamond [146], polar molecules [147], and magnetic atoms [148, 149].

To understand why thermalization is absent in the experiment, we employ various theoretical investigations. Exact diagonalization of a small ensemble of 14 spins shows qualitatively the same behavior as the experimental observation including the existence of the sharp cusp at strong disorder. Additionally, the numerics allow for studying the properties of the eigenspectrum which resembles the spectrum of the standard MBL system and is contradictory to the ETH. The specific characteristics of the spectrum of the non-thermalizing system can be understood from the existence of strongly interacting pairs which effectively decouple from the rest of the system. To further scrutinize this intuitive understanding, we introduce an effective model which treats the interaction within pairs exactly and the interactions between different pairs within mean-field approximation. This simplified model reproduces all qualitative features of both the experiment and the finite-size simulations, and it can analytically derive the existence of

the cusp feature from a distribution of pairs with random interaction strengths.

Strictly speaking, the results of Article [5] show the absence of thermalization only if an arbitrary small field is applied. This special case of zero external field is investigated in more detail in the article *"Pair localization in dipolar systems with tunable positional disorder"* (Article [6]). Here, we study numerically a one-dimensional system with power-law interactions and disorder due to random couplings with the aim to further establish the hypothesis that strongly interacting pairs are emergent local conserved quantities (LIOMs).

In this study, we have found that in the limit of strong disorder, a description in terms of independent pairs is able to reproduce the half-chain entanglement entropy calculated via exact diagonalization. To directly determine how well the eigenstates are captured by product states of pairs, we have calculated the participation ratio with respect to a pair basis. For strong disorder, the participation ratio increases with system size N with a power-law $1.5^{N/4}$ which is significantly slower compared to a thermalizing system where the participation ratio scales exponentially with system size. The dependence on system size is also small compared to the participation ratio calculated with respect to a product basis which scales with an exponent $N/2$.

Furthermore, Article [6] investigates the crossover between the thermalizing regime at weak disorder and localization at strong disorder. For this purpose, we compute the variance of the half-chain entropy over different disorder realizations for varying disorder strengths and system sizes. The location of the maximum variance determines the crossover between thermalization and localization. This location varies only weakly with system size, and also agrees well with the location of the crossover that we have calculated via the level spacing ratio or the Thouless parameter.

Absence of thermalization in an interacting system of thousands of quantum spins

Titus Franz,[1,*] Sebastian Geier,[1] Clément Hainaut,[1,2] Adrien Signoles,[1,3] Nithiwadee Thaicharoen,[1,4] Annika Tebben,[1] André Salzinger,[1] Adrian Braemer,[1,5] Martin Gärttner,[1,5,6,†] Gerhard Zürn,[1] and Matthias Weidemüller[1,‡]

[1] *Physikalisches Institut, Universität Heidelberg, Im Neuenheimer Feld 226, 69120 Heidelberg, Germany*
[2] *Univ. de Lille, CNRS, UMR 8523–PhLAM–Physique des Lasers, Atomes et Molécules, Lille, France*
[3] *PASQAL, 7 rue Léonard de Vinci, 91300 Massy, France*
[4] *Department of Physics and Materials Science, Faculty of Science, Chiang Mai University, 239 Huay Kaew Road, Muang, Chiang Mai, 50200, Thailand*
[5] *Kirchhoff-Institut für Physik, Universität Heidelberg, Im Neuenheimer Feld 227, 69120 Heidelberg, Germany*
[6] *Institut für Theoretische Physik, Ruprecht-Karls-Universität Heidelberg, Philosophenweg 16, 69120 Heidelberg, Germany*

(Dated: July 29, 2022)

Understanding how closed quantum systems dynamically approach thermal equilibrium presents a major unresolved problem in statistical physics. Generically, it is expected that non-integrable quantum systems thermalize as they comply with the Eigenstate Thermalization Hypothesis (ETH) [1–3]. A notable exception to this is the phenomenon of many-body localization [4, 5], where the emergence of local conserved quantities prevents thermalization, which has been observed in finite low-dimensional systems. We study an ensemble of Heisenberg spins with a tunable distribution of random coupling strengths realized by a Rydberg quantum simulator [6]. The total magnetization as a function of external field after a quench [7, 8] serves as a probe for thermalization. We find that such an isolated quantum system exhibits a non-thermalizing regime despite being non-integrable. It is shown that thermalization can be restored by reducing the disorder in the coupling strengths. As our system consists of up to 4000 spins, we thus show that closed quantum systems can fail to reach thermal equilibrium even at system sizes approaching the thermodynamic limit.

The success and accuracy of statistical mechanics to describe nature rests on the assumption that macroscopic systems quickly relax to thermal equilibrium. This complies with our everyday experience: The ripples on a pond caused by a rock being thrown into it disappear quickly leaving a calm surface. This apparent irreversibility of the macroscopic dynamics, despite the reversible laws describing the microscopic dynamics of the water molecules, is explained through the notion of typicality: Macroscopic observables, like the water flow at a specific point, take the same "typical" value for almost all allowed microstates of the system. Therefore, a system prepared in an atypical state will generically evolve into a typical state just because anything else is extremely unlikely. This notion is also expected to apply to quantum systems, where the microstates of the system are the eigenstates of the Hamiltonian operator. In this case, typicality means that local observables take the same values for all eigenstates consistent with dynamic constraints such as energy conservation [9]. As a result, local observables will generically relax towards equilibrium values which agree with a thermal ensemble description. This mechanism for quantum thermalization has been formalized through the ETH [1–3].

Notably, in disordered systems, the emergence of an extensive number of local conservation laws can invalidate the typicality assumption. As a consequence, quantum thermalization is absent even at infinite times as evidenced by the phenomenon of MBL [4, 5]. While this mechanism is firmly established for finite one-dimensional systems with disorder in external fields, the possibility of the absence of thermalization in systems approaching thermodynamic limit has been questioned [10–12]. In addition, many open questions remain about the possibility of violating ETH in higher dimensional systems [10, 11, 13–15] and for off-diagonal disorder [16–18].

This lack of understanding is rooted in the hardness of solving the out-of-equilibrium dynamics of strongly interacting quantum systems numerically on classical devices and in the scarcity of controlled perturbative approaches. Numerical exact diagonalization is limited to small system sizes of a few tens of particles where finite-size effects strongly affect the study of quantum thermalization [19]. Analytical treatments rely on phenomenological renormalization group approaches which involve uncontrolled approximations [20–23]. Quantum simulation experiments, fully controlled model systems that can be implemented, e.g. in cold atomic gases [6, 24–27], may help to overcome this problem. In these experiments, spatially resolved measurements

* franzt@physi.uni-heidelberg.de
† martin.gaerttner@kip.uni-heidelberg.de
‡ weidemueller@uni-heidelberg.de

can reveal the absence of transport and thereby demonstrate the failure of thermalization [28–31]. As a microscopic probe of thermalization, recent works have focused on the direct detection of entanglement entropy [32–34]. However, relying on full microscopic resolution, again, limits the scalability of these quantum simulations.

In the present work, we show that the absence of thermalization can be probed without the requirement for spatial resolution through macroscopic observables, allowing to scale up accessible system sizes. Specifically, we show that the late-time global magnetization reveals localization effects in a strongly interacting Heisenberg spin-system with transverse field and disordered coupling constants. We find through numerical simulations that the system equilibrates to a steady-state characterized by a sharp cusp at small transverse field, not present in a thermal description of the system. We confirm the persistence of these features in the large system limit through a quantum simulation experiment realizing a Heisenberg spin system in a 3D cloud of thousands of Rydberg atoms. By imposing correlations on the coupling constants, we observe that thermalization is reestablished.

I. THERMALIZATION IN ISOLATED QUANTUM SPIN SYSTEMS

The dynamics of a closed quantum system prepared in a state $|\psi_0\rangle$ is governed by the Schrödinger equation $i\hbar\partial_t |\psi(t)\rangle = \hat{H} |\psi(t)\rangle$ with system Hamiltonian $\hat{H}$. In terms of the eigenstates $|\phi_\alpha\rangle$ and eigenvalues E_α of $\hat{H}$, the time evolution of an observable $\widehat{\mathcal{O}}$ is given by

$$\langle\widehat{\mathcal{O}}\rangle = \langle\psi(t)|\widehat{\mathcal{O}}|\psi(t)\rangle = \sum_{\alpha,\,\beta} c_\alpha^\star c_\beta e^{i(E_\alpha - E_\beta)t}\mathcal{O}_{\alpha\beta}\,, \quad (1)$$

with $\mathcal{O}_{\alpha\beta} = \langle\phi_\alpha|\widehat{\mathcal{O}}|\phi_\beta\rangle$ and $c_\alpha = \langle\psi_0|\phi_\alpha\rangle$.

The system is said to be locally thermalizing if local observables $\langle\widehat{\mathcal{O}}\rangle$ relax to their microcanonical ensemble value $\langle\widehat{\mathcal{O}}\rangle_{\rm mc} = \mathcal{N}_{E_0,\Delta E}^{-1}\sum_{|E_0-E_\alpha|<\Delta E}\mathcal{O}_{\alpha\alpha}$, where $\mathcal{N}_{E_0,\Delta E}$ denotes the number of states within the energy window ΔE around $E_0 = \langle\psi_0|\hat{H}|\psi_0\rangle$, and stay close to it during most times [35].

The following set of conditions is sufficient for thermalization [35]: (i) Local observables equilibrate to the diagonal ensemble value $\langle\widehat{\mathcal{O}}\rangle_d = \sum_\alpha |c_\alpha|^2\mathcal{O}_{\alpha\alpha}$. (ii) The initial state is concentrated in energy, i.e. c_α is significantly different from zero only in a sufficiently small window of the eigenenergies E_α. (iii) ETH holds, i.e. $\mathcal{O}_{\alpha\alpha}$ is an approximately smooth function of E_α [1–3, 36]. Condition (i) applies in generic non-integrable systems, including MBL systems, as the time-dependent (off-diagonal) terms in Eq. (1) average to zero, or dephase, for non-degenerate eigenstates [37]. The latter two conditions guarantee the equivalence between diagonal and microcanonical ensemble. We investigate in the following whether in our system conditions (ii) and (iii) can be violated due to strong disorder which prevents thermalization.

We consider the quantum spin-1/2 Heisenberg XXZ-model (in units where $\hbar = 1$)

$$\hat{H}_{\rm int} = \frac{1}{2}\sum_{i,j} J_{ij}\left(\hat{s}_x^{(i)}\hat{s}_x^{(j)} + \hat{s}_y^{(i)}\hat{s}_y^{(j)} + \delta\hat{s}_z^{(i)}\hat{s}_z^{(j)}\right)\,, \quad (2)$$

with spin operators $\hat{s}_\alpha^{(i)} = \hat{\sigma}_\alpha^{(i)}/2$ ($\alpha \in \{x, y, z\}$) acting on spin i. The interactions between spins decay with a power law $J_{ij} = C_a r_{ij}^{-a}$, where r_{ij} are the distances between the spins i and j. The spins are distributed randomly with an imposed minimal distance $r_{\rm bl}$ resulting in a random but correlated distribution of couplings J_{ij} (Fig. 1a). This geometry is motivated by our experiments where the Rydberg blockade effect forbids two excitations being closer than $r_{\rm bl}$. The blockade constraint allows us to tune the strength of the disorder (illustrated in the insets of Fig. 1 c and d) from $r_{\rm bl} = 0$, corresponding to a fully disordered random system, towards the configuration of close-packing where $r_{\rm bl} = r_{\rm max}$ (see methods).

We initially prepare the system in the fully x-polarized state $|\psi_0\rangle = |{\rightarrow}\rangle_x^{\otimes N} = 2^{-N/2}(|{\uparrow}\rangle + |{\downarrow}\rangle)^{\otimes N}$ which shows no classical dephasing or dynamics in a mean-field description (see appendix H), and observe the dynamics of the average magnetization $\langle\hat{S}_x\rangle = \langle\sum_i \hat{s}_x^{(i)}\rangle/N$. Since this observable is an average over local (single-spin) observables, it should relax to its thermal value if the system is locally thermalizing.

II. MAGNETIZATION AS A PROBE FOR THERMALIZATION

The dashed line in Fig. 1b shows the time evolution of the magnetization in an ensemble of $N = 14$ spins at strong disorder ($r_{\rm bl} = 0.4r_{\rm max}$) and Van-der-Waals interactions ($a = 6$) simulated via exact diagonalization. Note that all data shown in Fig. 1 was averaged over 100 samples of random atom positions to decrease statistical fluctuations from random couplings (see methods). The magnetization relaxes to zero slowly, following a stretched exponential law as discussed in previous work [7, 38, 39], and reaches a steady-state on a time scale of $\sim 10J_{\rm median}^{-1}$ in units of the inverse median nearest neighbor interaction strength. The steady-state value agrees with diagonal and microcanonical ensemble predictions (orange and blue hollow arrows) as all eigenstates already have vanishing x-magnetization due

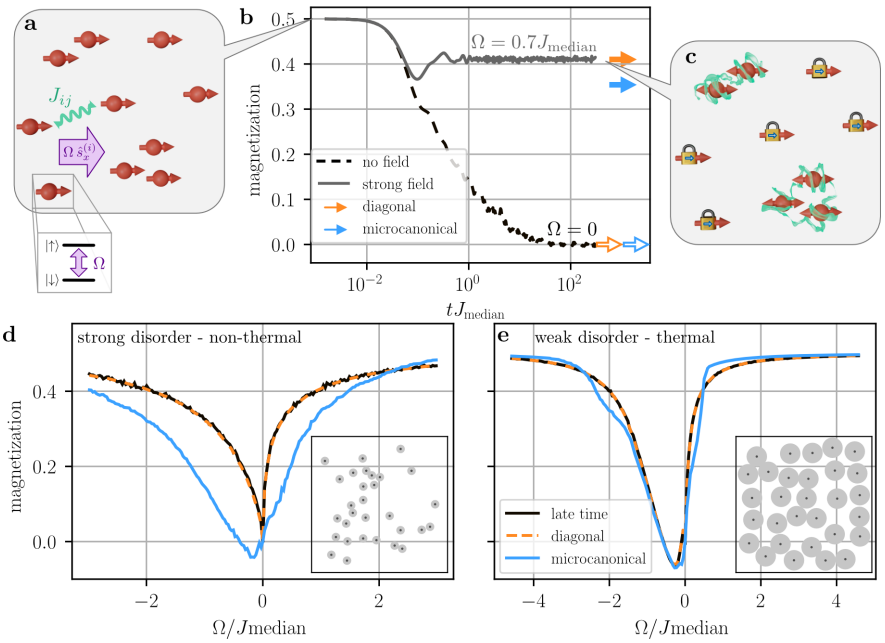

Figure 1. **Heisenberg spin systems in transverse fields. a,** Schematic illustration of the disordered spin system. Spins are positioned randomly and interact via power-law interactions described by Hamiltonian (2) with coupling constants J_{ij}. An external field represented by the violet arrow couples the energy levels of each spin-$\frac{1}{2}$ particle resonantly with a field strength Ω. The phase is chosen such that it corresponds to an external field aligned with the spins in x-direction as described by Hamiltonian (3). **b,** Relaxation of the magnetization of disordered Heisenberg spins without external field (dashed black line) and with an external field of $\Omega = 0.7J_{\text{median}}$ (solid black line). The expectation values obtained by diagonal (orange) and microcanonical (blue) ensembles are indicated with arrows. **c,** Schematic illustration of spin locking and the build-up of entanglement. Spins that are spaced far apart interact weakly, and the external field impedes the relaxation of the magnetization (symbolized by a padlock). On the contrary, strongly interacting spins build up entanglement and become effectively depolarized (represented by the green ribbon). **d** and **e,** Late time magnetization (solid orange line), diagonal ensemble description (dashed black line), and microcanonical ensemble (solid blue line) at $t = 100J_{\text{median}}$ as function of external field Ω/J_{median} for strong (**d**) and weak (**e**) disorder. The numerical simulations are obtained from 100 disorder averages by exact diagonalization of a Heisenberg Hamiltonian of 14 spins which are randomly distributed in a sphere with a minimal distance between the spins of $r_{\text{bl}} = 0.4r_{\text{max}}$ (strong disorder, **c**) and $r_{\text{bl}} = 0.8r_{\text{max}}$ (weak disorder, **d**).

to the conservation of $\sum_i \hat{s}_z^{(i)}$[1]. Hence the apparent relaxation of the magnetization to the thermal value is solely a consequence of the global $U(1)$ symmetry of the Hamiltonian.

This situation changes when adding a homogeneous transverse field term to the Hamiltonian

$$\hat{H}_{\text{ext}} = \Omega \sum_i \hat{s}_x^{(i)}, \tag{3}$$

which breaks the $U(1)$ symmetry. The solid line in Fig. 1b shows the case of $\Omega = 0.7J_{\text{median}}$. The magnetization quickly saturates at a non-zero value consistent with the diagonal ensemble prediction, hence it equilibrates, but is inconsistent with the microcanonical ensemble prediction, hence it does not thermalize.

An intuitive explanation of the spin locking effect leading to the large steady-state magnetization is shown in Fig. 1c. At any finite field strength Ω there will be a competition between the field term and the interaction term in the Hamiltonian. Spins that only interact weakly with their neighbors ($J_{ij} \ll \Omega$) stay polarized due to the spin locking effect [40], causing the magnetization to saturate at a positive value. In the strongly disordered regime, where the blockade radius r_{bl} is small, we will always encounter some pairs of closeby spins that interact very strongly ($J_{ij} \gg \Omega$). These pairs will depolarize and evolve into entangled states, however, they will decouple from the rest of the system as the energy splitting between their eigenstates will typically be much larger than any other terms in the Hamiltonian affecting the pair. This effect hinders further spreading of entanglement which would effectively depolarize the ensemble. A detailed description of this mechanism is found in Appendices H and I where

[1] From the conversation of $\hat{S}_z$, i.e. $[\hat{S}_z, \hat{H}_{\text{int}}] = 0$, it follows that $\langle \hat{S}_x \rangle = -i\langle [\hat{S}_y, \hat{S}_z] \rangle = 0$ for every eigenstate.

a mean-field model explaining the features observed in Fig. 1 is introduced.

Figure 1d shows the dependence of the late-time magnetization on the field strength Ω. We globally find agreement with the diagonal ensemble, meaning that the magnetization equilibrates. However, the microcanonical ensemble prediction deviates for all finite nonzero field strengths [2]. Strikingly, the late-time magnetization is strictly non-negative and shows a non-analytic feature (cusp) at $\Omega = 0$. This non-analyticity contradicts ETH (condition (iii)) where eigenstate expectation values are a smooth function of the eigenergy such that a small perturbation in the external field only leads to a smooth change of magnetization. Indeed, the thermal ensembles predict a smooth Ω-dependence with negative values at small negative fields.

When increasing the blockade radius to $r_{\mathrm{bl}} = 0.8 r_{\mathrm{max}}$ (Fig. 1e), thus decreasing the strength of the disorder, we find that the late-time magnetization agrees reasonably well with thermal ensemble predictions showing that the magnetization does thermalize at weak disorder.

III. EIGENSPECTRUM OF DISORDERED SPIN SYSTEMS

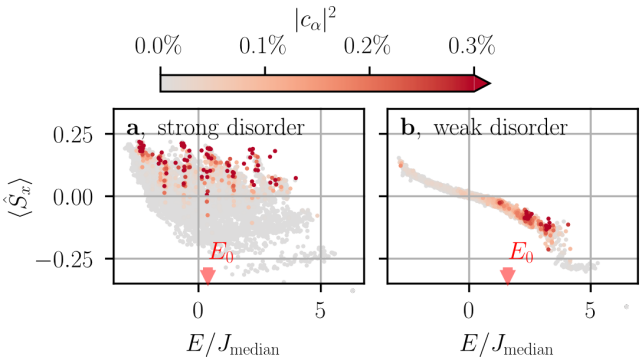

Figure 2. **Eigenstate expectation values for the magnetization and eigenstate occupation numbers.** Magnetization of each eigenstate α for a single disorder realization of 14 spins in a small negative locking field $\Omega = -0.3 J_{\mathrm{median}}$ for strong **a** and weak disorder **b** as defined in Figure 1. The color code shows the overlap $|c_\alpha|^2$ of each eigenstate with the initial state. Additional data like the distributions $\rho(E)$ of the thermal ensembles and the density of states are provided in appendix F.

[2] Note that choosing the canonical ensemble instead of the microcanonical ensemble gives the same predictions as shown in appendix E.

The observed absence of thermalization at strong disorder in numerical simulations of small systems of 14 spins is associated with a breakdown of the ETH. In order to illustrate this point, we analyze the eigenspectrum in Fig. 2. We find that at strong disorder (panel a), the eigenstate populations $|c_\alpha|^2$ (color encoded) are spread out over the entire spectrum, whereas, at weak disorder (panel b), eigenstates are populated mostly around E_0 (indicated by the red arrow). Also, the distribution of eigenstate expectation values $\mathcal{O}_{\alpha\alpha}$ for $\hat{\mathcal{O}} = \sum_i \hat{s}_x^{(i)}/N$ at any given energy is very broad in the case of strong disorder. In contrast, the magnetization expectation values are a smooth function of E_α in the case of weak disorder. We thus conclude that for small spin systems spectral localization of the initial state (ii) and ETH (iii) are violated for strong disorder.

The numerically observed breakdown of ETH can be understood within the simplified picture that spins can either be part of a strongly interacting pair or perfectly pinned by the external field (see Fig. 1 c). Within this picture two eigenstates can have similar energy while largely differing in magnetization because the energy penalty of flipping many spins can be compensated by changing the state of one strongly interacting pair, thus explaining the broad distribution observed in Fig. 2a. Conversely, two eigenstates with similar magnetization can be energetically far separated if they feature a strongly interacting pair in two different eigenstates leading to a large spectral spread of $|c_\alpha|^2$. This shows that the breakdown of ETH is rooted in the existence of strongly interacting pairs that effectively decouple from the rest of the system. Thus, the projectors onto the eigenstates of these pairs take the role of local integrals of motion, which in standard MBL models with random local fields are given by the individual spins [41–43]. We provide a more detailed discussion of the spectral properties in Appendix F.

We conclude from our numerical study that the non-negativity of the late time magnetization and its non-analytic dependence on Ω differ qualitatively from thermal ensemble predictions and are thus a clear sign of disorder-induced failure of thermalization. Many-body localization phenomena are known to be prone to finite size effects [19] which motivates us to probe the persistence of these features at significantly larger system sizes through a quantum simulation experiment.

IV. EXPERIMENTAL SIGNATURES OF BREAKDOWN OF THERMALIZATION

In our experiment, we encode the spin degree of freedom in highly excited Rydberg states $|\downarrow\rangle = |61S\rangle$ and $|\uparrow\rangle = |62S\rangle$ leading to Van-der-Waals interactions as described by Eq. (2) with $\delta = -0.7$, $a = 6$ and $C_6/(2\pi) = 1000\,\mathrm{GHz}\,\mu\mathrm{m}^6$. By coupling the spin states

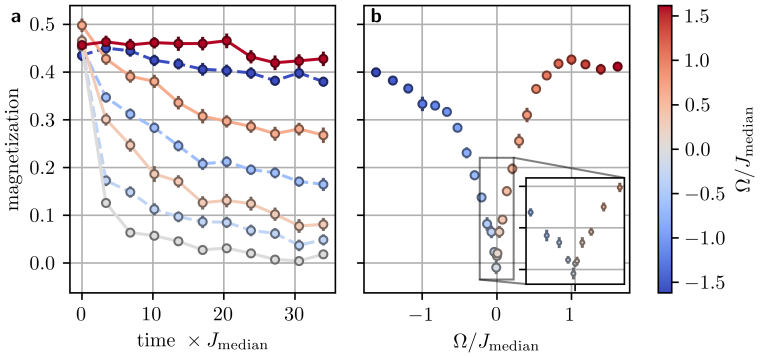

Figure 3. **Relaxation dynamics of the magnetization and late time magnetization as function of the transverse field in a cloud of 3000 spins. a,** Measured spin relaxation dynamcics for Van-der-Waals interactions for varying transverse field strengths ranging from 5.5 MHz (red) to $\Omega = -5.5$ MHz. **b,** Magnetization after 5 µs as a function of field strength Ω for Van-der-Waals interactions. The inset shows a zoom of the magnetization in vicinity of vanishing fields. The data was taken in a cloud of approximately 3000 spins with a median interaction strength of $J_{\mathrm{median}} = 3.4$ MHz.

with a microwave field Ω, we can initialize the spins in the x-polarized initial state $|\psi_0\rangle = |{\rightarrow}\rangle^{\otimes N}$, implement the external field $\hat{H}_{\mathrm{ext}}$ and read out tomographically the final magnetization (see methods for details of the experimental protocol). We choose the density of the Rydberg cloud such that the median interaction strength $J_{\mathrm{median}}/(2\pi) = 6.8$ MHz is large compared to the decay rate of the Rydberg atoms of $\Gamma/(2\pi) = 0.06$ MHz (see methods for more details on the distribution of the Rydberg atoms). At this density, the blockade radius $r_{\mathrm{bl}} = 5.7$ µm is still small compared to the close-packing limit $r_{\mathrm{max}} = 14$ µm, corresponding to the strong disorder regime (see Fig. 1 d).

The dynamics for different field strengths are shown in Fig. 3 a. For $\Omega = 0$ the system fully depolarizes after a few microseconds. For a weak field, the dynamics display the same rapid initial decay over 1 µs followed by slow saturation dynamics up to 10 µs. The saturation value of the magnetization depends on the strength and the sign of the external field which is expected due to the spin locking mechanism explained above. Figure 3b shows the late-time value of the magnetization (taken after 10 µs) as a function of the field strength. This curve features the same characteristics as the diagonal ensemble prediction obtained from exact diagonalization in the case of strong disorder (Fig. 1 d): In particular, we highlight the non-analytic feature at $\Omega = 0$ MHz, which we had identified as inconsistent with thermal ensemble predictions. We thus observe that a system of 3000 spins fails to reach a thermal state on time scales exceeding the typical relaxation time of the system.

V. RESTORING THERMALIZATION IN LONG-RANGE INTERACTING SPIN SYSTEMS

Exploiting the full versatility of the Rydberg platform, we can tune the range of interaction by implementing a dipolar interacting spin system using the Rydberg states $|{\downarrow}\rangle = |48S\rangle$ and $|{\uparrow}\rangle = |48P\rangle$. For the resulting Hamiltonian with $\delta = 0$, $C_3/(2\pi) = 1.15\,\mathrm{GHz\,\mu m^3}$ and a spatial anisotropy $J_{ij}(\theta) = (1 - 3\cos(\theta)^2)/2$, the interaction range $a = 3$ equals the dimension $d = 3$ of the system. Resonance counting arguments suggest that for $a > d$ the system should no longer be localized [17], rendering the critical case $a = d$ a particularly interesting one, even more so as numerical simulations strongly suffer from finite size effects in this case (see appendix G). Our experiments enable us to study this case for system sizes increased more than 100-fold compared to what is accessible numerically.

Fig. 4a shows the late-time dynamics taken after 10 µs for dipolar interaction in the strongly disordered regime of $r_{\mathrm{bl}} = 0.3 r_{\mathrm{max}}$ (time resolved data is provided in appendix B). Interestingly, this curve strongly resembles the case of the Van-der-Waals spin system: At large fields, $\Omega > 2.5$ MHz, compared to $J_{\mathrm{median}} \approx 1.4$ MHz, the magnetization is locked to the initial value. The asymmetry is strongly reduced because the sign of the interaction strength is angular dependent and no longer purely repulsive. Most importantly, the sharp cusp feature has remained unchanged, which suggests the absence of thermalization also in the case of a strongly disordered dipolar system.

Finally, to show that thermalizing behavior is established at weaker disorder, we have saturated the Rydberg excitations in the cloud in a strongly blockaded regime where $r_{\mathrm{bl}} = 0.5 r_{\mathrm{max}}$. In this case, as shown in see Fig. 4 b, the cusp feature disappears and a smooth

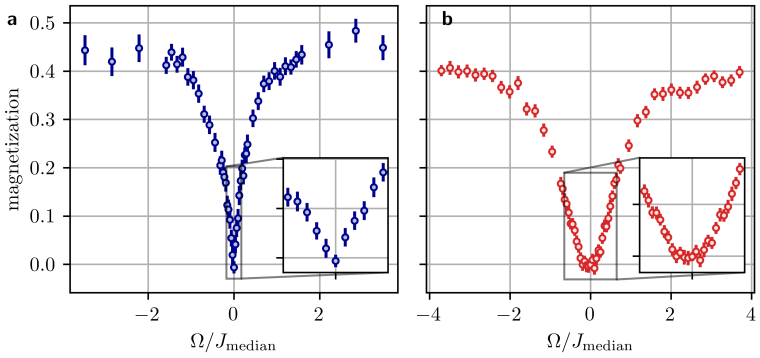

Figure 4. **Late time magnetization for different strength of disorder for a spin system interacting with dipole-dipole interactions**. **a**, At low density ($N = 1150$, $J_{\mathrm{median}} = 1.4\,\mathrm{MHz}$), corresponding to strong disorder ($r_{\mathrm{bl}} = 0.3 r_{\mathrm{max}}$), the late time magnetization exhibits the non-analyticity at zero field Ω expected for a non-thermal system. **b**, In the case of high density ($N = 3900$, $J_{\mathrm{median}} = 2.7\,\mathrm{MHz}$), respectively weak disorder ($r_{\mathrm{bl}} = 0.5 r_{\mathrm{max}}$), the late-time magnetization is a smooth function of the external field Ω, indicating the system to be thermalized.

dependence on the external field strength is recovered, qualitatively agreeing with thermal ensemble predictions.

VI. DISCUSSION AND OUTLOOK

We have observed non-thermalizing dynamics of powerlaw interacting spins with positional disorder by studying late-time magnetization after a quantum quench. The observed magnetization equilibrates rapidly under the unitary dynamics, and thermal ensemble predictions differ qualitatively from the observed late-time values (Appendix J). Recent theoretical works claim that systems with power-law interactions or with dimensions $D > 1$ thermalize due to rare ergodic regions that seed thermalizing avalanches [10, 11, 13–15] in the limit of infinite system sizes and evolution times. Yet, our observations demonstrate the absence of thermalization as expected for a system that is in a MBL phase. Thus, adopting the terminology of [11], we interpret our observation as an MBL *regime*, i.e. localization effects occurring at finite times and system sizes. We also note that the proliferation of thermalization avalanches should depend on the coordination number of the interaction graph (rather than the spatial dimension), which becomes small in the strongly disordered limit of our model [44, 45]. This would be consistent with the reestablishment of thermalization for more strongly correlated coupling constant corresponding to an increased coordination number. The characteristic features of our system, power-law interactions and static positional disorder, are naturally realized by a wide range of quantum simulation platforms beyond Rydberg atoms, including nuclear spins [46], color centers in diamond [47], polar molecules [48] and magnetic atoms [49, 50]. Our work thus paves a way to study quantum thermalization for a largely unexplored type of disordered systems in a scalable fashion.

VII. ACKNOWLEDGEMENTS

We acknowledge Shannon Whitlock, Renato Ferracini Alves, and Asier Piñeiro Orioli for contributing to the preliminary work for this study. We thank Dmitry A. Abanin and M. Rigol for helpful discussions. This work is part of and supported by the Deutsche Forschungsgemeinschaft (DFG, German Research Foundation) under Germany's Excellence Strategy EXC2181/1-390900948 (the Heidelberg STRUCTURES Excellence Cluster), within the Collaborative Research Centre "SFB 1225 (ISOQUANT)," the DFG Priority Program "GiRyd 1929," the European Union H2020 projects FET Proactive project RySQ (Grant No. 640378), and FET flagship project PASQuanS (Grant No. 817482), and the Heidelberg Center for Quantum Dynamics. T. F. acknowledges funding by a graduate scholarship of the Heidelberg University (LGFG). This work is supported by Deutsche Forschungsgesellschaft (DFG, German Research Foundation) under Germany's Excellence Strategy EXC2181/1-390900948 (the Heidelberg STRUCTURES Excellence Cluster). The authors acknowledge support by the state of Baden-Württemberg through bwHPC and the German Research Foundation (DFG) through Grant No. INST 40/575-1 FUGG (JUSTUS 2 cluster).

METHODS

Here we provide further details on the numeric simulations and both the experimental protocol and the spatial configuration of the Rydberg cloud.

Details on numerical simulations. To diagonalize Hamiltonian (2), we take into account the parity symmetry with respect to a global spin-flip $P_s = \prod_i^N \hat{\sigma}_x^{(i)}$ which reduces the dimension of the Hilbert space by a factor of two and ensures that the thermal ensemble calculations only take eigenstates into account states that have the same (positive) spin parity as the initial state $|\psi_0\rangle$[3].

To obtain the microcanonical expectation value, an appropriate energy window Δ_E needs to be chosen. In the thermodynamic limit, the size of this window should vanish $\Delta_E \to 0^+$. However, for finite-size systems, the energy window needs to be finite to ensure that a sufficient number of eigenstates contributes to the microcanonical ensemble. In Fig. 8 in appendix D we compare the microcanonical expectation values for energy windows ranging from $10^{-6} J_{\text{median}}$ to $10^{1} J_{\text{median}}$ and find that the microcanonical ensemble simulation is independent of the energy window Δ_E signifying that the finite window size does not change the microcanonical expectation values.

Details on experimental implementation. We start the experiment by trapping 10^6 Rubidium-87 in a cigar shaped dipole trap with a diameter of 300 µm (long axis) and 70 µm(short axis) at a temperature of 10 µK. We consider this gas to be frozen since the atoms move only a distance of $d_{\text{kin}} = t_{\text{exp}}\sqrt{\frac{3kT}{m}} = 0.5\,\mu\text{m}$ during an experimental cycle of $t_{\text{exp}} = 10\,\mu\text{s}$ which is small compared to the Rydberg blockade radius of $r_{\text{bl}} \approx 5\,\mu\text{m}$. After optically pumping the atoms into the state $|5S(F = 2, m_F = 2)\rangle$, we optically excite the atoms to the spin state $|\downarrow\rangle$ via a two-photon off-resonant excitation process (single-photon detuning of 98 MHz and two-photon Rabi frequency of 1 MHz). A global microwave $\pi/2$-pulse prepares the fully polarized initial state $|\psi_0\rangle = |{\rightarrow_x}\rangle^{\otimes N}$. In the case of Van-der-Waals interactions, the state $|61\rangle\, S$ is coupled resonantly to $|62\rangle\, S$ via a two-photon transition at a microwave frequency of 16.546 GHz which can be directly generated with a Keysight M8190A arbitrary waveform generator (AWG). For the dipolar interacting spin system, we couple the $|48S\rangle$ state resonantly with a single-photon transition at 35 GHz. This frequency is generated by mixing a 5 GHz signal of the Keysight M8190A AWG with an Anritsu MG3697C signal generator. The same microwave setup is used to realize the spin locking field where a phase shift of 90 degrees needs to be added such that the field aligns with the spins. This allows us to implement the transverse field term, Eq. (3), with field strengths up to $\Omega/(2\pi) = 10\,\text{MHz}$. After a time evolution t, the x-magnetization is rotated tomographically onto the z-axis by applying a second $\pi/2$-pulse with various phases. Finally, the magnetization is obtained from a measurement of the population of one of the two spin states via field ionization, and the other spin state is optically deexcited to the ground state. A visual representation of the measurement protocol can be found in appendix A, and a more detailed explanation of the determination of the magnetization was reported in a previous publication [7].

Details on the Rydberg distribution. In this work, we can tune the disorder with the Rydberg blockade effect, which imposes a minimal distance r_{bl} between the spins. At small blockade radius, the spins are distributed randomly in the cloud, while a large radius introduces strong correlation between the atom positions and hence the coupling strength. To quantify the disorder strength, we compare the blockade radius to the distance $r_{\text{max}} = 2[3\eta_{\text{cp}}/(4\pi\rho)]^{1/3}$ which corresponds to the distance between the spins in a close-packed arrangement at same density ρ and packing fraction $\eta_{\text{cp}} = \pi/\sqrt{18} \approx 0.74$.

In our experiment, we tune the spatial distribution of the Rydberg atoms by varying the volume of the ground state atoms with a short time-of-flight period after turning off the dipole trap and before exciting to the Rydberg states. Further, we can alter the Rydberg fraction by modifying the excitation time t_{exc}. We measure the resulting Rydberg density through depletion imaging [51] where we deduce the Rydberg distribution from the ground state atoms that are missing after Rydberg excitation. The measured parameters of the Rydberg distribution are presented in detail in Table I in appendix A.

To estimate the Rydberg blockade radius, we model the excitation dynamics by the simplified description introduced in [7] which assumes a hard-sphere model for the Rydberg blockade effect. This model sets an upper limit on the blockade radius $r_{\text{bl}} = \sqrt[6]{\frac{C_6}{\Gamma_{\text{eff}}}}$ by estimating the effective linewidth of the laser, based on the duration of the excitation pulse and power broadening. The latter is calculated self-consistently, taking into account the enhancement factor induced by collective Rabi oscillations within a superatom [52, 53].

This established model of the Rydberg cloud can be benchmarked using the experimentally measured time evolution without a locking field, which is known to be well described by semiclassical Discrete Truncated Wigner Approximation (DTWA) [7] (see Fig. 7 in ap-

[3] Only Fig. 16 **e - f** also shows both parity symmetric and anti-symmetric eigenstates. To highlight the symmetric eigenstates, these are plotted on top of the anti-symmetric ones.

pendix C). This simulation is highly sensitive to the exact value of the blockade radius, and we can deduce that the hard-sphere model slightly overestimates the Rydberg blockade effect in the case of Van-der-Waals interactions where a fitted value of $r_{\mathrm{bl}} = 5.7\,\mu\mathrm{m} = 0.4 r_{\mathrm{max}}$ describes the experiment perfectly. For the more long-range dipolar interactions, the blockade radius of $r_{\mathrm{bl}} = 6.5\,\mu\mathrm{m} = 0.5 r_{\mathrm{max}}$ is already a reasonable estimate leading to a good agreement between the experiment and DTWA simulation.

From the excitation model, we can also compute the median of the nearest neighbor interaction strength J_{median} which ranges from 0.78 MHz to 3.4 MHz depending on the experimental setting (see table I). The resulting time evolution can be considered unitary for up to $10\mu s$ which is an order of magnitude larger than the timescale of the experiment J_{median}^{-1}.

Appendix A: Illustration of the experimental protocol and parameters

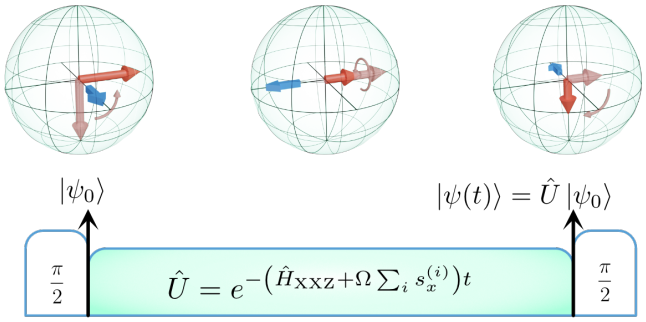

Figure 5. Experimental protocol: An initial $\pi/2$-pulse aligns the spins in x-direction. After unitary dynamics under the interaction Hamiltonian and the locking field, a second $\pi/2$-pulse with varying phases reads out the magnetization in the xy-plane. For each pulse, the Bloch spheres illustrate the spin state of the initial state (light red arrow), the final state (red arrow), and the direction of the external field (blue arrow).

Appendix B: Time evolution of the dipolar interacting spin system

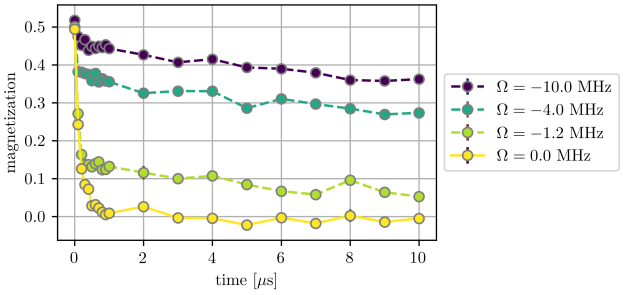

Figure 6. Time evolution of the dipolar interacting spin system. The experimental parameters for the time traces are identical to the quantum simulation shown in Fig. 4 b in the main text.

Analogously to Fig. 3 **a** in the main text, we also measured the time evolution of the magnetization for the dipolar interacting Rydberg spin system in the case of strong disorder for various external fields Ω. The resulting dynamics are shown in Fig. 6. Similar to the case of Van-der-Waals interactions shown in Fig. 3 **a** in the main text, the magnetization relaxes within a microsecond to zero in the case of zero applied field ($\Omega = 0$). With applied field, the dynamics show a rapid decay within the first microsecond, followed by a much slower relaxation until the final magnetization at 10 µs is reached. This late-time magnetization is plotted as a function of the external field in Fig. 4 in the main text.

Appendix C: Semiclassical simulations of the Ramsey decay

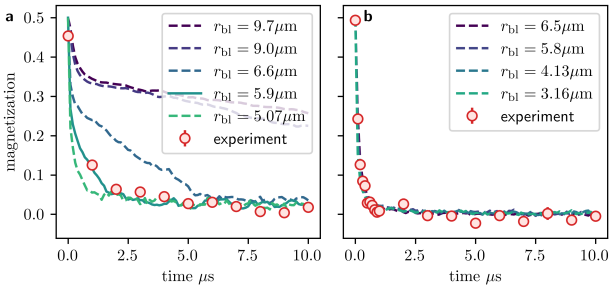

Figure 7. Semiclassical simulations using Discrete Truncated Wigner Approximation (DTWA) in the case of Van-der-Waals interactions (**a**) and dipolar interactions (**b**). The simulations are performed for realistic distributions of the Rydberg spins with the same density as the experiment (red dots), but for varying blockade radii. The maximal blockade radius corresponds to a linewidth of the Rydberg excitation determined by Fourier limit and power broadening. The simulation best fitting the experimental data is plotted as a solid line.

In previous work [7, 54], we could show that the semiclassical Discrete Truncated Wigner Approximation (DTWA) is well suited to describe the relaxation of the magnetization under the interaction Hamiltonian (2) defined in the main text. The main principle of DTWA is to sample classical time evolutions over different initial states such that the quantum uncertainty of the initial state is respected [55]. In Fig. 7, we compare the time evolution obtained from DTWA simulations for various blockade radii (solid lines) to the experimental data (red dots) in the case of Van-der-Waals (panel **a**) and dipolar interactions (panel **b**). It turns out that in the case of Van-der-Waals interactions, the resulting dynamics depend sensitively on the blockade radius, which allows estimating the correct blockade radius to be 5.9 µm. This radius is small compared to the blockade radius of 7.8 µm estimated from power broadening and the Fourier limit determined from the length of the excitation pulse. This discrepancy in expected and simulated blockade radius might be explained by a finite linewidth of the excitation lasers, a small detuning [56] or from underestimated Rydberg-Rydberg interactions. In the case of dipolar interactions, the DTWA dynamics are less sensitive to the size of the

	Van-der-Waals interactions (Figure 3 a and b)	Dipolar interactions (low density) (Figure 4 a)	Dipolar interactions (high density) (Figure 4 b)
t_{exc}	5 µs	1 µs	10 µs
Rydberg volume	69 µm × 43 µm × 37 µm	59 µm × 44 µm × 36 µm	59 µm × 34 µm × 30 µm
N_{Ryd}	2900	1150	3900
r_{bl}	5.7 µm = $0.4r_{\mathrm{max}}$	5.3 µm = $0.29r_{\mathrm{max}}$	6.5 µm = $0.5r_{\mathrm{max}}$
J_{median}	3.4 MHz	0.78 MHz	1.7 MHz

Table I. Experimental parameters. t_{exc} specifies the duration of the optical excitation to the Rydberg state, the Rydberg volume is specified by the radii ($1/e^2$) of the Rydberg cloud, N_{Ryd} denotes the derived Rydberg number, r_{bl} the blockade radius and J_{median} the obtained median nearest-neighbor interaction.

blockade radius. The reason might be the longer-range interactions which cause the dynamics to be less dominated by the nearest neighbors. As a result, the dynamics for a Rydberg distribution with a blockade radius estimated from the Fourier limit agrees already well with the experimental observation.

Appendix D: Sensitivity of the microcanonical ensemble on the energy window

To calculate the magnetization expectation value of the microcanonical ensemble, the average over all eigenstate expectation values within an energy window Δ_E is calculated. In the thermodynamic limit, it is possible to calculate the limit $\Delta_E \to 0$, but for a finite simulation, the energy window has to be chosen small but finite. To ensure that the choice of the energy window does not influence the magnetization expectation value of the microcanonical ensemble, we compare in Fig. 8 **a** the prediction of microcanonical ensembles for a large range of energy windows between $10^{-4}J_{\mathrm{median}}$ and $10^{1}J_{\mathrm{median}}$. Indeed, we find that the simulations agree if the energy window is small enough, i.e. $\Delta_E/J_{\mathrm{median}} < 10^{-3}$. In particular, all curves are smooth and feature a negative magnetization at small negative fields. The existence of this large region of energy windows is a strong hint that the microcanonical expectation value is no longer dependent on details of the finite size system, indicating that the simulation is already converged for 14 spins. Importantly, any microcanonical ensemble prediction differs qualitatively from the diagonal ensemble (red dashed line in Fig. 8 **a**) for *any* choice of Δ_E.

Fig. 8 **b** shows how many eigenstates are populated within a given energy window Δ_E. This quantity is important to ensure that the window size is varied in a meaningful way, i.e. that a different number of eigenstates are populated for different window sizes. For the smallest window, on average less than a single eigenstate is populated [4] which leads to large fluctuations of the magnetization. Contrary, for a large energy window of $10^{1}J_{\mathrm{median}}$, almost all eigenstates are populated by the microcanonical ensemble. Within the region where $\Delta_E/J_{\mathrm{median}} < 10^{-3}$ and the microcanonical ensemble is converged, the number of populated eigenstates varies from 1 to 300 which highlights the insensitivity of the microcanonical ensemble with respect to the width of the energy window.

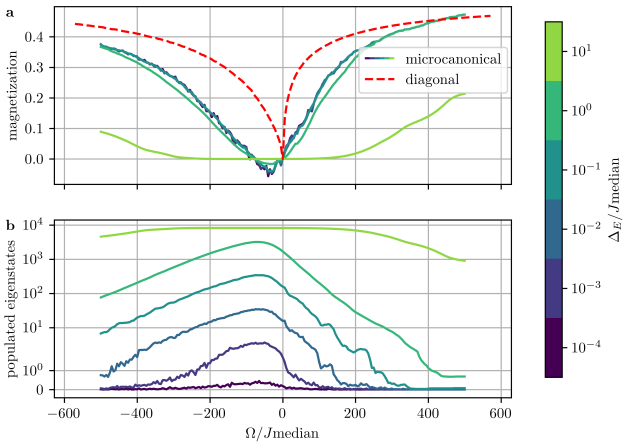

Figure 8. Microcanonical ensemble for different widths of the energy window Δ_E ranging from $10^{-6}J_{\mathrm{median}}$ to $101J_{\mathrm{median}}$. The simulations are performed for the same system parameters as in Figure 1 of the main text (Heisenberg XXZ interactions with anisotropy $\delta = -0.7$, power law interactions $J_{ij} = \frac{C_6}{r^6}$, 100 disorder averages, 14 spins randomly distributed in a sphere with a minimal distance between the spins of $r_{\mathrm{bl}} = 0.4r_{\mathrm{max}}$). **a,** Magnetization as a function of $\Omega/J_{\mathrm{median}}$ for the microcanonical ensembles for different energy windows Δ_E (solid lines) and the diagonal ensemble (dashed red line). **b,** Number of populated eigenstates as a function of $\Omega/J_{\mathrm{median}}$ for different energy windows Δ_E.

[4] If no eigenstate is within the energy window, the algorithm determines the magnetization from the closest eigenstate in energy.

Appendix E: Ensemble equivalence

In this work, we exemplary compute the microcanonical expectation values to show the behavior of a thermal system. It should be noted that one could as well choose the canonical ensemble $\langle\widehat{\mathcal{O}}\rangle_{\mathrm{c}} = Z^{-1}\sum_\alpha \mathcal{O}_{\alpha\alpha}e^{-\beta E_\alpha}$ (with inverse temperature β satisfying $E_0 = \langle\hat{H}\rangle_{\mathrm{c}}$ and partition function Z) as thermal ensembles become equivalent in the limit of large system sizes for short-range interacting systems [9]. Indeed, we find good agreement between the microcanonical ensemble and the canonical ensemble expectation value in the case of both strong and weak disorder (see Fig. 9). This agreement shows that thermal ensemble equivalence already holds at this moderate system size of 14 spins.

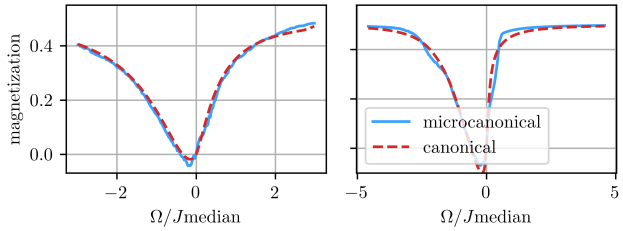

Figure 9. Comparison of the microcanonical (solid blue line) and the canonical ensemble (dashed red line) in the case of strong (panel **a**) and weak disoroder (panel **b**). For each thermal ensemble, the magnetization is plotted as a function of the external field Ω

Appendix F: Spectral properties for varying disorder strength

Figure 10 gives additional details of the simulations shown in Fig. 1 and 2 of the main text. The middle and right columns represent the same simulation as in the main text for the strong and weak disordered systems, respectively.

The left column shows an even more strongly disordered case (smaller blockade radius), where all ensembles mutually disagree. For this very strong disorder, a sawtooth profile is visible where the magnetization in some regions of the spectrum depends linearly on energy (Fig. 10 a). As a consequence of extremely strong interacting pairs, the spectrum is energetically split into far apart blocks. In between, the density of states is zero (Fig. 10 d), which might be a sign of finite-size effects and indicate that the simulation is not yet converged to the thermodynamic limit. To explain how the sawtooth profile of the eigenstate expectation values emerges from disorder, we can consider a simplified scenario of a single strongly interacting pair where $J_{ij}^{\mathrm{strong}} \gg \Omega$ surrounded by N weakly interacting spins

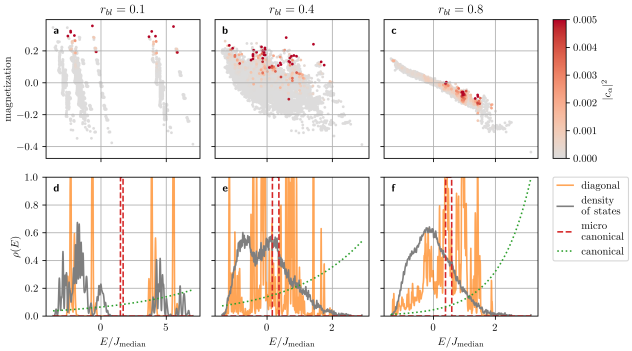

Figure 10. Same as Fig. 2 with three different blockade radii $r_{\mathrm{bl}} = 0.1a_0$ (left column), $r_{\mathrm{bl}} = 0.4a_0$ (central column), and $r_{\mathrm{bl}} = 0.8a_0$ (right column). Top row (**a - c**: Eigenstate expectation value of the magnetization for a single disorder realization at $\Omega = -0.2J_{\mathrm{median}}$ for all eigenstates as a function of eigenenergy. The color encodes the eigenstate occupation $|\langle\psi_0|\phi_\alpha\rangle|^2$. Bottom row (**d - f**): Energy distributions $\rho(E)$ of the diagonal ensemble (solid orange line), microcanonical ensemble (dashed red line), and canonical ensemble (dotted green line) for the same disorder realization and field as in the top row. The solid gray line shows the density of states. The diagonal ensemble and density of states are obtained after a Gaussian kernel density estimation with bandwidth $0.01J_{\mathrm{median}}$, the energy gap of the microcanonical ensemble is $\Delta_E = 0.1J_{\mathrm{median}}$.

where $\Omega \gg J_{ij}^{\mathrm{weak}}$ (see Fig. 1 a and c). To find approximate eigenstates for this system, we may first diagonalize the strongly interacting pair giving rise to two occupied eigenstates separated in energy by J_{ij}^{strong}. The remaining spins can be approximately assumed to be non-interacting leading to 2^N configurations with energies $-\frac{N\Omega}{2}, -\frac{(N-1)\Omega}{2}, \ldots, \frac{(N-1)\Omega}{2}, \frac{N\Omega}{2}$. As a result, the spectrum is divided into two regions, each associated with one of the eigenstates of the strongly interacting pair; Within each region, magnetization is determined by the weakly interacting spins and depends linearly on energy with a slope $\frac{1}{N\Omega}$. In the case where $J_{ij}^{\mathrm{strong}} \approx N\Omega$, this scenario yields two states depicted by Fig. 1c of the main text that features similar eigenenergy but vastly different magnetization. We expect eigenstates where the weakly interacting spins are strongly polarized to share a significant wavefunction overlap with the fully magnetized initial state. However, these states may have completely different eigenenergies due to the internal state of the strongly interacting spins.

The central column shows a slightly less disordered system ("strong disorder" in the main text). Here, the microcanonical and canonical ensemble agree, but they differ from the diagonal one (Fig. 10 e). Like the strongly disordered case depicted in the left column of Fig. 10, strongly interacting pairs induce large variations of the eigenstate expectation values. However, due

to the non-negligible blockade effect, the existence of extremely strong interacting pairs is prohibited. Therefore, the eigenspectrum is not split into clearly distinguishable blocks (Fig. 10 e), and as a consequence, the density of states becomes a smooth function without gaps. This smoothness might be indicative of a reasonable convergence of the simulation. Additional disorder realizations for this case are shown in Fig. 11. Qualitatively, they show very similar behavior, including a large variation of eigenstate expectation values and an extended spread of eigenstate occupation numbers.

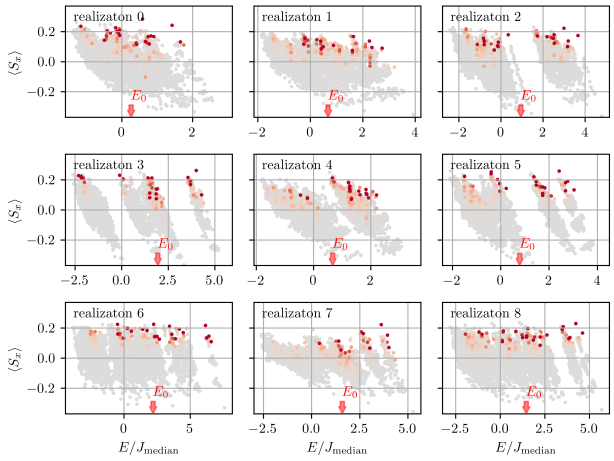

Figure 11. Similar to Fig. 10 b, Eigenstate expectation values of the magnetization for 9 different disorder realizations at $\Omega = -0.2 J_{\mathrm{median}}$ and $r_{\mathrm{bl}} = 0.4 r_{\mathrm{max}}$ for all eigenstates as a function of eigenenergy. The color encodes the eigenstate occupation $|c_\alpha|^2 = |\langle \psi_0 | \phi_\alpha \rangle|^2$.

For weak disorder (right column in Fig. 10), all ensemble predictions agree, which indicates thermalization (Fig. 1 e). Quantum thermalization is confirmed by the eigenspectrum, which shows a smooth dependency of the eigenstate magnetization as a function of eigenenergy (Fig. 10 c) following ETH. Also, the eigenstate occupation (orange line in Fig. 10 f) is clearly peaked at the energy of the initial state as expected in a thermalizing system. However, this peak is still relatively broad compared to the energy window of the microcanonical ensemble (dashed red line in Fig. 10 i). This broadening of the eigenstate occupation number is a well-known finite size effect that is also present in other numerical studies [36].

Appendix G: Numerical simulations for dipolar interactions

The simulations in the main text shown in Fig. 1 and 2 are performed in a Van-der-Waals interacting

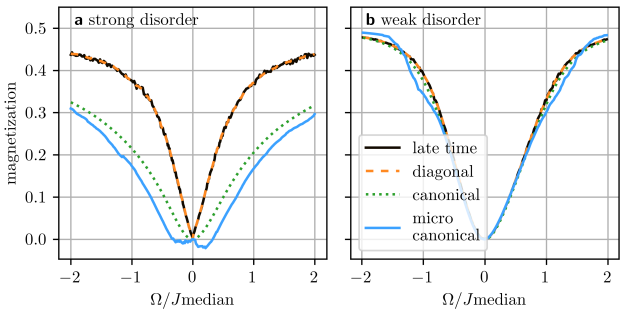

Figure 12. Similar to Fig. 1 **d** and **e** from the main text, but for dipolar interactions. The simulations are also obtained from 100 disorder averages by exact diagonalization of 14 spins, but the blockade radii are chosen differently ($r_{\mathrm{bl}} = 0.01 r_{\mathrm{max}}$ for strong disorder and $r_{\mathrm{bl}} = 0.4 r_{\mathrm{max}}$ weak disorder) to compensate for the more long-range interactions.

system with purely repulsive interactions and a power-law $a = 6$. Changing the system to dipolar interaction modifies these two characteristics: The sign of the interactions becomes dependent on the angle θ between the quantization axis and the interatomic axis proportional to $1 - 3\cos(\theta)^2$ and the interactions are more long-range with $a = 3$. This section will investigate how these changes alter the system dynamics and the steady-state properties.

Fig. 12 compares the late-time magnetization (dashed black line), the diagonal ensemble (solid orange line), the microcanonical ensemble expectation value (solid blue line) and the canonical ensemble (dotted green line) in the case of strong (panel **a**) and weak disorder (**b**). As in the case of Van-der-Waals interactions, the late-time magnetization agrees almost perfectly with the diagonal ensemble for both strong and weak disorders. This agreement shows that the system has equilibrated to a steady-state. Also, we can observe that the thermal ensembles (canonical and microcanonical) agree with the steady-state only in the case of weak disorder. For strong disorder, the thermal ensembles predict a magnetization being consistently lower than the steady-state value. This disagreement indicates, just like in the case of Van-der-Waals interaction, that the system appears to not thermalize at strong positional disorder.

Besides these similarities, the dipolar interacting system behaves in some aspects drastically different compared to the Van-der-Waals interacting spins. Most notably, the magnetization is almost perfectly symmetric with respect to the sign of the applied external field. This is explained by the spatial anisotropy which effectively cancels any mean-field shift $\beta_\alpha^{(i)} = \sum_j J_{ij} \langle \hat{s}_\alpha^{(j)} \rangle$ ($\alpha \in \{x, y, z\}$ on atom i which causes the asymmetry (see appendix H for a derivation of the anisotropy from

a mean-field model).

A more subtle difference between Van-der-Waals and dipolar interactions is the existence of the sharp cusp behavior around zero external fields. Unambiguously, the magnetization shows no sharp cusp in the case of weak disorder, just as we would expect from a thermalizing system. In comparison, the strongly disordered case shows much steeper slopes, albeit the non-analyticity is less pronounced compared to the case of Van-der-Waals interactions. In the inset of Figure 13, the dashed black line shows the diagonal ensemble expectation value in a zoom at small fields. Here, we can identify a small peaked structure at extremely small fields $|\Omega| < 0.01 J_{\text{median}}$ which might correspond to the non-analyticity observed in the case of Van-der-Waals interactions. Aside from this small region, the curve looks smooth, reminiscent of thermalization.

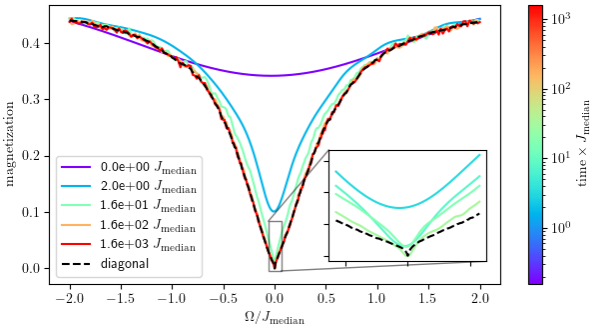

Figure 13. Similar to Fig. 11, Eigenstate expectation values of the magnetization for 9 different disorder realizations at $\Omega = -0.15 J_{\text{median}}$ and $r_{\text{bl}} = 0.1 r_{\text{max}}$ for all eigenstates as a function of eigenenergy. The color encodes the eigenstate occupation $|\langle\psi_0|\phi_\alpha\rangle|^2$.

The solid lines in Fig. 13 show the time-evolution of the magnetization, the time. At early times up to $\approx 10 J_{\text{median}}$, the magnetization depends smoothly on the external field Ω, and the magnetization is strictly positive. After $\approx 10 J_{\text{median}}$, the dynamics without external fields have already almost reached a steady-state, whereas the magnetization continues to decrease if an external field is applied. As a result, the magnetization at $\approx 10 J_{\text{median}}$ features the steepest slope. In comparison, the steady-state, just like the diagonal ensemble, appears to be rather smooth apart from the small region within $|\Omega| < 0.01 J_{\text{median}}$ showing the peaked structure.

This ambiguity concerning the existence of a cusp feature and hence thermalization shows most drastically when analyzing the eigenspectrum. Fig 14 shows the eigenstate expectation values and occupation numbers for 9 different disorder realizations for a dipolar interacting system with $r_{\text{bl}} = 0.1 r_{\text{max}}$. Interestingly, some realizations like realization 2, 3, and 5 show a scattered distribution of eigenstate expectation values which strongly resemble the strongly disordered case of Van-der-Waals interactions. These disorder realizations are inconsistent with ETH (condition (iii) in the main text). Contrary, other realizations, like realization 4, 7, and 8, exhibit a smooth dependence of the magnetization as a function of eigenenergy being compatible with ETH. In summary, we can't conclude from the numeric simulations of only 14 dipolar interacting spins whether the system thermalizes or not. This uncertainty might be a consequence of the more long-range interactions with $a = d = 3$, which generally favors thermalization.

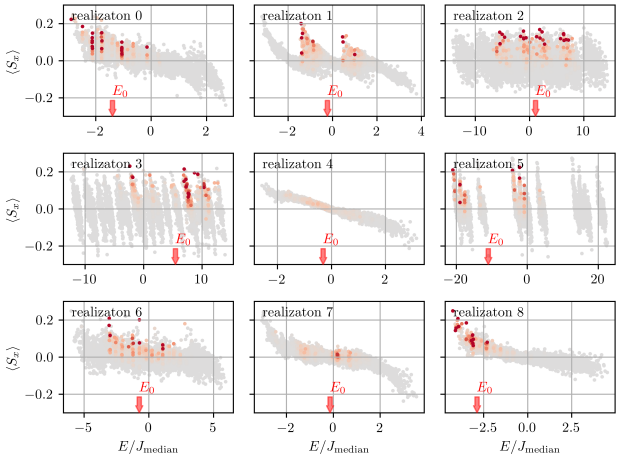

Figure 14. Similar to Fig. 11, Eigenstate expectation values of the magnetization for 9 different disorder realizations at $\Omega = -0.15 J_{\text{median}}$ and $r_{\text{bl}} = 0.1 r_{\text{max}}$ for all eigenstates as a function of eigenenergy. The color encodes the eigenstate occupation $|\langle\psi_0|\phi_\alpha\rangle|^2$.

Appendix H: Mean-field model

It is often helpful to employ a mean-field approximation to obtain an intuitive understanding of the dynamics of interacting quantum systems. In this approximation, the Hamiltonian $\hat{H}_{\text{int}} + \hat{H}_{\text{iext}}$ becomes

$$\hat{H}_{\text{mf}} = \sum_i \left(\left(\beta_x^{(i)} + \Omega \right) s_x^{(i)} + \beta_y^{(i)} s_y^{(i)} + \beta_z^{(i)} s_z^{(i)} \right) \quad \text{(H1)}$$

where we defined the mean field $\beta_\alpha^{(i)} = \sum_j J_{ij} \langle \hat{s}_\alpha^{(j)} \rangle$ ($\alpha \in \{x, y, z\}$. Since the initial state is fully polarized in x-direction, the only non-zero component of the mean field is $\beta_x^{(i)}$ and the Hamiltonian simplifies to

$$\hat{H}_{\text{mf}} = \sum_i \left(\beta_x^{(i)} + \Omega \right) s_x^{(i)}. \quad \text{(H2)}$$

The resulting dynamics is a precession around the x-axis. Therefore in mean-field approximation, the initial

state remains fully polarized and does not evolve at all, which is in stark contrast to the observed magnetization decay. Nonetheless, the mean-field picture provides an intuitive explanation for the asymmetry observed in the diagonal ensemble description of Fig. 1 c: For positive fields Ω, the external field and the mean-field add up to a large effective field which leads to a strong spin locking effect. On the other hand, at small negative fields where $\Omega \approx -\beta_x^{(i)}$, the two components cancel each other, and the spin locking effect is diminished.

Appendix I: Pair mean-field model

In this appendix, we introduce an approximation that remedies the shortcomings of the naive mean-field model by treating strongly interacting pairs of spins exactly and adding the effects of interactions between pairs on the mean-field level. This approximation provides an intuitive picture that allows us to explain all the observed features of the long-time magnetization (positivity, cusp, asymmetry).

For a single interacting pair, in the basis $\{|{\rightarrow\rightarrow}\rangle, |{\rightarrow\leftarrow}\rangle, |{\leftarrow\rightarrow}\rangle, |{\leftarrow\leftarrow}\rangle\}$, Hamiltonian (2) reads

$$\hat{H}_{\text{pair}} = 2J\left(\Delta \hat{s}_x^{(1)}\hat{s}_x^{(2)} + \hat{s}_y^{(1)}\hat{s}_y^{(2)} + \hat{s}_z^{(1)}\hat{s}_z^{(2)}\right) + \Omega\sum_{i=1}^{2}\hat{s}_z^{(i)} \tag{I1}$$

$$= \begin{pmatrix} J+\Omega & 0 & 0 & J(\Delta-1) \\ 0 & -J & J(\Delta+1) & 0 \\ 0 & J(\Delta+1) & -J & 0 \\ J(\Delta-1) & 0 & 0 & J-\Omega \end{pmatrix} \tag{I2}$$

where we defined $J = J_{01}/4$. Out of the four eigenstates of this Hamiltonian, only two have non-zero overlap with the initial state $|{\rightarrow\rightarrow}\rangle$ (see table II). Therefore, each interacting pair can be seen as an effective two-level system on its own, with a modified interaction between these "renormalized" spins. This ansatz of diagonalizing the strongest interacting pairs first can be seen as a first step in a real-space strong-disorder renormalization group treatment [20–23]. Here, we do not aim to proceed further in this renormalization scheme, but instead, we use the basis of eigenstates of strongly interacting pairs to derive an intuitive understanding of the physics within mean-field theory.

In contrast to a single spin which does not show any dynamics, a strongly interacting pair features oscillatory dynamics. Using the definition given in the main text, we can calculate the diagonal ensemble expectation value for single pair:

$$\overline{\langle \hat{S}_x\rangle_{\text{pair}}} = \frac{\Omega^2}{2(\Omega^2+j^2)} \tag{I3}$$

where we introduced $j = J(\Delta - 1)$. It should be noted that this diagonal ensemble does not describe the steady-state but rather the time average over the oscillations. The magnetization expectation value predicted by the diagonal ensemble of a single interacting pair represents an inverted Lorentz profile with width $j/2$, which features a quadratic dependence on Ω around zero (see Figure 15(a)). However, if we average over multiple pairs with different interaction strengths j, the diagonal ensemble value becomes more meaningful since we can assume that the different oscillation frequencies dephase. Also, the behavior of the magnetization changes: For example, assuming a uniform distribution of $j \in [0, \Delta_j]$[5], we obtain

$$\frac{1}{\Delta_j}\int_0^{\Delta_j} \overline{\langle \hat{S}_x\rangle_{\text{pair}}}\,\mathrm{d}j = \frac{\Omega}{2\Delta_j}\arctan\left(\frac{\Delta_j}{\Omega}\right) \tag{I4}$$

which shows the non-analytic cusp feature at $\Omega = 0$ (see Figure 15(b)). Close to the non-analytic point, the magnetization increases linearly with a slope $\dfrac{\pi}{4\Delta_j}$ inversely proportional to the width of the distribution of interaction strengths. Therefore, we can conclude that the non-analyticity is a direct consequence of disorder and the resulting broad distribution of nearest neighbor interaction strengths.

To obtain an even more realistic model and to understand additional features like the asymmetry, we add a mean-field interaction between pairs. For this purpose, we replace the external field with an effective mean-field acting on spin i:

$$\Omega \rightarrow \Omega_i = \Omega + \sum_j J_{ij}^{\text{inter}}\langle \hat{s}_x^{(j)}\rangle \tag{I5}$$

As a first example, we may consider a periodic chain of equally spaced pairs where all pairs are identical and the mean-field shift arising from interactions between the pairs is J^{inter}. In this case, the diagonal ensemble expectation value can be calculated by solving the self-consistent equation

$$\overline{\langle \hat{S}_x\rangle} = \frac{1}{2}\frac{\left(\Omega + J^{\text{inter}}\overline{\langle \hat{S}_x\rangle}\right)^2}{\left(\Omega + J^{\text{inter}}\overline{\langle \hat{S}_x\rangle}\right)^2 + j^2}. \tag{I6}$$

Since the right-hand side of the equation only contains squares, the magnetization is still positive or zero.

[5] For distributions like $j \in [j_{\min}, \Delta_j]$ that do not feature arbitrary small interaction strengths, a small region of approximate size $\Omega < |\frac{j_{\min}}{\Delta_j}|$ exists where magnetization is a smooth function of external field.

Eigenvalue	Eigenvector	Occupation	Magnetization
$J\Delta$	$\frac{1}{\sqrt{2}}\left(\|{\rightarrow\leftarrow}\rangle + \|{\leftarrow\rightarrow}\rangle\right)$	0	0
$-J(2+\Delta)$	$\frac{1}{\sqrt{2}}\left(\|{\rightarrow\leftarrow}\rangle - \|{\leftarrow\rightarrow}\rangle\right)$	0	0
$J - \sqrt{\Omega^2 + J^2(\Delta-1)^2}$	$\sqrt{\frac{1}{2} - \frac{\Omega}{2\sqrt{\Omega^2+j^2}}}\|{\rightarrow\rightarrow}\rangle + \sqrt{\frac{1}{2} + \frac{\Omega}{2\sqrt{\Omega^2+j^2}}}\|{\leftarrow\leftarrow}\rangle$	$\frac{1}{2} - \frac{\Omega}{2\sqrt{\Omega^2+j^2}}$	$-\frac{\Omega}{2\sqrt{\Omega^2+j^2}}$
$J + \sqrt{\Omega^2 + J^2(\Delta-1)^2}$	$\sqrt{\frac{1}{2} + \frac{\Omega}{2\sqrt{\Omega^2+j^2}}}\|{\rightarrow\rightarrow}\rangle + \sqrt{\frac{1}{2} - \frac{\Omega}{2\sqrt{\Omega^2+j^2}}}\|{\leftarrow\leftarrow}\rangle$	$\frac{1}{2} + \frac{\Omega}{2\sqrt{\Omega^2+j^2}}$	$\frac{\Omega}{2\sqrt{\Omega^2+j^2}}$

Table II. Properties of the four eigenstates of a single interacting spin pair. To simplify notation, we introduced $j = J(\Delta - 1)$.

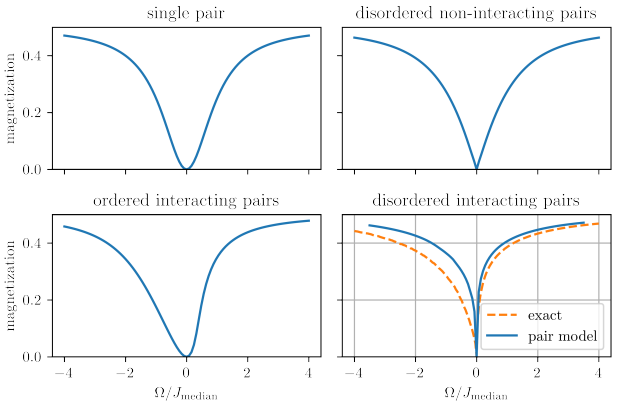

Figure 15. The diagonal ensemble expectation value of the magnetization as a function of applied external field Ω for (**a**) a single pair, (**b**) a disorder average of single pairs with interaction chosen randomly in the interval $J \in [0, 1]$, (**c**) a system of identical pairs that interact with mean field interaction $J_{\text{inter}} = 1.5 * J$, and (**d**) a realistic random distribution with power-law interactions, as described in the text. For the latter, the dashed orange line shows the full quantum mechanical solution obtained by exact diagonalization for the same system.

Therefore, for positive external fields Ω, the effective field is larger than the external field ($\Omega_i \geq \Omega$), leading to an enhanced spin locking effect. Consequently, mean-field leads to an increased magnetization compared to the case of independent pairs. For negative Ω, the external field is anti-aligned with the mean-field, and the resulting magnetization is decreased. Thus, the dependence of the magnetization as a function of field strength is asymmetric (see Figure 15(c)). In conclusion, we can attribute the asymmetry to mean-field interaction between different pairs.

In order to model the disordered spin system realized experimentally, we apply the pair model to an ensemble of spins with randomly chosen positions. We cluster the spins i into pairs p in such a way that the sum over all pair distances is minimized. Naturally, the interaction j_p of a pair p consisting of spins i and j is given by the interaction strength between the spins. The interaction strength J_{pq}^{inter} between pair p and q can be obtained from the strongest interaction J_{ij} where spin i is in pair p and j in q respectively. Now, we solve the system of self-consistent equations

$$\overline{\langle \hat{s}_x^p \rangle} = \frac{1}{2} \frac{\left(\Omega + \sum_q (J_{pq}^{\text{inter}} \overline{\langle \hat{s}_x^q \rangle})\right)^2}{\left(\Omega + \sum_q (J_{pq}^{\text{inter}} \overline{\langle \hat{s}_x^q \rangle})\right)^2 + j_p^2}. \tag{I7}$$

The resulting magnetization curve obtained after disorder averaging (see blue line in Figure 15(d)) closely resembles the exact diagonal ensemble prediction (orange line). Importantly, all qualitative features are captured, including a positive magnetization which is asymmetric with respect to the external field and shows a sharp cusp at zero field. The remaining discrepancy between the pair model and the exact solution, in particular the stronger asymmetry of the exact solution, can be attributed to clusters of spins containing more than two atoms where quantum fluctuations decrease the magnetization even further than predicted by the pair mean-field model.

We conclude that the heuristic pair mean-field model provides an intuitive understanding of the diagonal ensemble prediction. Furthermore, we can also apply it to investigate the microcanonical ensemble. To this end, we assume that the microcanonical ensemble expectation value is determined solely by the eigenstate closest in energy to the energy E_0 of the initial state. Without mean-field interaction, the energy of the system E_0 is closer to the upper eigenstate featuring positive magnetization for positive fields (respectively closer to the lower eigenstate for negative fields) (see Figure 16 (**a** and **b**). Thus, E_0 is always closer to the positively polarized eigenstate and we expect a positive magnetization for the microcanonical ensemble for all field values Ω. This changes when we take into account the mean-field interaction between pairs. Due to the assumption

that the system is exactly in a single eigenstate, we can calculate the magnetization of each eigenstate via the self-consistent equation

$$\langle \hat{s}_x \rangle_\pm = \pm \frac{\Omega + J^{\text{inter}} \langle \hat{s}_x \rangle_\pm}{2\sqrt{(\Omega + J^{\text{inter}} \langle \hat{s}_x \rangle_\pm)^2 + j^2}} \,. \tag{I8}$$

The resulting effective field $\Omega + J^{\text{inter}} \langle \hat{s}_x \rangle_\pm$ changes the eigenvalues, and the spectrum becomes asymmetric with respect to the lower and upper branch. Most strikingly, a region of small negative fields exists where the energy of the system E_0 is closer to the upper eigenstate which features a negative magnetization (compare the dashed gray line showing E_0 with the solid gray line showing the center between the eigenstates in Figure 16 (**c** and **d**)). This explains why the magnetization of the microcanonical ensemble can become negative for small negative Ω.

Comparing this model to a many-body spectrum obtained by exact diagonalization of the full quantum mechanical Hamiltonian, we notice that the highest and lowest excited states show the same features as the two eigenstates of a single pair in the mean-field model. Additionally, in between these two states, we find a plethora of further eigenstates. In a microcanonical description, the eigenstates closest to the energy of the system are populated. Therefore, for small negative fields, the microcanonical ensemble populates states which are closer in energy to the highest excited state. Since these states typically feature negative magnetization, we obtain a negative magnetization for the microcanonical ensemble similar to the red line in Figure 1 **c** in the main text.

The right column of Figure 16 also shows the eigenstate occupation for each of the studies systems. Notably, we can see that not only the eigenstates closest in energy to E_0 are populated. Rather, the occupation is highly correlated with the magnetization of the eigenstate. Therefore, the assumption of the microcanonical ensemble is not justified leading to the qualitative different behavior of the microcanonical and diagonal ensembles.

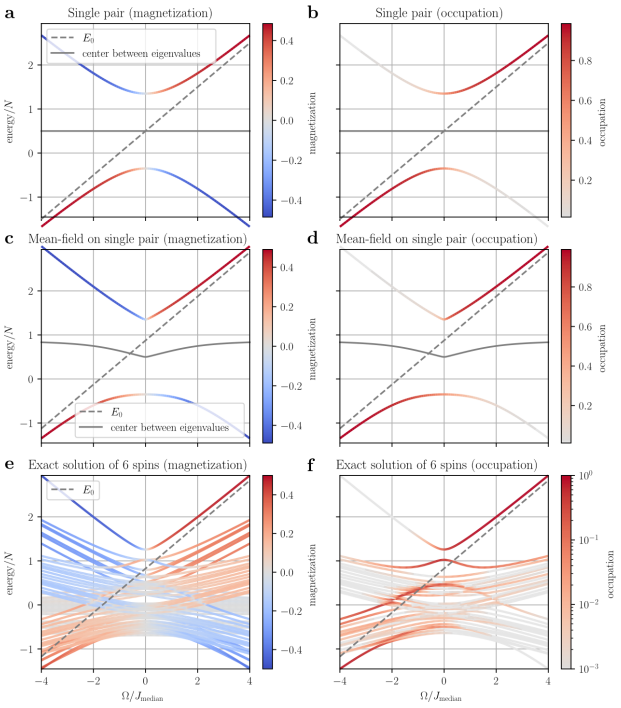

Figure 16. Eigenvalue spectra and eigenstate properties for pairs of spins compared to properties of the full many-body spectrum. In the left column, the color gradient encodes the magnetization of each eigenstate. In the right column, the color gradient represents the wavefunction overlap of the eigenstate with the initial state of fully x-polarized spins. Panels **a** and **b** show the eigenstate properties of a single pair given in Table II. Panels **c** and **d** show the eigenstates of a pair including the mean-field shift caused by the surrounding pairs according to eq. (I8). The full many-body spectrum of a disordered system of $N = 6$ spins is shown in panels **e** and **f**. The qualitative correspondence between the middle row and the extremal states in the lower row is clearly visible, showing that the pair mean-field picture may provide an intuitive understanding of the properties of the many-body spectrum.

Appendix J: Finite size scaling

To strengthen confidence in our results, we perform finite-size scaling on a one-dimensional system with periodic boundary conditions (at $r_b = 0.5 r_{\text{max}}$ with vander-Waals interactions). This analysis shows that the main qualitative difference between diagonal and thermal ensembles, being the thermal ensembles' dip below zero magnetization at small negative field strength, appears to be stable. Figure 17 c and 17 d show that the position and depth of the minimum are not yet perfectly converged but seems to stabilize around at small negative values. There is no clear drift visible, meaning the thermal ensembles minimum is indeed negative and at small negative external field.

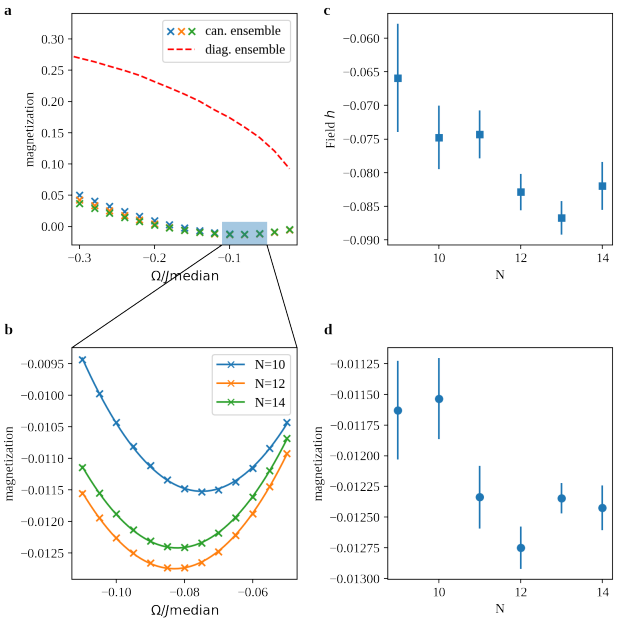

Figure 17. Finite size scaling methodology. **a,** shows an overview of diagonal and canonical ensembles. We obtain detailed data **(b)** around the minima for different N and perform a quadratic fit to extract the position **(c)** and depth **(d)** of the minima.

[1] J. M. Deutsch, Physical Review A **43**, 2046 (1991).
[2] M. Srednicki, Journal of Physics A , 14 (1999).
[3] M. Srednicki, Physical Review E **50**, 888 (1994).
[4] R. Nandkishore and D. A. Huse, Annual Review of Condensed Matter Physics **6**, 15 (2015).
[5] D. A. Abanin, E. Altman, I. Bloch, and M. Serbyn, Reviews of Modern Physics **91**, 021001 (2019).
[6] A. Browaeys and T. Lahaye, Nature Physics **16**, 132 (2020).
[7] A. Signoles, T. Franz, R. Ferracini Alves, M. Gärttner, S. Whitlock, G. Zürn, and M. Weidemüller, Physical Review X **11**, 011011 (2021).
[8] S. Geier, N. Thaicharoen, C. Hainaut, T. Franz, A. Salzinger, A. Tebben, D. Grimshandl, G. Zürn, and M. Weidemüller, Science **374**, 1149 (2021).
[9] T. Mori, T. N. Ikeda, E. Kaminishi, and M. Ueda, Journal of Physics B: Atomic, Molecular and Optical Physics **51**, 112001 (2018).
[10] W. De Roeck and F. Huveneers, Physical Review B **95**, 155129 (2017).
[11] A. Morningstar, L. Colmenarez, V. Khemani, D. J. Luitz, and D. A. Huse, Physical Review B **105**, 174205 (2022).
[12] D. Sels and A. Polkovnikov, "Thermalization of dilute impurities in one dimensional spin chains," (2022), arXiv:2105.09348 [cond-mat, physics:quant-ph].
[13] D. J. Luitz, F. Huveneers, and W. De Roeck, Physical Review Letters **119**, 150602 (2017).
[14] P. Ponte, C. R. Laumann, D. A. Huse, and A. Chandran, Philosophical Transactions of the Royal Society A: Mathematical, Physical and Engineering Sciences **375**, 20160428 (2017).
[15] T. Thiery, F. Huveneers, M. Müller, and W. De Roeck, Physical Review Letters **121**, 140601 (2018).
[16] A. L. Burin, "Energy delocalization in strongly disordered systems induced by the long-range many-body interaction," (2006), arXiv:cond-mat/0611387.
[17] N. Y. Yao, C. R. Laumann, S. Gopalakrishnan, M. Knap, M. Müller, E. A. Demler, and M. D. Lukin, Physical Review Letters **113**, 243002 (2014).
[18] D. B. Gutman, I. V. Protopopov, A. L. Burin, I. V. Gornyi, R. A. Santos, and A. D. Mirlin, Physical Review B **93**, 245427 (2016).
[19] D. A. Abanin, J. H. Bardarson, G. De Tomasi, S. Gopalakrishnan, V. Khemani, S. A. Parameswaran, F. Pollmann, A. C. Potter, M. Serbyn, and R. Vasseur, Annals of Physics **427**, 168415 (2021).
[20] D. Pekker, G. Refael, E. Altman, E. Demler, and V. Oganesyan, Physical Review X **4**, 011052 (2014).

[21] R. Vasseur, A. J. Friedman, S. A. Parameswaran, and A. C. Potter, Physical Review B **93**, 134207 (2016).

[22] R. Vasseur, A. C. Potter, and S. A. Parameswaran, Physical Review Letters **114**, 217201 (2015).

[23] R. Vosk and E. Altman, Physical Review Letters **110**, 067204 (2013).

[24] I. Bloch, J. Dalibard, and W. Zwerger, Reviews of Modern Physics **80**, 885 (2008).

[25] T. Esslinger, Annual Review of Condensed Matter Physics **1**, 129 (2010).

[26] I. Bloch, J. Dalibard, and S. Nascimbène, Nature Physics **8**, 267 (2012).

[27] C. Gross and I. Bloch, Science **357**, 995 (2017).

[28] M. Schreiber, S. S. Hodgman, P. Bordia, H. P. Lüschen, M. H. Fischer, R. Vosk, E. Altman, U. Schneider, and I. Bloch, Science **349**, 842 (2015).

[29] P. Bordia, H. P. Lüschen, S. S. Hodgman, M. Schreiber, I. Bloch, and U. Schneider, Physical Review Letters **116**, 140401 (2016).

[30] J.-y. Choi, S. Hild, J. Zeiher, P. Schauß, A. Rubio-Abadal, T. Yefsah, V. Khemani, D. A. Huse, I. Bloch, and C. Gross, Science **352**, 1547 (2016).

[31] J. Smith, A. Lee, P. Richerme, B. Neyenhuis, P. W. Hess, P. Hauke, M. Heyl, D. A. Huse, and C. Monroe, Nature Physics **12**, 907 (2016).

[32] A. M. Kaufman, M. E. Tai, A. Lukin, M. Rispoli, R. Schittko, P. M. Preiss, and M. Greiner, Science **353**, 794 (2016).

[33] A. Lukin, M. Rispoli, R. Schittko, M. E. Tai, A. M. Kaufman, S. Choi, V. Khemani, J. Léonard, and M. Greiner, Science **364**, 256 (2019).

[34] J. Léonard, M. Rispoli, A. Lukin, R. Schittko, S. Kim, J. Kwan, D. Sels, E. Demler, and M. Greiner, (2020).

[35] C. Gogolin and J. Eisert, Reports on Progress in Physics **79**, 056001 (2016).

[36] M. Rigol, V. Dunjko, and M. Olshanii, Nature **452**, 854 (2008).

[37] N. Linden, S. Popescu, A. J. Short, and A. Winter, Physical Review E **79**, 061103 (2009).

[38] P. Schultzen, T. Franz, S. Geier, A. Salzinger, A. Tebben, C. Hainaut, G. Zürn, M. Weidemüller, and M. Gärttner, Physical Review B **105**, L020201 (2022).

[39] P. Schultzen, T. Franz, C. Hainaut, S. Geier, A. Salzinger, A. Tebben, G. Zürn, M. Gärttner, and M. Weidemüller, Physical Review B **105**, L100201 (2022).

[40] H. Günther, *NMR Spectroscopy: Basic Principles, Concepts and Applications in Chemistry*, third, completely revised and updated edition ed. (Wiley-VCH, Weinheim, 2013).

[41] M. Serbyn, Z. Papić, and D. A. Abanin, Physical Review Letters **111**, 127201 (2013).

[42] D. A. Huse, R. Nandkishore, and V. Oganesyan, Physical Review B **90**, 174202 (2014).

[43] J. Z. Imbrie, Journal of Statistical Physics **163**, 998 (2016).

[44] N. Defenu, A. Trombettoni, and A. Codello, Physical Review E **92**, 052113 (2015).

[45] A. P. Millán, G. Gori, F. Battiston, T. Enss, and N. Defenu, Physical Review Research **3**, 023015 (2021).

[46] G. A. Álvarez, D. Suter, and R. Kaiser, Science **349**, 846 (2015).

[47] G. Waldherr, Y. Wang, S. Zaiser, M. Jamali, T. Schulte-Herbrüggen, H. Abe, T. Ohshima, J. Isoya, J. F. Du, P. Neumann, and J. Wrachtrup, Nature **506**, 204 (2014).

[48] B. Yan, S. A. Moses, B. Gadway, J. P. Covey, K. R. A. Hazzard, A. M. Rey, D. S. Jin, and J. Ye, Nature **501**, 521 (2013).

[49] A. de Paz, A. Sharma, A. Chotia, E. Maréchal, J. H. Huckans, P. Pedri, L. Santos, O. Gorceix, L. Vernac, and B. Laburthe-Tolra, Phys. Rev. Lett. **111**, 185305 (2013).

[50] S. Baier, M. J. Mark, D. Petter, K. Aikawa, L. Chomaz, Z. Cai, M. Baranov, P. Zoller, and F. Ferlaino, Science **352**, 201 (2016).

[51] M. Ferreira-Cao, V. Gavryusev, T. Franz, R. F. Alves, A. Signoles, G. Zürn, and M. Weidemüller, Journal of Physics B: Atomic, Molecular and Optical Physics **53**, 084004 (2020).

[52] H. Weimer, R. Löw, T. Pfau, and H. P. Büchler, Physical Review Letters **101**, 250601 (2008).

[53] M. Gärttner, K. P. Heeg, T. Gasenzer, and J. Evers, Physical Review A **86**, 033422 (2012).

[54] A. P. Orioli, A. Signoles, H. Wildhagen, G. Günter, J. Berges, S. Whitlock, and M. Weidemüller, Physical Review Letters **120**, 063601 (2018).

[55] J. Schachenmayer, A. Pikovski, and A. M. Rey, Physical Review X **5**, 011022 (2015).

[56] T. Amthor, C. Giese, C. S. Hofmann, and M. Weidemüller, Physical Review Letters **104**, 013001 (2010).

Pair localization in dipolar systems with tunable positional disorder

Adrian Braemer,[1,*] Titus Franz,[1] Matthias Weidemüller,[1] and Martin Gärttner[1,2,3,†]

[1] *Physikalisches Institut, Universität Heidelberg, Im Neuenheimer Feld 226, 69120 Heidelberg, Germany*
[2] *Kirchhoff-Institut für Physik, Universität Heidelberg, Im Neuenheimer Feld 227, 69120 Heidelberg, Germany*
[3] *Institut für Theoretische Physik, Ruprecht-Karls-Universität Heidelberg, Philosophenweg 16, 69120 Heidelberg, Germany*

(Dated: August 1, 2022)

Strongly interacting quantum systems subject to quenched disorder exhibit intriguing phenomena such as glassiness and many-body localization. Theoretical studies have mainly focused on disorder in the from of random potentials, while many experimental realizations naturally feature disorder in the interparticle interactions. Inspired by cold Rydberg gases, where such disorder can be engineered using the dipole blockade effect, we study a Heisenberg XXZ spin model where the disorder is exclusively due to random spin-spin couplings, arising from power-law interactions between randomly positioned spins. Using established spectral and eigenstate properties and entanglement entropy, we show that this system exhibits a localization crossover and identify strongly interacting pairs as emergent local conserved quantities in the system, leading to an intuitive physical picture consistent with our numerical results.

I. INTRODUCTION

Understanding how an isolated quantum system prepared out of equilibrium, can exhibit thermal properties at late times, i.e. how it thermalizes, has challenged quantum physicists for almost a century. The eigenstate thermalization hypothesis (ETH) [1, 2] offers a generic mechanism to explain this phenomenon but makes strong assumptions on the structure of energy eigenstates in terms of the matrix elements of local operators. Nonetheless, it has been shown numerically that a large class of quantum systems complies with ETH and thermalizes [3, 4]. A notable exception are strongly disordered systems in which transport is absent and the system retains memory of the initial state at arbitrary times [5–8].

This phenomenon, called many-body localization (MBL), has been verified for small systems including, but not limited to, spin-systems with random potentials [9–11], random nearest [12–14] and next-to-nearest neighbour interactions [15, 16], and power-law interactions [17–21] using a combination of exact numerical approaches and heuristic arguments like the strong disorder renormalization group (SDRG) [22–25] to generalize to large systems.

Recently, claims have been made that this localization phenomenology may not be stable in the thermodynamic limit due to thermal inclusions [26–34]. These are small, more ordered subregions thought to thermalize with their surrounding and thus slowly pushing the system towards thermalization. Unfortunately, these regions are very rare and thus only start appearing in large systems far beyond the reach of numerical methods. This raises the question, whether this instability is relevant for quantum simulation experiments, being finite in size and limited by coherence time. In this paper, we only focus on the phenomenology of localization in finite systems and subsequently use the term "localized regime" instead of a "phase" following the terminology of [28].

Complementary to numerical works there are a number of experimental results falling into roughly two classes: Experiments with single particle resolution, including optical lattices [35–38] and trapped ions [39], and experiments based on macroscopic samples, like NV centers in diamond [40] or NMR systems [41]. The former offer precise control, but are rather limited in size, while the latter can realize much larger systems at the expense of flexibility, in particular lack of programmable disorder. Cold gases of Rydberg atoms implement dipolar dynamics with random couplings (similar to NMR systems or NV centers) and allow for control of the disorder strength and even the power-law of the interaction at rather large particle numbers [42], which makes them a powerful platform for studying localization phenomena.

Motivated by recent progress on quantum simulations with Rydberg atoms [42–45], we consider a power-law interacting spin system where the disorder is due to randomly positioned spins respecting a blockade condition, which induces disordered couplings. In this setup, the strength of the disorder can be tuned by changing the density of particles or, equivalently, the minimal distance between them. Starting out in a ordered system, where the blockade radius is of order of the mean inter-particle distance, we show numerically that this system exhibits a crossover to a localized regime at small blockade and apply a SDRG approach to derive a simple model based on strongly interacting pairs, which captures the properties of the eigenstates in the localized regime well. Our study thus adds to the body of numerical works on MBL, focusing on dipolar systems with tunable positional disorder, and is highly relevant to experimental efforts, as a wide range of quantum simulation platforms feature dipolar interactions.

* adrian.braemer@kip.uni-heidelberg.de
† martin.gaerttner@kip.uni-heidelberg.de

II. LOCALIZATION IN A RYDBERG GAS

A. System

We consider the Heisenberg XXZ spin model described by the Hamiltonian ($\hbar = 1$)

$$\hat{H} = \frac{1}{2}\sum_{i\neq j} J_{ij} \underbrace{\left(\hat{S}_x^{(i)}\hat{S}_x^{(j)} + \hat{S}_y^{(i)}\hat{S}_y^{(j)} + \Delta\hat{S}_z^{(i)}\hat{S}_z^{(j)}\right)}_{\equiv H_{\text{pair}}^{(i)(j)}} \quad (1)$$

where $\hat{S}_\alpha^{(k)}$ (with $\alpha \in \{x, y, z\}$) denotes the spin-$\frac{1}{2}$ operators acting on the k-th spin. The coupling J_{ij} between spins i and j at positions x_i and x_j is given by $J_{ij} = \frac{C_\alpha}{|x_i - x_j|^\alpha}$, where C_α is an interaction coefficient which we set to $C_\alpha = 1$. In experimental realizations of this model with Rydberg atoms, the values of the anisotropy parameter Δ and interaction exponent α are controllable via the choice of the Rydberg states encoding the two spin states. The cases $\alpha = 3$, $\Delta = 0$ (dipolar exchange) and $\alpha = 6$, $\Delta \approx -0.7$ (van-der-Waals) have been realized experimentally [42, 44]. For typical cloud temperatures and time scales of the spin dynamics the atom positions can be regarded as fixed (frozen gas approximation).

During the initial Rydberg excitation, the spins are subjected to the Rydberg blockade [46] which means no two spins can be closer than some distance r_b, called the blockade radius. This feature allows one to tune the strength of disorder via the sample's density: In a very dilute sample, the mean inter-spin distance is much larger than the blockade radius r_b and thus positions are essentially uncorrelated. In the other extreme, the spins are tightly packed and exhibit strong spatial correlation.

We quantify the strength of disorder by the ratio W of the system's total volume V over total blocked volume V_{block} or, equivalently, by the ratio of Wigner-Seitz radius a_0, which is half of the mean inter-spin distance, to the blockade radius r_b to the power of the dimension d,

$$W = \frac{V}{V_{\text{block}}} = \left(\frac{a_0}{r_b}\right)^d . \quad (2)$$

For $d = 1$, the minimal value of $W_{min} = \frac{1}{2}$ is attained for a translationally invariant chain with spacing $2a_0 = r_b$, as illustrated in Fig. 1(a).

B. Effective pair description

This model differs from the random field Heisenberg model, which has been studied extensively in the MBL literature, as no disordered potentials are considered. Thus it may not be immediately apparent, why this system features localization and what constitutes the local conserved quantitites akin to the l-bits [47] in the standard scenario. Here we provide a phenomenological picture in the spirit of the SDRG suggesting that localization should appear due to strongly interacting pairs.

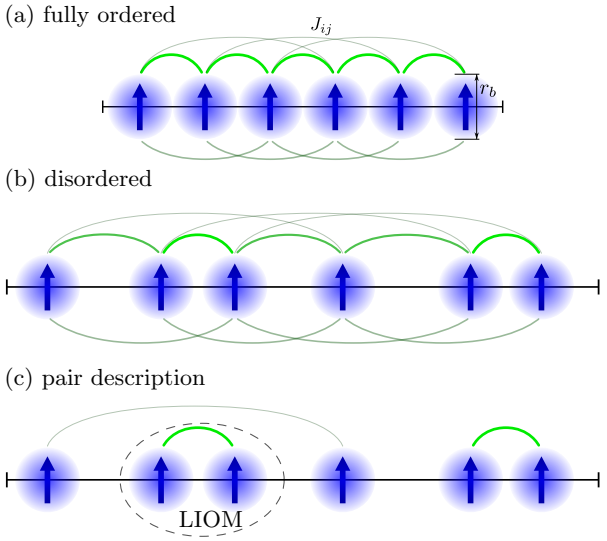

FIG. 1. **Pair description.** The blockade constraint (blue shadings) enables tuning of disorder in the couplings (green lines) from fully ordered (a) to disordered (b). In the latter case a perturbative treatment to first order yields a description in terms of strongly correlated pairs (c) subject to an Ising-like interaction (not depicted). These pairs constitute local integrals of motion (LIOM).

Consider a strongly disordered cloud of N spins described by Eq. (1) like the example depicted in Fig. 1(b). Due to the power-law interactions, coupling strengths vary strongly between different pairs of atoms, symbolized by the width and brightness of the green lines. This motivates us to employ a perturbative treatment, in which we single out the strongest pair coupling and consider all other couplings as a perturbation. In the example shown in Fig. 1(b), the two rightmost spins share the strongest coupling and we can see that it is much stronger than the other couplings of either one of the spins to the rest of the system. Using perturbation theory to first order, we find that the pair of spins almost decouples from the rest of the system leaving only an effective Ising-like interaction, which is unimportant for the further procedure and thus not shown in the figure. For details on the calculations involved, see appendix A.

We may now repeat this procedure of eliminating couplings between pairs and rest system by identifying the next strongest interaction among the remaining spins which, in this example, is the coupling between the second and third spin. Eliminating the respective couplings as well leaves us with the effective pairs shown in Fig. 1(c). Note that in an ordered system, as shown in Fig. 1(a), this perturbative treatment is not applicable as not all neglected couplings can be considered small. We also note that the order of eliminations is not important as long as each time the inner-pair coupling is much larger than the couplings between pair and rest. Concretely, for the given example, choosing the coupling between spins 2 and 3 in Fig. 1(b) first in the pair elimination process

does not change the result.

The great advantage of this ansatz is that we can now give a simple description of the whole many-body spectrum. Diagonalizing H_{pair} (see Eq 1), we find two maximally entangled eigenstates $|\pm\rangle = 1/\sqrt{2}(|\uparrow\downarrow\rangle \pm |\downarrow\uparrow\rangle)$ at energies $E_\pm = \pm 2 - \Delta$ and two degenerate states $|\uparrow\uparrow\rangle$, $|\downarrow\downarrow\rangle$ at energy $E_d = \Delta$, which we will refer to as $|\updownarrow\updownarrow\rangle$. The Ising-like interaction between pairs does not act on the entangled states $|\pm\rangle$ and is diagonal w.r.t. to $|\updownarrow\updownarrow\rangle$. Thus, in the pair picture, the eigenstates of the full system are now given by tensor products of these four pair eigenstates. We refer to this basis as the "pair basis".

In the many-body spectrum, the degeneracy between the pair states $|\uparrow\uparrow\rangle$ and $|\downarrow\downarrow\rangle$ is lifted due to the emerging Ising-like interaction. However, we note that this splitting is small compared to the splitting between the other pair eigenstates as it emerges from first order perturbation theory.

The pair picture is analogous to the l-bit picture often used MBL, where strong local disorder potentials lead to the emergence of quasi-local conserved quantities $\hat{\tau}^{(i)} \sim \hat{\sigma}_z^{(i)}$ [47, 48]. Here, we see that each projector on a pair's eigenstate constitutes an approximately conserved quantity and hence is a local integral of motion (LIOM). Thus, we established a description akin to the l-bit picture of MBL for this disordered Heisenberg model, where the role of LIOMs is taken by strongly interacting pairs.

While this ansatz is heuristic and neglects all higher resonances, that may play a crucial role in delocalizing the system, it will nonetheless turn out to be useful for interpreting and understanding the spectral and eigenstate properties reported in the following.

III. NUMERICAL RESULTS

To minimize boundary effects, we consider a one-dimensional system with periodic boundary conditions [49] of up to $N = 16$ spins governed by Eq. (1) and perform exact diagonalisation on the sector of smallest positive magnetisation. We fix the interaction exponent to $\alpha = 6$, corresponding to a Van-der-Waals interactions, and set $\Delta = -0.73$ (cf. [42]). We do not expect a strong dependence of our results on the precise value of Δ as long as one steers clear from regions around points where additional symmetries emerge.

For each disorder strength W, we generate 2000 configurations, perform a full diagonalisation and compute several well established indicators for the localization transition from the spectrum. We always average over all eigenstates/-values as restricting to the bulk of the spectrum does not lead to qualitative changes in the observed behavior. For a description of the algorithm for choosing the configurations, we refer to appendix C. All code used for this paper can be found at [50].

The following sections discuss different indicators of localization with the aim to establish the localization crossover in this model and employ the pair model for interpretation and predictions. The last section directly compares the pair basis to the eigenstates, thus demonstrating it's validity.

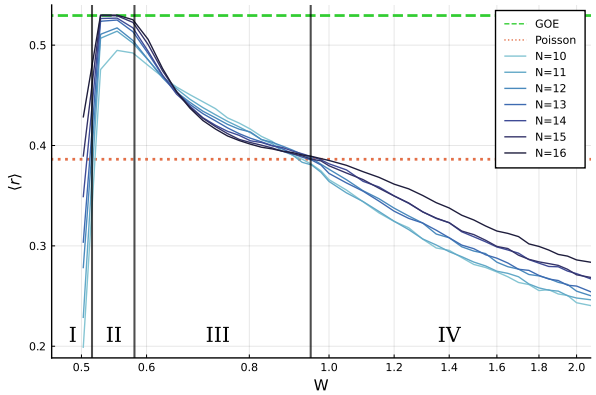

FIG. 2. **Level-spacing ratio.** With increasing disorder the LSR shows a crossover from an ergodic value to its Poissonian value and below. We identify four major regions where the physics is governed by (I) translational symmetry breaking, (II) thermal behavior, (III) the localization crossover and (IV) localization. The horizontal lines show random-matrix theory predictions.

A. Level spacing ratio

The spectral average of the level spacing ratio (LSR), defined as [51]

$$\langle r \rangle = \frac{1}{|\mathcal{H}|} \sum_n \min\left(\frac{E_{n+2} - E_{n+1}}{E_{n+1} - E_n}, \frac{E_{n+1} - E_n}{E_{n+2} - E_{n+1}} \right), \quad (3)$$

is a simple way of characterizing the distribution of differences between adjacent energy levels. For thermalizing (ergodic) systems, the Hamiltonian is expected to show a mean LSR resembling a random matrix from the Gaussian orthogonal ensemble (GOE), because its eigenvectors essentially look like random vectors. Thus one can use random matrix theory to obtain $\langle r \rangle_{\text{thermal}} = 4 - 2\sqrt{3} \approx 0.536$ [52].

On the other hand, in localized systems the eigenvalues follow a Poisson distribution, since they are essentially sums of randomly distributed energies from the l-bits the system consists of. Computing the mean LSR in this case yields $\langle r \rangle_{\text{MBL}} = 2\ln 2 - 1 \approx 0.386$ [52].

Comparing with the numerical results in Fig. 2 and focusing on the central parts first, we find the mean LSR reaches its thermal value for large enough systems and weak disorder (II) dropping towards the Poissonian value for stronger disorder (III). With growing system size, the thermal plateau (II) broadens, marking a parameter region where the system appears ergodic. But while the plateau broadens, the drop-off (III) for increasing disorder strength becomes steeper, meaning the crossover becomes sharper as the system gets larger.

Considering very strong disorder (IV), the mean LSR drops even below the Poissonian value, which indicates level attraction. This effect can be explained by the pair model: As stated earlier, the $|\updownarrow\updownarrow\rangle$ states' degeneracy is lifted by the effective Ising-like terms from 1st order perturbation theory, which means the split is of smaller magnitude compared to the intra-pair interactions. For small systems with comparatively low spectral density, this means that the small lifting likely fails to mix the formerly degenerate states into their surrounding spectrum. Thus the LSR still reflects the near degeneracy within the pairs, leading to level-attraction.

A similar argument can be made at very weak disorder (I): Here the source of the degeneracy is the proximity to the perfectly ordered case at $W = 0.5$ which has an additional translation invariance. Weak disorder breaks that symmetry but couples the symmetry sectors only weakly, leading again to a very small energetic splitting of degenerate states. We want to emphasize the reason for level attraction being very different in nature in (I) and (IV): Whereas in (I) the system is close to a system with obvious conserved quantities due to symmetries, in (IV) there is the emergent integrability of the MBL regime[8].

We conclude, that, in analogy to standard MBL, we find a crossover in the level spacing distribution from a regime with level repulsion to Poissonian gaps indicating a localization crossover. At very strong disorder, we even find a region with level attraction, the source of which can be explained by the effective pair model.

B. Thouless parameter

Complementary to eigenvalue statistics, we also probe eigenstate properties by computing the Thouless parameter

$$\mathcal{G}_n = \ln \frac{|\langle n|\hat{V}|n+1\rangle|}{E'_{n+1} - E'_n} \tag{4}$$

introduced by Serbyn *et al.*[53]. This quantity is akin to the Thouless conductance in single particle systems and quantifies how well two states $|n\rangle$,$|n+1\rangle$ with perturbed energies $E'_n = E_n + \langle n|\hat{V}|n\rangle$ are coupled by a local perturbation $\hat{V}$. In the thermal phase, states of similar energy will have similar spatial structures, whereas in the localized phase, eigenstates are products of LIOM eigenstates and thus typically vary drastically from one to the next. One can derive the scaling of the average $\mathcal{G}$ in the thermal regime to be $\mathcal{G} \propto \log|\mathcal{H}|$ and in the localized regime to be $\mathcal{G} \propto -\log|\mathcal{H}|$, leading to the natural definition of the location of the crossover to be the point where $\mathcal{G} = \text{constant}$[53].

Figure 3 shows results using local operator $\hat{V}_1 = \hat{S}^{(1)}_z$. Data for local operators $\hat{V}_2 = \hat{S}^{(1)}_z \hat{S}^{(2)}_z$ and $\hat{V}_3 = \hat{S}^{(1)}_+ \hat{S}^{(2)}_- + \text{h.c.}$ is visually identical. There is a very clear point, where all curves intersect each other indicating the crossover's location. To the right of the crossing point in the localized regime, the curves are roughly evenly spaced, reflecting the expectation of $\mathcal{G} \propto -\log|\mathcal{H}|$, clearly signaling the localized regime.

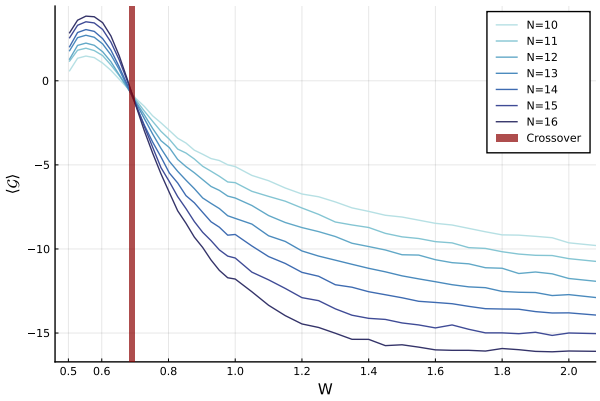

FIG. 3. **Thouless parameter.** Spectrally averaged $\mathcal{G}$ vs. disorder strength W. Data shown uses local operator $\hat{W} = \sigma^1_z$.

C. Half-chain entropy

Having shown, that there is indeed a localization crossover, we now demonstrate that our effective pair model is indeed a good approximation. We start by probing the half-chain entropy, $S = -\operatorname{Tr}\rho_A \log_2 \rho_A$, with $\rho_A = \operatorname{Tr}_B(\rho)$, i.e. the entanglement entropy between two halves of the chain. For that we select $\lfloor \frac{N}{2} \rfloor$ consecutive spins and trace out the rest, resulting in two cuts due to the periodic boundary conditions, and average over all N possible choices of connected subsystems and all eigenstates.

In an ergodic system, all bulk states should exhibit volume-law entanglement meaning $S \propto N$. In contrast, in a localized setting all states show area-law entanglement, which for $d = 1$ means $S = \text{const}$ [3, 54].

To compute the half-chain entropy predicted by the pair model, we need to determine how many pairs are divided by each cut and how often these pairs are found in one of the entangled states $|\pm\rangle = 1/\sqrt{2}(|\uparrow\downarrow\rangle \pm |\downarrow\uparrow\rangle)$. Not all pairs consist of adjacent spins (see Fig. 1c), so a cut can separate more than one pair. The amount of cut bonds is easily determined from the position data alone, by adding up the distances between paired spins. Respecting periodic boundary conditions of the system yields an additional factor of two, since there are two cuts needed to divide the chain.

Considering the entropy contribution of a single bond, if we were to average over all possible configurations of pair states, each cut bond would contribute half an ebit on average, as half of the pair states are maximally entangled and the other half not entangled at all. However, here we consider the sector of smallest positive magnetization, which yields a slightly larger entropy, because it favors the entangled states $|\pm\rangle$ (which have zero net

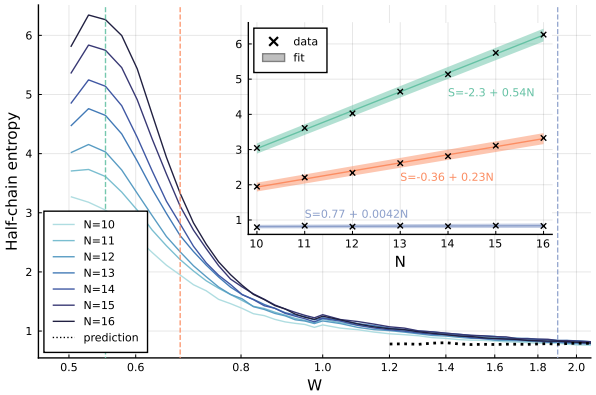

FIG. 4. **Half-chain entropy.** Average of half-chain entropy for different system sizes across disorder and prediction by pair description (black dashed line). Inset: Linear fits at fixed disorder strengths indicated by the vertical dashed lines in the main panel.

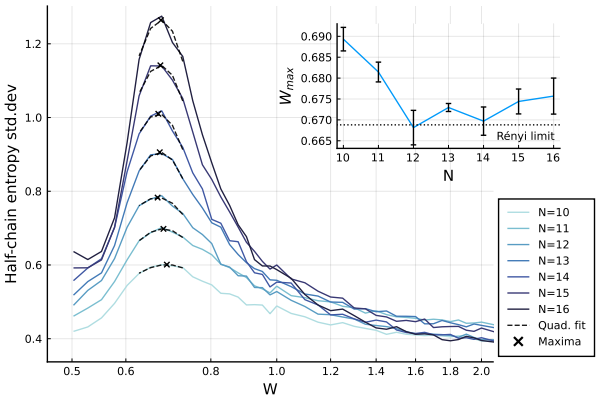

FIG. 5. **Standard deviation of half-chain entropy.** The main plot shows the standard deviation of the half-chain entropy across disorder realizations exhibiting a clear maximum around which a quadratic polynomial is fitted. Inset: Position of the maximum as extracted by the fits. Errors shown are statistical errors extracted from the fits.

magnetization) over the fully polarized ones. This modification can be computed exactly (see appendix B for details).

Taking into account both the effects of non-local pairs and of the fixed total magnetization, we can compute a prediction for the entanglement entropy directly from the interaction matrix J_{ij}. Figure 4 shows both the numerically computed values for different system sizes (solid) and pair-model prediction (dashed).

We clearly see the change between the ergodic and localized regime for the numerically computed data. For strong disorder all lines collapse, confirming on one hand the area law entanglement expected in the localized phase and, on the other hand, validating the pair model as it predicts the strong-disorder limit with striking accuracy.

Another piece of information that we can access easily via the half-chain entropy is the location of the crossover. To determine it, we calculate the variance of the half chain entropy over different disorder realizations and extract the maximum for each chain length N via a quadratic fit [15]. Figure 5 shows no strong dependence of the crossover point on N in the range of accessible system sizes.

Interestingly, the crossover location is very close the density given by Rényi's parking constant, or jamming limit, which is the maximal density attainable, by randomly placing non-overlapping unit intervals on the number line [55]. As in experiments with Rydberg spins atom positions result from such a random process, this could imply, that these experiments might not be able to reach the densities required for observing the fully ergodic regime. However, it is unclear how the crossover location generalizes to higher dimensions and larger systems.

D. Participation ratio

Now that we have seen, that the pair model captures the spatial entanglement structure of the exact eigenstates, we compare the predicted eigenstates directly to the exact ones by computing the participation ratio (PR). Intuitively, it measures how many states of a reference basis $\mathcal{B} = \{|b\rangle\}$ contribute to a given eigenstate $|\phi_n\rangle$

$$\mathrm{PR}_{\mathcal{B}}(|\phi_n\rangle) = \left(\sum_{b\in\mathcal{B}} |\langle b|\phi_n\rangle|^4\right)^{-1} . \tag{5}$$

Usually in the MBL context, one chooses a product basis as reference, because a low PR relative to product basis means the eigenstates are close to product states. "Low" in this context means a sublinear scaling of PR with the dimension of the Hilbert space $\mathcal{H}$: PR $\propto |\mathcal{H}|^\tau$ where $\tau < 1$. In contrast, a thermalizing system always has PR $\propto |\mathcal{H}|$ with respect to any product basis [56–58].

Here we compare two different reference bases, the z-basis $\mathcal{Z} = \{|\uparrow\rangle, |\downarrow\rangle\}^{\otimes N}$ and the pair basis $\mathcal{P} = \{|\pm\rangle, |\updownarrow\rangle\}^{\otimes N/2}$, introduced above, to determine how well the pair model describes the eigenstates. If the pair basis $\mathcal{P}$ was exactly equal to the eigenbasis, its PR would be exactly 1. In this case the expected PR with respect to the z-basis, averaged over the Hilbert space, $\mathcal{Z}$ will be $1.5^{N/2}$, because a single pair has an average PR of 1.5. However, we only consider the sector of smallest positive magnetization, which increases the expected PR by a similar line of reasoning as for the entropy in the previous section.

Figure 6(a) shows the PR relative to the two reference bases as a fraction of the Hilbert space dimension $|\mathcal{H}|$. We see that the weakly disordered regime indeed has ergodic eigenstates as the curves collapse onto each other. The

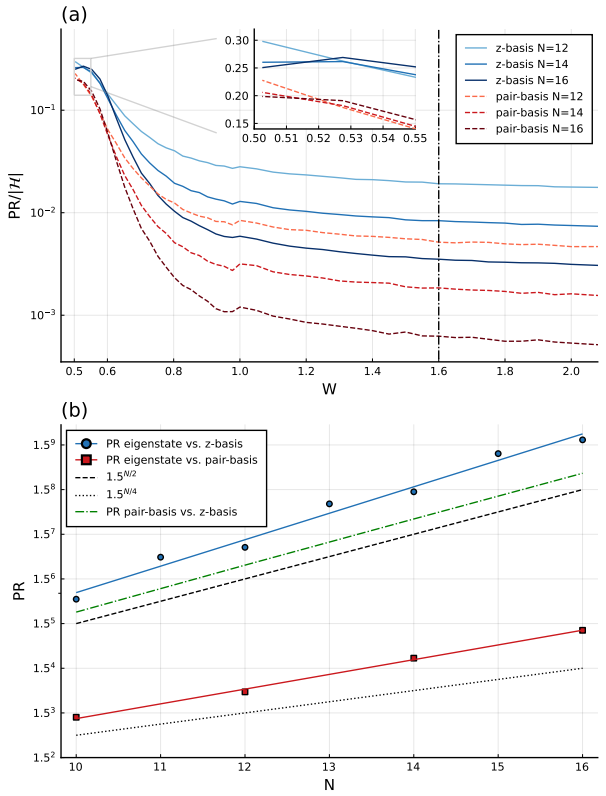

FIG. 6. **Participation ratio.** (a) PR relative to Hilbert space dimension $|\mathcal{H}|$ for different reference bases: z-basis in blue, pair basis in red. The inset shows a magnification of the region towards perfectly ordered systems. (b) shows the growth in absolute PR with increasing system size in the localized regime. The used value of W is indicated by the dash-dotted line in (a).

small offset between the two reference bases is plausible, since a thermal systems eigenstates express volume law entanglement and thus the overlap with a product basis like $\mathcal{Z}$ is minimal. The states of the pair basis contain pairwise entanglement and are thus a bit closer, which manifest as slightly lower PR. Around $W = 0.6$ the scaling with $|\mathcal{H}|$ starts to change to a sublinear relation as we crossover to the localized regime.

Checking the PR deep in the localized phase (at around $W = 1.67$) in Fig. 6(b), we can see that the PR relative to the z-basis (blue line) is slightly, but systematically, larger than the pair model's prediction (dashed green line). Consistent with this observation, we see that the PR relative to the pair basis (red line), while being much smaller, is still not constant across system sizes.

We conclude, that the pair states offer a good first order approximation of the true eigenstates, but there are higher order resonances that lead to further hybridization for some states. The exponent of the remaining dependence on system size is close to $N/4$, which hints at effects stemming from interactions between pairs.

IV. CONCLUSIONS

We analyzed a disordered Heisenberg XXZ spin model with power-law interaction and positional disorder, which is naturally realized by many quantum simulation platforms. Among these, cold Rydberg gases allow for easy tuning of the disorder via the sample's density due to the Rydberg blockade. By using standard MBL indicators, we showed numerically that this system undergoes a localization crossover, which we interpreted in terms of a simple physical model derived using an SDRG ansatz. This model, consisting of an effective Ising model of strongly interacting pairs of spins, was verified by considering the participation ratio of eigenstates with the conjectured basis, which is drastically reduced compared to the participation ratio relative to the z-basis. Still, there was a weak dependence on system size left, which means there are higher order corrections to our model. Nonetheless, we also showed that this simple model can already predict the entanglement entropy of the system nearly perfectly.

With this model at hand, we can now make predictions for large systems which may be tested in quantum simulation experiments. Of course, one of the most interesting questions will be, whether the location of the crossover shifts towards stronger disorder for large systems, indicating a transition at infinite disorder strength in the thermodynamic limit. For this purpose the easy tunability of the disorder is a great advantage as both sides of the crossover can be probed on the same platform by changing the system parameters.

Note that the pair model cannot be used to predict the crossover itself as it essentially requires the assumption that one can find strongly interacting pairs, which is only justified in the strongly disordered regime. Recent arguments for the absence of localization postulate the existence of rare thermal subregions within the system [26–34]. This would of course break the base assumption of the pair model. A possible direction for future research would be to extended the model to include not only pairs but also larger clusters, which would require one to track all the kinds of interactions between clusters of different sizes.

Interestingly, the dimensionality of the system does not directly influence the pair model. As long as the couplings are sufficiently disordered, such that pairs can be defined, it will be a good approximation. Thus it suffices to study how the distribution of couplings changes with respect to the dimensionality d of the space and coupling power α. Similar to resonance counting arguments arguments [59], we conjecture the requirement $d < \alpha$ for the pair model to be applicable. Hence, we expect our results, while acquired in $d = 1$, to generalize well to $d > 1$.

V. ACKNOWLEDGEMENTS

We thank Dima Abanin for his stimulating input. For numerical simulations we used the Julia programming language [60]. The authors acknowledge support by the state of Baden-Württemberg through bwHPC and the German Research Foundation (DFG) through grant no INST 40/575-1 FUGG (JUSTUS 2 cluster). This work is supported by the Deutsche Forschungsgemeinschaft (DFG, German Research Foundation) under Germany's Excellence Strategy EXC 2181/1 - 390900948 (the Heidelberg STRUCTURES Excellence Cluster) and under SFB 1225 ISOQUANT - 27381111.

Appendix A: Derivation of pair picture

Here we derive the pair model of the main text by means of Schrieffer-Wolff transformations [61]. Starting with the full Hamiltonian of the system

$$H_{XXZ} = \sum_{i,j} J_{ij} \underbrace{\left(S_+^{(i)} S_-^{(j)} + S_-^{(i)} S_+^{(j)} + 2\Delta S_z^{(i)} S_z^{(j)}\right)}_{\equiv H_{\text{pair}}^{(i)(j)}} \tag{A1}$$

suppose w.l.o.g. that $J_{12} \gg J_{1j}, J_{2j}$ and set $H_0 = J_{12} H_{\text{pair}}^{(1)(2)}$ and $V = H_{XXZ} - H_0$. We label the eigenvectors and eigenenergies of H_{pair} like:

state k	energy E_k	vector $\lvert k\rangle$
1	$2-\Delta$	$\sqrt{2}^{-1}(\lvert\uparrow\downarrow\rangle + \lvert\downarrow\uparrow\rangle)$
2	Δ	$\lvert\uparrow\uparrow\rangle$
3	Δ	$\lvert\downarrow\downarrow\rangle$
4	$-2-\Delta$	$\sqrt{2}^{-1}(\lvert\uparrow\downarrow\rangle - \lvert\downarrow\uparrow\rangle)$

The projectors on these states are consequently named $P_k = \lvert k\rangle\langle k\rvert \otimes \mathbb{1}$, but since the middle 2 states are degenerate, we need to use the projector on the full eigenspace and call it $P_{23} = P_2 + P_3$.

To first order only diagonal terms $P_k V P_k$ contribute, which in this case means the pair decouples and only an effective Ising term remains:

$$\begin{aligned}\hat{H} &= \sum_{i,j} J_{ij} \hat{H}_{\text{pair}}^{(i)(j)} &\text{(A2)}\\ &\approx J_{12}\hat{H}_{\text{pair}}^{(1)(2)} + \sum_{i,j>2} J_{ij}\hat{H}_{\text{pair}}^{(i)(j)} \\ &\quad + \hat{S}_z^{(1)(2)} \sum_{i>2} \tilde{\Delta}_i \hat{S}_z^{(i)} + \mathcal{O}(\hat{V}^2) &\text{(A3)}\end{aligned}$$

where $2\hat{S}_z^{(1)(2)} = \lvert\uparrow\uparrow\rangle\langle\uparrow\uparrow\rvert - \lvert\downarrow\downarrow\rangle\langle\downarrow\downarrow\rvert$ is akin to a spin-1 magnetization operator and $\tilde{\Delta}_i = \Delta(J_{1i} + J_{2i})$ is the renormalized Ising coupling. Note, that this first order term lifts the apparent degeneracy of the $\lvert\uparrow\uparrow\rangle$ and $\lvert\downarrow\downarrow\rangle$ states. This elimination is a good approximation, if the interaction within the pair is much stronger than any other interaction between a spin of the pair and some other spin.

We can now repeat this elimination step with remaining spins by incorporating the effective Ising terms into V. This is justified because its coupling is small and it is already first order perturbation theory and thus including it into the zeroth order of the next pair would mix expansion orders inconsistently.

Further eliminations, now generate effective Ising terms between the states $\lvert\uparrow\uparrow\rangle$ and $\lvert\downarrow\downarrow\rangle$ of the eliminated pairs. After pairing up all spins, we find

$$\begin{aligned}\hat{H} &= \sum_{i,j} J_{ij} \hat{H}_{\text{pair}}^{(i)(j)} &\text{(A4)}\\ &\approx \sum_{\langle i,j\rangle} J_{ij}\hat{H}_{\text{pair}}^{(i)(j)} + \sum_{\langle i,j\rangle,\langle i',j'\rangle} \tilde{\Delta}_{(i,j),(i',j')} \hat{S}_z^{(i)(j)} \hat{S}_z^{(i')(j')} &\text{(A5)}\end{aligned}$$

where the sum over $\langle i,j\rangle$ denotes pairs of spins and $\tilde{\Delta}_{(i,j),(i',j')} = \Delta(J_{i,i'} + J_{j,i'} + J_{i,j'} + J_{j,j'})$.

Also note that with each elimination step mean interparticle distance grows and thus the disorder in the system increases [62, 63] making it more likely for later elimination steps to be good approximations.

Appendix B: Pair entropy in a specific magnetization sector

Averaged over all states, each cut separating a pair gives an average entropy of $\frac{1}{2}$, since two of the pair's eigenstates are fully entangled and the other two possess no entanglement. However, when we consider a sector of fixed magnetization, this simple argument does no longer hold as there are now dependencies among the eigenstates given by the external constraint. Sectors around zero magnetization will have more entropy on average and strongly magnetized sectors less, simply because the strongest magnetized eigenstates posses no entropy.

Given N the number pairs of spins where N_+, N_-, and N_0 pairs occupy the states $\lvert\uparrow\uparrow\rangle$, $\lvert\downarrow\downarrow\rangle$, and $\lvert\uparrow\downarrow\rangle \pm \lvert\downarrow\uparrow\rangle$, we find the number of possible configuration with these amounts to be

$$C(N_+, N_-, N_0) = \binom{N}{N_0}\binom{N-N_0}{N_+} 2^{N_0} \tag{B1}$$

In the end we need the number of configurations $\mathcal{C}(N,r) = \sum_{N_0} \mathcal{C}(N,r,N_0)$ given a total amount of pairs N and an magnetization imbalance $r = N_+ - N_-$, where

$$\mathcal{C}(N,r,N_0) = \sum_{0\le N_+,N_-} C(N_+,N_-,N_0)\delta_{N,N_++N_-+N_0}\delta_{r,N_+-N_-}. \tag{B2}$$

To evaluate this expression, we compute the generating function

$$\mathcal{Z}(x,y,z) = \sum_{N>0} x^N \sum_{-N\le r\le N} y^r \sum_{N_0>0} z^{N_0}\mathcal{C}(N,r,N_0) \tag{B3}$$

$$= \sum_{0\le N_+,N_0,N_-} x^{N_++N_0+N_-} y^{N_+-N_-} z^{N_0} C(N_+,N_-,N_0) \tag{B4}$$

$$= \sum_{0\le N_-} \left(\frac{x}{y}\right)^{N_-} \sum_{0\le N_+} (xy)^{N_+} \binom{N_++N_-}{N_+} \sum_{N_0} \binom{N}{N_0} (2z)^{N_0} \tag{B5}$$

$$= \frac{y}{y-2xyz-xy^2-x} \tag{B6}$$

where we used the fact that $(1-x)^{-k-1} = \sum_n \binom{n+k}{k} x^n$ twice and then a geometric series.

From that follows directly, that

$$\mathcal{Z}(x,y,1) = \sum_{N>0} x^N \sum_{-N\le r\le N} y^r \mathcal{C}(N,r) \tag{B7}$$

$$= \frac{y}{y-2xy-xy^2-x} \tag{B8}$$

$$= \frac{1}{1-x\frac{(y+1)^2}{y}} \tag{B9}$$

$$= \sum_{0\le k} x^k \left(\frac{(y+1)^2}{y}\right)^k \tag{B10}$$

$$= \sum_{0\le k} x^k \sum_{0\le l\le 2k} y^{l-k} \binom{2k}{l} \tag{B11}$$

and thus by identification of terms

$$\mathcal{C}(N,r) = \binom{2N}{r+N} \quad . \tag{B12}$$

Singling out a specific pair and asking how often it is in on of the entangled states given a set of configurations described by values for (N_+,N_0,N_-), we find that it's the case in

$$S(N_+,N_-,N_0) = 2C(N_+,N_-,N_0-1) = \frac{N_0}{N} C(N_+,N_-,N_0) \tag{B13}$$

configurations. Again we want to find this number for a total amount of pairs N and an magnetization imbalance $r = N_+ - N_-$. Fortunately, we can find the generating function $\mathcal{Z}_\mathcal{S}(x,y,z)$ of $\mathcal{S}(N,r,N_0) = \frac{N_0}{N} C(N,r,N_0)$ by means of $\mathcal{Z}$:

$$\mathcal{Z}_\mathcal{S}(x,y,z) = \int \frac{\mathrm{d}x}{x} z\frac{\partial}{\partial z} \mathcal{Z}(x,y,z) \tag{B14}$$

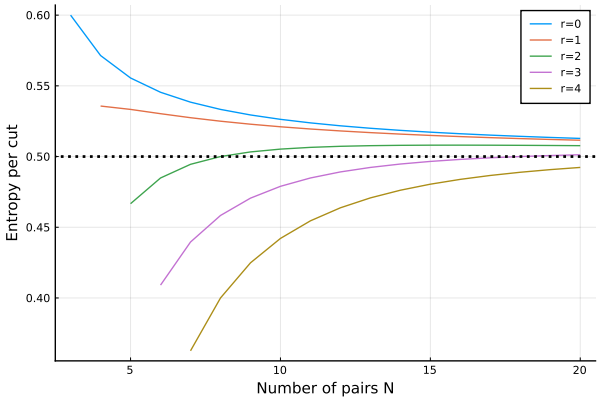

FIG. 7. Entropy value of a single cut for different magnetization sectors.

So we compute:

$$\mathcal{Z}_\mathcal{S}(x,y,z=1) = \sum_N x^N \sum_r y^r \mathcal{S}(N,r) \tag{B15}$$

$$= \int \frac{\mathrm{d}x}{x} \frac{2xy^2}{(y-x(y+1))^2} \tag{B16}$$

$$= \frac{2y^2}{(y+1)^2} \frac{1}{y-x(y+1)^2} \tag{B17}$$

$$= 2\sum_k x^k \sum_l y^{l-k+1} \binom{2k-2}{l} \tag{B18}$$

$$\Rightarrow \mathcal{S}(N,r) = 2\binom{2N-2}{r+N-1} \tag{B19}$$

Thus cutting a single pair contributes

$$\bar{S}(N,r) = \frac{\mathcal{S}(N,r)}{\mathcal{C}(N,r)} \tag{B20}$$

$$= 2\frac{N^2-r^2}{4N^2-2N} \tag{B21}$$

bits of entropy on average over all states in a given magnetization sector.

For the prediction of the average entropy in Fig. 4, we extracted the size of the pairs from the position data, which directly determines how many times a pair is cut, when moving along the chain. The number of cut pairs is then divided by the number of cuts made – which equal to the number of spins – and multiplied by the average entropy contributed by cutting a pair, computed here.

Appendix C: Drawing blockaded positions

In the following, we restrict ourselves to N spins in $d = 1$ dimension and measure every distance in units of the blockade radius r_b. We define the density of spins $0 \le \rho = \frac{1}{2W} \le 1$, the corresponding volume of the space $L = \frac{N}{\rho}$ and set out to construct a scheme to efficiently generate

a set of independently drawn positions $\{x_i\}$, that respect the blockade condition

$$|x_i - x_j| \geq r_b \qquad \forall i \neq j. \tag{C1}$$

A priori, all positions are drawn i.i.d. from a uniform distribution over the full space $\mathcal{U}[0, L]$ and the naive way would be to just draw N positions and reject the sample if the blockade condition (Eq. C1) is violated. This is essentially equivalent to a random sequential adsorption process where the expected density in $d = 1$ is given by Renyi's parking constant $m \approx 0.748$ [55]. It directly follows, that the rejection rate will become essentially 1 for any $\rho > m$ and we certainly will not get close to the fully ordered regime.

To circumvent this problem, we parameterise the positions like

$$x_i = is + \sigma_i, \tag{C2}$$

where $s = \frac{1}{\rho} = 2W$ is the mean inter-spin distance and $\sigma_i \sim \mathcal{U}[-\sigma, \sigma]$ are i.i.d. random variables. For $\sigma = \frac{L}{2}$ this ansatz is certainly equivalent to the naive scheme.

Note that, in the highly ordered case $\rho = 1 - \epsilon$, where ϵ is small, each realization of the experiment looks essentially like a regularly spaced chain with $s = \frac{1}{1-\epsilon} \approx r_b(1 + \epsilon)$ where each site has small fluctuations around the mean. This means, in this limit we get away with choosing $\sigma \approx \epsilon$.

For our simulations, we used the just described method in the region $W < 1.0$ and chose $\sigma = 1.5(\frac{1}{\rho} - 1)$. For $W \geq 1.0$, we used the naive sampling strategy. One can see a slight jump in all plots at $W = 1.0$ where the sampling method changes.

[1] M. Srednicki, Physical Review E **50**, 888 (1994), arXiv:cond-mat/9403051.
[2] J. M. Deutsch, Reports on Progress in Physics **81**, 082001 (2018), arXiv:1805.01616.
[3] C. Gogolin and J. Eisert, Reports on Progress in Physics **79**, 056001 (2016).
[4] L. D'Alessio, Y. Kafri, A. Polkovnikov, and M. Rigol, Advances in Physics **65**, 239 (2016).
[5] R. Nandkishore and D. A. Huse, Annual Review of Condensed Matter Physics **6**, 15 (2015).
[6] D. A. Abanin and Z. Papić, Annalen der Physik **529**, 1700169 (2017), arXiv:1705.09103.
[7] R. M. Nandkishore and S. L. Sondhi, Physical Review X **7**, 041021 (2017), arXiv:1705.06290 [cond-mat, physics:quant-ph].
[8] D. A. Abanin, E. Altman, I. Bloch, and M. Serbyn, Reviews of Modern Physics **91**, 021001 (2019), arXiv:1804.11065.
[9] M. Znidaric, T. Prosen, and P. Prelovsek, Physical Review B **77**, 064426 (2008), arXiv:0706.2539.
[10] D. J. Luitz, N. Laflorencie, and F. Alet, Physical Review B **91**, 081103(R) (2015), arXiv:1411.0660.
[11] P. Sierant, M. Lewenstein, and J. Zakrzewski, Physical Review Letters **125**, 156601 (2020), arXiv:2005.09534.
[12] R. Vasseur, A. J. Friedman, S. A. Parameswaran, and A. C. Potter, Physical Review B **93**, 134207 (2016).
[13] I. V. Protopopov, R. K. Panda, T. Parolini, A. Scardicchio, E. Demler, and D. A. Abanin, Physical Review X **10**, 011025 (2020).
[14] T. Chanda, P. Sierant, and J. Zakrzewski, Physical Review Research **2**, 032045(R) (2020), arXiv:2006.02860.
[15] J. A. Kjäll, J. H. Bardarson, and F. Pollmann, Physical Review Letters **113**, 107204 (2014).
[16] M. S. Bahovadinov, D. V. Kurlov, S. I. Matveenko, B. L. Altshuler, and G. V. Shlyapnikov, Many-body localization transition in a frustrated XY chain (2022), arXiv:2111.12687 [cond-mat].
[17] A. L. Burin, Physical Review B **91**, 094202 (2015).
[18] S. Schiffer, J. Wang, X.-J. Liu, and H. Hu, Physical Review A **100**, 063619 (2019).
[19] S. Roy and D. E. Logan, SciPost Physics **7**, 042 (2019).
[20] A. Safavi-Naini, M. L. Wall, O. L. Acevedo, A. M. Rey, and R. M. Nandkishore, Physical Review A **99**, 033610 (2019).
[21] Y. Mohdeb, J. Vahedi, and S. Kettemann, Excited-Eigenstate Entanglement Properties of XX Spin Chains with Random Long-Range Interactions (2022), arXiv:2201.10607.
[22] D. Pekker, G. Refael, E. Altman, E. Demler, and V. Oganesyan, Physical Review X **4**, 011052 (2014).
[23] A. C. Potter, R. Vasseur, and S. A. Parameswaran, Physical Review X **5**, 031033 (2015), arXiv:1501.03501.
[24] R. Vosk, D. A. Huse, and E. Altman, Physical Review X **5**, 031032 (2015).
[25] C. Monthus, Journal of Physics A: Mathematical and Theoretical **51**, 275302 (2018).
[26] W. De Roeck and F. Huveneers, Physical Review B **95**, 155129 (2017).
[27] D. J. Luitz, F. Huveneers, and W. De Roeck, Physical Review Letters **119**, 150602 (2017).
[28] A. Morningstar, L. Colmenarez, V. Khemani, D. J. Luitz, and D. A. Huse, arXiv:2107.05642 [cond-mat, physics:quant-ph] (2022), arXiv:2107.05642 [cond-mat, physics:quant-ph].
[29] D. Sels and A. Polkovnikov, Physical Review E **104**, 054105 (2021), arXiv:2009.04501.
[30] D. Sels and A. Polkovnikov, Thermalization of dilute impurities in one dimensional spin chains (2022), arXiv:2105.09348 [cond-mat, physics:quant-ph].
[31] D. Sels, Markovian baths and quantum avalanches (2021).
[32] T. Thiery, F. Huveneers, M. Müller, and W. De Roeck, Physical Review Letters **121**, 140601 (2018).
[33] P. Ponte, C. R. Laumann, D. A. Huse, and A. Chandran, Philosophical Transactions of the Royal Society A: Mathematical, Physical and Engineering Sciences **375**, 20160428 (2017).
[34] M. Pandey, P. W. Claeys, D. K. Campbell, A. Polkovnikov, and D. Sels, Physical Review X **10**, 041017 (2020).

[35] S. S. Kondov, W. R. McGehee, W. Xu, and B. DeMarco, Physical Review Letters **114**, 083002 (2015).

[36] M. Schreiber, S. S. Hodgman, P. Bordia, H. P. Lüschen, M. H. Fischer, R. Vosk, E. Altman, U. Schneider, and I. Bloch, Science **349**, 842 (2015).

[37] P. Bordia, H. P. Lüschen, S. S. Hodgman, M. Schreiber, I. Bloch, and U. Schneider, Physical Review Letters **116**, 140401 (2016).

[38] A. Lukin, M. Rispoli, R. Schittko, M. E. Tai, A. M. Kaufman, S. Choi, V. Khemani, J. Léonard, and M. Greiner, Science **364**, 256 (2019).

[39] J. Smith, A. Lee, P. Richerme, B. Neyenhuis, P. W. Hess, P. Hauke, M. Heyl, D. A. Huse, and C. Monroe, Nature Physics **12**, 907 (2016).

[40] G. Kucsko, S. Choi, J. Choi, P. C. Maurer, H. Zhou, R. Landig, H. Sumiya, S. Onoda, J. Isoya, F. Jelezko, E. Demler, N. Y. Yao, and M. D. Lukin, Physical Review Letters **121**, 023601 (2018).

[41] K. X. Wei, C. Ramanathan, and P. Cappellaro, Physical Review Letters **120**, 070501 (2018).

[42] A. Signoles, T. Franz, R. F. Alves, M. Gärttner, S. Whitlock, G. Zürn, and M. Weidemüller, Physical Review X **11**, 011011 (2021), arXiv:1909.11959.

[43] A. P. Orioli, A. Signoles, H. Wildhagen, G. Günter, J. Berges, S. Whitlock, and M. Weidemüller, Physical Review Letters **120**, 063601 (2018).

[44] S. Geier, N. Thaicharoen, C. Hainaut, T. Franz, A. Salzinger, A. Tebben, D. Grimshandl, G. Zürn, and M. Weidemüller, Science **374**, 1149 (2021).

[45] T. Franz, S. Geier, C. Hainaut, A. Signoles, N. Thaicharoen, A. Tebben, A. Salzinger, A. Braemer, M. Gärttner, G. Zürn, and M. Weidemüller, Absence of thermalization in an interacting system of thousands of quantum spins (2022), arXiv:2207.14216 [cond-mat, physics:physics, physics:quant-ph].

[46] M. D. Lukin, M. Fleischhauer, R. Cote, L. M. Duan, D. Jaksch, J. I. Cirac, and P. Zoller, Physical Review Letters **87**, 037901 (2001).

[47] D. A. Huse, R. Nandkishore, and V. Oganesyan, Physical Review B **90**, 174202 (2014).

[48] M. Serbyn, Z. Papić, and D. A. Abanin, Physical Review Letters **111**, 127201 (2013).

[49] Only the closest copy of each spin is considered for the interaction.

[50] `https://github.com/abraemer/Pair-localization-paper`.

[51] V. Oganesyan and D. A. Huse, Physical Review B **75**, 155111 (2007), arXiv:cond-mat/0610854.

[52] Y. Y. Atas, E. Bogomolny, O. Giraud, and G. Roux, Physical Review Letters **110**, 084101 (2013), arXiv:1212.5611.

[53] M. Serbyn, Z. Papić, and D. A. Abanin, Physical Review X **5**, 041047 (2015), arXiv:1507.01635.

[54] J. Eisert, M. Cramer, and M. B. Plenio, Reviews of Modern Physics **82**, 277 (2010), arXiv:0808.3773.

[55] A. Rényi, Publications of the Mathematical Institute of the Hungarian Academy of Sciences **3**, 109 (1958).

[56] M. Serbyn, Z. Papić, and D. A. Abanin, Physical Review B **96**, 104201 (2017).

[57] N. Macé, F. Alet, and N. Laflorencie, Physical Review Letters **123**, 180601 (2019).

[58] D. J. Luitz, I. Khaymovich, and Y. Bar Lev, SciPost Physics Core **2**, 006 (2020).

[59] N. Y. Yao, C. R. Laumann, S. Gopalakrishnan, M. Knap, M. Müller, E. A. Demler, and M. D. Lukin, Physical Review Letters **113**, 243002 (2014), arXiv:1311.7151.

[60] J. Bezanson, A. Edelman, S. Karpinski, and V. B. Shah, SIAM Review **59**, 65 (2017).

[61] S. Bravyi, D. P. DiVincenzo, and D. Loss, Annals of Physics **326**, 2793 (2011).

[62] D. S. Fisher, Physical Review B **50**, 3799 (1994).

[63] R. Vasseur, A. C. Potter, and S. A. Parameswaran, Physical Review Letters **114**, 217201 (2015).

8 CONCLUSION

In Part I of this thesis, we have discovered that strongly disordered spin systems feature slow, universal relaxation dynamics such that they remain out-of-equilibrium on experimentally relevant timescales and hence are non-ergodic (see Figure 5.1 (a-c)). In the following, we will discuss Part II, where we have explored whether a steady-state can break ergodicity and be non-thermal. We will summarize how it was achieved to explore this question by measurements of the global magnetization. Also, we will provide an intuitive picture of how the emergence of quasi-local integrals of motion leads to the absence of thermalization and investigate how this absence of thermalization is related to the strength of disorder in the system. Finally, we will discuss whether quantum thermalization is also absent in the thermodynamic limit.

GLOBAL MAGNETIZATION AS A PROBE FOR THE ABSENCE OF THERMALIZATION

In the first part, the measurement of the global magnetization after a Ramsey sequence has provided a useful tool to study the slow relaxation dynamics because all observed dynamics are beyond mean-field prediction. However, at late times, both the magnetization and the ensemble-averaged single-spin purity will have relaxed to zero, which was explained by the global U(1) symmetry of the system. Therefore, both the diagonal ensemble, which describes the steady state of a quantum system, and all thermal ensembles predict a fully depolarized state (see Figure 8.1 (a)). Thus, the total magnetization seems to be not an adequate observable to distinguish a localizing from a thermalizing system.

To overcome this challenge, we have applied an external field in Part II of this thesis to break the global U(1) symmetry. If the field was aligned orthogonally to the direction of the spins, the field would induce Rabi oscillations which are damped due to interactions (see Figure 8.1 (b)). This experiment has been also accomplished in a dipolar interacting spin-1/2 system realized with Rydberg atoms [76]. This investigation has revealed that the damping of the oscillations is not completely captured by mean-field approximation and that primordial quantum fluctuations need to be taken into account to quantitatively explain the observed dynamics. However, this configuration of the external field does not benefit from the previously discussed advantages of the initial state, which does not evolve at all within mean-field

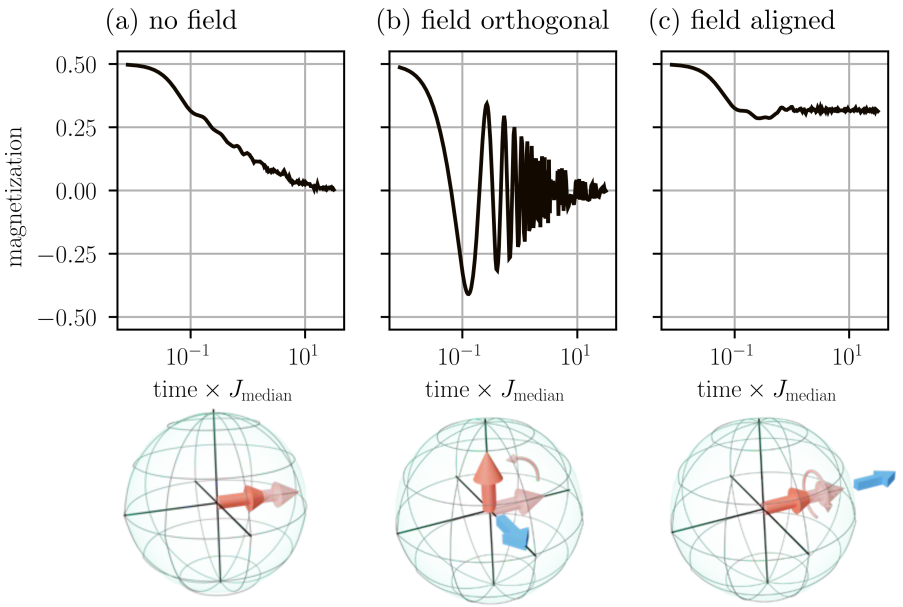

Figure 8.1: Relaxation dynamics of a disordered quantum spin system with external field applied. The upper column shows the time evolution of the magnetization, the lower column illustrates the field configuration on a Bloch sphere. The red arrow depicts the evolution of the magnetization expectation value from early (pale red) to later times (bright red). The blue arrow shows the direction of the field. (a) If no external field is applied, the magnetization relaxes to zero. (b) If the field is orthogonal to the direction of the spins, the magnetization features an oscillation that is effectively damped to zero by interactions. (c) If the field is aligned in the direction of the spins, the external field effectively locks the weakly interacting spins. Therefore, the steady-state magnetization becomes dependent on the field strength.

approximation. In addition, the magnetization is still expected to relax to zero at late times. Both of these disadvantages can be overcome if the external field is aligned in the direction of the spins (see Figure 8.1 (c)). In this case, the initial state is still an eigenstate of the mean-field Hamiltonian such that any dynamics are still a consequence of quantum fluctuations. Most importantly, the external field locks the magnetization at a finite value dependent on the interplay of interactions and field strength.

The idea of this thesis has been to compare this dependence of the steady state magnetization on the strength of the external field with the expectation from thermal ensembles. For a thermal system, this curve is expected to be smooth, which we could show in numerical simulations of up to 14 spins of dipolar and Van-der-Waals interacting systems. However, in both exact numerical simulations and the experiment, we have found a sharp cusp feature if the system is sufficiently strongly disordered. Therefore, we can conclude that the system has

not thermalized even at late times when the magnetization is already decayed to zero.

The advantage of this measurement protocol is that it does not rely on microscopic resolution like transport measurements which are typically used to study localization [62, 63, 64, 65]. Even more challenging are measurements of how the entanglement entropy scales with system size [29, 30, 31]. This simplicity of our method allows us to probe the absence of thermalization for system sizes approaching the thermodynamic limit. In addition, measurements of the global magnetization are feasible in a range of various quantum simulator platforms ranging from polar molecules [147] over nuclear spins [145] and color centers in diamond [146] to magnetic atoms [148, 149] which paves the way toward studying quantum thermalization for a large class of disordered spin systems in a scalable fashion.

PAIRS AS LOCAL INTEGRALS OF MOTION

In Part I of this thesis, we have already seen that small, localized clusters of spins can explain the universal relaxation dynamics of disordered spin systems. In Part II, we were able to extend this model by including mean-field interactions between multiple pairs (see Figure 8.2). Thereby, the pair model can also qualitatively reproduce the dependence of the late-time magnetization on the external field including the features that indicate the absence of thermalization, like the observed asymmetry and the sharp cusp (see also supplement I in Article [5]).

In addition, the existence of strongly interacting pairs is also able to reproduce many properties calculated via exact diagonalization. For example, isolated pairs can reproduce the scaling of the half-chain entanglement entropy with system size (Article [6]). Also, we could confirm by calculating the participation ratio that product states of eigenstates of localized pairs are a good approximation to the real eigenstates of a full quantum system (Article [6]). Finally, the existence of strongly interacting pairs also explains the properties of the eigenspectrum including the observation that the initial state is not energetically localized in the spectrum, and that ETH is violated in small spin systems (supplement F in Article [5]).

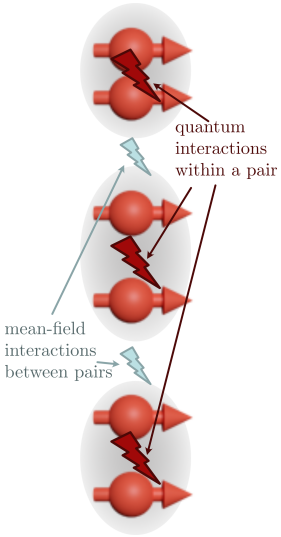

Figure 8.2: A simplified model that takes into account the full quantum interactions within strongly interacting pairs, but treats interactions between different pairs only within mean-field approximation.

The finding that localized clusters of spins lead to an absence of thermalization relates quantum spin systems where disorder is due to random couplings to the phenomenon of many-body localization [37, 135, 38]. In the prototypical MBL system, a strong disorder in the external field term leads to the breakdown of thermalization. In these systems, transport is inhibited due to the emergence of local integrals of motions (LIOMs) $\tau_\alpha^{(i)} = \hat{U}\sigma_\alpha^{(i)}\hat{U}^\dagger$ which are single-spin operators $\sigma_\alpha^{(i)}$ ($\alpha \in \{x, y, z\}$) transformed by a quasilocal operator $\hat{U}$ [39, 151] (see Figure 8.3 (a)). In the case discussed in this thesis, where the

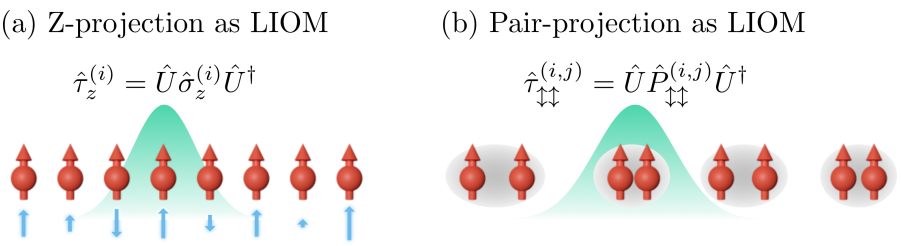

Figure 8.3: Illustration of LIOMs. (a) For the standard model of MBL where disorder is due to random external fields (represented by blue arrows), the LIOM is the Pauli operator σ_z transformed by a local rotation $\hat{U}$ with exponentially decaying support (illustrated by green area). Adapted from [150]. (b) If the disorder is due to random couplings, projectors $\hat{P}_{\updownarrow\updownarrow}$ onto the eigenstates of local pairs play the role of LIOMs.

couplings are random instead of the external field, we propose that projectors onto the eigenstates of pairs play the role of LIOMs (see Figure 8.3 (b)).

CROSSOVER BETWEEN THE THERMALIZING AND NON-THERMALIZING REGIME

At weak disorder, we expect the isolated quantum system to thermalize according to ETH. Indeed, numerical simulations in Article [5] have shown that the sharp cusp feature disappears for an increased blockade radius indicating thermalization. As expected from ensemble equivalence in a thermal system [134], the diagonal ensemble expectation value is consistent with thermal ensembles like the microcanonical and the canonical ensembles. Only the microcanonical ensemble shows small deviations at large external field values, which can be attributed to finite size effects leading to gaps in the spectrum such that the microcanonical ensemble averages over too few eigenstates. Generally, the ensembles coincide even to a larger degree compared to the numerical investigation in [27], where the canonical ensemble slightly deviates from the diagonal and microcanonical ensembles.

To access the thermalizing regime in the experiment, we have saturated the Rydberg excitation leading to a strong Rydberg blockade effect which reduces the spatial disorder. In addition, we have changed the spin system from a Van-der-Waals interacting system to a dipolar interacting system. The more long-range interactions couple each spin to a large number of neighboring spins at a similar coupling strength which effectively decreases disorder even further. In this regime, the cusp feature disappears, and the steady state magnetization becomes a smooth function of the applied locking field. This shows that it is possible to tune from a non-thermalizing to a thermalizing system by decreasing the strength of the disorder and increasing the range of interactions.

The finding of both a thermalizing and a non-thermalizing regime opens the question of whether, at a given strength of disorder, a phase transition between these regimes occurs [151, 130, 152]. In MBL systems, the existence of this putative transition is actively discussed. Some of the open questions involve at which strength of disorder this transition occurs [42], whether the transition is rather a crossover, and what the scaling properties at this transition are [153, 154, 155]. In the following, we aim to discuss the existence of this transition for quantum systems where the disorder is due to random coupling.

In Article [6], we have numerically probed how tuning the strength of disorder by the blockade radius affects the crossover between the thermalizing regime at weak disorder and localization at strong disorder. For this purpose, the variance of the half-chain entropy over different disorder realizations was computed for varying disorder strengths and system sizes. The location of the maximum variance determines the crossover between thermalization and localization. This location varies only weakly with system size, and also agrees well with the location of the crossover calculated via the level spacing ratio or the Thouless parameter. However, it should be noted that in MBL systems, finite-size scaling is highly challenging, and strong finite size effects exist even at system sizes of up to 20 spins, potentially leading to false conclusions about a possible localization transition [28].

In addition to the blockade radius, the range of the power-law interactions also changes the effective disorder in the system and influences the MBL transition. For short-range interactions ($\alpha > d$), each spin interacts mostly with its nearest neighbor, and the coupling to other spins further away is strongly reduced. In this limit, we expect local pairs to describe the system in a good approximation. On the other hand, long-range interactions ($\alpha < d$) couple each spin to a large number of neighboring spins at a similar coupling strength, which increases the probability of delocalizing the MBL phase. This discussion can be made more quantitative by resonance counting arguments suggesting that $\alpha = d$ is the critical case between thermalization and localization [48].

Indeed, the numerical simulations studying ETH in this critical case (appendix G in Article [5]) show that the cusp feature, indicating the absence of thermalization, is less pronounced and only visible in the limit of a vanishing blockade radius compared to the case of Van-der-Waals interactions ($\alpha = 6 = 2d$). Also, the simulation in the case $\alpha = d$ suffers from strong finite size effects which are also indicative of a critical case.

ABSENCE OF QUANTUM THERMALIZATION IN THE THERMODYNAMIC LIMIT

It remains an open question whether a localization phase exists at infinite late times and for infinite system sizes, or whether thermalization is always recovered in the thermodynamic limit.

The numerical simulations have the advantage of being able to compute the whole eigenspectrum, entanglement entropy, and expectation values at infinite late times. However, they are limited to small system sizes of up to 16 spins depending on the symmetry of the Hamiltonian.

Using the quantum simulator experiment, we could drastically increase the available system size to up to 4000 spins. These large systems are well beyond the reach of quantum simulations on classical computers because the Hilbert space grows exponentially in system size. Generally, ETH is expected to become exponentially more precise with system size [156, 157]. Therefore, we can assume that the system size is sufficiently large to probe the thermodynamic limit. However, to prove the existence of an MBL phase in the true thermodynamic limit, it would be required to confirm the absence of thermalization at both infinite system size and infinite late times. The experiment is limited to finite observation times of 10 µs which is chosen to be short compared to the Rydberg lifetime to ensure unitary dynamics. During this time, at interaction strengths of $J_{\text{median}} = 0.78\,\text{MHz}$ for the Van-der-Waals interacting system, respectively $J_{\text{median}} = 3.4\,\text{MHz}$ for the dipolar interacting system, information can spread maximally over 8 to 30 neighbors corresponding roughly to the radius of our 3D system assuming ballistic transport. Yet, due to disorder, the velocity of spreading of correlations might be drastically reduced such that the steady state of the system might be reached only at much later times.

Therefore, adapting the terminology of Morningstar et. al. [42], we interpret our observation not as an MBL phase, but as an MBL regime, i.e., the absence of thermalization at either finite time or finite system size.

Understanding whether and how thermalization might be recovered in the thermodynamic limit is an important goal for future research. One approach would be to extend the numerical investigation of the crossover between thermalization and localization of Article [6] to larger system sizes. For example, shift invert methods could possibly calculate exact eigenstates of a part of the spectrum for up to 26 spins [158]. Unfortunately, it is expected that some delocalization processes are based on rare events and can possibly not be directly observed in the small systems accessible by numerics based on exact diagonalization. One example of these processes is the existence of resonances between distant spins. These system-wide resonances are known to delocalize Anderson-isolators for long-range interacting systems where the power-law exponent α is smaller than the dimension

d [32]. In the prototypical MBL scenario where disorder is due to random external fields, resonances between two pairs of spins even lead to thermalization in systems where $\alpha < 2d$ [159, 160]. It might be a promising approach to extend this analysis of the probability for resonances to systems with disorder due to random couplings along the lines of [161]. Even if no system-wide resonances exist in systems where $\alpha > 2d$, rare weakly disordered regions could exist that thermalize and seed thermalizing avalanches. These are claimed to delocalize the standard model of MBL with power-law interactions or in $d > 1$ [41, 44, 45, 46, 42]. This process of thermalizing avalanches could be directly studied in both numerics and experiments by coupling disordered quantum systems to a thermal region and observing if and how avalanches of thermalization get transported through the medium.

If isolated quantum systems with disorder due to random couplings thermalized at infinite times (Figure 5.1 (e)), the here observed absence of thermalization would rather hint toward ergodicity breaking due to anomalously slow relaxation similar to spin glasses. This type of ergodicity breaking due to glassines in long-range interacting quantum systems was recently theoretically explored for the Kotliar-Anderson-Stein spin glass model [161]. This leads to the question of whether and how glassiness and localization are related, whether an MBL and a spin glass phase might coexist [162, 163] or whether the two phases are separated by a phase transition [131, 127]. An exciting aspect for future experiments would be the measurement of the Edwards-Anderson correlator, which is the spin glass order parameter [164], allowing us to confirm directly the existence of spin glass order in non-ergodic systems.

Independent of whether disordered quantum spin systems eventually thermalize in the thermodynamic limit, this thesis has shown that disorder leads to ergodicity breaking for remarkably long times. During this time, the strongly interacting many-body system can be efficiently described by small localized clusters, already a description via pairs is sufficient to capture the qualitative behavior for both the glassy dynamics (Part I) and the quasi-steady-state magnetization (Part II). This enormous simplification leads to a universal behavior of disordered quantum spin systems in the sense that dynamics become independent of the strength of disorder, the symmetry and type of the Hamiltonian, and the energy of the initial state. In addition, the localization avoids heating in driven Floquet systems, which paves the way for studying new emergent phenomena like time crystals (see next chapter for a more detailed discussion of the next steps on the Heidelberg Rydberg experiment).

9

NEXT STEPS ON THE HEIDELBERG RYDBERG QUANTUM SIMULATOR PLATFORM

In his famous essay *"More is Different"*, P. W. Anderson describes how the complexity of a large ensemble of elementary particles can lead to qualitatively different behavior [165]. In this spirit, the physics of a single Rydberg atom is well-understood thanks to enormous progress being made in the understanding and experimental control of hydrogen-like atoms since the discovery of the simple formula for the emission of electromagnetic radiation in hydrogen by Johann Balmer and Johannes Rydberg at the end of the 19th century. However, the interplay of many strongly interacting Rydberg atoms leads to the emergence of new phenomena, which became a new area of active research in recent years. This thesis has used a large ensemble of Rydberg atoms for quantum simulations of disordered spin systems. Here, Rydberg atoms are just a tool featuring long lifetimes and strong interactions well suited for studying generic many-body physics like glassy dynamics, quantum thermalization, or many-body localization.

In the following, we propose the next steps on the Rydberg quantum simulator platform which build on the results presented in this thesis and aim to further deepen the understanding of far-from-equilibrium dynamics of disordered quantum spin systems.

GLASSY DYNAMICS AT LOW ENERGY DENSITIES: A MANY-BODY MOBILITY EDGE AND AGING?

A key difference between the quantum system discussed in this thesis and classical spin glasses is the role of thermal fluctuations. In classical spin glasses, dynamics are induced by thermal fluctuations. Hence, the temperature of the sample plays a decisive role, the stretching exponent generally is temperature dependent, and the glassy dynamics break down above a critical, spin glass temperature [112]. So, the ergodicity breaking in spin glasses is a phenomenon that can be associated with low temperatures, where the system is trapped in local minima of the free energy landscape, where the system can be described as in quasi thermal equilibrium. This contrasts with the quench experiment presented in this thesis, where we have excited eigenstates spread over the whole energy spectrum.

This leads to the question of how dynamics in disordered quantum spin systems depend on the energy density of the initial state. An interesting aspect could be the existence of a mobility edge, a critical energy density that separates an ergodic delocalizing from

a non-ergodic localizing phase. This mobility edge is well known to exist for the Anderson transition [32, 166], and was proposed as a many-body mobility edge for many-body localizing systems [163, 161]. Interestingly, the many-body mobility edge does not necessarily coincide with the spin glass transition, which is found at even lower energy densities[130, 54, 131, 127].

A possible protocol to probe the low energy spectrum of the disordered quantum spin system would be to initiate the spins in the x-direction of the Bloch sphere and lock the magnetization using a strong external field that is aligned in the direction of the spins. In this configuration, the spins are prepared in the paramagnetic ground state of the transverse field spin Hamiltonian. Subsequently, the strength of the field can be slowly reduced, such that the system remains mostly adiabatically in the ground state. Depending on the speed of the field ramp, this protocol can prepare various initial states at different energies.

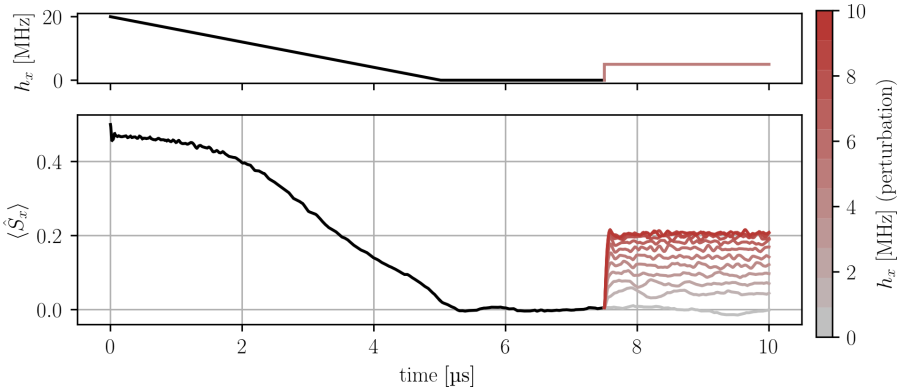

Figure 9.1: Preparing low energy density states by adiabatic ramps. (a) Initially, a strong locking field is aligned with the spins in x-direction. Slowly, this field is ramped to zero. A sudden quench of the field allows probing of the linear response. (b) Magnetization as a function of time for the protocol depicted in (a). During the slow initial ramp of the external field, the magnetization slowly relaxes to zero. The quench of the external field leads to a sudden response of the magnetization which depends on the external field h_x after the quench (color-coded in red (strong field) to grey (zero field)).

If the external field is sufficiently slowly ramped to zero, the resulting state is fully depolarized but the response to a small perturbation in the external field is finite and depends linearly on the strength of the external field (see Figure 9.1). The measurement of the linear response corresponds to the measurement of the unequal time commutator, and it enables a variety of new experiments: Firstly, the dependence of the linear response on the ramp speed might reveal signatures of the many-body mobility edge or a possible spin glass phase transition. Secondly, the dynamics of the response might depend on the waiting time

between the ramp and the perturbation. This phenomenon is called *aging* and is known in spin glass systems where the thermoremanent magnetization (TRM) relaxes slower if more time has passed since the cooling of the sample [20]. Finally, in thermal equilibrium, the responses to a coherent and an incoherent perturbation are related via the fluctuation-dissipation theorem [167, 168]. For a non-interacting system, we have already devised a protocol and shown the proof of principle that the fluctuation-dissipation theorem can be measured with Rydberg atoms [12]. If the fluctuation-dissipation theorem is fulfilled, this allows the measurement of temperature in a thermal quantum spin system. Otherwise, if the fluctuation-dissipation theorem does not hold, this directly shows the absence of thermalization. For a spin glass system, a generalized fluctuation-dissipation theorem holds where the effective temperature is time-dependent [169].

MEASUREMENT OF LOCAL OBSERVABLES BY FLUORESCENCE IMAGING

In this thesis, we have shown that global measurements, like the magnetization, can reveal new insights into how disordered quantum spin systems relax, and even probe the absence of thermalization. In the previous section, we proposed a series of measurements, which also only rely on global observables, to further explore thermalization, many-body localization, and a possible spin glass phase. In this section, we want to give an overview of possibilities to probe local observables in Rydberg spin systems.

Since no closed optical transition exists for Rydberg states, Rydberg atoms can not be directly imaged by fluorescence or absorption imaging. This problem can be avoided by probing Rydberg atoms with an ion microscope which can resolve atoms with high spatial resolution [170]. Alternatively, Rydberg atoms can be de-excited to the ground state, which can then be imaged, for example, by fluorescence imaging. However, for this last method to work, no additional atoms must populate the ground state such that only the Rydberg atoms are detected.

An elegant solution to this problem is to trap individual ground state atoms in optical tweezer arrays [171, 172, 173, 60]. Using a stimulated Raman adiabatic passage (STIRAP), these can be excited with high efficiency to Rydberg atoms such that no additional ground state atoms remain [174]. The optical tweezer arrays also feature additional advantages like the possibility to position the atoms in arbitrary geometries [175], and they can trap the atoms during fluorescence imaging. Tweezer arrays allow imaging atoms with single-atom resolution, which allows the direct observation of transport. In the context of spin glasses, the single atom resolution enables the direct observation of the Edwards-Anderson spin glass order parameter.

An alternative approach to removing the ground state atoms is to apply a strong magnetic field that separates states with different magnetic quantum numbers in energy. This allows to optically pump the ground states atoms in states with different magnetic quantum numbers that are no longer resonant to the imaging light. The required magnetic field strengths can be provided by the MOT coils in the Heidelberg Rydberg experiment, which can be switched from Anti-Helmholtz to Helmholtz configuration with an H-bridge (see section Section 2.2.1). A new imaging system has already been designed and build for the Heidelberg Rydberg experiment which features a spatial resolution of 5 µm for the 780 nm imaging light. This resolution is similar to the blockade radius obtained by exciting the Rydberg state $|48S\rangle$ with a 1 µs excitation pulse. Fluorescence imaging of Rydberg atoms would enable us to directly observe the transport of avalanches of thermalization that originate from thermal regions that are coupled to the disordered Rydberg system.

FLOQUET MBL AND TIME CRYSTALS

One of the main results of this thesis was the observation of an MBL regime. For future experiments, MBL might be a tool that avoids heating of the many-body system in driven Floquet systems. This opens the path toward studying new emergent phenomena like time crystals [176]. A time crystal is a many-body phenomenon in driven quantum systems where the discrete-time translation symmetry is spontaneously broken. Since the original proposal by Frank Wilczek in 2012 [177, 178], the theoretical understanding of time crystals has made enormous progress, and time crystals have been observed in various experiments [179, 180, 181, 182]. Still, many open questions remain, especially about the importance of many-body localization for the existence of a time crystalline phase, whether time crystals are robust with respect to coupling to an external bath [183], and about the properties of the phase transition between a time crystal and a trivial Floquet insulator [184].

Figure 9.2 shows preliminary results of time-crystalline behavior observed in the Heidelberg Rydberg quantum simulator. Here, we have applied a sequence of $\pi/2$-pulses which each inverse the z-magnetization (Figure 9.2 (a)). The oscillation is damped due to interactions during the pulses and possible small phase errors. If the duration of each pulse has an error of 2%, the spins are rotated slightly too far after each pulse. As a result, the magnetization reveals a beating signal (Figure 9.2 (b)). In Figure 9.2 (c), we let the system interact for 45 ns in between each $\pi/2$-pulse. This interaction stabilizes the oscillation at the original frequency without the 2% error, such that the beating is no longer visible on the signal and the decay of the oscillation is reduced. This robustness of the periodic order to perturbation

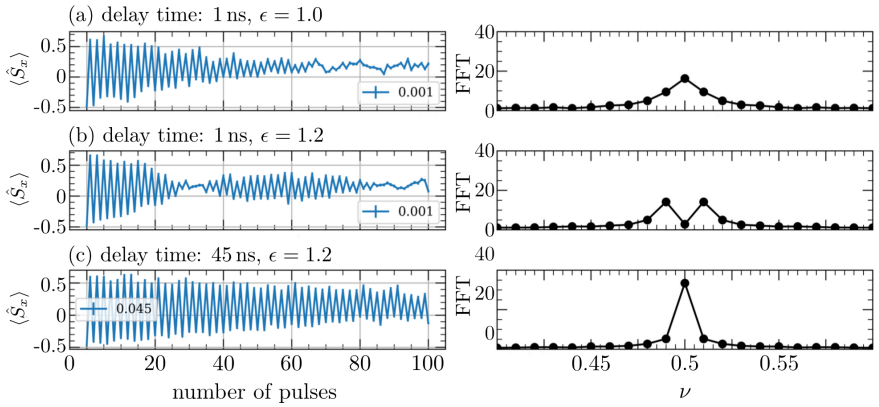

Figure 9.2: Preliminary signature of a time crystalline phase. (a) A sequence of $\pi/2$-pulses leads to a damped oscillation (left panel) of the magnetization at a period of 2 pulses. In Fourier space (right panel), this corresponds to a frequency of 0.5. (b) Increasing the pulse duration by 2% induces a beating, which can be seen in Fourier space as the emergence of 2 peaks. (c)By introducing a delay time of 45 ns in between each $\pi/2$-pulse, the interaction restores the original frequency and reduces the damping of the oscillation.

due to interactions presents a first signature of a time-crystal similar to the experiments of Choi et. al. [179].

[14] Feynman, R. P. **1970a**. *Feynman Lectures on Physics*. Boston, MA: Addison Wesley Longman. ISBN: 978-0-201-02115-8.

[15] Landau, L. D. and Lifshitz, E. M. **Jan. 1980**. "CHAPTER IV - IDEAL GASES." In: *Statistical Physics (Third Edition)*. Ed. by L. D. Landau and E. M. Lifshitz. Oxford: Butterworth-Heinemann, pp. 111–157. ISBN: 978-0-08-057046-4. DOI: 10.1016/B978-0-08-057046-4.50011-7.

[16] Landau, L. D. and Lifshitz, E. M. **Jan. 1980**. "CHAPTER XIV - PHASE TRANSITIONS OF THE SECOND KIND AND CRITICAL PHENOMENA." In: *Statistical Physics (Third Edition)*. Ed. by L. D. Landau and E. M. Lifshitz. Oxford: Butterworth-Heinemann, pp. 446–516. ISBN: 978-0-08-057046-4. DOI: 10.1016/B978-0-08-057046-4.50021-X.

[17] Boltzmann, L. **1896**. *Vorlesungen über Gastheorie*. Leipzig: J.A. Barth.

[18] Groenewold, H. J. **Oct. 1946**. "On the Principles of Elementary Quantum Mechanics." In: *Physica* 12.7, pp. 405–460. ISSN: 0031-8914. DOI: 10.1016/S0031-8914(46)80059-4.

[19] Maxwell, J. C. **1872**. *Theory of Heat*. 3d ed. Text-Books of Science. London: Longmans, Green, and co.

[20] Binder, K. and Young, A. P. **Oct. 1986**. "Spin Glasses: Experimental Facts, Theoretical Concepts, and Open Questions." In: *Reviews of Modern Physics* 58.4, pp. 801–976. ISSN: 0034-6861. DOI: 10.1103/RevModPhys.58.801.

[21] Palmer, R. G. et al. **Sept. 1984**. "Models of Hierarchically Constrained Dynamics for Glassy Relaxation." In: *Physical Review Letters* 53.10, pp. 958–961. ISSN: 0031-9007. DOI: 10.1103/PhysRevLett.53.958.

[22] Benettin, G. et al. **2014a**. "Ergodicity: How Can It Be Broken?" In: *Large Deviations in Physics*, pp. 29–70. DOI: 10.1007/978-3-642-54251-0_2.

[23] Ueda, M. **Dec. 2020**. "Quantum Equilibration, Thermalization and Prethermalization in Ultracold Atoms." In: *Nature Reviews Physics* 2.12, pp. 669–681. ISSN: 2522-5820. DOI: 10.1038/s42254-020-0237-x.

[24] Deutsch, J. M. **Feb. 1991**. "Quantum Statistical Mechanics in a Closed System." In: *Physical Review A* 43.4, pp. 2046–2049. ISSN: 1050-2947, 1094-1622. DOI: 10.1103/PhysRevA.43.2046.

[25] Srednicki, M. **Aug. 1994**. "Chaos and Quantum Thermalization." In: *Physical Review E* 50.2, pp. 888–901. ISSN: 1063-651X, 1095-3787. DOI: 10.1103/PhysRevE.50.888.

[26] Srednicki, M. **1999**. "The Approach to Thermal Equilibrium in Quantized Chaotic Systems." In: *Journal of Physics A*, p. 14.

[27] Rigol, M. et al. **Apr. 2008**. "Thermalization and Its Mechanism for Generic Isolated Quantum Systems." In: *Nature* 452.7189, pp. 854–858. ISSN: 1476-4687. DOI: 10.1038/nature06838.

[28] Abanin, D. A. et al. **Apr. 2021**. "Distinguishing Localization from Chaos: Challenges in Finite-Size Systems." In: *Annals of Physics* 427, p. 168415. ISSN: 0003-4916. DOI: 10.1016/j.aop.2021.168415.

[29] Kaufman, A. M. et al. **Aug. 2016**. "Quantum Thermalization through Entanglement in an Isolated Many-Body System." In: *Science* 353.6301, pp. 794–800. DOI: 10.1126/science.aaf6725.

[30] Lukin, A. et al. **Apr. 2019**. "Probing Entanglement in a Many-Body–Localized System." In: *Science* 364.6437, pp. 256–260. DOI: 10.1126/science.aau0818.

[31] Léonard, J. et al. **Dec. 2020**. "Signatures of Bath-Induced Quantum Avalanches in a Many-Body–Localized System." In.

[32] Anderson, P. W. **Mar. 1958**. "Absence of Diffusion in Certain Random Lattices." In: *Physical Review* 109.5, pp. 1492–1505. ISSN: 0031-899X. DOI: 10.1103/PhysRev.109.1492.

[33] Prüfer, M. et al. **Nov. 2018**. "Observation of Universal Dynamics in a Spinor Bose Gas Far from Equilibrium." In: *Nature* 563.7730, pp. 217–220. ISSN: 1476-4687. DOI: 10.1038/s41586-018-0659-0.

[34] Eigen, C. et al. **Nov. 2018**. "Universal Prethermal Dynamics of Bose Gases Quenched to Unitarity." In: *Nature* 563.7730, pp. 221–224. ISSN: 1476-4687. DOI: 10.1038/s41586-018-0674-1.

[35] Peng, P. et al. **Apr. 2021**. "Floquet Prethermalization in Dipolar Spin Chains." In: *Nature Physics* 17.4, pp. 444–447. ISSN: 1745-2481. DOI: 10.1038/s41567-020-01120-z.

[36] Rubio-Abadal, A. et al. **May 2020**. "Floquet Prethermalization in a Bose-Hubbard System." In: *Physical Review X* 10.2, p. 021044. ISSN: 2160-3308. DOI: 10.1103/PhysRevX.10.021044.

[37] Nandkishore, R. and Huse, D. A. **Mar. 2015**. "Many-Body Localization and Thermalization in Quantum Statistical Mechanics." In: *Annual Review of Condensed Matter Physics* 6.1, pp. 15–38. ISSN: 1947-5454, 1947-5462. DOI: 10.1146/annurev-conmatphys-031214-014726.

[38] Abanin, D. A. et al. **May 2019**. "Colloquium: Many-Body Localization, Thermalization, and Entanglement." In: *Reviews of Modern Physics* 91.2, p. 021001. ISSN: 0034-6861, 1539-0756. DOI: 10.1103/RevModPhys.91.021001.

[39] Serbyn, M. et al. **Sept. 2013**. "Local Conservation Laws and the Structure of the Many-Body Localized States." In: *Physical*

Review Letters 111.12, p. 127201. DOI: 10.1103/PhysRevLett.111.127201.

[40] Huse, D. A. et al. **Nov. 2014**. "Phenomenology of Fully Many-Body-Localized Systems." In: *Physical Review B* 90.17, p. 174202. DOI: 10.1103/PhysRevB.90.174202.

[41] De Roeck, W. and Huveneers, F. **Apr. 2017**. "Stability and Instability towards Delocalization in Many-Body Localization Systems." In: *Physical Review B* 95.15, p. 155129. DOI: 10.1103/PhysRevB.95.155129.

[42] Morningstar, A. et al. **May 2022**. "Avalanches and Many-Body Resonances in Many-Body Localized Systems." In: *Physical Review B* 105.17, p. 174205. DOI: 10.1103/PhysRevB.105.174205.

[43] Sels, D. and Polkovnikov, A. **Apr. 2022**. *Thermalization of Dilute Impurities in One Dimensional Spin Chains*. arXiv: 2105.09348 [cond-mat, physics:quant-ph].

[44] Luitz, D. J. et al. **Oct. 2017**. "How a Small Quantum Bath Can Thermalize Long Localized Chains." In: *Physical Review Letters* 119.15, p. 150602. DOI: 10.1103/PhysRevLett.119.150602.

[45] Ponte, P. et al. **Dec. 2017**. "Thermal Inclusions: How One Spin Can Destroy a Many-Body Localized Phase." In: *Philosophical Transactions of the Royal Society A: Mathematical, Physical and Engineering Sciences* 375.2108, p. 20160428. DOI: 10.1098/rsta.2016.0428.

[46] Thiery, T. et al. **Oct. 2018**. "Many-Body Delocalization as a Quantum Avalanche." In: *Physical Review Letters* 121.14, p. 140601. DOI: 10.1103/PhysRevLett.121.140601.

[47] Burin, A. L. **Nov. 2006**. *Energy Delocalization in Strongly Disordered Systems Induced by the Long-Range Many-Body Interaction*. arXiv: cond-mat/0611387.

[48] Yao, N. Y. et al. **Dec. 2014**. "Many-Body Localization in Dipolar Systems." In: *Physical Review Letters* 113.24, p. 243002. DOI: 10.1103/PhysRevLett.113.243002.

[49] Gutman, D. B. et al. **June 2016**. "Energy Transport in the Anderson Insulator." In: *Physical Review B* 93.24, p. 245427. DOI: 10.1103/PhysRevB.93.245427.

[50] Bellman, R. **1984b**. *Dynamic Programming*. Princeton, NJ: Princeton Univ. Pr. ISBN: 978-0-691-07951-6.

[51] Bellman, R. **2015b**. *Adaptive Control Processes: A Guided Tour*. Princeton, N.J.: Princeton University Press. ISBN: 978-1-4008-7466-8.

[52] Pekker, D. et al. **Mar. 2014**. "Hilbert-Glass Transition: New Universality of Temperature-Tuned Many-Body Dynamical Quantum Criticality." In: *Physical Review X* 4.1, p. 011052. ISSN: 2160-3308. DOI: 10.1103/PhysRevX.4.011052.

[53] Vasseur, R. et al. **Apr. 2016**. "Particle-Hole Symmetry, Many-Body Localization, and Topological Edge Modes." In: *Physical*

Review B 93.13, p. 134207. ISSN: 2469-9950, 2469-9969. DOI: 10.1103/PhysRevB.93.134207.

[54] Vasseur, R. et al. **May 2015**. "Quantum Criticality of Hot Random Spin Chains." In: *Physical Review Letters* 114.21, p. 217201. ISSN: 0031-9007, 1079-7114. DOI: 10.1103/PhysRevLett.114.217201.

[55] Vosk, R. and Altman, E. **Feb. 2013**. "Many-Body Localization in One Dimension as a Dynamical Renormalization Group Fixed Point." In: *Physical Review Letters* 110.6, p. 067204. ISSN: 0031-9007, 1079-7114. DOI: 10.1103/PhysRevLett.110.067204.

[56] Bloch, I. et al. **July 2008**. "Many-Body Physics with Ultracold Gases." In: *Reviews of Modern Physics* 80.3, pp. 885–964. DOI: 10.1103/RevModPhys.80.885.

[57] Esslinger, T. **Aug. 2010**. "Fermi-Hubbard Physics with Atoms in an Optical Lattice." In: *Annual Review of Condensed Matter Physics* 1.1, pp. 129–152. ISSN: 1947-5454, 1947-5462. DOI: 10.1146/annurev-conmatphys-070909-104059.

[58] Bloch, I. et al. **2012a**. "Quantum Simulations with Ultracold Quantum Gases." In: *Nature Physics* 8.4, pp. 267–276. ISSN: 17452473. DOI: 10.1038/nphys2259.

[59] Gross, C. and Bloch, I. **Sept. 2017**. "Quantum Simulations with Ultracold Atoms in Optical Lattices." In: *Science* 357.6355, pp. 995–1001. ISSN: 0036-8075, 1095-9203. DOI: 10.1126/science.aal3837.

[60] Browaeys, A. and Lahaye, T. **Feb. 2020**. "Many-Body Physics with Individually Controlled Rydberg Atoms." In: *Nature Physics* 16.2, pp. 132–142. ISSN: 1745-2481. DOI: 10.1038/s41567-019-0733-z.

[61] Daley, A. J. et al. **July 2022**. "Practical Quantum Advantage in Quantum Simulation." In: *Nature* 607.7920, pp. 667–676. ISSN: 1476-4687. DOI: 10.1038/s41586-022-04940-6.

[62] Schreiber, M. et al. **Aug. 2015**. "Observation of Many-Body Localization of Interacting Fermions in a Quasirandom Optical Lattice." In: *Science* 349.6250, pp. 842–845. ISSN: 0036-8075, 1095-9203. DOI: 10.1126/science.aaa7432.

[63] Bordia, P. et al. **Apr. 2016**. "Coupling Identical One-Dimensional Many-Body Localized Systems." In: *Physical Review Letters* 116.14, p. 140401. ISSN: 0031-9007, 1079-7114. DOI: 10.1103/PhysRevLett.116.140401.

[64] Choi, J.-y. et al. **June 2016**. "Exploring the Many-Body Localization Transition in Two Dimensions." In: *Science* 352.6293, pp. 1547–1552. DOI: 10.1126/science.aaf8834.

[65] Smith, J. et al. **Oct. 2016**. "Many-Body Localization in a Quantum Simulator with Programmable Random Disorder." In: *Nature Physics* 12.10, pp. 907–911. ISSN: 1745-2481. DOI: 10.1038/nphys3783.

[66] Edelstein, S. A. and Gallagher, T. F. **1979a**. *Rydberg Atoms*. Vol. 14. Cambridge: Cambridge University Press. ISBN: 978-0-511-52453-0. DOI: 10.1016/S0065-2199(08)60132-3.

[67] Walker, T. G. and Saffman, M. **2008c**. "Consequences of Zeeman Degeneracy for the van Der Waals Blockade between Rydberg Atoms." In: *Physical Review A - Atomic, Molecular, and Optical Physics* 77.3, pp. 1–18. ISSN: 10502947. DOI: 10.1103/PhysRevA.77.032723. arXiv: 0712.3438.

[68] Bijnen, R. R. V. **2013c**. "Quantum Engineering with Ultracold Atoms." In: DOI: 10.6100/IR754785.

[69] Whitlock, S. et al. **Apr. 2017**. "Simulating Quantum Spin Models Using Rydberg-excited Atomic Ensembles in Magnetic Microtrap Arrays." In: *Journal of Physics B: Atomic, Molecular and Optical Physics* 50.7, p. 074001. ISSN: 0953-4075. DOI: 10.1088/1361-6455/aa6149.

[70] Lukin, M. D. et al. **June 2001**. "Dipole Blockade and Quantum Information Processing in Mesoscopic Atomic Ensembles." In: *Physical Review Letters* 87.3, p. 037901. ISSN: 0031-9007, 1079-7114. DOI: 10.1103/PhysRevLett.87.037901.

[71] Weimer, H. et al. **Dec. 2008**. "Quantum Critical Behavior in Strongly Interacting Rydberg Gases." In: *Physical Review Letters* 101.25, p. 250601. ISSN: 0031-9007, 1079-7114. DOI: 10.1103/PhysRevLett.101.250601.

[72] Gärttner, M. et al. **Sept. 2012**. "Finite-Size Effects in Strongly Interacting Rydberg Gases." In: *Physical Review A* 86.3, p. 033422. DOI: 10.1103/PhysRevA.86.033422.

[73] Hofmann, C. S. et al. **2014e**. "An Experimental Approach for Investigating Many-Body Phenomena in Rydberg-interacting Quantum Systems." In: *Frontiers of Physics* 9.5, pp. 571–586. ISSN: 20950470. DOI: 10.1007/s11467-013-0396-7. arXiv: 1307.1074.

[74] Bijnen, R. R. V. **2013d**. "Quantum Engineering with Ultracold Atoms." In: DOI: 10.6100/IR754785.

[75] Barredo, D. et al. **Mar. 2015**. "Coherent Excitation Transfer in a Spin Chain of Three Rydberg Atoms." In: *Physical Review Letters* 114.11, p. 113002. ISSN: 0031-9007, 1079-7114. DOI: 10.1103/PhysRevLett.114.113002.

[76] Orioli, A. P. et al. **Feb. 2018**. "Relaxation of an Isolated Dipolar-Interacting Rydberg Quantum Spin System." In: *Physical Review Letters* 120.6, p. 063601. ISSN: 0031-9007, 1079-7114. DOI: 10.1103/PhysRevLett.120.063601.

[77] Saffman, M. et al. **Aug. 2010**. "Quantum Information with Rydberg Atoms." In: *Reviews of Modern Physics* 82.3, pp. 2313–2363. DOI: 10.1103/RevModPhys.82.2313.

[78] Jaksch, D. et al. **Sept. 2000**. "Fast Quantum Gates for Neutral Atoms." In: *Physical Review Letters* 85.10, pp. 2208–2211. ISSN: 0031-9007, 1079-7114. DOI: 10.1103/PhysRevLett.85.2208.

[79] Weimer, H. et al. **May 2010**. "A Rydberg Quantum Simulator." In: *Nature Physics* 6.5, pp. 382–388. ISSN: 1745-2481. DOI: 10.1038/nphys1614.

[80] Bernien, H. et al. **Nov. 2017**. "Probing Many-Body Dynamics on a 51-Atom Quantum Simulator." In: *Nature* 551.7682, pp. 579–584. ISSN: 0028-0836. DOI: 10.1038/nature24622.

[81] Ferracini Alves, R. **2022d**. "Realization of a Heisenberg XXZ Spin System Using Rydberg Atoms." In: DOI: 10.11588/HEIDOK.00031511.

[82] Franz, T. **June 2018**. "Quantum simulation of relaxation dynamics of a Heisenberg Hamiltonian using Rydberg spins." MA thesis. Heidelberg.

[83] Ferreira-Cao, M., [...], **Franz, T.**, et al. **Mar. 2020**. "Depletion Imaging of Rydberg Atoms in Cold Atomic Gases." In: *Journal of Physics B: Atomic, Molecular and Optical Physics* 53.8, p. 084004. ISSN: 0953-4075. DOI: 10.1088/1361-6455/ab7427.

[84] Signoles*, A. **Franz*, T.** et al. **Jan. 2021**. "Glassy Dynamics in a Disordered Heisenberg Quantum Spin System." In: *Physical Review X* 11.1, p. 011011. ISSN: 2160-3308. DOI: 10.1103/PhysRevX.11.011011.

[85] Zeiher, J. et al. **Aug. 2015**. "Microscopic Characterization of Scalable Coherent Rydberg Superatoms." In: *Physical Review X* 5.3, p. 031015. DOI: 10.1103/PhysRevX.5.031015.

[86] Geier, S. **Sept. 2019**. "Engineering Rydberg-spin Hamiltonian Using Microwave Pulse Sequences." MA thesis. Heidelberg.

[87] Geier, S., [...], **Franz, T.**, et al. **Nov. 2021**. "Floquet Hamiltonian Engineering of an Isolated Many-Body Spin System." In: *Science* 374.6571, pp. 1149–1152. ISSN: 0036-8075, 1095-9203. DOI: 10.1126/science.abd9547.

[88] Scholl, P., [...], **Franz, T.**, et al. **Apr. 2022**. "Microwave Engineering of Programmable XXZ Hamiltonians in Arrays of Rydberg Atoms." In: *PRX Quantum* 3.2, p. 020303. DOI: 10.1103/PRXQuantum.3.020303.

[89] Salzinger, A., [...], **Franz, T.**, et al. **Jan. 2022**. "Measuring the Fluctuation-Dissipation Relation of Single Driven Rydberg Qubits with Engineered Dephasing." In: *In preparation*.

[90] Damburg, R. J. and Kolosov, V. V. **Dec. 1976**. "A Hydrogen Atom in a Uniform Electric Field." In: *Journal of Physics B: Atomic and Molecular Physics* 9.18, p. 3149. ISSN: 0022-3700. DOI: 10.1088/0022-3700/9/18/006.

[91] Damburg, R. J. and Kolosov, V. V. **June 1978**. "An Asymptotic Approach to the Stark Effect for the Hydrogen Atom." In:

Journal of Physics B: Atomic and Molecular Physics 11.11, p. 1921. ISSN: 0022-3700. DOI: 10.1088/0022-3700/11/11/009.

[92] Damburg, R. J. and Kolosov, V. V. **Aug. 1979**. "A Hydrogen Atom in a Uniform Electric Field. III." In: *Journal of Physics B: Atomic and Molecular Physics* 12.16, p. 2637. ISSN: 0022-3700. DOI: 10.1088/0022-3700/12/16/011.

[93] Damburg, R. J. and Kolosov, V. V. **Mar. 1981**. "A Hydrogen Atom in a Uniform Electric Field. IV." In: *Journal of Physics B: Atomic and Molecular Physics* 14.5, p. 829. ISSN: 0022-3700. DOI: 10.1088/0022-3700/14/5/015.

[94] Šibalić, N. et al. **Nov. 2017**. "ARC: An Open-Source Library for Calculating Properties of Alkali Rydberg Atoms." In: *Computer Physics Communications* 220, pp. 319–331. ISSN: 0010-4655. DOI: 10.1016/j.cpc.2017.06.015.

[95] Inglis, D. R. and Teller, E. **1939**. "Ionic Depression of Series Limits in One-Electron Spectra." In: *The Astrophysical Journal* 90, p. 439.

[96] Gallagher, T. F. et al. **Dec. 1981**. "Spin-Orbit Effect in the Electric Field Ionization of Rb and Cs." In: *Physical Review A* 24.6, pp. 3249–3251. ISSN: 0556-2791. DOI: 10.1103/PhysRevA.24.3249.

[97] Anderson, S. E. et al. **Dec. 2011**. "Trapping Rydberg Atoms in an Optical Lattice." In: *Physical Review Letters* 107.26, p. 263001. ISSN: 0031-9007, 1079-7114. DOI: 10.1103/PhysRevLett.107.263001.

[98] Gregoric, V. C. et al. **Dec. 2018**. "Improving the State Selectivity of Field Ionization with Quantum Control." In: *Physical Review A* 98.6, p. 063404. DOI: 10.1103/PhysRevA.98.063404.

[99] Müller, A. **Mar. 2019**. *State Selective Field Ionization in an Apparatus for Large Optical Access*.

[100] Bayes, T. **Jan. 1763**. "An Essay towards Solving a Problem in the Doctrine of Chances." In: *Philosophical Transactions of the Royal Society of London* 53, pp. 370–418. DOI: 10.1098/rstl.1763.0053.

[101] Jaynes, E. T. and Bretthorst, G. L. **2003**. *Probability Theory: The Logic of Science*. Cambridge, UK ; New York, NY: Cambridge University Press. ISBN: 978-0-521-59271-0.

[102] Ferreira Cao, M. **2017h**. "Control and Characterisation of a Rydberg Spin System to Explore Many-Body Physics." PhD thesis. Ruperto-Carola-University of Heidelberg.

[103] Debye, P. **Aug. 1913**. "Zur Theorie Des Anomalen Dispersion Der Langwelligen Elektrischen Strahlung." In: 15, pp. 777–793.

[104] Levitt, M. H. **2001b**. *Spin Dynamics : Basics of Nuclear Magnetic Resonance*. Chichester ; New York : John Wiley & Sons. ISBN: 978-0-471-48921-4 978-0-471-48922-1.

[105] Cugliandolo, L. F. **Dec. 2002**. *Dynamics of Glassy Systems*. arXiv: cond-mat/0210312.

[106] Parisi, G. **May 2006**. "Spin Glasses and Fragile Glasses: Statics, Dynamics, and Complexity." In: *Proceedings of the National Academy of Sciences of the United States of America* 103.21, pp. 7948–7955. ISSN: 0027-8424. DOI: 10.1073/pnas.0601120103.

[107] Anderson, P. W. **Mar. 1988**. "Spin Glass II: Is There a Phase Transition?" In: *Physics Today* 41.3, pp. 9–9. ISSN: 0031-9228. DOI: 10.1063/1.2811336.

[108] Mulder, C. A. M. et al. **Feb. 1981**. "Susceptibility of the Cu Mn Spin-Glass: Frequency and Field Dependences." In: *Physical Review B* 23.3, pp. 1384–1396. ISSN: 0163-1829. DOI: 10.1103/PhysRevB.23.1384.

[109] Anderson, P. W. **Mar. 1990**. "Spin Glass VII: Spin Glass as Paradigm." In: *Physics Today* 43.3, pp. 9–11. ISSN: 0031-9228. DOI: 10.1063/1.2810479.

[110] Katzgraber, H. G. et al. **June 2006**. "Universality in Three-Dimensional Ising Spin Glasses: A Monte Carlo Study." In: *Physical Review B* 73.22, p. 224432. ISSN: 1098-0121, 1550-235X. DOI: 10.1103/PhysRevB.73.224432.

[111] Sachdev, S. **Apr. 2011**. *Quantum Phase Transitions*. Second. Cambridge University Press. ISBN: 978-0-521-51468-2 978-0-511-97376-5. DOI: 10.1017/CBO9780511973765.

[112] Chamberlin, R. V. et al. **Mar. 1984**. "Time Decay of the Remanent Magnetization in Spin-Glasses." In: *Physical Review Letters* 52.10, pp. 867–870. DOI: 10.1103/PhysRevLett.52.867.

[113] Kohlrausch, R. **1854**. "Theorie Des Elektrischen Rückstandes in Der Leidener Flasche." In: *Annalen der Physik und Chemie* 167.2, pp. 179–214. ISSN: 00033804. DOI: 10.1002/andp.18541670203.

[114] Phillips, J. C. **Sept. 1996**. "Stretched Exponential Relaxation in Molecular and Electronic Glasses." In: *Reports on Progress in Physics* 59.9, pp. 1133–1207. ISSN: 00344885. DOI: 10.1088/0034-4885/59/9/003.

[115] Klafter, J. and Shlesinger, M. F. **Feb. 1986**. "On the Relationship among Three Theories of Relaxation in Disordered Systems." In: *Proceedings of the National Academy of Sciences* 83.4, pp. 848–851. DOI: 10.1073/pnas.83.4.848.

[116] De Dominicis, C. et al. **1985**. "Stretched Exponential Relaxation in Systems with Random Free Energies." In: *Journal de Physique Lettres* 46.11, pp. 463–466. ISSN: 0302-072X. DOI: 10.1051/jphyslet:019850046011046300.

[117] Choi, J. et al. "Depolarization Dynamics in a Strongly Interacting Solid-State Spin Ensemble." In: DOI: 10.1103/PhysRevLett.118.093601.

[118] Lüschen, H. P. et al. **Mar. 2017**. "Signatures of Many-Body Localization in a Controlled Open Quantum System." In: *Physical*

Review X 7.1, p. 11034. ISSN: 21603308. DOI: 10.1103/PhysRevX.7.011034.

[119] Everest, B. et al. **Jan. 2017**. "Role of Interactions in a Dissipative Many-Body Localized System." In: *Physical Review B* 95.2, p. 024310. DOI: 10.1103/PhysRevB.95.024310.

[120] Schachenmayer, J. et al. **Feb. 2015**. "Many-Body Quantum Spin Dynamics with Monte Carlo Trajectories on a Discrete Phase Space." In: *Physical Review X* 5.1, p. 011022. ISSN: 2160-3308. DOI: 10.1103/PhysRevX.5.011022.

[121] Emch, G. G. **1966**. "Non-Markovian Model for the Approach to Equilibrium." In: DOI: 10.1063/1.1705023.

[122] Radin, C. **Oct. 1970**. "Approach to Equilibrium in a Simple Model." In: *Journal of Mathematical Physics* 11.10, pp. 2945–2955. ISSN: 00222488. DOI: 10.1063/1.1665079.

[123] Dmitriev, D. V. et al. **2002b**. "The Anisotropic Heisenberg Model in a Transverse Magnetic Field." In: *Journal of Experimental and Theoretical Physics* 95.3, pp. 538–549. ISSN: 1090-6509. DOI: 10.1134/1.1513828. arXiv: cond-mat/0204590.

[124] Pal, A. and Huse, D. A. **Nov. 2010**. "Many-Body Localization Phase Transition." In: *Physical Review B* 82.17, p. 174411. DOI: 10.1103/PhysRevB.82.174411.

[125] De Luca, A. and Scardicchio, A. **Feb. 2013**. "Ergodicity Breaking in a Model Showing Many-Body Localization." In: *EPL (Europhysics Letters)* 101.3, p. 37003. ISSN: 0295-5075, 1286-4854. DOI: 10.1209/0295-5075/101/37003.

[126] Luitz, D. J. et al. **Feb. 2015**. "Many-Body Localization Edge in the Random-Field Heisenberg Chain." In: *Physical Review B* 91.8, p. 081103. ISSN: 1098-0121, 1550-235X. DOI: 10.1103/PhysRevB.91.081103.

[127] Slagle, K. et al. **July 2016**. "Disordered XYZ Spin Chain Simulations Using the Spectrum Bifurcation Renormalization Group." In: *Physical Review B* 94.1, p. 014205. ISSN: 24699969. DOI: 10.1103/PhysRevB.94.014205.

[128] Hazzard, K. R. A. et al. **Nov. 2014**. "Many-Body Dynamics of Dipolar Molecules in an Optical Lattice." In: *Physical Review Letters* 113.19, p. 195302. DOI: 10.1103/PhysRevLett.113.195302.

[129] Cho, H. et al. **Dec. 2006**. "Decay of Highly Correlated Spin States in a Dipolar-Coupled Solid: NMR Study of Ca F 2." In: *Physical Review B* 74.22, p. 224434. ISSN: 1098-0121, 1550-235X. DOI: 10.1103/PhysRevB.74.224434.

[130] Pekker, D. et al. **Mar. 2014**. "Hilbert-Glass Transition: New Universality of Temperature-Tuned Many-Body Dynamical Quantum Criticality." In: *Physical Review X* 4.1, p. 011052. ISSN: 2160-3308. DOI: 10.1103/PhysRevX.4.011052.

[131] You, Y.-Z. et al. **Mar. 2016**. "Entanglement Holographic Mapping of Many-Body Localized System by Spectrum Bifurcation

Renormalization Group." In: *Physical Review B* 93.10, p. 104205. ISSN: 2469-9950, 2469-9969. DOI: 10.1103/PhysRevB.93.104205.

[132] Kirkpatrick, S. and Sherrington, D. **June 1978**. "Infinite-Ranged Models of Spin-Glasses." In: *Physical Review B* 17.11, pp. 4384–4403. DOI: 10.1103/PhysRevB.17.4384.

[133] Mézard, M. et al. **Mar. 1984**. "Nature of the Spin-Glass Phase." In: *Physical Review Letters* 52.13, pp. 1156–1159. ISSN: 0031-9007. DOI: 10.1103/PhysRevLett.52.1156.

[134] Mori, T. et al. **May 2018**. "Thermalization and Prethermalization in Isolated Quantum Systems: A Theoretical Overview." In: *Journal of Physics B: Atomic, Molecular and Optical Physics* 51.11, p. 112001. ISSN: 0953-4075. DOI: 10.1088/1361-6455/aabcdf.

[135] D'Alessio, L. et al. **May 2016**. "From Quantum Chaos and Eigenstate Thermalization to Statistical Mechanics and Thermodynamics." In: *Advances in Physics* 65.3, pp. 239–362. ISSN: 0001-8732, 1460-6976. DOI: 10.1080/00018732.2016.1198134. arXiv: 1509.06411.

[136] Swingle, B. **Oct. 2018**. "Unscrambling the Physics of Out-of-Time-Order Correlators." In: *Nature Physics* 14.10, pp. 988–990. ISSN: 1745-2481. DOI: 10.1038/s41567-018-0295-5.

[137] Reimann, P. **Nov. 2008**. "Foundation of Statistical Mechanics under Experimentally Realistic Conditions." In: *Physical Review Letters* 101.19, p. 190403. ISSN: 0031-9007, 1079-7114. DOI: 10.1103/PhysRevLett.101.190403.

[138] Tasaki, H. **June 2016**. "Typicality of Thermal Equilibrium and Thermalization in Isolated Macroscopic Quantum Systems." In: *Journal of Statistical Physics* 163.5, pp. 937–997. ISSN: 1572-9613. DOI: 10.1007/s10955-016-1511-2.

[139] Brydges, T. et al. **Apr. 2019**. "Probing Rényi Entanglement Entropy via Randomized Measurements." In: *Science* 364.6437, pp. 260–263. DOI: 10.1126/science.aau4963.

[140] Ishii, T. and Mori, T. **July 2019**. "Strong Eigenstate Thermalization within a Generalized Shell in Noninteracting Integrable Systems." In: *Physical Review E* 100.1, p. 012139. ISSN: 2470-0045, 2470-0053. DOI: 10.1103/PhysRevE.100.012139.

[141] Cassidy, A. C. et al. **Apr. 2011**. "Generalized Thermalization in an Integrable Lattice System." In: *Physical Review Letters* 106.14, p. 140405. DOI: 10.1103/PhysRevLett.106.140405.

[142] Evers, F. and Mirlin, A. D. **Oct. 2008**. "Anderson Transitions." In: *Reviews of Modern Physics* 80.4, pp. 1355–1417. DOI: 10.1103/RevModPhys.80.1355.

[143] Žnidarič, M. et al. **Feb. 2008**. "Many-Body Localization in the Heisenberg XXZ Magnet in a Random Field." In: *Physical Review B* 77.6, p. 064426. DOI: 10.1103/PhysRevB.77.064426.

[144] Günther, H. **2013f**. *NMR Spectroscopy: Basic Principles, Concepts and Applications in Chemistry*. Third, completely revised and

updated edition. Weinheim: Wiley-VCH. ISBN: 978-3-527-33000-3 978-3-527-33004-1.

[145] Álvarez, G. A. et al. **Aug. 2015**. "Localization-delocalization transition in the dynamics of dipolar-coupled nuclear spins." In: *Science* 349.6250, p. 846. URL: http://science.sciencemag.org/content/349/6250/846.abstract.

[146] Waldherr, G. et al. **2014h**. "Quantum error correction in a solid-state hybrid spin register." In: *Nature* 506.7487, pp. 204–207. ISSN: 1476-4687. URL: https://doi.org/10.1038/nature12919.

[147] Yan, B. et al. **Sept. 2013**. "Observation of dipolar spin-exchange interactions with lattice-confined polar molecules." In: *Nature* 501.7468, pp. 521–525. DOI: 10.1038/nature12483. URL: http://dx.doi.org/10.1038/nature12483.

[148] de Paz, A. et al. **Oct. 2013**. "Nonequilibrium Quantum Magnetism in a Dipolar Lattice Gas." In: *Phys. Rev. Lett.* 111 (18), p. 185305. DOI: 10.1103/PhysRevLett.111.185305. URL: https://link.aps.org/doi/10.1103/PhysRevLett.111.185305.

[149] Baier, S. et al. **2016k**. "Extended Bose-Hubbard models with ultracold magnetic atoms." In: *Science* 352.6282, pp. 201–205. ISSN: 0036-8075. DOI: 10.1126/science.aac9812. URL: https://science.sciencemag.org/content/352/6282/201.

[150] Abanin, D. A. and Papić, Z. **2017k**. "Recent Progress in Many-Body Localization." In: *Annalen der Physik* 529.7, p. 1700169. ISSN: 1521-3889. DOI: 10.1002/andp.201700169.

[151] Huse, D. A. et al. **July 2013**. "Localization-Protected Quantum Order." In: *Physical Review B* 88.1, p. 014206. ISSN: 1098-0121, 1550-235X. DOI: 10.1103/PhysRevB.88.014206.

[152] Chandran, A. et al. **Apr. 2014**. "Many-Body Localization and Symmetry-Protected Topological Order." In: *Physical Review B* 89.14, p. 144201. DOI: 10.1103/PhysRevB.89.144201.

[153] Khemani, V. et al. **Apr. 2017**. "Critical Properties of the Many-Body Localization Transition." In: *Physical Review X* 7.2, p. 021013. DOI: 10.1103/PhysRevX.7.021013.

[154] Morningstar, A. et al. **Sept. 2020**. "Many-Body Localization near the Critical Point." In: *Physical Review B* 102.12, p. 125134. DOI: 10.1103/PhysRevB.102.125134.

[155] Lenarčič, Z. et al. **Sept. 2020**. "Critical Behavior near the Many-Body Localization Transition in Driven Open Systems." In: *Physical Review Letters* 125.11, p. 116601. DOI: 10.1103/PhysRevLett.125.116601.

[156] Beugeling, W. et al. **Apr. 2014**. "Finite-Size Scaling of Eigenstate Thermalization." In: *Physical Review E* 89.4, p. 042112. DOI: 10.1103/PhysRevE.89.042112.

[157] Steinigeweg, R. et al. **Apr. 2014**. "Pushing the Limits of the Eigenstate Thermalization Hypothesis towards Mesoscopic Quantum Systems." In: *Physical Review Letters* 112.13, p. 130403.

ISSN: 0031-9007, 1079-7114. DOI: 10.1103/PhysRevLett.112.130403.

[158] Pietracaprina, F. et al. **Nov. 2018**. "Shift-Invert Diagonalization of Large Many-Body Localizing Spin Chains." In: *SciPost Physics* 5.5, p. 045. ISSN: 2542-4653. DOI: 10.21468/SciPostPhys.5.5.045.

[159] Yao, N. Y. et al. **Dec. 2014**. "Many-Body Localization in Dipolar Systems." In: *Physical Review Letters* 113.24, p. 243002.

[160] Gutman, D. B. et al. **June 2016**. "Energy Transport in the Anderson Insulator." In: *Physical Review B* 93.24, p. 245427. DOI: 10.1103/PhysRevB.93.245427.

[161] Rademaker, L. and Abanin, D. A. **Dec. 2020**. "Slow Nonthermalizing Dynamics in a Quantum Spin Glass." In: *Physical Review Letters* 125.26, p. 260405. ISSN: 0031-9007, 1079-7114. DOI: 10.1103/PhysRevLett.125.260405.

[162] Kjäll, J. A. et al. **Sept. 2014**. "Many-Body Localization in a Disordered Quantum Ising Chain." In: *Physical Review Letters* 113.10, p. 107204. DOI: 10.1103/PhysRevLett.113.107204.

[163] Laumann, C. R. et al. **Nov. 2014**. "Many-Body Mobility Edge in a Mean-Field Quantum Spin Glass." In: *Physical Review Letters* 113.20, p. 200405. ISSN: 0031-9007, 1079-7114. DOI: 10.1103/PhysRevLett.113.200405.

[164] Edwards, S. F. and Anderson, P. W. **May 1975**. "Theory of Spin Glasses." In: *Journal of Physics F: Metal Physics* 5.5, pp. 965–974. ISSN: 0305-4608. DOI: 10.1088/0305-4608/5/5/017.

[165] Anderson, P. W. **Aug. 1972**. "More Is Different." In: *Science* 177.4047, pp. 393–396. DOI: 10.1126/science.177.4047.393.

[166] Mott, S. N. **Nov. 1978**. "Metal–Insulator Transitions." In: *Physics Today* 31.11, pp. 42–47. ISSN: 0031-9228. DOI: 10.1063/1.2994815.

[167] Schuckert, A. and Knap, M. **Dec. 2020**. "Probing Eigenstate Thermalization in Quantum Simulators via Fluctuation-Dissipation Relations." In: *Physical Review Research* 2.4, p. 043315. DOI: 10.1103/PhysRevResearch.2.043315.

[168] Geier, K. T. and Hauke, P. **Apr. 2021**. *From Non-Hermitian Linear Response to Dynamical Correlations and Fluctuation-Dissipation Relations in Quantum Many-Body Systems*. DOI: 10.48550/arXiv.2104.03983. arXiv: 2104.03983 [cond-mat, physics:quant-ph].

[169] Parisi, G. **Dec. 2007**. "Spin Glass Theory: Numerical and Experimental Results in Three-Dimensional Systems." In: *Physica A: Statistical Mechanics and its Applications*. Disorder and Complexity 386.2, pp. 611–624. ISSN: 0378-4371. DOI: 10.1016/j.physa.2007.09.001.

[170] Veit, C. et al. **Feb. 2021**. "Pulsed Ion Microscope to Probe Quantum Gases." In: *Physical Review X* 11.1, p. 011036. DOI: 10.1103/PhysRevX.11.011036.

[171] Kim, H. et al. **Oct. 2016**. "In Situ Single-Atom Array Synthesis Using Dynamic Holographic Optical Tweezers." In: *Nature Communications* 7.1, p. 13317. ISSN: 2041-1723. DOI: 10.1038/ncomms13317.

[172] Endres, M. et al. **Nov. 2016**. "Atom-by-Atom Assembly of Defect-Free One-Dimensional Cold Atom Arrays." In: *Science* 354.6315, pp. 1024–1027. DOI: 10.1126/science.aah3752.

[173] Barredo, D. et al. **Nov. 2016**. "An Atom-by-Atom Assembler of Defect-Free Arbitrary Two-Dimensional Atomic Arrays." In: *Science* 354.6315, pp. 1021–1023. DOI: 10.1126/science.aah3778.

[174] de Léséleuc, S. et al. **Aug. 2019**. "Observation of a Symmetry-Protected Topological Phase of Interacting Bosons with Rydberg Atoms." In: *Science* 365.6455, pp. 775–780. DOI: 10.1126/science.aav9105.

[175] Barredo, D. et al. **2018j**. "Synthetic Three-Dimensional Atomic Structures Assembled Atom by Atom." In: *Nature* 561.7721, pp. 79–82. ISSN: 14764687. DOI: 10.1038/s41586-018-0450-2. arXiv: 1712.02727.

[176] Else, D. V. et al. **Mar. 2020**. "Discrete Time Crystals." In: *Annual Review of Condensed Matter Physics* 11.1, pp. 467–499. ISSN: 1947-5454, 1947-5462. DOI: 10.1146/annurev-conmatphys-031119-050658.

[177] Wilczek, F. **Oct. 2012**. "Quantum Time Crystals." In: *Physical Review Letters* 109.16, p. 160401. DOI: 10.1103/PhysRevLett.109.160401.

[178] Shapere, A. and Wilczek, F. **Oct. 2012**. "Classical Time Crystals." In: *Physical Review Letters* 109.16, p. 160402. DOI: 10.1103/PhysRevLett.109.160402.

[179] Choi, S. et al. **Mar. 2017**. "Observation of Discrete Time-Crystalline Order in a Disordered Dipolar Many-Body System." In: *Nature* 543.7644, pp. 221–225. ISSN: 1476-4687. DOI: 10.1038/nature21426.

[180] Zhang, J. et al. **Mar. 2017**. "Observation of a Discrete Time Crystal." In: *Nature* 543.7644, pp. 217–220. ISSN: 0028-0836.

[181] Rovny, J. et al. **May 2018**. "Observation of Discrete-Time-Crystal Signatures in an Ordered Dipolar Many-Body System." In: *Physical Review Letters* 120.18, p. 180603. DOI: 10.1103/PhysRevLett.120.180603.

[182] Mi, X. et al. **Nov. 2021**. "Time-Crystalline Eigenstate Order on a Quantum Processor." In: *Nature*, pp. 1–1. ISSN: 1476-4687. DOI: 10.1038/s41586-021-04257-w.

[183] Lazarides, A. and Moessner, R. **May 2017**. "Fate of a Discrete Time Crystal in an Open System." In: *Physical Review B* 95.19, p. 195135. DOI: 10.1103/PhysRevB.95.195135.

[184] Yao, N. Y. et al. **Jan. 2017**. "Discrete Time Crystals: Rigidity, Criticality, and Realizations." In: *Physical review letters* 118.3, p. 030401. ISSN: 1079-7114. DOI: 10.1103/PhysRevLett.118.030401.

ACKNOWLEDGMENTS

First, I would like to thank my supervisor Matthias Weidemüller who has persuaded me to come back to the Heidelberg Rydberg experiment for my Ph.D. thesis. I highly appreciate your great advice, the inspiration I took from our countless discussions, and the active and open research environment that you have provided in your group. I will always remember this special time in Heidelberg as a time of intense learning and research, but it was also a time of fun and it provided me the opportunity to meet amazing people. Without the support of these people, this work would not have been possible.

I would like to thank Markus Oberthaler for reviewing this thesis, and the other members of the committee Jörg Evers and Tilman Enss.

I am grateful for all the people involved in my collaborations, especially Martin Gärttner who has always helped with great insight into the theory of many-body physics and details of numerical simulations, Shannon Whitlock who has always shared his deep understanding and intuition of physics with me, and the groups of Antoine Browaeys and Kenji Ohmori who have realized amazing experiments.

Also, I would like to thank Gerhard Zürn who was essential to the success of the experiments and who has always helped in every possible way with problems related or unrelated to physics.

My special gratitude goes to Nithiwadee Thaicharoen, Clément Hainaut and Adrien Signoles whose support has helped tremendously, especially when facing very complex problems or for the preparation of manuscripts.

Thank you, Rydberg team, it was a pleasure to work with you: Sebastian Geier, working with you is always so productive and enjoyable, especially when we plan our next measurements in a bar in Paris. Philipp Schultzen, it was always a pleasure to work with you and dwell together deep into the physics of disordered spins even though you have never touched a mirror in the lab. Annika Tebben, it is amazing how you can be both, so talented and organized in the lab, and how you can be a nice person to hang out and have fun with. André Salzinger, thank you for all the creative ideas, for the music you play in the lab and for the noise you engineer to perturb the spins. Renato Ferracini Alves, I'm so grateful that you have had the patience to teach us all how to code python with style, we definitely need to meet in Brussels! Thank you, Adrian Braemer for the amazing discussion on symmetries and renormalization group flows, Miguel Ferreira Cao, for introducing me to the Rydberg physics experiment

and Eduard Braun, for helping on the last steps of this journey. I wish you all the best for the future of this experiment! I would also like to thank the Bachelor and Master students Alexander Müller, Theresa Gier, Haowei Li, Henrik Zahn, Maximilan Müllenbach, Moritz Hornung, Sebastian Bok, Carlos Brandl, Mathurin Choblet, David Grimshandl, Lorenz Luger, Charles Möhl, Julia Siegl and Karen Wadenpfuhl.

I would also like to thank Claudia Kraemer for the administrative support and the members of the IT department and the mechanic and electronic workshops.

I'm grateful for the funding of the graduate scholarship of the Heidelberg University (LGFG) and the monetary, technical and creative support of the Heidelberg Graduate School for Physics HGSFP, the International Max Planck Research School for Quantum Dynamics IMPRS-QD, the Collaborative Research Centre SFB ISOQUANT, the DFG Priority Program GiRyd, the FET flagship project PASQuanS, the Excellence Cluster STRUCTURES, and bwHPC (JUSTUS 2 cluster).

Finally, I would like to thank my friends and family who have always supported me over the last years. I thank my parents who taught me to recognize how exciting life is and to always stay curious and my brother with whom I can talk for hours about quantum thermalization, neuropathology, and life in general. Most importantly, thank you, Paula, for the amazing time we could share together, and that you have always been there for me.